frontiers | Research Topics

Mechanisms and early warning strategies of geotechnical disasters

Edited by
Bisheng Wu, Wenzhuo Cao and Guangjin Wang

Published in
Frontiers in Earth Science
Frontiers in Environmental Science

ISSN 1664-8714
ISBN 978-2-8325-4359-7
DOI 10.3389/978-2-8325-4359-7

About Frontiers

Frontiers is more than just an open access publisher of scholarly articles: it is a pioneering approach to the world of academia, radically improving the way scholarly research is managed. The grand vision of Frontiers is a world where all people have an equal opportunity to seek, share and generate knowledge. Frontiers provides immediate and permanent online open access to all its publications, but this alone is not enough to realize our grand goals.

Frontiers journal series

The Frontiers journal series is a multi-tier and interdisciplinary set of open-access, online journals, promising a paradigm shift from the current review, selection and dissemination processes in academic publishing. All Frontiers journals are driven by researchers for researchers; therefore, they constitute a service to the scholarly community. At the same time, the *Frontiers journal series* operates on a revolutionary invention, the tiered publishing system, initially addressing specific communities of scholars, and gradually climbing up to broader public understanding, thus serving the interests of the lay society, too.

Dedication to quality

Each Frontiers article is a landmark of the highest quality, thanks to genuinely collaborative interactions between authors and review editors, who include some of the world's best academicians. Research must be certified by peers before entering a stream of knowledge that may eventually reach the public - and shape society; therefore, Frontiers only applies the most rigorous and unbiased reviews. Frontiers revolutionizes research publishing by freely delivering the most outstanding research, evaluated with no bias from both the academic and social point of view. By applying the most advanced information technologies, Frontiers is catapulting scholarly publishing into a new generation.

What are Frontiers Research Topics?

Frontiers Research Topics are very popular trademarks of the *Frontiers journals series*: they are collections of at least ten articles, all centered on a particular subject. With their unique mix of varied contributions from Original Research to Review Articles, Frontiers Research Topics unify the most influential researchers, the latest key findings and historical advances in a hot research area.

Find out more on how to host your own Frontiers Research Topic or contribute to one as an author by contacting the Frontiers editorial office: frontiersin.org/about/contact

Mechanisms and early warning strategies of geotechnical disasters

Topic editors

Bisheng Wu — Tsinghua University, China

Wenzhuo Cao — Imperial College London, United Kingdom

Guangjin Wang — Kunming University of Science and Technology, China

Citation

Wu, B., Cao, W., Wang, G., eds. (2024). *Mechanisms and early warning strategies of geotechnical disasters*. Lausanne: Frontiers Media SA.

doi: 10.3389/978-2-8325-4359-7

Table of contents

frontiers | Frontiers in Earth Science

TYPE Original Research
PUBLISHED 19 January 2023
DOI 10.3389/feart.2023.1123529

OPEN ACCESS

EDITED BY
Guangjin Wang,
Kunming University of Science and Technology, China

REVIEWED BY
Guanxi Yan,
The University of Queensland, Australia
Yulong Chen,
China University of Mining and Technology, China

*CORRESPONDENCE
Shangwei Wu,
2017027@cqust.edu.cn
Jia Qin,
xizaorengui@sina.com
Xiaohua Liu,
2021207059@cqust.edu.cn

SPECIALTY SECTION
This article was submitted to Environmental Informatics and Remote Sensing, a section of the journal Frontiers in Earth Science

RECEIVED 14 December 2022
ACCEPTED 09 January 2023
PUBLISHED 19 January 2023

CITATION
Jing X, Wu S, Qin J, Li X, Liu X, Zhang Y, Mao J and Nie W (2023), Multiscale mechanical characterizations of ultrafine tailings mixed with incineration slag. *Front. Earth Sci.* 11:1123529. doi: 10.3389/feart.2023.1123529

Multiscale mechanical characterizations of ultrafine tailings mixed with incineration slag

Xiaofei Jing[1], Shangwei Wu[1]*, Jia Qin[2]*, Xiaoshuang Li[3], Xiaohua Liu[1]*, Yuanzhen Zhang[1], Jingxin Mao[1] and Wen Nie[4]

[1]School of Safety Engineering, Chongqing University of Science and Technology, Chongqing, China, [2]Chongqing Chuandongnan Survey & Design Institute Co., Ltd., Chongqing, China, [3]School of Civil Engineering, Shaoxing University, Shaoxing, China, [4]Key Laboratory of Safety and Health for Metal Mines, Maanshan, China

Adding a type of municipal solid waste (incinerator slag) into ultrafine tailings can effectively enhance the mechanical properties of tailings. With an aim to study the macro- and micro-mechanical properties of the tailings slag mixture (TSM), the strength parameters (internal friction angle, cohesion) and micro-mechanical properties with different slag contents were analyzed by geotechnical experiments and particle flow simulations, respectively. The macroscale experimental results demonstrated that the strength parameters of TSM were much higher than that of tailings. Strength parameters also showed non-linear-rising trends with increasing slag content. For the slag content of 40%, the maximum cohesiveness of TSM was determined at 65.2 kPa, and the corresponding friction angle was 39.9°C. Furthermore, the Particle Flow Code (PFC) micro-simulation software was used to analyze the micro-mechanical characteristics of the TSM at different slag contents. The microscale simulation outcomes indicated that the particle transport, particularly in their moving directions, became increasingly chaotic with an increase in the slag content; also, the slag particles significantly impacted the shear processing zone of the TSM. These experimental and numerical results brought more scientific insights into the shear failure mechanism of TSM.

KEYWORDS

ultrafine tailings, municipal solid waste, incineration slag, tailings-slag mixture (TSM), macro- and micro-mechanical characteristics

1 Introduction

In recent years, the number of ultrafine tailings reservoirs have been increasing gradually (Li et al., 2019; Shi et al., 2020; Han et al., 2022). However, the research efforts on ultrafine tailings particles are still inadequate, thereby inconducive to future sustainable development (Jing et al., 2019; Jing et al., 2021; Liu et al., 2021; Wang et al., 2022). The physical and chemical properties and engineering characteristics of slag show that slag exhibits aggregate properties. Additionally, it has many advantages, such as its high production, the massive reserve of resources, small organic content, and no radioactive harm (Huber et al., 2020). As a result, sustainable objectives, including effectively reducing slag accumulation and improving its recycling value, have become two main focuses in social research (Kumar and Singh, 2021; Joseph et al., 2022). However, the macro-mechanical properties and micro-mechanism of ultra-fine tailings particle reinforcement have not been comprehensively studied by far (Wang et al., 2020). Still, it needs to be continuously explored and further investigated in depth. Therefore,

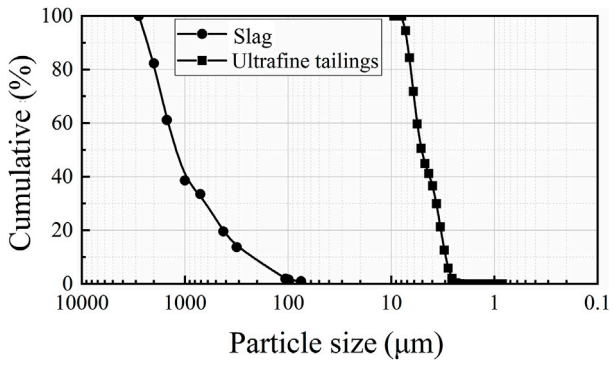

FIGURE 1
Particle size distributions of ultrafine tailings and slag particles.

characterizing the mechanical properties and failure mechanism of TSM is a pressing issue on demand of a series of urgent and compelling resolutions in geotechnical engineering.

TSM has similar structural characteristics to the soil-rock mixture (SRM). As the slag particles have a certain cohesion compared with ordinary rocks, the difference in material characteristics affects the mechanical properties of TSM. Most of the physical and mechanical properties of the SRM have been studied in three ways: laboratory testing, numerical simulation, and theoretical analysis (Chen et al., 2021; Li et al., 2022). Xing et al. (2020) used particle flow software to simulate the triaxial test numerically and elucidated the micro-mechanism of SRM with different rock content. Yin et al. (2011) used PFC discrete element particle flow to perform a micro-simulation of the triaxial test and additionally incorporated it with macroscopic mechanical properties to study the micro characteristics of hybrids. Jo et al. (2011) and Liu (2021) used PFC-2D to establish particle clusters of different shapes and the correlation between particle shape and macroscopic mechanical properties and deformation characteristics. Wang, (2017) studied the SRM through theoretical analysis, laboratory experiments, digital image processing, and PFC numerical simulation. The particle size of slag particles is different from that of ultrafine tailings, so there are similarities between TSM and SRM in terms of particle size scale differences. Therefore, the structure of TSM can refer to the structure analysis of SRM.

In this paper, the physical properties of TSM were primarily investigated. The microscopic failure deformation characteristic of TSM was subsequentially analyzed based on the observations from macroscopic experiments and microscopic numerical simulations. The microstructural variation of TSM resulting from various mixing ratios of tailings and slag particles was also studied. After collecting two experimental materials (alumina ultrafine-grained tailings from a mining area in Nanchuan, Chongqing, China, and incinerator slag from a domestic waste power plant in Chongqing), the triaxial tests were carried out on the slag-curing tailings specimens to unveil the influence of incinerator slag on the mechanical characteristics of TSM at macroscale. With the numerical simulation software of discrete element method (PFC, Itasca Inc.), the micro-mechanical properties of TSM were further studied at microscale to explore the micro-mechanics in TSM.

2 Study the shear strength characteristics of TSM

2.1 Fundamental characteristics of experimental materials

The fundamental properties of ultrafine-grained tailings and slag materials were examined independently by following the "Geotechnical Test Method Standard" (GB/T50123-2019, the Natural Standard of China). The particle size distributions of both ultrafine tailings and incinerator slag are shown in Figure 1. The standard testing outcomes are summarized in Table 1, which provides *in-situ* dry density, moisture content, and Atterberg limits for laboratory test preparation. The range of optimal moisture content of tailings reservoirs is 20%–24% (Yang and Li, 2020). In consideration of the impact of the *in-situ* tailings specimen's moisture content, the moisture content of the tailings-slag mixture specimen was adjusted to 20%, which is smaller than the moisture content of the *in-situ* tailings specimen in tailings reservoirs.

TSM and SRM both have a significant degree of structural similarity. Investigations on SRM have shown that a general coarse particle content of 30% and 70% (*via* mass fraction, mass/mass) are the two so-defined characteristics of SRM (Simoni and Houlsby, 2006); similarly, the slag contents of 0%–70% were selected in this study, as the primary research scope serving for TSM rather than SRM. The particle size distributions of the TSM in eight different slag contents (0%–70%) are shown in Figure 2. The corresponding dry densities, consolidation compression coefficients, and permeability coefficients in Table 2 were experimentally determined by following the "Geotechnical Test Method Standard" (GB/T50123-2019, the natural standard of China).

2.2 Triaxial tests

The triaxial tests in this study adopted the TSZ-2 series of automatic triaxial instruments, and the tested specimen dimensions were 61.8 mm in diameter and 125 mm in height. The drained shear tests, also known as consolidated-drained (CD), were carried out by following triaxial testing procedures to determine the physical and mechanical parameters of the tested specimens. The testing steps in detail are as follows:

(1) Preparing the triaxial specimens by mixing slag and tailings at mass ratios of 0%, 10%, 20%, 30%, 40%, 50%, 60%, and 70%, respectively; after adding slag to the tailings according to the aforementioned slag contents, then adding distilled water until the specimen moisture content reaching 20%;
(2) Checking and preparing the triaxial test instrument according to the instructions in the manual;
(3) After the installation of the specimens, saturating each tested specimen with a uniform saturation time of 1 h, followed by a Skempton B-test until the B = 0.98, also as known as the pore pressure coefficient;
(4) Three values of triaxial cell pressure, including confining pressure = 100 kPa/200 kPa/300 kPa, were selected in the controlling-acquisition interface of these triaxial tests on a computer; the mechanical tests were then initiated once the

TABLE 1 Material physics indicators.

Material	*In-situ* moisture content (%)	Maximum dry density	Liquid limits	Plastic limit
Ultrafine tailings	23	1.93 g/cm^3	44.65%	36.70%
Slag	16.8	1.61 g/cm^3	—	—

TABLE 2 Fundamental and mechanical properties of TSM in different slag contents.

Slag content (%)	0	10	20	30	40	50	60	70
Dry density (g/cm^3)	1.61	1.65	1.70	1.75	1.80	1.85	1.81	1.85
Compression coefficient a_v (MPa^{-1})	0.31	0.27	0.30	0.23	0.24	0.29	0.27	0.25
Permeability coefficient (10^{-4} cm/s)	0.09	0.15	0.18	0.17	0.21	1.63	2.02	4.23

TABLE 3 Triaxial test results.

Slag content (%)	Shear strength (kPa)			Internal friction angle φ (°)	Cohesion c (kPa)
	100	200	300		
0	245.25	460.18	655.62	30.43	12.40
10	284.50	477.33	703.16	30.77	19.70
20	455.58	789.05	1,131.20	38.91	27.80
30	600.72	972.10	1,340.93	40.48	53.30
40	690.54	908.22	1,385.60	39.90	65.20
50	798.37	1,280.10	1770.30	45.10	64.20
60	735.36	1,230.20	1738.90	45.64	47.10
70	915.60	1,119.90	1866.40	45.97	56.10

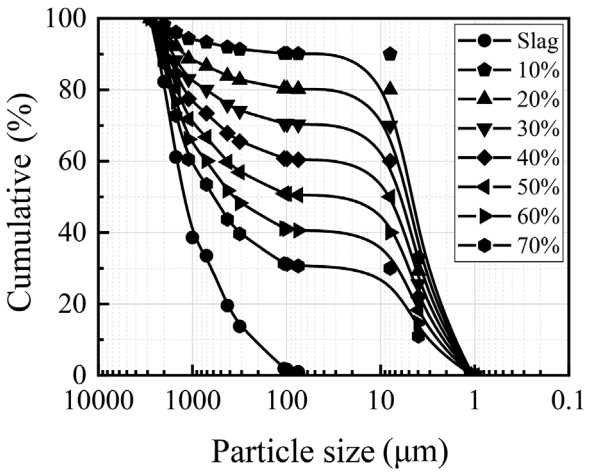

FIGURE 2
Particle size distributions of TSM with various slag content (0%–70%).

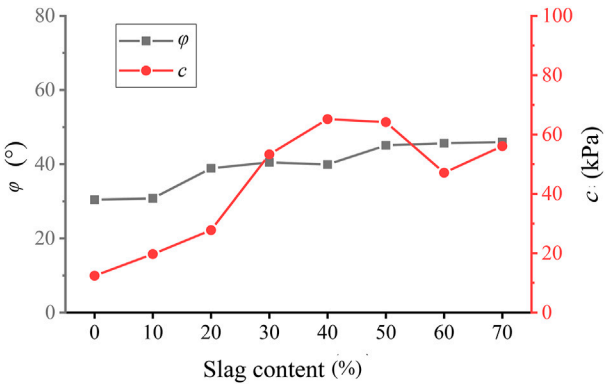

FIGURE 3
The shear strength parameters of TSM varying with slag content.

settings and parameters had been established; the strain rate of 0.08 mm/min was achieved by continuously adjusting through the operation interface until shear failure occurred;

(5) The datasets of stress and deformation were instantaneously saved in the computer from the beginning to the end of the test.

2.2.1 Triaxial test results

Table 3 shows the results of the triaxial test. The shear strength of seven TSM specimens under the previously introduced loading

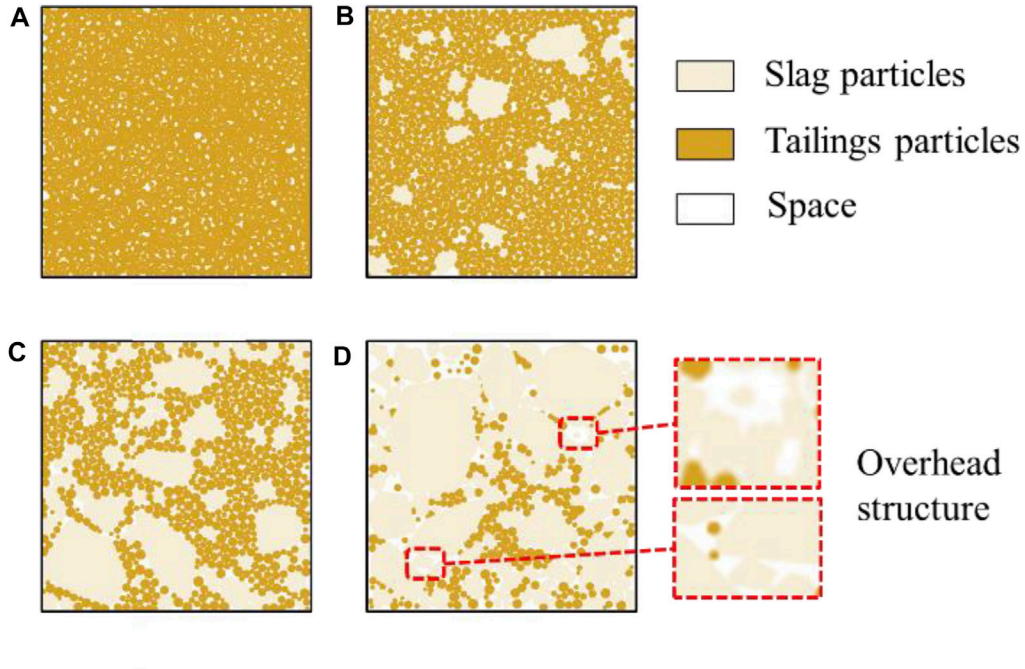

FIGURE 4
Schematic diagrams of TSM microstructure analysis.

conditions was higher than that of pure ultrafine tailings. The shear strength was increased with the increase in slag content. When the slag content reached 50%, the corresponding shear strengths under 100 kPa, 200 kPa, and 300 kPa pressure loads were 798.37 kPa, 1,280.1 kPa, and 1770.3 kPa, respectively. As for the slag content of 60%, the shear strength slightly decreased compared to the slag content of 50%. Except that the shear strength reduction was minor with increasing the slag content of TSM from 50% to 60%, it was still able to observe and elucidate that the continuous increase in slag content led to the shear strength enhancement.

Figure 3 shows that the internal friction (φ) and cohesion (c) of TSM were greater than those of pure ultrafine tailings. When the slag content was between 20% and 50%, the internal friction angle and cohesion of TSM gradually increased, while the internal friction angle and cohesion increased progressively, reaching 40%–50%. When slag content approached 60%, the cohesion suddenly dropped to 45.28 kPa. Overall, the TSM internal friction angle monotonically increased with increasing slag content. In contrast, it could not observe such a monotonic increasing relationship between the TSM cohesion and slag content, as there were two turning points at the slag contents of 40% and 60%. Despite those two turning points, the TSM cohesion could be increased by adding more slag in tailings.

Figure 4 illustrates the TSM microstructure, including the morphology, structural characteristics, and mechanical properties of both tailings and slag. According to the significant friction angle in slag, the addition of slag could influence the shear motion of TSM when the slag content was in a low range (0%–30%). As the overall TSM microstructure was more similar to the pure ultrafine tailings, the low range of slag content had less influence on the TSM cohesion (see Figure 4A, B). With increasing slag content up to 40%–50%, the ultrafine tailings and slag particles in the TSM could not contact each other to form an excellent interlocking-type microstructure, as shown in Figure 4C. Therefore, the physical and mechanical properties of the TSM should be influenced by the interparticle interactions between ultrafine tailings and slag. When the slag content exceeded 60%, the cohesion dropped sharply, and a turning point of the internal friction angle could be found. Due to the high slag content leading to the TSM microstructure mainly comprised of the slag microstructure, ultrafine tailings had minor contributions to such microstructures, as shown in Figure 4D. As a result, the tailings and slag particles were squeezed to move, consequentially forming a relatively unstable microstructure of TSM. In summary, the TSM microstructure evolvement induced by varying tailings and slag contents depended on the slag and tailings microstructures. Specifically, the coarse slag particles separated by surrounding ultrafine tailings resulted in inconsistently monotonic increases in TSM cohesion; i.e., the TSM cohesion was significantly reduced for a range of high slag content (50%–70%).

2.2.2 Analysis and comparison of shear strength characteristics

The shear strength parameters of TSM were much higher than that of pure ultrafine tailings. TSM has similar structural characteristics to the SRM. This section compares the shear strength parameters determined by the triaxial tests with the shear strength parameters obtained from the previously published literature of the relevant SRM. The internal friction angle of TSM exhibits an upward trend with the increase of slag content, similar to the experimental observations

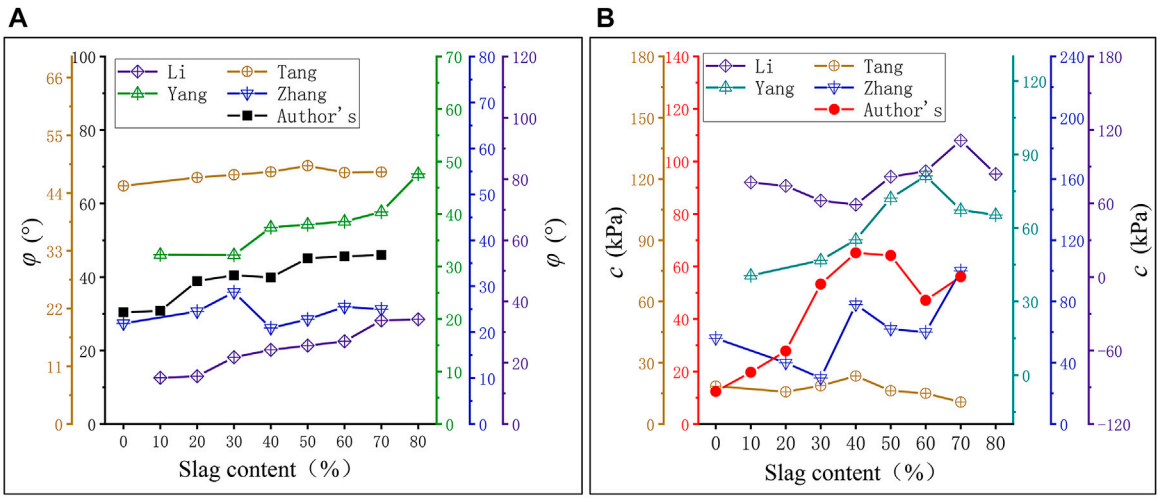

FIGURE 5
Comparison of shear strength parameters (TSM versus RSM): **(A)** The relationship between slag content and internal friction angle, **(B)** The relationship between slag content and cohesion.

reported by Tang et al. (2018), Zhang et al., 2021, and Li et al. (2007). Those observed trends are almost identical (see Figure 5A), whereas the only divergence is in the different slopes of the friction angle-slag content correlations when slag content is over 10%. It indicates that adding slag significantly affects the internal friction angle of TSM for a value of slag content higher than 10%.

The TSM cohesions measured by the triaxial tests are compared with those of the relevant SRM literature, as shown in Figure 5B. The results show that the cohesions of TSM gradually increased with increasing slag content. When the slag content is less than 40%, its strengthening tendency resembles the experimental results provided by Yang et al. (2016); When the slag content is higher than or equal to 40%, the trend seems closer to that presented by Zhang et al. (2021).

In assistance with analyzing the change of shear strength parameters compared to that of SRM, it is able to conclude that when the slag content is in a lower range (0%–20%), TSM is in a relatively dense microstructure containing limited numbers of slag particles in contact, the cohesion of TSM mainly depends on the tailings content and density, as shown in Figure 4A, B. When the slag content is in an intermediate range (30%–60%), the TSM microstructure exhibits a slag skeleton whose void spaces are filled with tailing particles (see Figure 4B, C). It also implies that those slag particles play a leading role in providing the skeleton stress during the triaxial shear test under the consolidated-drained condition. Until the triaxial loading action squeezes most fine particles out of the unstable slag skeleton, slag particles start to contact each other in order to form particle-particle interlocks. Therefore, the shear strength parameters of slag particles differ from that of the SRM due to the different material compositions and microstructural development (TSM versus SRM).

In conclusion, the inclusion of slag significantly increases the TSM shear strength, including both friction angle and cohesion, based on the experimental results presented in this study. The primary reason was that the material compositions and microstructure of slag skeleton have more decisive effects on the cohesiveness of pure ultrafine tailings in comparison to that of ordinary waste rock.

3 Manuscript formatting numerical simulation of micro-mechanical characteristics of the tailings-slag mixture

3.1 Development of numerical model by particle-discrete element method

3.1.1 Numerical models and element selection

The numerical simulation of the standard triaxial test in this research project was mainly divided into the following parts:

(1) The PFC-2D of the standard triaxial shear test was a well-developed model; the simulation settings included the left and right boundaries in modeling the flexible wall in the horizontal direction (see walls 3# and 4# in Figure 6A), the top and bottom boundaries in modeling the loading plate in the vertical direction (see the walls 1# and 2# in Figure 6A), the tested specimen in the spatial dimensions of 61.8 mm × 125 mm (diameter × length); to eliminate the impacts of friction between the walls and particles, the values of tangential contact stiffness and wall friction were set zero;
(2) In simulating the standard triaxial shear test, the left and right flexible walls (3# and 4#) were imposed by the stress boundary conditions to emulate the minimum principal stress (σ_3) in the standard triaxial test;
(3) The top and bottom loading plates (1# and 2#) were also imposed by the stress boundary conditions to emulate the mechanical loading device applying the maximum principal stress (σ_1) in the standard triaxial test.

Figure 6A shows the modeling setup of the standard triaxial test established in this study. Since the strength and stiffness of the TSM-particle skeleton were significantly more than that of the ultrafine tailings matrix, it was more applicable to employ clump clusters to model irregular slag particles for this custom-designed standard

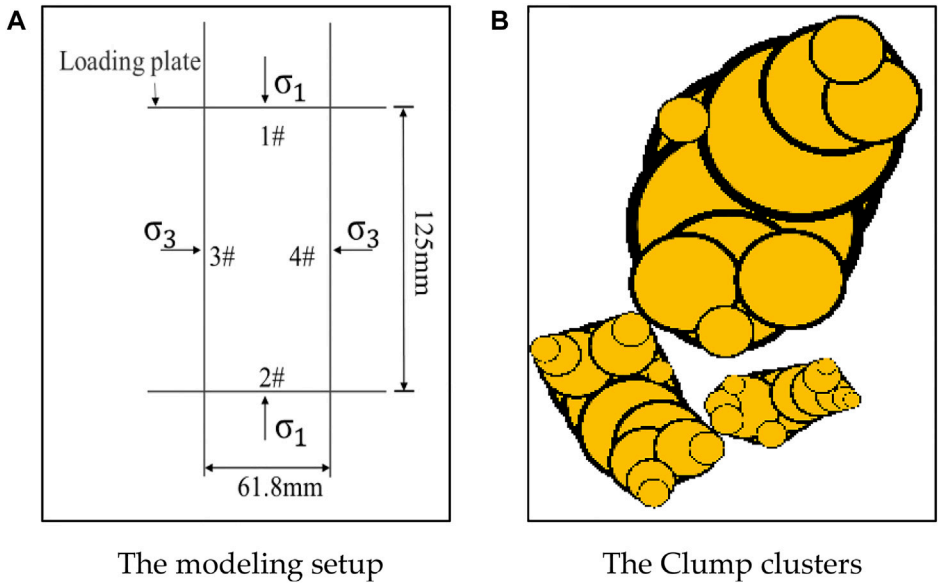

FIGURE 6
Numerical simulation model for standard triaxial tests: **(A)** The modeling setup, **(B)** The clump clusters.

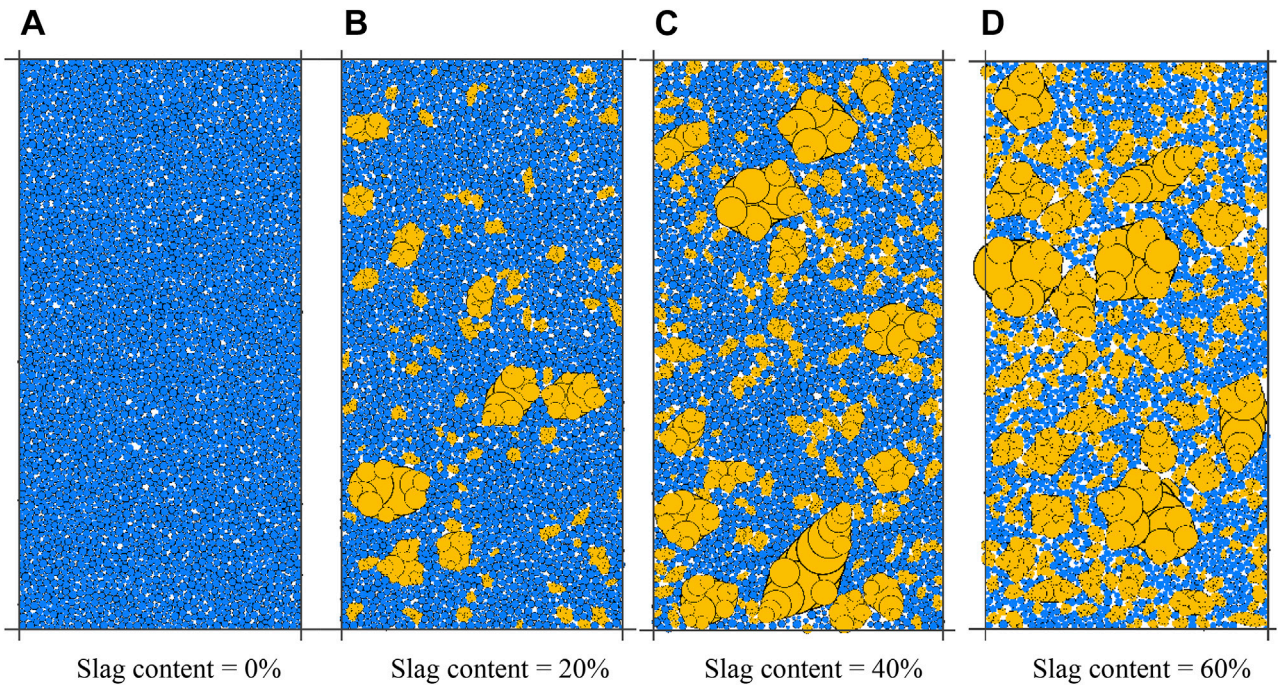

FIGURE 7
TSM specimens in different slag contents (0%–60%) generated by PFC-2D: **(A)** slag content = 0%, **(B)** slag content = 20%, **(C)** slag content = 40%, and **(D)** slag content = 60%.

triaxial simulation. Figure 6B shows an instance of the clump clusters generated in PFC-2D.

This numerical simulation adopted the same material settings and boundary and loading conditions as the standard triaxial test previously introduced (e.g., the material properties, mechanical parameters, boundary conditions, and loading rate). The modeled TSM specimens with a slag content of 0%, 20%, 40%, and 60% were digitally reconstructed based on the slag contents of the TSM specimens in the standard triaxial test. However, due to a large amount of ultra-fine particles in the simulating domain, the

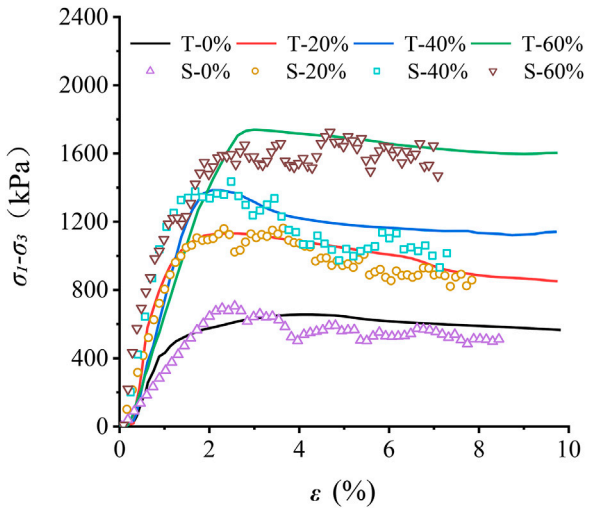

FIGURE 8
The deviator stress-strain curves of TSM specimens with four slag contents provided by the standard triaxial tests (T) and numerically simulated triaxial tests (S).

computational expense was significantly high, further leading to a relatively low computational efficiency. To overcome this issue, slag particles smaller than 0.5 mm were terminated to be generated in the simulating domain, according to the slag particle size of 0.5–1 mm in Figure 1. With this particle packing scheme available in PFC-2D (discrete element method), the particle-package models having different slag contents were eventually established, as shown in Figure 7, to study the influence of various slag contents on the mechanical properties of TSM.

3.1.2 Determination of micro-mechanical parameters for the simulated TSM specimens

For numerically modeling the TSM specimens using PFC-2D, the macroscopic mechanical behavior of the numerically simulated TSM specimens depends on the microscopic parameters, such as particle size, interparticle bonding modulus, interparticle bonding strength, interparticle bonding stiffness ratio, etc.; i.e., the microscopic parameters have significant effects on the macroscopic parameters of the mechanical constitutive relationship, including friction angle, cohesion, peak shear strength, Young's elastic modulus, Poisson's ratio, etc. (Xu and Ren, 2014; Feng et al., 2021).

In order to replicate the standard triaxial test by this newly established numerical model, the deviator stress-strain curves determined by both physical tests and numerical simulations should mutually agree well. The mechanical loading conditions, such as the vertical loading rate and confining pressure, were identically set to the discrete element numerical simulation in PFC-2D. The deviator stress-strain curves and macroscopic mechanical parameters were obtained through the standard triaxial tests (see T-labeled deviator stress-strain curves in Figure 8). Based on the experimental results, a group of micro-mechanical parameters was initially approximated for the numerical simulation of the standard triaxial test. Then, these parameters were repeatedly adjusted by following the "trial and error" method until the macroscopic mechanical characteristics of the tested TSM specimens were obtained with these approximated microscopic parameters. The most suitable micro-mechanical parameters were finally determined by continuously updating the values of these parameters after iteratively comparing the simulated outcomes with the experimental results. The fundamental and micro-mechanical parameters of the TSM specimens selected in this simulation are given in Table 4.

3.2 Analysis and discussions of numerical simulation results

3.2.1 Comparison of deviator stress-strain curve between experiment and simulation

As aforementioned, the mechanical loading conditions of the discrete element numerical simulation were identical to the loading rates and confining pressure applied in the standard triaxial tests. Therefore, to evaluate if the numerical model can effectively simulate the actual tests, the deviator stress-strain curves collected from both experimental tests and numerical simulations are henceforth compared. Also, it is convincing that the macroscopic mechanical parameters of the TSM specimens could be accurately determined when there were good agreements between experimental and numerical outcomes.

As for the simulated constraint pressure of 300 kPa, the deviator stress-strain curves outputted from experimental and numerical triaxial tests are compared in Figure 8. When the slag content was in a lower range of 0%–20%, the deviator stress continued to grow with the increase of vertical displacement indicated by strain (ε). After reaching the yielding point, the elastic deformation was followed by plastic deformation, while the deviator stress remained at a relatively constant value. The deviator stress-strain curves without apparent peak shear stress manifested the mechanical yielding followed by plastic deformation. When the slag content was in a higher range of 40%–60%, the deviator stress-strain curve mainly went through three stages: hardening, softening, and residual deformation. Specifically, those curves had apparent peak deviator stress, manifesting the transition from hardening to softening. As can be seen from Figure 8, the peak of deviator stress increased with increasing slag content. Also, the simulated curves more closely matched the deviator stress-strain relationship provided by the standard triaxial test, supporting that the numerical simulation succeeded in emulating the standard triaxial shear test under the consolidated-drain condition.

3.2.2 Analysis of mechanical characteristics

The macroscopic mechanical response of TSM with different slag contents was obtained by numerically simulating the standard triaxial tests. In addition, the deformation and shear failure mechanism of TSM and the intrinsic mechanism of the slag content's impact on its strength were also examined at microscale.

(1) Particle motion characterization:

The transporting direction of the TSM particles and the formation of the shear processing zone could be observed after outputting the vector plot of the particle velocity field for the numerical simulation of standard triaxial tests by PFC-2D. Under a confining pressure of 300 kPa, the microstructure, particle mobility, and shear processing

TABLE 4 Fundamental and mechanical parameters of the simulated TSM specimens.

Category	Density ($kg·m^{-3}$)	Coefficient of friction	Interparticle bonding stiffness (Pa)	Interparticle bonding stiffness ratio	Normal bonding strength (N)	Tangential bonding strength (N)
Tailings grain	1,580	0.5	5×10^{7}	1	1×10^{4}	1×10^{4}
Slag grain	1,210	0.75	1×10^{8}	1	1×10^{2}	1×10^{2}

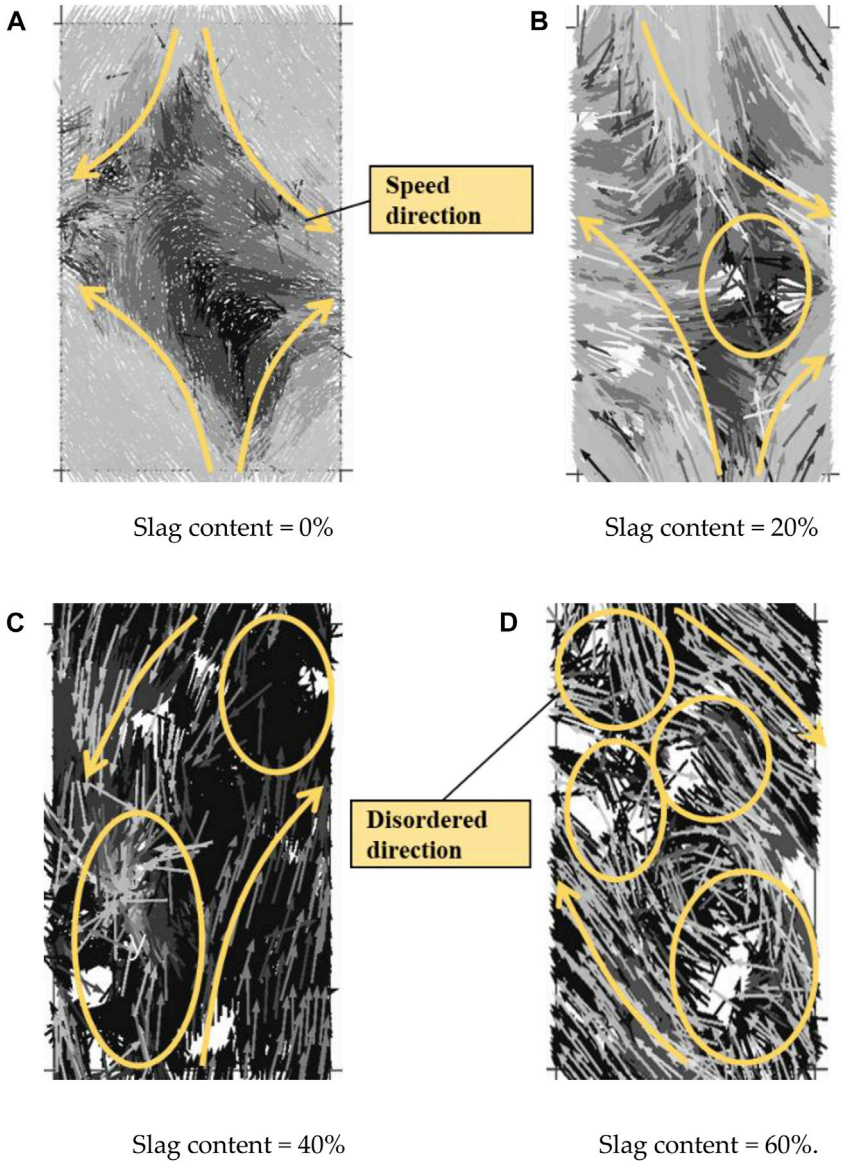

FIGURE 9
The vector plot of particle velocities for the confining pressure of 300 kPa: **(A)** slag content = 0%, **(B)** slag content = 20%, **(C)** slag content = 40%, and **(D)** slag content = 60%.

zone, which collaboratively dominated the characteristics of TSM containing 0%, 20%, 40%, and 60% slag, were examined with this simulation outcome.

The vector plot of the particle velocity field for confining pressure of 300 kPa is shown in Figure 9. The particle velocity field was plotted after completing the loading process of standard triaxial tests in simulation. The color contrast from light to dark represented the magnitude of velocity from higher to lower. The arrow in yellow color sketched the primary direction of the particle velocity. The yellow circle highlighted the disorderly portion of the particle velocity direction.

By comparing the particle velocity field of TSM specimens in different contents, it is evident that as for the slag content of 0%, the particles move from the direction of vertical load to the direction of

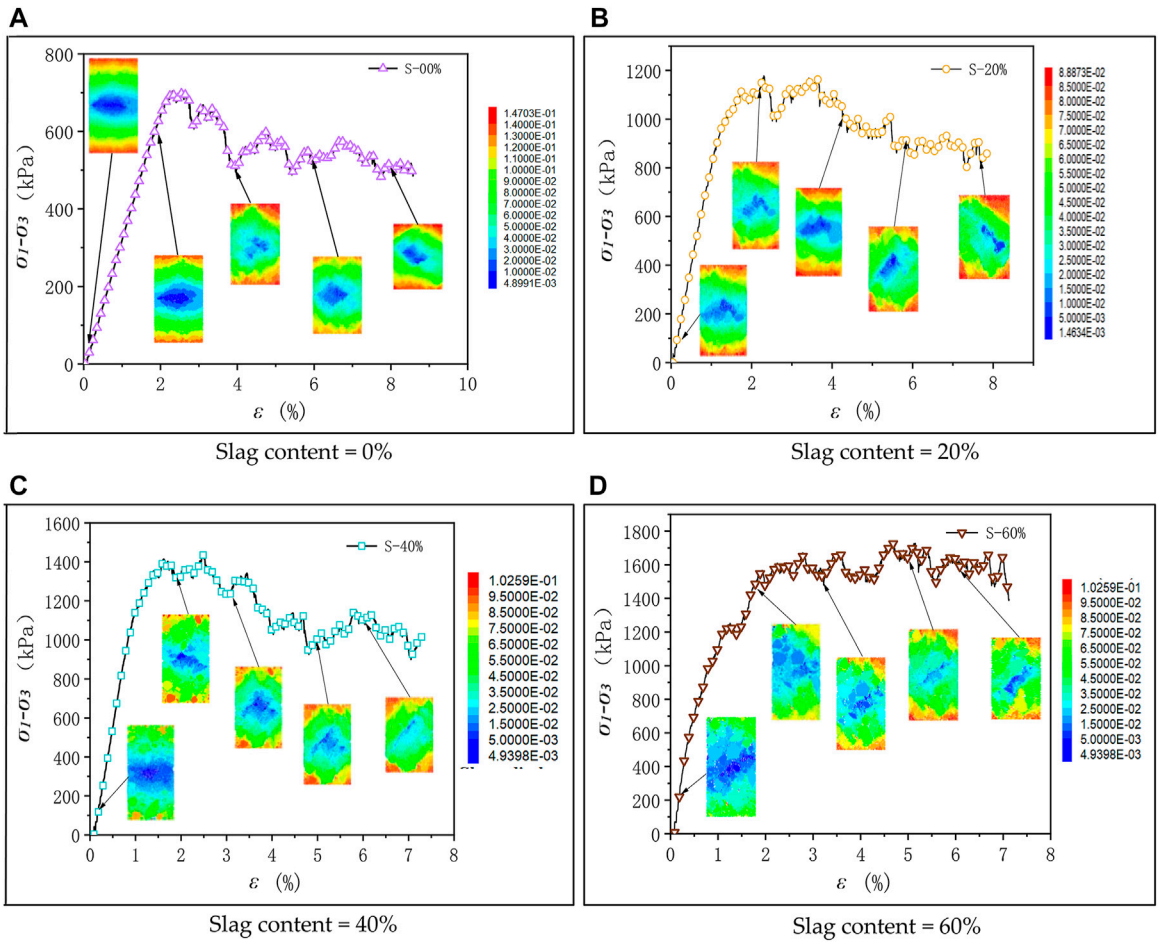

FIGURE 10
Displacement contour plots at five stages along the deviator stress-strain curves of the four TSM specimens with **(A)** slag content = 0%, **(B)** slag content = 20%, **(C)** slag content = 40%, and **(D)** slag content = 60% when the confining pressure of 300 kPa.

confining load (see Figure 9A). A few particles in the middle of the specimen were invertedly moved. The shear processing zone was not apparent, and the simulated specimen finally exhibited its deformation in the bulging form, which was similar to the final state of the deformation observed from the standard triaxial test.

While the slag content was adjusted to 20%, the particle velocity direction started to diverge due to the influence of the slag particles. As a result, the shear processing zone began to appear, for which the development of the shear processing zone was mainly affected by the velocity direction of the ultrafine tailings particles.

For the slag content reaching up to 40%, the influence of coarse particle transport on the movement of fine particles was significantly increased. The extrusion and mutual movement between particles were more prominent. The moving direction of fine particles (tailings) was mainly around the transporting tracks of coarse particles (slag). The typical movement of ultrafine tailings particles and slag particles affected the development of the shear processing zone.

When the fine content was much lower than the coarse content, as the slag content of 60% in Figure 9D, the particle transport became more chaotic, precisely in their moving directions. The coarse particles significantly impacted the development of shear processing zones in the TSM specimens.

In conclusion, in terms of the loading conditions, deforming behavior, failure mode, and deviator stress-strain relationships, the numerical simulation outcomes agreed well with the experimental results of the standard triaxial tests for the TSM specimens prepared with four different slag contents (0%–60%). Furthermore, due to the capability of observing the particle movements inside the simulated specimen, this numerical simulation has an undebatable value in analyzing the micro-mechanical characteristics of TSM.

(2) Displacement and failure characterizations:

The standard triaxial tests simulated with PFC-2D could provide the variation of particle displacements, which might be later utilized to analyze the microscopic damage inside the TSM specimens. For instance, Figure 10 demonstrates the displacement contour plots at five deforming stages along the deviator stress-strain curves of the TSM specimens having four different slag content (0%–60%) when the confining pressure was 300 kPa. In those displacement contour plots, the contouring regions assigned by dark blue denote the lowest displacement increment; in contrast, the contour regions filled with red denote the highest displacement increment.

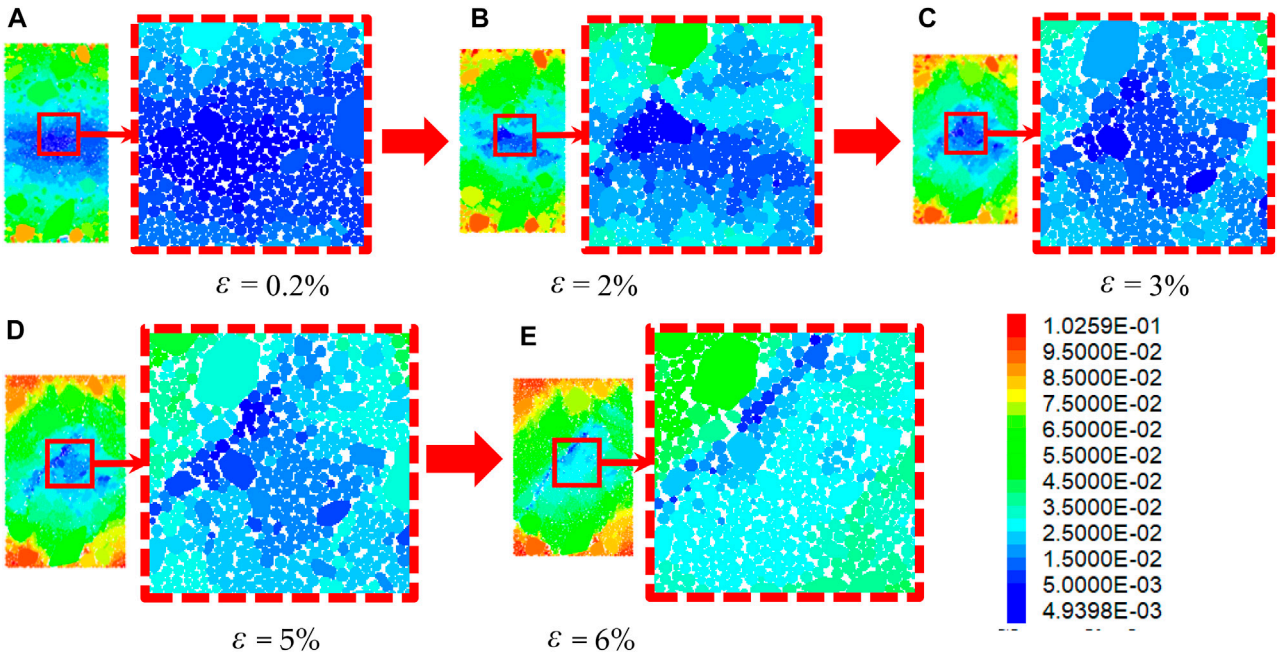

FIGURE 11
The evolution of particle displacement in the shear processing zone for the slag content of 40% at five stages: **(A)** ε = 0.2%, **(B)** ε = 2%, **(C)** ε = 3%, **(D)** ε = 5%, and **(E)** ε = 6%.

As seen in Figure 10A, since the initiation of the vertical loading to apply deviator stress, the particles nearby the boundaries of the TSM specimen began to move, and the particles centrally located in the specimen encountered minor movements. With the axial strain increasing (ε > 2%), the centrally located particles initiated distortions. When the axial strain reached around 4%, the displacement variations of those interior particles were most significant, mainly due to the stress-induced relocations of the majority of the particles. Moreover, given that the particle size of the pure tailings specimen (slag content = 0%) was uniform, the simulated specimen finally encountered the bulging failure without any apparent shear processing zone, as demonstrated by the contour plot of specimen's final displacement (ε = 8%) in Figure 10A.

By observing the displacement contour plots for the TSM specimens (slag content = 20%) in Figure 10B, particle displacements varied dramatically with the increased deviator stress. When the vertical loading began, the displacement increments of the particles inside each TSM specimen were similar to the displacement increments of the pure fine particles in Figure 10A. Such an agreement on particle displacement contour was attributable to the fact that most of the TSM particles at this stage were composed of ultrafine tailings. Thus, displacement contour plots at the first stage ($\varepsilon \leq$ 2%) in Figure 10A, B were highly similar. When the axial strain was 2%, the stress began concentrating along a potential shearing plane, and most of the particles inside the specimen had substantial displacements. Since the stress concentration area inside the TSM specimen gradually expanded, the tailing particles were partially blocked by coarse-sized slag particles. As a result, the ultrafine tailings particles were not evenly distributed inside the entire TSM specimen. The shearing processing zone was consequentially formed in the specimen, as the contour plots of ε > 5% in Figure 10B.

When the slag content of a TSM specimen was increased to 60% (see Figure 10D), the stress-induced particle redistribution at the beginning of loading ($\varepsilon \leq$ 2%) was insignificant. One possible explanation was that the TSM specimens with a high slag content had a significant amount of interior voids and a matrix consisting of slag particles. As a result, the stress was mainly distributed through the skeleton formed by the coarse-sized slag particles rather than ultrafine tailings particles. Another explanation might be that the anisotropy of the slag particles in the specimen influenced the stress concentration. During the entire loading process to apply deviator stress, the development of the shear processing zone in this TSM specimen became more apparent, implying that the specimen was more susceptible to plastic deformation predominated by shear failure.

The particle redistributing process in the TSM specimen of 40% slag content (see Figures 10C, Figure 11) was additionally compared with those of the TSM specimens of 0% and 20% slag contents (see Figure 10A, B). At the beginning of vertically compressive loading, the TSM specimen with 40% slag content had more minor particle displacements in the middle of this specimen (see Figure 11A) in comparison to the other two TSM specimens with less slag content (0% and 20%). The primary reason might be that adding slag particles into tailings increased the proportion of coarse particles in the TSM specimens. Specifically, compared to pure ultrafine particles, coarse and fine particles in such a mixture were more difficult to rotate and flip under the same loading condition provided by the deviator stress. Therefore, at the initial stage (ε = 0.2%), the vertical compression loading resulted in minimal variations of particle displacement. However, when the vertical axial strain was close to 2%, it could be observed that the specimen appeared to form stress concentration (see Figure 11B). Later, the more uniform distribution of the coarse particles in the TSM specimen with 40% slag content dispersed the

stress concentration, which was mainly reflected in the vertical axial strain of 3%, 5%, and 6%, corresponding to the displacement contour plots in Figure 11C–E.

The stress exerted on the slag particles during the stress redistribution process was anisotropic due to the different sizes and shapes of the slag particles. Hence, prominent shear processing zones appeared in the TSM specimen when continuous deviator stress was applied. Furthermore, within the duration of the vertically compressive loading process, it was evident that from the beginning stage of the formation of slag particles to the final stage of displacements of both slag particles and their surrounding tailings particles, the particle displacements in the TSM specimen initially exhibited a gradual increment and then increased significantly. Therefore, it was able to observe and conclude that when the slag content was 40%, the transition from the tailings particles originally being surrounded by slag particles to the slag particles eventually being surrounded by tailings particles consequentially led to the changes in particle displacement for the TSM specimen of 40% slag content. This phenomenon could also be explained by the fact that the TSM has the highest cohesion at a slag content of 40%, causing the most remarkable difference in peak deviator stress.

Despite the research findings above, it should be noted that this work has its natural limitations in both experiments and numerical simulations. First and foremost, the saturated condition was only considered in the triaxial tests. However, the *in-situ* might encounter a partially saturated condition, which requires technical support of unsaturated soil seepage and mechanism (Yan et al., 2022a). Second, trapping bubbles inside the pore structure can be further considered as a mechanism reducing friction between interparticle, which might lead to different research findings compared to a fully saturated condition (Ma et al., 2015; Ma et al., 2022). Last, the Darcy and non-Darcy flow as well as its corresponding flow regimes could locally exist in pore structure, so it requires further investigation of particular types of seepage flow in gravel-sized particles (Yan et al., 2022b).

4 Conclusion

Based on a literature review of the relevant research on the SRM and TSM, it is found that there have been inadequate experimental and numerical explorations of TSM in different slag content at macro- and micro-scale. Therefore, a series of standard triaxial tests were systematically carried out on TSM specimens with various slag contents (0%–60%) to investigate this research objective further. As a result, the macroscopic physical and mechanical characteristics of the TSM sample with different slag contents were obtained, as well as the effects of various slag contents on the macroscopic mechanical performance and interparticle structure of the TSM specimens. Subsequentially, the microscopic failure mechanism within the standard triaxial test and the interparticle interaction between incinerator slag and ultrafine tailings were examined by applying discrete element simulation with PFC-2D. The main conclusions obtained by experimental and numerical methods could be summarized as follows.

(1) The standard triaxial tests were used to analyze the deviator stress-strain relationships, the macroscopic deformation mechanism, and shear failure mode under a series of different testing conditions by varying slag contents and triaxial loads. The shear strengths of all selected TSM specimens were higher than that of pure ultrafine tailings. The fundamental shear strength parameters, including internal friction angle and cohesion, increased with increasing the slag content from 0% to 40%. Then, those parameters decreased slightly when the slag content was increased from 40% to 60%. The maximum cohesion was observed when the slag content was 40%. Therefore, even though the incremental resolution of slag content was 10%, the optimum slag content of 40% could be roughly estimated for engineering practice.

(2) The standard triaxial tests were modeled using the discrete element method with numerical simulation software of PFC-2D to explore the microscopic mechanism further. Referring to the deviator stress-strain curves determined by the standard triaxial tests, these numerical simulations generated curves almost overlapping with those experimental results. The shear processing zone inside the TSM specimens of various slag contents was also investigated. The micro-mechanical features were analyzed by taking advantage of the velocity vector plot and displacement contour plot provided by these simulations. With the increasing slag content in the TSM specimens, the particle movement and flipping direction became much more chaotic under the triaxial shear loading conditions. The addition of slag particles significantly impacted the development of the shear processing zone in the TSM specimen. As for the slag content of 40%, when the vertical axial strain increased, the matrix consisting of slag particles primarily encountered the most stress concentration, which was then diverged and transmitted to the surrounding tailings particles. Finally, after this stress redistribution process, the tailings and slag particles mutually interacted to present the shear failure mode with a significant shearing plane in the TSM specimen, in contrast to the budging failure mode without an apparent shearing plane inside the specimen of pure ultrafine tailings.

Data availability statement

The original contributions presented in the study are included in the article/supplementary material, further inquiries can be directed to the corresponding authors.

Author contributions

Conceptualization, SW, XL; Methodology, XJ, WN; Validation, WN; Supervision, SW; Writing—Original Draft Preparation, XL, YZ and JM, Writing—Review and Editing, XJ, JQ.

Funding

This research is funded by National Natural Science Foundation of China (Grants No. 51974051), the China Occupational Safety and Health Association (CXCY-2021-19), the Self-made Equipment Foundation of Chongqing University of Science and Technology (No. ZZSB2019013), the Graduate Innovation Program Project of Chongqing University of Science and Technology (Grants No. YKJCX2120702, YKJCX2120719, and YKJCX2120721).

Conflict of interest

Author JQ was employed by Chongqing Chuandongnan Survey & Design Institute Co., Ltd.

The remaining authors declare that the research was conducted in the absence of any commercial or financial relationships that could be construed as a potential conflict of interest.

Publisher's note

References

Chen, X., Jing, X., Cai, H., Wang, Y., and Ye, L. (2021). Hydraulic erosion rate of reinforced tailings: Laboratory investigation and prediction model. *Advances in Materials Science and Engineering*. 2021, 1–13. doi:10.1155/2021/8764862

Feng, K., Deng, H., and Sun, C. (2021). Particle flow simulation study on uniaxial compression of coal sample with prefabricated fracture. *IOP Conference Series: Earth and Environmental Science*. 859 (1), 1755–1769. doi:10.1088/1755-1315/859/1/012069

Han, C., Tan, Y., Chu, L., Song, W., and Yu, X. (2022). Flocculation and settlement characteristics of ultrafine tailings and microscopic characteristics of flocs. *Minerals* 12 (2), 221. doi:10.3390/MIN12020221

Huber, F., Korotenko, E., Šyc, M., and Fellner, J. (2020). Material and chemical composition of municipal solid waste incineration bottom ash fractions with different densities. *Journal of Material Cycles and Waste Management*. 23 (1), 394–401. doi:10.1007/s10163-020-01109-z

Jing, X., Chen, Y., Williams, D. J., Serna, M. L., and Zheng, H. (2019). Overtopping failure of a reinforced tailings dam: Laboratory investigation and forecasting model of dam failure. *Water* 11 (2), 315. doi:10.3390/w11020315

Jing, X., Pan, C., Chen, Y., Li, X., Wang, W., and Hu, X. (2021). Improvement effect of reticular glass fibers on the mechanical properties of tailings sand with the lenticle (layered sandy soil). *Water* 13 (10), 1379. doi:10.3390/W13101379

Jo, S. A., Kim, E. K., Cho, G. C., and Lee, S. W. (2011). Particle shape and crushing effects on direct shear behavior using DEM. *Soils Found.* 51 (4), 701–712. doi:10.3208/sandf.51.701

Joseph, A. M., Matthys, S., and De Belie, N. (2022). Properties of concrete with recycled aggregates giving a second life to municipal solid waste incineration bottom ash concrete. *Sustainability* 14 (8), 4679. doi:10.3390/SU14084679

Kumar, S., and Singh, D. (2021). Municipal solid waste incineration bottom ash: A competent raw material with new possibilities. *Innovative Infrastructure Solutions* 6 (4), 201. doi:10.1007/S41062-021-00567-0

Li, C., Shi, Y., Liu, P., and Guo, N. (2019). "Analysis of the sedimentation characteristics of ultrafine tailings based on an orthogonal experiment," in In 5th ISRM Young Scholars' Symposium on Rock Mechanics and International Symposium on Rock Engineering for Innovative Future, September 2019, 1–13. doi:10.1155/2019/5137092

Li, W. S., Ding, X. L., and Wu, A. Q. (2007). Study on the degree of weakening of water storage on the direct shear strength parameters of soil-stone mixture in the Three Gorges Reservoir Area. *Rock Soil Mech.* 28 (7), 1338–1342. doi:10.16285/j.rsm.2007.07.010

Li, X., Peng, J., Xie, Y., Li, Q., Zhou, T., Wang, J., et al. (2022). Influence of high-temperature treatment on strength and failure behaviors of a quartz-rich sandstone under true triaxial condition. *Lithosphere* 2022 (10), 3086647. doi:10.2113/2022/3086647

Liu, K., Cai, H., Jing, X., Chen, Y., Li, L., Wu, S., et al. (2021). Study on hydraulic incipient motion model of reinforced tailings. *Water* 13 (15), 2033. doi:10.3390/W13152033

Liu, N. (2021). Numerical simulation of foundation pit-slope based on PFC. *World Scientific Research Journal*. 7 (9), 87–96. doi:10.6911/WSRJ.202109.7(9).0013

Ma, Y., Kong, X. Z., Scheuermann, A., Galindo-Torres, S., Bringemeier, D., and Li, L. (2015). Microbubble transport in water-saturated porous media. *Water Resources Research*. 51 (6), 4359–4373. doi:10.1002/2014wr016019

Ma, Y., Yan, G., and Scheuermann, A. (2022). Discrete bubble flow in granular porous media via multiphase computational fluid dynamic simulation. *Frontiers in Earth Science*. 10, 947625. doi:10.3389/feart.2022.947625

Shi, Y., Li, C., Song, Z., and Liu, P. (2020). "Experimental study on curing of ultrafine tailings sand based on an orthogonal test," in International Conference on Ecological Resources, Energy, Construction, Transportation and Materials, Shanghai, China, December 2020. doi:10.3390/MIN1202022110

Simoni, A., and Houlsby, G. T. (2006). The direct shear strength and dilatancy of sand-gravel mixtures. *Geotechnical and Geological Engineering*. 24 (3), 523–549. doi:10.1007/s10706-004-5832-6

Tang, J., Xu, D., and Liu, H. (2018). Effect of stone content on shear characteristics of soil-stone mixture. *Rock and Soil Mechanics*. 39 (1), 93–102. doi:10.16285/j.rsm.2017.1527

Wang, P. (2017). *PFC simulation of large-scale triaxial test of soil-stone hybrid and its micro mechanical properties*. Chongqing, China: Ph.D. dissertation in Chongqing University.

Wang, G., Tian, S., Hu, B., Kong, X., and Chen, J. (2020). An experimental study on tailings deposition characteristics and variation of tailings dam saturation line. *Geomech. Eng.* 23 (1), 85–92. doi:10.12989/gae.2020.23.1.085

Wang, G., Zhao, B., Wu, B., Zhang, C., and Liu, W. (2022). Intelligent prediction of slope stability based on visual exploratory data analysis of 77 *in situ* cases. *International Journal of Mining Science and Technology*. 33 (1), 49–60. doi:10.1016/j.ijmst.2022.07.00

Xing, K., Zhou, Z., Yang, H., and Liu, B. (2020). Macro–meso freeze–thaw damage mechanism of soil–rock mixtures with different rock contents. *International Journal of Pavement Engineering*. 21 (1), 9–19. doi:10.1080/10298436.2018.1435879

Xu, L., and Ren, Q. W. (2014). Particle flow simulation of direct shear test of rock discontinuities. *Advanced Materials Research*. 1065-1069 (1065), 159–163. doi:10.4028/www.scientific.net/amr.1065-1069

Yan, G., Bore, T., Bhuyan, H., Schlaeger, S., and Scheuermann, A. (2022). The technical challenges for applying unsaturated soil sensors to conduct laboratory-scale seepage experiments. *Sensors* 22 (10), 3724. doi:10.3390/S22103724

Yan, G., Shi, H., Ma, Y., Scheuermann, A., and Li, L. (2022). Intrinsic permeabilities of transparent soil under various aqueous environmental conditions. *Géotechnique Letters*. 12 (3), 225–231. doi:10.1680/jgele.22.00049

Yang, J. H., Dong, J. Y., and Huang, Z. Q. (2016). Large-scale straight shear test study on shear strength characteristics of bulk under different rock content conditions. *Chinese Journal of Geotechnical Engineering*. 38 (2), 161–166. doi:10.11779/CJGE2016S2026

Yang, S., and Li, X. Q. (2020). Simulation analysis of large-scale straight shear test of soil-stone mixture based on 3D discrete element particle flow. *Engineering Science and Technology*. 52 (3), 78–85. doi:10.15961/j.jsuese.201900111

Yin, Y. C., Zhao, T. B., Tan, Y. L., and Zang, C. W. (2011). Particle flow simulation of rock uniaxial compression process. *Applied Mechanics and Materials*. 90-93, 497–500. doi:10.4028/www.scientific.net/amm.90-93.497

Zhang, Z. P., Fu, X. D., and Sheng, Q. (2021). Nonlinear failure strength criterion of soil-stone mixture based on rock content index. *Chinese Journal of Rock Mechanics and Engineering*. 40 (8), 1–15. doi:10.13722/j.cnki.jrme.2020.0854

frontiers | Frontiers in Earth Science

TYPE Original Research
PUBLISHED 03 February 2023
DOI 10.3389/feart.2023.1132635

OPEN ACCESS

EDITED BY
Guangjin Wang,
Kunming University of Science and Technology, China

REVIEWED BY
Wei Sun,
Sun Yat-sen University, China
Yuanchao Zhang,
Fuzhou University, China

*CORRESPONDENCE
Youliang Fang,
fang_youliang@126.com
Yanying Li,
liyy21@mails.jlu.edu.cn

SPECIALTY SECTION
This article was submitted to Environmental Informatics and Remote Sensing, a section of the journal Frontiers in Earth Science

RECEIVED 27 December 2022
ACCEPTED 23 January 2023
PUBLISHED 03 February 2023

CITATION
Li B, Fang Y, Li Y and Zhu C (2023), Dynamics of debris flow-induced impacting onto rigid barrier with material source erosion-entrainment process. *Front. Earth Sci.* 11:1132635. doi: 10.3389/feart.2023.1132635

Dynamics of debris flow-induced impacting onto rigid barrier with material source erosion-entrainment process

Bailong Li[1,2,3], Youliang Fang[1,2,3]*, Yanying Li[4]* and Chun Zhu[5]

[1]College of Civil Engineering and Architecture, Hebei University, Baoding, China, [2]Hebei Civil Engineering Monitoring and Evaluation Technology Innovation Center, Baoding, China, [3]Engineering Research Center of Zero-Carbon Energy Buildings and Measurement Techniques, Ministry of Education, Baoding, China, [4]College of Construction Engineering, Jilin University, Changchun, China, [5]School of Earth Sciences and Engineering, Hohai University, Nanjing, China

The dynamics of debris flow impact considering the material source erosion-entrainment process is analyzed using a coupled SPH-DEM-FEM method. A complex coupled dynamic model of a debris flow, the erodible material source, and a rigid barrier is established in this paper. The applicability of the coupled SPH-DEM-FEM method for calculating the impact force of debris flow on the rigid barrier is verified by comparing the model with the laboratory test. The strain softening model is used to simulate the process from solid state to transition state and finally to liquid state of erodible material source. The impact force caused by debris flow considering the source erosion-entrainment process and the dynamic response of a rigid barrier is also analyzed. The results show that the volume of debris fluid, impact force, and dynamic response of a rigid barrier considering source erosion–entrainment are significantly greater than those of the original model. According to the calculation results, the existing formula for the impact force of a debris flow is then modified. The coupled numerical analysis method and the calculated results help to clarify the influence of erosion-entrainment, modify the calculation of the impact force of debris flow, and optimize the design of the rigid barrier.

KEYWORDS

erosion-entrainment, SPH-DEM-FEM, rigid barrier, debris flow-induced impacting, dynamic response analysis

1 Introduction

Debris flows are widespread in mountainous areas around the world. It is a unique flood caused by rainstorms and earthquakes (Yin et al., 2016). A debris flow typically is high-speed, has a large volume of sediment and water, and is highly destructive. It can produce a tremendous impact on structures along the way (Tang et al., 2012). The initial volume does not always determine the debris flow volume, according to the literature (Hungr et al., 2005; Wang et al., 2021; Lei et al., 2022). In general, debris flows with small initial volumes can rapidly increase by several or even tens of orders of magnitude in volume through source erosion and entrainment processes (Shang et al., 2003; Wang et al., 2003; Zaginaev et al., 2019; Wang et al., 2022). Source erosion and entrainment processes significantly increase the debris flow volume and impact, which should be considered in the dynamic model (Chen et al., 2006; Wang et al., 2020; Guo et al., 2022; Wang et al., 2022; Wang et al., 2023).

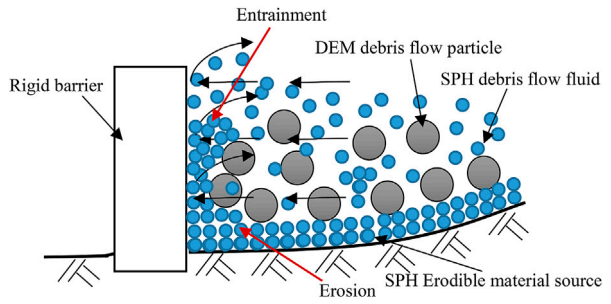

FIGURE 1
Schematic diagram of the erosion-entrainment model.

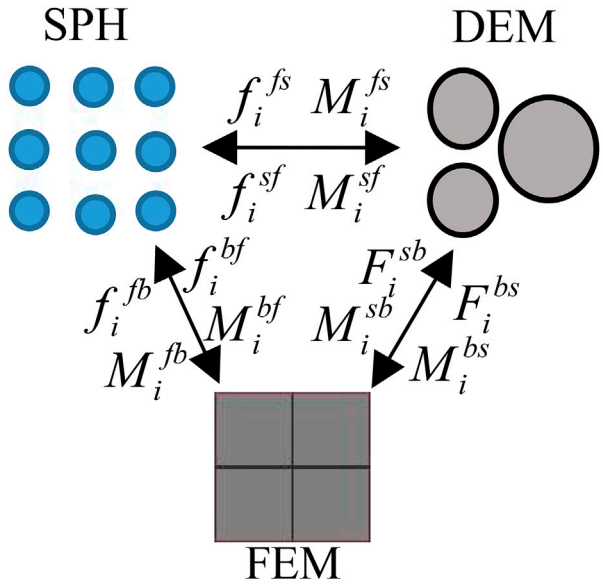

FIGURE 2
Schematic diagram of SPH-DEM-FEM coupling numerical model.

Debris flows erosion and entrainment of the material are caused by the high-speed collision between debris flow particles and the fluidization effect on the erodible material source (Federico and Cesali, 2015; Wang et al., 2021). When a debris flow passes through an erodible material source, it erodes if the shear stress on the source body is greater than the strength of the material source (Armanini et al., 2009; Luna et al., 2012). At this point, the erodible material source changes from a solid state to a transition state. Fluidization occurs when the erodible material source is eroded, and entrainment occurs and forms part of the debris flow. At this point, the erodible material source changes from a transition state to a liquid state (Mangeney et al., 2007; Mangeney et al., 2010; Li et al., 2022a). To improve the reliability of the debris flow dynamic model, a complex constitutive model of the erodible material source should be considered (Lee and Jeong, 2018). Research on the impact force of debris flows considering the erosion—entrainment process is performed through theoretical research, laboratory tests, and numerical simulations (Gao et al., 2017; Choi et al., 2021). However, the research and application of complex constitutive model of erosion is limited.

The impact force caused by debris flow causes the barrier to break, so the theoretical calculation of the peak value of debris flow impact force is essential (Scheidl et al., 2013; Thouret et al., 2020). Hydrostatic, hydrodynamic, and hybrid theories are commonly used to calculate the peak impact force (Calvetti et al., 2017; Li S. et al., 2020; Sha et al., 2023). Hydrostatic theory estimates the impact pressure by considering the empirical coefficient k based on static pressure (Armanini, 1997; Proske et al., 2011; Bugnion et al., 2012). Fluid dynamics theory is derived from the momentum conservation equation and is the peak impact pressure theory related to the flow rate change rate and impact pressure (Hungr et al., 1984; Hu et al., 2011; Scheidl et al., 2021). The hybrid theory of debris flow considers both hydrostatics and hydrodynamics theories. By adding or multiplying the two theories, a calculation model suitable for the actual situation in the field can be obtained (Arattano et al., 2003; Huang et al., 2007). However, the theory of debris flow impact force considering erosion is relatively little in the present literature. Moreover, the impact of the impact coefficient of debris flow needs further study (Liu et al., 2020; Roelofs et al., 2022).

Many researchers have conducted laboratory tests on debris flow considering the erosion-entrainment process (Hungr et al., 1984; Mangeney et al., 2010; Lee et al., 2022). Mangeney et al. (2010) conducted laboratory tests on the debris flow erosion-entrainment process to study the influencing factors such as topographic slope, flow distance, and thickness of the erodible layer. The results indicated that the erosion process increases liquidity by almost 40%. Haas et al. (2016) studied the influence of different types of debris flow on the erosion-entrainment process. It was concluded that the average erosion depth increased with increased water content and particle size. Tian et al. (2014) studied the calculation of debris flow resistance during the erosion-entrainment process. The literature shows that fluid resistance on an erodible material source was significantly greater than that of a rigid rock bed. The calculation formula of debris flow resistance considering the erosion-entrainment process was obtained through dimensionless multiple regression analysis. However, there are many factors influencing the laboratory tests of debris flow erosion and the test are relatively expensive (Fuchu et al., 1999).

Many scholars have used numerical methods to study the debris flow impact in the erosion-entrainment process (Peng et al., 2011; Fan et al., 2019; Li X. et al., 2022). Due to the entrainment process of debris flow erosion and the complexity of its interaction with a barrier, the mixed media method has a natural advantage (Liu and He, 2020). Lee et al. (Lee and Jeong, 2018; Jeong and Lee, 2019; Lee et al., 2019) conducted a series of studies on the impact of debris flow and barrier in the erosion-entrainment process by adopting the coupled CEL method. The traditional static impact force model was modified by coupling numerical analysis. Leonardi et al. (Leonardi et al., 2013; Leonardi et al., 2015; Leonardi et al., 2016) used the coupled LBM-DEM to calculate the numerical value of a debris flow. The calculation results provided an essential reference for considering the interaction between debris flow and the barrier in the erosion-entrainment process. The failure mechanism of the barrier was also analyzed. Li et al. (2018) adopted the coupled CFD - DEM to study the interaction between debris flow and the barrier. A debris flow study considering the erosion process was performed. The research results helped to determine the impact force of debris flow. Li et al. (Li B. et al., 2020; Li et al., 2022b) adopted the SPH-DEM-FEM method to study the interaction model of two-phase debris flow and the barrier. The research results were of great significance to the design of the barrier. However, current research focuses on the effect

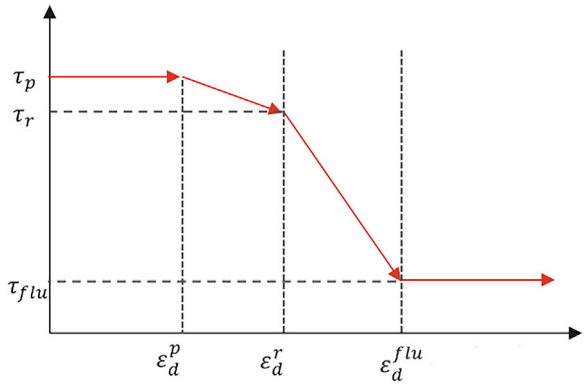

FIGURE 3
Strain softening model of an erodible material source Lee et al. (2019).

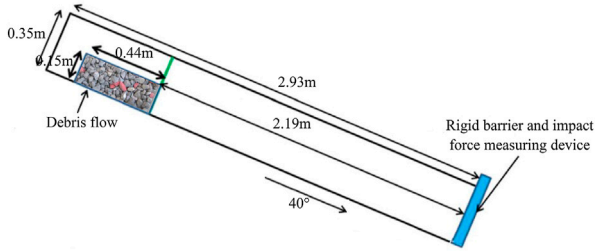

FIGURE 4
Schematic diagram of laboratory test of debris flow Jiang et al. (2013).

of single-phase flow on erosion. Literature on the effects of two-phase flow on erosion is relatively rare.

In summary, current research on the interaction between debris flow and the barrier in the erosion-entailing process primarily uses laboratory experiments, while coupled numerical analysis methods are rarely used. Coupled SPH-DEM-FEM technology can be well adapted to the simulation and calculation in the complex case of particle-fluid-structure. The coupled SPH-DEM-FEM method cannot only avoid the mesh distortion and analysis failure of two-phase debris flow but also accurately simulates the strain softening model of erodible material source and accurately calculate the barrier (Li et al., 2022b). This technique can be used to construct and calculate the complex coupled dynamic model of debris flow, erodible material source, and rigid barrier.

2 Computational assumptions and construction of coupled numerical model

2.1 Computational assumptions

The following calculation assumptions were made for debris flow and the barrier model considering erosion-entrainment processes.

1. Because the actual source of erodible material is rock mass, deformation can be neglected. The bottom of the channel is simplified as rigid material in this paper.
2. Because the movement law of the material source satisfies Newton's second law when the debris flow starts, to simplify the complexity of the model, the DEM is used to calculate.
3. The main research objects are the impact force of debris flow and the dynamic response of the barrier, so the channel is simplified.
4. Due to the considerable differences in the performance of particles, fluids, and barrier structures, the SPH-DEM-FEM coupled numerical analysis method is used for numerical analysis and calculation to reflect their respective characteristics.

Based on the above calculation assumptions and model simplification, the schematic diagram of the interaction model between debris flow and the barrier considering the erosion-entrainment process is shown in Figure 1. The erodible material source was calculated by the SPH method and strain softening constitutive model. The DEM numerical analysis method was used to analyze the loose material source particles during debris flow initiation. The barrier and channel were numerically simulated by the finite element method.

2.2 Construction of DEM model for debris flow particles

Because the motion of debris f l o w particles conforms to Newton's second law, DEM is used for calculations, as shown in Eq. 1 (Džiugys and Peters, 2001):

$$\left.\begin{aligned} m_i\ddot{\boldsymbol{u}}_i &= m_i g + \sum_{k=1}^{m_p}\left(\boldsymbol{f}_{n,ik} + \boldsymbol{f}_{t,ik}\right) \\ I_i\ddot{\boldsymbol{\theta}}_i &= \sum_{k=1}^{m_p}\boldsymbol{T}_{ik} \end{aligned}\right\} \tag{1}$$

Where m_i and $\ddot{\boldsymbol{u}}_i$ are the mass and translational acceleration of the debris flow particles, respectively; I_i and $\ddot{\boldsymbol{\theta}}_i$ are the moment of the inertia and rotational acceleration of the tdebris flow particles, respectively; $\boldsymbol{f}_{n,ik}$ and $\boldsymbol{f}_{t,ik}$ are the normal and tangential contact forces of the debris flow particles on adjacent particles I, respectively; $\boldsymbol{T}_{ik}$ is the moment of action of the debris flow particles on adjacent particles.

The resultant external force and torque on debris flow particles are shown in Eq. 2:

$$\left.\begin{aligned} F_i &= \sum_{j=1}^{k}\left(f_{nij} + f_{tij}\right) \\ T_i &= \sum_{j=1}^{k} r_i\left(f_{sij}\cdot n_t\right) \end{aligned}\right\} \tag{2}$$

In the formula, $\boldsymbol{f}_s$ is the friction force; $\boldsymbol{f}_{nij}$ and $\boldsymbol{f}_{tij}$ are the contact forces.

2.3 Construction of SPH model for debris flow fluid and erodible material source

The debris flow fluid and erodible material source body are constructed using the SPH method, and the approximate function of the example is shown in Eq. 3 (Li B. et al., 2020):

$$f(r_i) = \int_{\Omega} f(r')W(\boldsymbol{r} - \boldsymbol{r}', h)d\boldsymbol{r}' \tag{3}$$

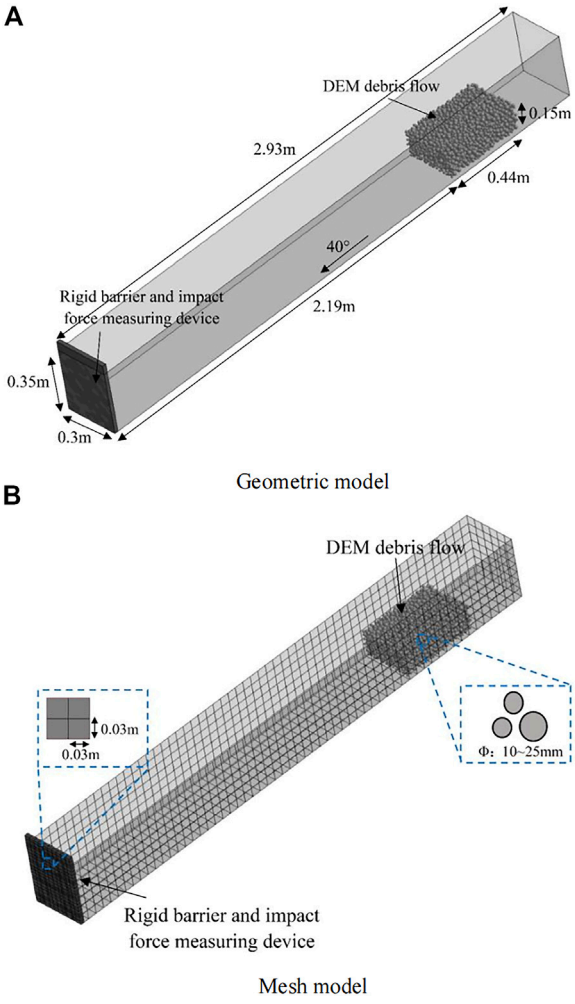

FIGURE 5
The coupled DEM-FEM numerical model of debris flow impact **(A)** Geometric model **(B)** Mesh model.

The function W can be expressed by Eq. 4:

$$W(x,h) = \frac{1}{h(x)^d}\theta(x) \tag{4}$$

Where h is the smooth length and d is the dimension.

The smooth kernel function adopts Eq. 5:

$$\theta(u) = C \times \begin{cases} 1 - \frac{3}{2}u^2 + \frac{3}{4}u^3; /u/ \le 1 \\ \frac{1}{4}(2-u)3; 1 \le /u/ \le 2 \\ 0; 2 < /u/ \end{cases} \tag{5}$$

Where C is a constant.

2.4 Construction of SPH-DEM-FEM coupling mode

The algorithm between debris flow particles and a rigid barrier is calculated by Eq. 6 (Li et al., 2022a):

TABLE 1 DEM-FEM coupling numerical simulation parameters.

Type	DEM	Rigid barrier	Channel
Constitutive model	Elastic	Elastic	Rigid
Density (kg/m3)	2,500	2,300	2,300
Elastic modulus (MPa)	100	24,000	30,000
Poisson's ratio	0.25	0.2	0.24
Friction coefficient	1.4	0.466	0.384
Citation	Shen et al. (2018)	Law (2015)	Law (2015)

$$\left.\begin{aligned} m_i\ddot{u}_i &= m_i g + \sum_{k=1}^{m}\left(f_{n,ik} + f_{t,ik}\right) + \sum_{j=1}^{l}\left(f_{n,ij} + f_{t,ij}\right) \\ I_i\ddot{\theta}_i &= \sum_{k=1}^{m} T_{ik} + \sum_{j=1}^{l} T_{ij} \\ M\ddot{X} + C\dot{X} + KX &= f_a + f_b \end{aligned}\right\} \tag{6}$$

Where f_a is the load of FE; f_b is the contact force among DEM-FEM.

The coupling algorithm between debris flow fluid, erodible material source and a rigid barrier is calculated with Eq. 7:

$$M\ddot{U} + CU + Kd = F + F_C \tag{7}$$

Where F is the external load; F_C is the contact force among SPH-FEM.

The coupling algorithm between debris flow fluid, erodible material source body, and debris flow particles is calculated using Eq. 8 (Li et al., 2022a). The schematic diagram of SPH-DEM-FEM coupling numerical model is shown in Figure 2:

$$\left.\begin{aligned} m_i^s\frac{du_i^s}{dt} &= F_i^c + F_i^{bs} + m_i^f f_i^{fs} \\ I_i^s\frac{d\omega_i^s}{dt} &= M_i^c + M_i^{fs} + M_i^{bs} \\ \frac{du_i^f}{dt} &= -\sum_{j=1}^{N} m_j\left(\frac{p_i}{\rho_i^2} + \frac{p_j}{\rho_j^2} + \Pi_{ij} + R_{ij}f_{ij}^4\right)\nabla_i W_{ij} + f_i^{sf} + f_i^{bf} \end{aligned}\right\} \tag{8}$$

Where, b, s and f represent FE, DEM and SPH.

2.5 Constitutive model of erodible material source

Erosion occurs when the shear stress exerted by debris flow on an erodible material source exceeds the strength of the material source. It goes from a solid state to a transition state. Then entrainment is generated and transformed into a flow state. In this paper, the strain softening model proposed by Lee et al. (Lee and Jeong, 2018; Jeong and Lee, 2019; Lee et al., 2019) is used to simulate the erosion-entrainment process. The strain softening model of an erodible material source is shown in Figure 3.

3 Model verification

3.1 DEM-FEM debris flow model verification

The indoor debris flow impact tests conducted by Jiang et al. (2013) were used to verify the model. The schematic diagram of the indoor test is shown in Figure 4. The DEM-FEM coupling numerical model is consistent with the indoor test. The channel is 2.93 m long.

FIGURE 6
Comparison of debris flow impact process: **(A)** Laboratory test Jiang et al. (2013); **(B)** Numerical simulation results.

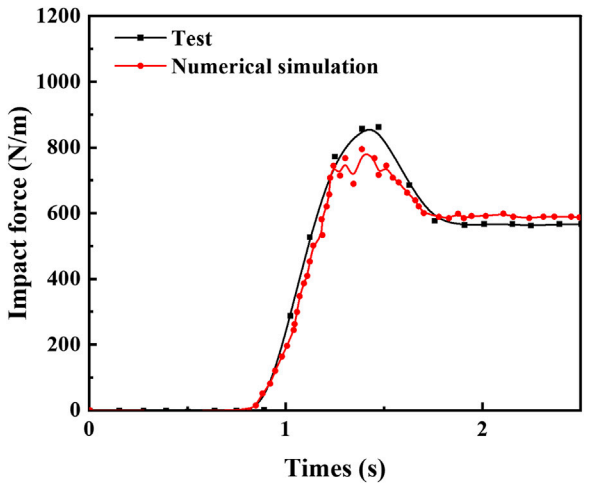

FIGURE 7
Comparison of the time history curves of the indoor test and numerical simulation impact force.

FIGURE 8
Laboratory test diagram of debris flow (Moriguchi et al. [54]).

The gradient of the channel is 40°, and the initial source volume is 0.019 m^3. The diameter of debris flow particles ranges from 10 mm to 25 mm. As the proportion of particles less than 10 mm in the sample is relatively low, the particles less than 10 mm are ignored in this paper.

The simulation parameters are consistent with the indoor test and simulation parameters conducted by Jiang et al. (2013). The whole process of the test is entirely reproduced by using the coupled DEM-FEM method. The initial volume and starting conditions of debris flow in the DEM particle simulation test are consistent with the test. Because the fraction of particles below 10 mm in the sample is relatively low, the fraction smaller than 10 mm is ignored in the numerical simulation. The slope of the debris flow channel is 40°, and a rigid body element is used for simulation. The geometric model is shown in Figure 5A, and the mesh model is shown in Figure 5B.

The barrier structure material of the numerical model is consistent with the test. C40 concrete is selected, and the elastic model is used as the constitutive model. The specific material parameters are consistent with the literature (Jiang et al., 2013). DEM particles are adopted for debris flow, and the elastic model is adopted for the constitutive model. As the minimum dry weight in the test is 1,350 kg/m^3, the DEM particle density is set as 2,500 kg/m^3 according to the literature. The friction coefficients of particle, rigid

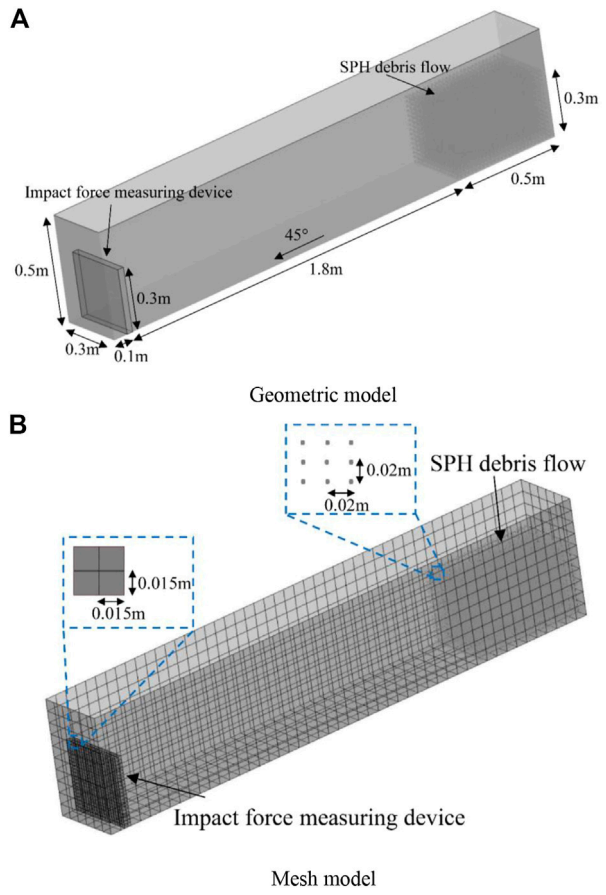

FIGURE 9
The coupled SPH-FEM numerical debris flow impact model **(A)** Geometric model **(B)** Mesh model.

barrier, and channel are 1.4, 0.466, and 0.384, respectively. The specific parameters are consistent with the numerical simulation parameters conducted by Shen et al. (2018) and Law (2015), as shown in Table 1.

The effectiveness of the DEM-FEM coupling method is verified by comparison with the impact test of debris flow, as shown in Figure 6. Figure 6A shows the indoor test results, and Figure 6B shows the simulation results. The impact process and debris flow shape of numerical simulation laboratory test results are consistent with those of laboratory physical model tests. The process of debris flow impact in different time periods is compared in the paper, and the experimental results are basically consistent with the numerical simulation results.

Figure 7 shows the time history curves of the impact force for the indoor test and the numerical simulation. The two time history curves are in agreement. Although there are some errors in the comparison results, the error rate ranges between 2.1%–7.7%, indicating the model's applicability and reliability.

3.2 Verification of SPH-FEM debris flow model

The debris flow indoor test conducted by Moriguchi et al. [54] is used for model verification. Figure 8 shows the laboratory test. The

TABLE 2 The coupled SPH-FEM numerical simulation parameters.

Type	SPH	Rigid barrier	Channel
Constitutive model	Bingham	Elastic	Rigid
Density (kg/m^3)	1,379	2,500	2,300
Elastic modulus (MPa)	5	24,000	21,000
ϕ' (°)	35	–	–
c' (kPa)	0	–	–
Citation	Moriguchi et al. (2009)	Law (2015)	Law (2015)

coupled SPH-FEM model is consistent with the indoor test. The length of the debris flow flume is 1.8 m, the width is 0.3 m, and the slope is adjustable between 45° and 65°.

The simulation parameters are consistent with the indoor test of debris flow conducted by Moriguchi et al. (2009). The whole test process is entirely reproduced by the coupling SPH-FEM numerical analysis method. The initial volume and starting conditions of debris flow in the SPH particle simulation test are consistent with the test. The adopted slope of the debris flow flume varied between 45°, 50°, 55°, 60°, and 65°. The geometric model is shown in Figure 9A, and the mesh models are shown in Figure 9B. The numerical model parameters are entirely consistent with the test [54]. The simulation parameters are shown in Table 2.

The comparison of the impact process between the indoor test and numerical simulation of debris flow at different times (t=0.4 s, t=0.8 s, t=1.2 s, t=1.6 s) is shown in Figure 10. Figure 10A shows the impact process of the laboratory test, and Figure 10B shows the impact process of coupled numerical simulation. The impact process of the indoor test is consistent with the coupled numerical simulation.

Figure 11 shows the comparison of the impact force time history curve when the slope of the debris flow flume is 45°, 55°, 60°, and 65°, respectively. Although there are some errors in the comparison of the results, the error rate ranges 1.9%–8.6%, indicating the applicability of the model.

4 Establishment of model

4.1 Geometric model and mesh model

The model is established according to the actual terrain of a typical debris flow channel in Nanjiao Gully, Fangshan District, Beijing. The model is simplified using the calculation assumptions in Section 2.1. The simplified slope of the channel in the debris flow forming area is 35°, and the slope of the channel in the debris flow erosion area is 20°. According to the field investigation results, the thickness of the erodible material source is set to 0.5 m. The geometric model of debris flow and rigid barrier considering the source erosion-entrainment process is shown in Figure 12A. The model consists of the DEM debris flow initiating material source, SPH erodible material source, FEM rigid barrier, and the channel. The width of the model is 1 m. The starting length of debris flow is 5 m, and the length of the erosion area is 10 m.

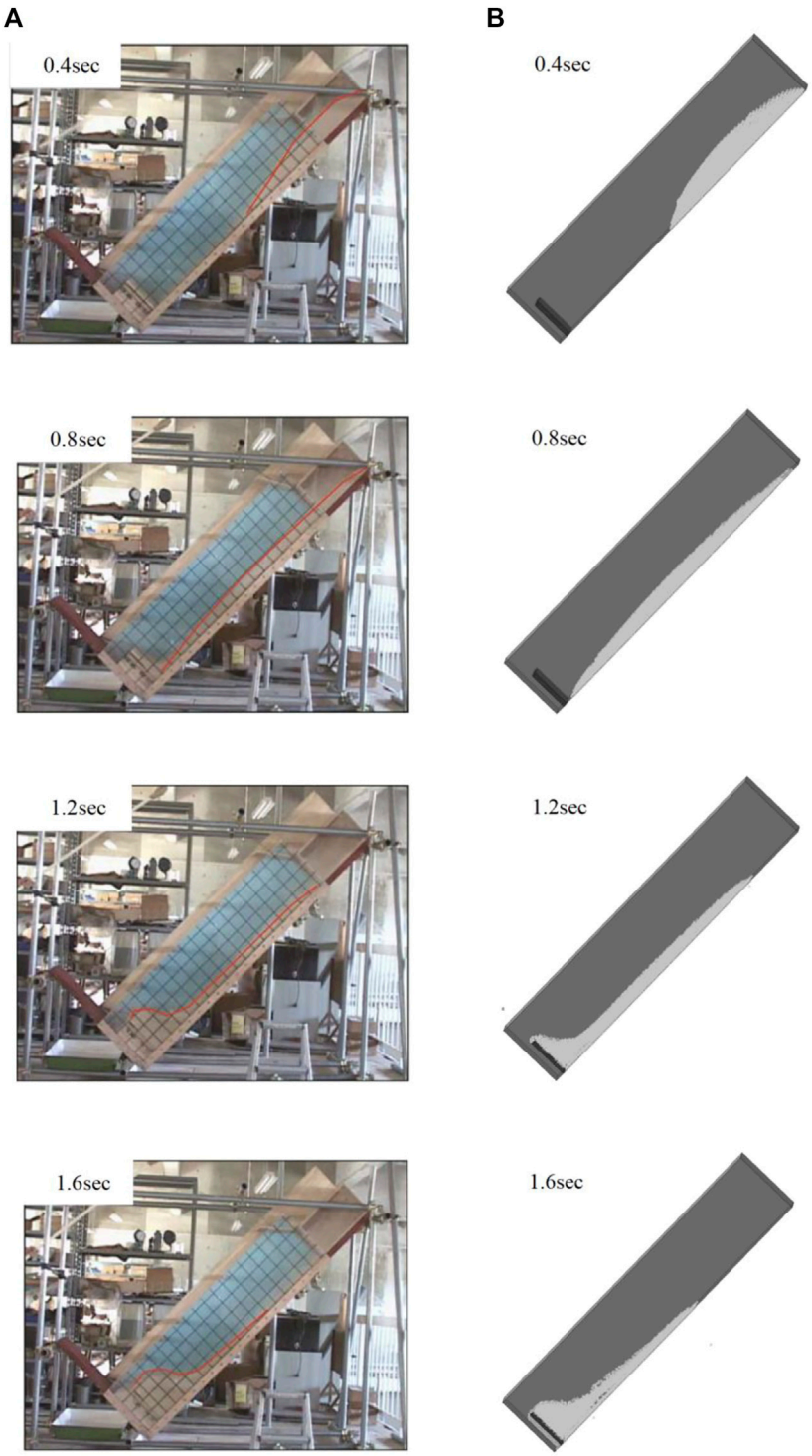

FIGURE 10
Comparison of debris flow impact process **(A)** Laboratory test (Moriguchi et al. [54]); **(B)** Numerical simulation results.

The mesh models of the debris flow and rigid barrier considering the source erosion-entrainment process are shown in Figure 12B. C3D8R hexahedron element with the size of 0.1 m is used for the rigid barrier. DEM particles with a particle diameter of 10–25 mm are used as the starting source of debris flow. SPH particles with a spacing of 0.05 m are used as the erodible source.

4.2 Basic parameters and boundary conditions of the simulation

The strain softening model in Section 2.5 is used for the erodible material source. The elastic constitutive model is used for the DEM material source particles. The elastic constitutive model is used for the

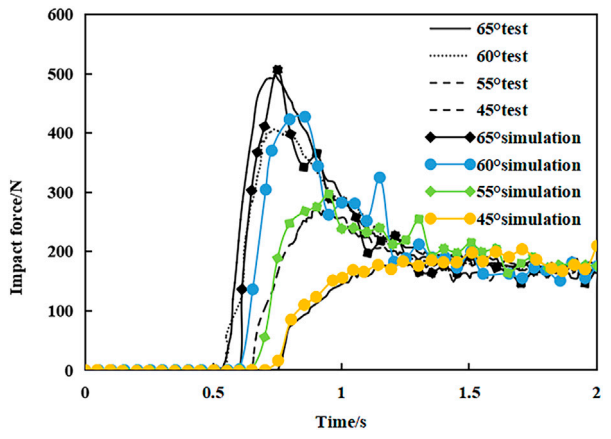

FIGURE 11
Comparison of impact force time history curve between test and numerical simulation.

rigid barrier. The rigid constitutive model is adopted for the channel. Specific simulation parameters are shown in Table 3. The volume of initial provenance and the erosion thickness of soil layer were determined based on field investigation and field tests.

All degrees of freedom of the channel are fixed, and the bottom of the barrier is fixed. The debris flow starts under gravity and enters the flow area, producing an erosion-entrainment effect and finally impacting the barrier. The calculation time is 10 s, and the process from the debris flow starting to erosion-entrainment to impact is simulated.

5 Results and discussion

In this paper, the coupled numerical simulation analysis of the debris flow impact process, debris flow impact force time history, and barrier displacement time history with or without considering the erosion-entrainment process is carried out by the established model. Finally, the parameters of the debris flow impact force formula are modified, which provides a reference for debris flow prevention and the design of a barrier.

5.1 Comparison of debris flow impact process

The impact process and velocity vector results of debris flow with and without the erosion-entrainment process are analyzed in this section to study the impact of the erosion-entrainment process on the debris flow impact process. Figure 13A shows

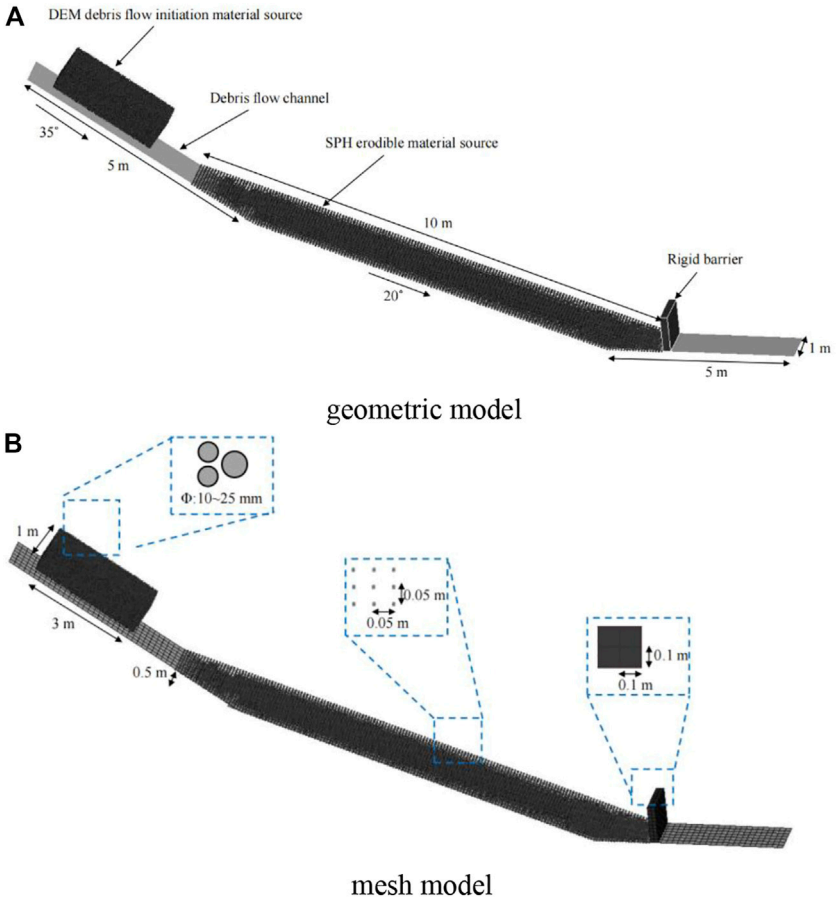

FIGURE 12
Debris flow and barrier model considering the erosion-entrainment process **(A)** geometric model **(B)** mesh model.

TABLE 3 Basic parameters of numerical simulation.

Type	DEM	SPH	Rigid barrier	Channel
Constitutive model	Elastic	Strain softening model	Elastic	Rigid
Density (kg/m^3)	2,500	1800–1,500	2,500	2,300
Elastic modulus (MPa)	30,000	5	24,000	21,000
φ' (°)	–	30–5	–	–
c' (kPa)	–	5–0.1	–	–
ε_d^p, ε_d^r, ε_d^{flu}	–	0.03, 0.1, 0.2	–	–
Citation	Shen et al. (2018)	Li et al. (2018)	Law (2015)	Law (2015)

the impact process and velocity vector results of debris flow without the erosion-entrainment process. Figure 13B compares the effects of including or excluding the erosion-entrainment process.

The volume of debris flow is always the source volume when the debris flow starts, and all of the debris flow is intercepted by the barrier. The case considering the erosion-entrainment process is shown in Figure 13A. The debris flow volume increases rapidly with the erosion-entrainment process and significantly impacts the barrier. Due to the increased debris flow volume, many debris flows rush out of the rigid barrier.

When the time is 0.7 s, the debris flow starts and flows through the erosion area to produce an erosion-entrainment effect on the erodible material source. At 1.5 s, apparent concave erosion occurs, further intensifying the entrainment process. At 2.6 s, the debris flow velocity reaches a maximum of 5.98 m/s, while the maximum velocity without the erosion-entrainment process is only 3.02 m/s. At 3.3 s, the debris flow starts to impact the barrier, and the debris flow velocity rapidly drops. At 4.1 s, the debris flow rushes out of the barrier. At this time, the impact height reaches the maximum, about 2.16 times higher than without the erosion-entrainment process. When the time is 5.0 s, the debris flow is deposited at the bottom of the barrier. When the time is 6.0 s, the debris flow finally becomes a static load. However, the impact process of debris flow without considering erosion at the same time is significantly different. Both impact velocity and impact height, the former is significantly greater than the latter.

5.2 Flow velocity and impact height of debris flow

The comparison of debris flow velocity with and without the erosion-entrainment process is shown in Figure 14. When the time is 2.6 s, the debris flow velocity reaches the maximum of 5.98 m/s. The maximum velocity without the erosion-entrainment process is only 3.02 m/s. The debris flow velocity considering the erosion-entrainment process is 1.98 times that without the erosion-entrainment process.

Figure 15 compares the impact height of debris flow with and without the erosion-entrainment process. At 4.1 s, the impact height of debris flow reaches a maximum of 2.07 m. The maximum impact height without the erosion-entrainment process is only 0.96 m. The impact height of debris flow considering the erosion-entrainment process is 2.16 times higher than without the process.

5.3 Impact force of debris flow and dynamic response of barrier

The comparison of the impact force of a debris flow with and without the erosion-entrainment process is shown in Figure 16. When the time is 4.1 s, the impact force of debris flow reaches the maximum of 155.65 kN/m^2. The maximum impact force without the erosion-entrainment process is only 75.22 kN/m^2. The debris flow velocity considering the erosion-entrainment process is 2.07 times that without the erosion-entrainment process.

Figure 17 compares the displacement time history of the barrier with and without the erosion-entrainment process. At 4.1 s, the displacement time history of the barrier reaches a maximum of 1.75 mm. The maximum impact height without the erosion-entrainment process is only 0.82 mm. The impact height of debris flow considering the erosion-entrainment process is 2.13 times that without the process.

5.4 Analysis and discussion

As seen from Figure 14, without considering the erosion-entrainment effect, the debris flow is in direct contact with the soil layer and deposits, and the flow velocity significantly decreases. The maximum velocity of debris flow with and without the erosion-entrainment process is 5.98 m/s and 3.02 m/s, respectively, and the time of maximum velocity is inconsistent. In the case of erosion-entrainment, the properties of erodible material sources change, and the thickness and velocity of the debris flow are significantly improved. This also shows the validity of the strain softening constitutive model in coupled numerical analysis.

As shown in Figure 15, the impact height of debris flow also significantly differs when the erosion-entrainment effect is considered or not. The maximum impact height is 2.07 m, rapidly dropping to 1.24 m after reaching the peak. Regardless of the erosion-entrainment process, the maximum impact height is only 0.96 m, and it slowly rises to its peak. This shows that the impact trend of debris flow is significantly different when the erosion-entrainment process is considered or not, and the former has prominent movement characteristics.

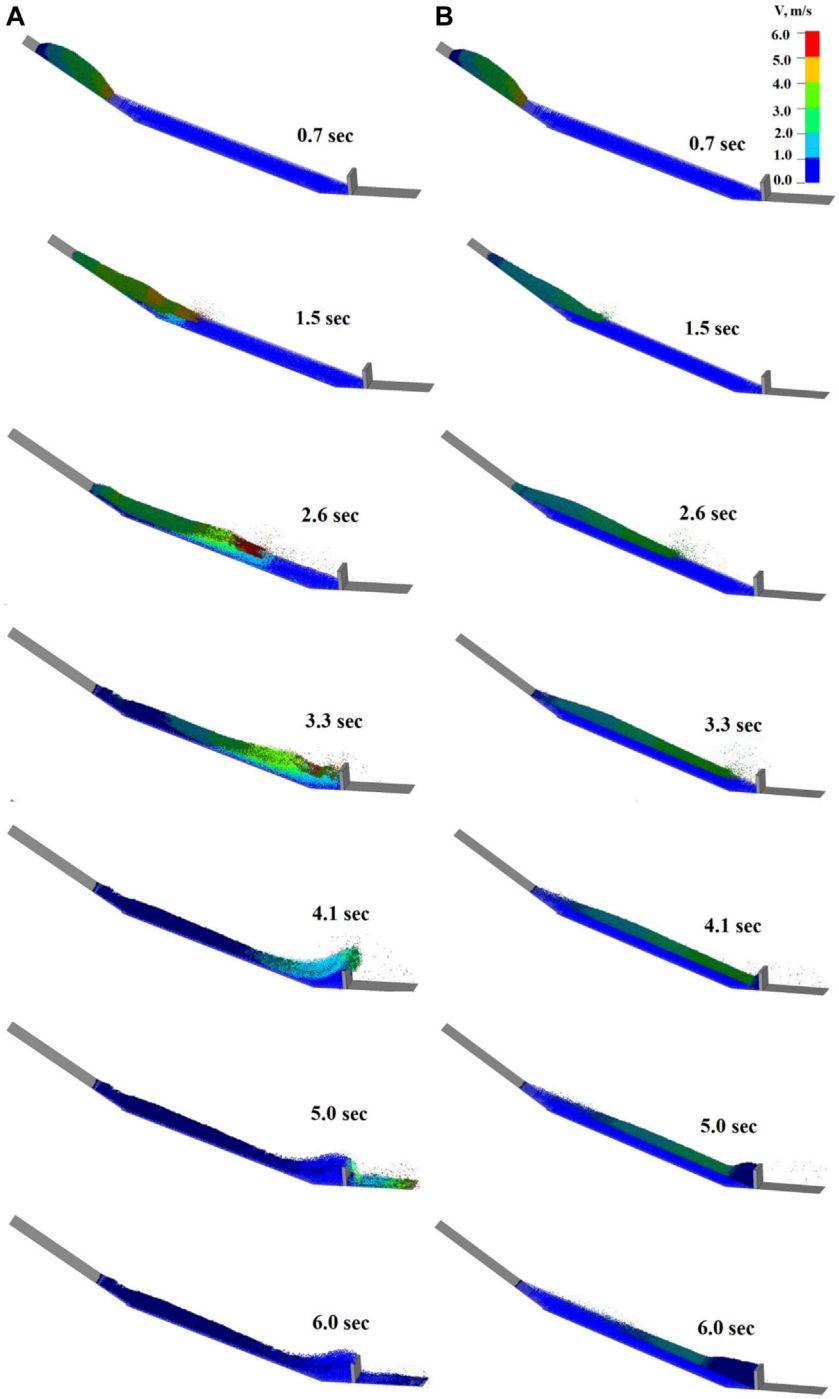

FIGURE 13
Comparison of debris flow impact process and velocity vector results with and without erosion-entrainment process.

As shown in Figure 16, the time history of debris flow impact force is also significantly different with and without the consideration of erosion-entrainment. The maximum impact force in the erosion-entrainment process is 155.65 kN/m^2 and rapidly drops to 91.77 kN/m^2 after reaching the peak value. Regardless of the erosion-entrainment process, the maximum impact force is only 75.22 kN/m^2, slowly rising to its peak. This shows that the impact force law of debris flow is significantly different when the erosion-entrainment process is considered. The former mainly corresponds to the fluid dynamics theory, while the latter is more suitable for calculation using the hydrostatic theory.

As seen in Figure 17, the dynamic response of the barrier is consistent with the law of debris flow impact force. In the design of the barrier, the hydrodynamic model is recommended because the

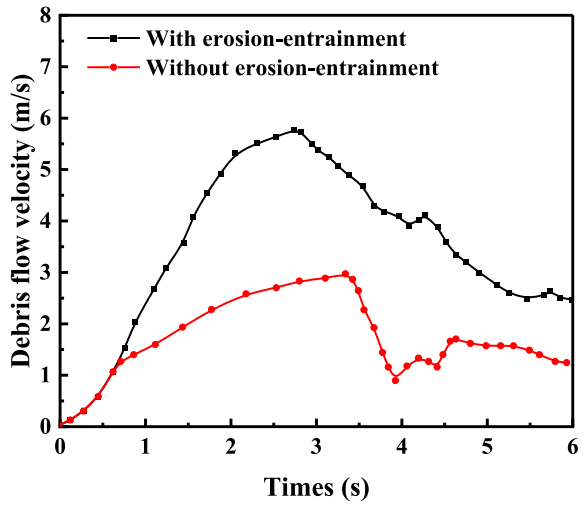

FIGURE 14
Comparison of debris flow velocity results.

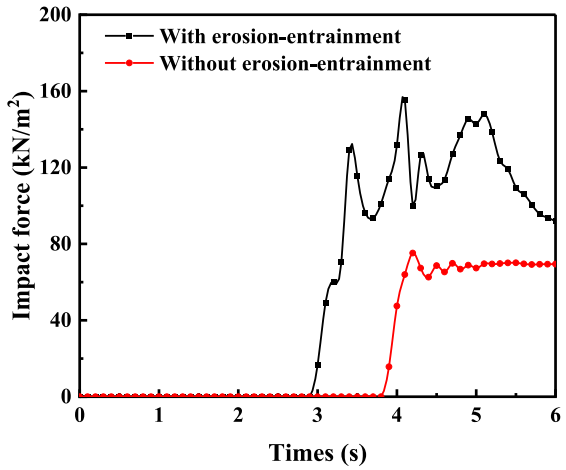

FIGURE 16
Time history results of the impact force.

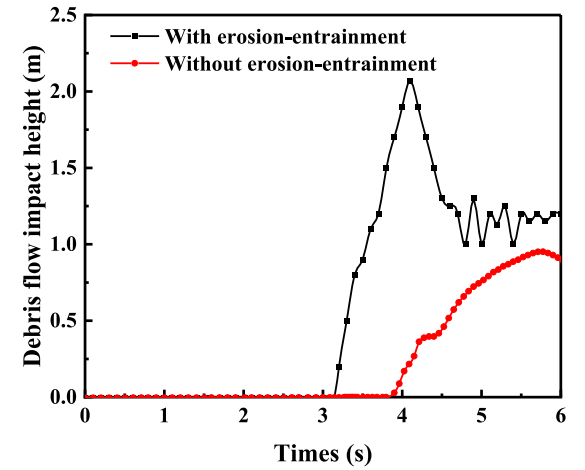

FIGURE 15
Comparison of impact height results.

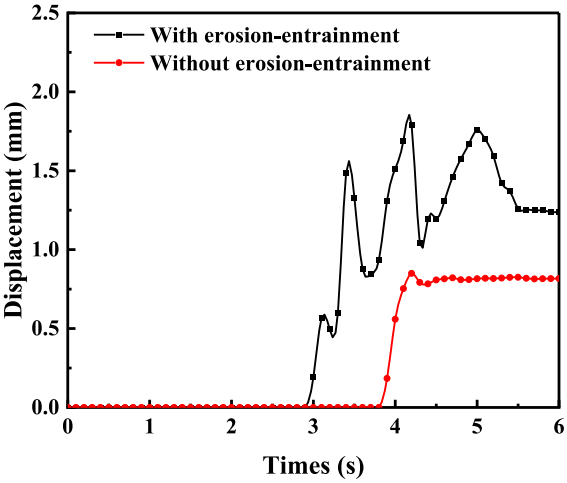

FIGURE 17
Time history results of the displacement.

law of debris flow impact force considering the erosion-entrainment process is significantly different from that without considering the process. It is suggested to modify the empirical formula of the debris flow impact force to consider erosion-entrainment. The existing calculation formula of debris flow impact force based on hydrodynamics is shown in Eq. 9 (Hungr et al., 2005):

$$P_{max} = a \cdot \rho \cdot v^2 \tag{9}$$

Here P_{max} is the peak impact force; a is the empirical coefficient; ρ and v are the density and velocity of debris flow, respectively.

It is suggested to use the erosion-entrainment correction coefficient γ to modify the parameters of the empirical formula of debris flow impact force considering the erosion-entrainment effect:

$$P_{max} = \gamma \cdot a \cdot \rho \cdot v^2 \tag{10}$$

Here, γ is the erosion-entrainment correction coefficient.

As a result of this paper's numerical calculation, the debris flow velocity considering the erosion-entrainment process is 2.07 times that without the process. It is recommended that the erosion-entrainment correction coefficient ranges from 2 to 10.

6 Conclusion

This paper establishes a complex coupled dynamic model of debris flow, erodible material source, and rigid barrier based on the coupled SPH-DEM-FEM algorithm. The following research has been carried out:

A complex coupling dynamic model of debris flow, erodible material source, and a rigid barrier is established in this paper. By comparing the model with the laboratory test, the applicability of the coupled SPH-DEM-FEM method to the analysis of the impact force

caused by debris flow is verified. The strain softening model is used to simulate the process of the erodible material source from solid state to transition state and finally to liquid state. The impact force caused by debris flow and the dynamic response of a rigid barrier, considering the process of source erosion-entrainment, is analyzed. The results show that the volume of debris flow, impact force, and dynamic response of a rigid barrier considering source erosion entrainment are significantly greater than the original model. The existing formula of debris flow impact force is modified in this paper according to the calculation results. The coupled numerical analysis method and research results help to clarify the impact of erosion-entrainment, the calculation of debris flow impact force, and the design of a rigid barrier.

(1) Using the coupled SPH-DEM-FEM algorithm, a complex coupling dynamic model of debris flow, erodible material source, and rigid barrier is established using the strain softening model. By comparing the model with the laboratory tests, the applicability of the coupled SPH-DEM-FEM method to the analysis of the impact force caused by debris flow is verified.
(2) The impact process and velocity vector of debris flow with and without source erosion-entrainment are analyzed. In the former, due to the increase of debris flow volume, many debris flows rush out of the barrier, while the latter is completely intercepted. The coupled numerical model can simulate the erosion-entrainment process of the erodible material source.
(3) Comparative analysis of flow velocity and impact height of debris flow with and without source erosion-entrainment is shown. Considering the erosion-entrainment process, the maximum velocity and impact height of debris flow are 5.98 m/s and 2.07 m, respectively, 1.98 times and 2.16 times than when not considering the process. The results show that the erosion-entrainment effect significantly changes the debris flow.
(4) A comparative analysis of the time history of debris flow impact force and the time history of the rigid barrier displacement is carried out with and without considering source erosion-entrainment action. Considering the erosion-entrainment process, the peak impact force of debris flow and the peak displacement of the rigid barrier are 155.65 kN/m^2 and 1.75 mm, respectively, which are 2.07 times and 2.13 times than without considering the process. The erosion-entrainment correction coefficient is introduced to modify the parameters of the existing calculation formula of debris flow impact force based on hydrodynamics based on the calculation results. The research results have a reference value for calculating the debris flow impact force and the barrier design.

Data availability statement

The raw data supporting the conclusions of this article will be made available by the authors, without undue reservation.

Author contributions

Writing—original draft preparation, software, methodology BL; validation, investigation, writing—review and editing YF; data curation, writing—review and editing YL; validation and investigation CZ. All authors have read and agreed to the published version of the manuscript.

Funding

This work was funded by the High-level Innovative Talents Program of Hebei University (grant numbers 521100222055).

Conflict of interest

The authors declare that the research was conducted in the absence of any commercial or financial relationships that could be construed as a potential conflict of interest.

Publisher's note

All claims expressed in this article are solely those of the authors and do not necessarily represent those of their affiliated organizations, or those of the publisher, the editors and the reviewers. Any product that may be evaluated in this article, or claim that may be made by its manufacturer, is not guaranteed or endorsed by the publisher.

References

Arattano, M., Franzi, L. J. N. H., and Sciences, E. S. (2003). On the evaluation of debris flows dynamics by means of mathematical models. *Nat. Hazards Earth Syst. Sci.* 3, 539–544. doi:10.5194/nhess-3-539-2003

Armanini, A., Fraccarollo, L., and Rosatti, G. (2009). Two-dimensional simulation of debris flows in erodible channels. *Comput. Geosciences* 35, 993–1006. doi:10.1016/j.cageo.2007.11.008

Armanini, A. (1997). "On the dynamic impact of debris flows," in *Recent developments on debris flows*. Editors A. Armanini and M. Michiue (Berlin, Heidelberg: Springer), 208–226.

Bugnion, L., Mcardell, B. W., Bartelt, P., and Wendeler, C. (2012). Measurements of hillslope debris flow impact pressure on obstacles. *Landslides* 9, 179–187. doi:10.1007/s10346-011-0294-4

Calvetti, F., Di Prisco, C. G., and Vairaktaris, E. (2017). DEM assessment of impact forces of dry granular masses on rigid barriers. *Acta Geotech.* 12, 129–144. doi:10.1007/s11440-016-0434-z

Chen, H., Crosta, G. B., and Lee, C. F. (2006). Erosional effects on runout of fast landslides, debris flows and avalanches: A numerical investigation. *debris flows avalanches a Numer. investigation* 56, 305–322. doi:10.1680/geot.2006.56.5.305

Choi, S.-K., Park, J.-Y., Lee, D.-H., Lee, S.-R., Kim, Y.-T., and Kwon, T.-H. (2021). Assessment of barrier location effect on debris flow based on smoothed particle hydrodynamics (SPH) simulation on 3D terrains. *Landslides* 18, 217–234. doi:10.1007/s10346-020-01477-5

Džiugys, A., and Peters, B. J. G. M. (2001). An approach to simulate the motion of spherical and non-spherical fuel particles in combustion chambers. *Granul. Matter* 3, 231–266. doi:10.1007/pl00010918

Fan, X., Scaringi, G., Korup, O., West, A. J., Van Westen, C. J., Tanyas, H., et al. (2019). Earthquake-induced chains of geologic hazards: Patterns, mechanisms, and impacts. *Rev. Geophys.* 57, 421–503. doi:10.1029/2018rg000626

Federico, F., and Cesali, C. (2015). An energy-based approach to predict debris flow mobility and analyze empirical relationships. *Can. Geotechnical J.* 52, 2113–2133. doi:10.1139/cgj-2015-0107

Fuchu, D., Lee, C., and Sijing, W. J. E. G. (1999). Analysis of rainstorm-induced slide-debris flows on natural terrain of Lantau Island, Hong Kong. *Hong Kong* 51, 279–290. doi:10.1016/s0013-7952(98)00047-7

Gao, L., Zhang, L. M., and Chen, H. X. (2017). Two-dimensional simulation of debris flow impact pressures on buildings. *Eng. Geol.* 226, 236–244. doi:10.1016/j.enggeo.2017.06.012

Guo, J., Cui, Y., Xu, W., Yin, Y., Li, Y., and Jin, W. (2022). Numerical investigation of the landslide-debris flow transformation process considering topographic and entrainment effects: A case study. *Landslides* 19, 773–788. doi:10.1007/s10346-021-01791-6

Haas, T. D., and Woerkom, T. V. J. E. S. P. (2016). Bed scour by debris flows: Experimental investigation of effects of debris-flow composition. *Earth Surf. Process. Landforms*, 41(13), pp.1951–1966.https://doi.org/doi:10.1002/esp.3963

Hu, K. H., Wei, F. Q., and Li, Y. (2011). Real-time measurement and preliminary analysis of debris-flow impact force at Jiangjia Ravine, China. *Earth Surf. Process. Landforms* 36, 1268–1278. doi:10.1002/esp.2155

Huang, H.-P., Yang, K.-C., and Lai, S.-W. J. M. (2007). Impact force of debris flow on filter dam. *momentum* 9 (2), 03218.

Hungr, O., Mcdougall, S., and Bovis, M. (2005). "Entrainment of material by debris flows," in *Debris-flow hazards and related phenomena*. Editors M. Jakob and O. Hungr (Berlin, Heidelberg: Springer), 135–158.

Hungr, O., Morgan, G. C., and Kellerhals, R. (1984). Quantitative analysis of debris torrent hazards for design of remedial measures. *Can. Geotechnical J.* 21, 663–677. doi:10.1139/t84-073

Jeong, S., and Lee, K. J. C. (2019). Analysis of the impact force of debris flows on a check dam by using a coupled Eulerian-Lagrangian (CEL) method. *Comput. Geotechnics* 116, 103214.

Jiang, Y.-J., Towhata, I. J. R. M., and Engineering, R. (2013). Experimental study of dry granular flow and impact behavior against a rigid retaining wall. *Rock Mech. Rock Eng.* 46, 713–729. doi:10.1007/s00603-012-0293-3

Law, P. H. (2015). *Computational study of granular debris flow impact on rigid barriers and baffles*. Hong Kong: Hong Kong University of Science and Technology.

Lee, K., and Jeong, S. (2018). Large deformation FE analysis of a debris flow with entrainment of the soil layer. *Comput. geotechnics* 96, 258–268. doi:10.1016/j.compgeo.2017.11.008

Lee, K., Kim, Y., Ko, J., and Jeong, S. (2019). A study on the debris flow-induced impact force on check dam with-and without-entrainment. *Comput. Geotech.* 113, 103104. doi:10.1016/j.compgeo.2019.103104

Lee, S., An, H., Kim, M., Lee, G., and Shin, H. (2022). Evaluation of different erosion–entrainment models in debris-flow simulation. *Landslides 19*, 2075–2090.

Lei, Z., Wu, B., Wu, S., Nie, Y., Cheng, S., and Zhang, C. (2022). A material point-finite element (MPM-FEM) model for simulating three-dimensional soil-structure interactions with the hybrid contact method. *Comput. geotechnics* 152, 105009. doi:10.1016/j.compgeo.2022.105009

Leonardi, A., Wittel, F. K., Mendoza, M., and Herrmann, H. J. (2015). "Lattice-Boltzmann method for geophysical plastic flows," in *Recent advances in modeling landslides and debris flows* (Berlin/Heidelberg, Germany: Springer), 131–140.

Leonardi, A., Wittel, F. K., Mendoza, M., and Herrmann, J. (2013). "Multiphase debris flow simulations with the discrete element method coupled with a lattice-Boltzmann fluid", in: Procdeedings of the Particles III: proceedings of the III International Conference on Particle-Based Methods: fundamentals and applications: CIMNE), 276–287.September 2013

Leonardi, A., Wittel, F. K., Mendoza, M., Vetter, R., Herrmann, H. J. J. C. a. C., and Engineering, I. (2016). Particle–fluid–structure interaction for debris flow impact on flexible barriers. *Computer-Aided Civ. Infrastructure Eng.* 31, 323–333. doi:10.1111/mice.12165

Li, B.-L., Wang, C.-M., and Li, Y.-Y. J. L. (2022b). Study on dynamic response of blocking structure and debris flow impulsive force considering. *Mater. Source Eros.* 2022, 1252637.

Li, B.-L., Wang, C.-M., and Li, Y.-Y. (2022a). Study on dynamic response of blocking structure and debris flow impulsive force considering material source erosion. *Lithosphere* 2022, 1252637. doi:10.2113/2022/1252637

Li, B., Wang, C., Li, Y., Liu, Y., Jiang, N., Liang, Z., et al. (2020a). Dynamic response analysis of retaining dam under the impact of solid-liquid two-phase debris flow based on the coupled SPH-DEM-FEM method. *Geofluids* 2020, 6635378. doi:10.1155/2020/6635378

Li, S., Peng, C., Wu, W., Wang, S., Chen, X., Chen, J., et al. (2020b). Role of baffle shape on debris flow impact in step-pool channel: An SPH study. *Landslides* 17, 2099–2111. doi:10.1007/s10346-020-01410-w

Li, X., Sovilla, B., Ligneau, C., Jiang, C., and Gaume, J. (2022c). Different erosion and entrainment mechanisms in snow avalanches. *Mech. Res. Commun. 124*, 103914.

Li, X., Zhao, J. J. I. J. F. N., and Geomechanics, A. M. I. (2018). A unified CFD-DEM approach for modeling of debris flow impacts on flexible barriers. *Int. J. Numer. Anal. Methods Geomech.* 42, 1643–1670. doi:10.1002/nag.2806

Liu, W., and He, S. J. L. (2020). Comprehensive modelling of runoff-generated debris flow from formation to propagation in a catchment. *Landslides* 17, 1529–1544. doi:10.1007/s10346-020-01383-w

Liu, W., Yan, S., and He, S. J. E. G. (2020). A simple method to evaluate the performance of an intercept dam for debris-flow mitigation. *Eng. Geol.* 276, 105771.

Luna, B. Q., Remaître, A., Van Asch, T. W. J., Malet, J. P., and Van Westen, C. J. (2012). Analysis of debris flow behavior with a one dimensional run-out model incorporating entrainment. *Eng. Geol.* 128, 63–75. doi:10.1016/j.enggeo.2011.04.007

Mangeney, A., Roche, O., Hungr, O., Mangold, N., Faccanoni, G., and Lucas, A. (2010). Erosion and mobility in granular collapse over sloping beds. *J. Geophys. Res. Earth Surf.* 115, F03040. doi:10.1029/2009jf001462

Mangeney, A., Tsimring, L. S., Volfson, D., Aranson, I. S., and Bouchut, F. (2007). Avalanche mobility induced by the presence of an erodible bed and associated entrainment. *Geophys. Res. Lett.* 34, L22401. doi:10.1029/2007gl031348

Moriguchi, S., Borja, R. I., Yashima, A., and Sawada, K. J. a. G. (2009). Estimating the impact force generated by granular flow on a rigid obstruction. *Acta Geotech.* 4, 57–71. doi:10.1007/s11440-009-0084-5

Peng, H., Zhao, Y., Cui, P., Zhang, W., Chen, X., and Chen, X. J. J. O. M. S. (2011). Two-dimensional numerical model for debris flows in the jiangjia gully, yunnan province. *Yunnan Prov.* 8, 757–766. doi:10.1007/s11629-011-2043-5

Proske, D., Suda, J., and Hübl, J. (2011). Debris flow impact estimation for breakers. *Georisk Assess. Manag. Risk Eng. Syst. Geohazards* 5, 143–155. doi:10.1080/17499518.2010.516227

Roelofs, L., Colucci, P., and De Haas, T. (2022). How debris-flow composition affects bed erosion quantity and mechanisms: An experimental assessment. *Earth Surf. Process. Landforms 147*, 2151–2169.

Scheidl, C., Chiari, M., Kaitna, R., Müllegger, M., Krawtschuk, A., Zimmermann, T., et al. (2013). Analysing debris-flow impact models, based on a small scale modelling approach. *Surv. Geophys.* 34, 121–140. doi:10.1007/s10712-012-9199-6

Scheidl, J., Vetyukov, Y., Schmidrathner, C., Schulmeister, K., and Proschek, M. J. I. J. O. M. S. (2021). Mixed Eulerian–Lagrangian shell model for lateral run-off in a steel belt drive and its experimental validation. *Int. J. Mech. Sci.* 204, 106572.

Sha, S., Dyson, A. P., Kefayati, G., and Tolooiyan, A. (2023). Simulation of debris flow-barrier interaction using the smoothed particle hydrodynamics and coupled Eulerian Lagrangian methods. *Finite Elem. Analysis Des.* 214, 103864. doi:10.1016/j.finel.2022.103864

Shang, Y. J., Yang, Z. F., Li, L. H., Liu, D., Liao, Q. L., and Wang, Y. C. (2003). A super-large landslide in tibet in 2000: Background, occurrence, disaster, and origin. *Geomorphology* 54, 225–243. doi:10.1016/s0169-555x(02)00358-6

Shen, W., Zhao, T., Zhao, J., Dai, F., and Zhou, G. G. J. E. G. (2018). Quantifying the impact of dry debris flow against a rigid barrier by DEM analyses. *Eng. Geol.* 241, 86–96. doi:10.1016/j.enggeo.2018.05.011

Tang, C., Van Asch, T. W. J., Chang, M., Chen, G. Q., Zhao, X. H., and Huang, X. C. (2012). Catastrophic debris flows on 13 August 2010 in the Qingping area, southwestern China: The combined effects of a strong earthquake and subsequent rainstorms. *Geomorphology* 139-140, 559–576. doi:10.1016/j.geomorph.2011.12.021

Thouret, J. C., Antoine, S., Magill, C., and Ollier, C. (2020). Lahars and debris flows: Characteristics and impacts. *Earth-Science Rev.* 201, 103003. doi:10.1016/j.earscirev.2019.103003

Tian, M., Hu, K.-H., Ma, C., and Lei, F.-H. J. J. O. H. E. (2014). Effect of bed sediment entrainment on debris-flow resistance. *J. Hydraulic Eng.* 140, 115–120.

Wang, G., Hu, B., Tian, S., Ai, M., Liu, W., and Kong, X. (2021). Seepage field characteristic and stability analysis of tailings dam under action of chemical solution. *Sci. Rep.* 11, 4073. doi:10.1038/s41598-021-83671-6

Wang, G., Sassa, K., and Fukuoka, H. (2003). Downslope volume enlargement of a debris slide–debris flow in the 1999 Hiroshima, Japan, rainstorm. *Eng. Geol.* 69, 309–330. doi:10.1016/s0013-7952(02)00289-2

Wang, G., Tian, S., Hu, B., Kong, X., and Chen, J. (2020). An experimental study on tailings deposition characteristics and variation of tailings dam saturation line. *Geomechanics Eng.* 23, 85–92.

Wang, G., Zhao, B., Lan, R., Liu, D., Wu, B., Li, Y., et al. (2022). Experimental study on failure model of tailings dam overtopping under heavy rainfall. *Lithosphere*, 5922501.

Wang, G., Zhao, B., Wu, B., Zhang, C., and Liu, W. (2023). Intelligent prediction of slope stability based on visual exploratory data analysis of 77 *in situ* cases. *Int. J. Min. Sci. Technol.* 33, 49–61.

Wang, W., Yin, Y., Wei, Y., Zhu, S., Li, J., Meng, H., et al. (2021). Investigation and characteristic analysis of a high-position rockslide avalanche in Fangshan District, Beijing, China. *Bull. Eng. Geol. Environ.* 80, 2069–2084. doi:10.1007/s10064-020-02098-x

Yin, Y., Cheng, Y., Liang, J., and Wang, W. (2016). Heavy-rainfall-induced catastrophic rockslide-debris flow at sanxicun, dujiangyan, after the wenchuan ms 8.0 earthquake. *Landslides* 13, 9–23. doi:10.1007/s10346-015-0554-9

Zaginaev, V., Petrakov, D., Erokhin, S., Meleshko, A., Stoffel, M., and Ballesteros-Cánovas, J. A. (2019). Geomorphic control on regional glacier lake outburst flood and debris flow activity over northern Tien Shan. *Glob. Planet. Change* 176, 50–59. doi:10.1016/j.gloplacha.2019.03.003

frontiers | Frontiers in Earth Science

TYPE Original Research
PUBLISHED 21 February 2023
DOI 10.3389/feart.2023.1128167

OPEN ACCESS

EDITED BY
Guangjin Wang,
Kunming University of Science and Technology, China

REVIEWED BY
Yingjie Li,
China University of Mining and Technology, Beijing, China
Wen Zhang,
Jilin University, China

*CORRESPONDENCE
Lu Xia,
xialu@cugb.edu.cn

SPECIALTY SECTION
This article was submitted to Environmental Informatics and Remote Sensing, a section of the journal Frontiers in Earth Science

RECEIVED 20 December 2022
ACCEPTED 08 February 2023
PUBLISHED 21 February 2023

CITATION
Ma T and Xia L (2023), The influence of normal distribution dispersion of fracture size on blockiness and REV of fractured rock masses.
Front. Earth Sci. 11:1128167.
doi: 10.3389/feart.2023.1128167

The influence of normal distribution dispersion of fracture size on blockiness and REV of fractured rock masses

Tiantian Ma[1] and Lu Xia[2]*

[1]School of Water Resources and Environment, China University of Geosciences, Beijing, China, [2]Key Laboratory of Groundwater Conservation of MWR, School of Water Resources and Environment, China University of Geosciences, Beijing, China

The fractures of different sizes in rock masses are important for describing rock fragmentation. The distribution dispersion of fracture size influences the blockiness level of the rock masses. Based on a normal statistical distribution, the volume ratio of blocks to rock (*B*) was obtained to describe the blockiness level. For exploring the effect of the dispersion of fracture size on blockiness level and the representative elementary volume (REV) of rock masses, the laboratory model and numerical simulation were established, and the theory of statistics and the method of analytical solution were applied. In addition, 4,525 practical rock models were established to qualitatively reproduce the behavior of *B* with changing domain size. The results show that by comparing the degree of convergence, the REV of a rock mass is determined by the fracture size rather than the degree of fracture dispersion. The value of *B* increases with the distribution dispersion of fracture size, indicating a higher blockiness level. From the experimental analysis of coin tossing, when the number of trials exceeds 69, the random results are nearly stable. In this study, 100 calculations were performed. A formula to calculate the blockiness by considering the dispersion degrees of fracture size was obtained. Moreover, a positive linear correlation between *B* and the coefficient of variation of fracture size was obtained. The rate of increase in *B* has a parabolic relationship with the ratio of fracture size to fracture spacing (*L*).

KEYWORDS

dispersion of fracture sizes, normal distribution, representative elementary volume, blockiness, rock masses, the numerical model

1 Introduction

The typical unit volume or the representative elementary volume (REV) is the minimum volume that represents a material on a large scale. The concept of the REV is an indispensable basis for understanding fractured rock masses, and the existence of a REV is the premise of continuum theory and the finite element theory. This continuum method is important for solving large rock problems (Wang et al., 2022b; Lei et al., 2022). When the REV size is very small, the theory of continuous media can be applied directly. However, the application of this theory to fractured rock masses is limited. For example, the representativeness of the permeability tensor and the applicability of porous medium theory depend on the existence of a REV in the rock mass (Bear, 1972; Long and Billaux, 1987; Wang et al., 2003). A REV is the basic and key index of rock mechanical properties

(Xiang and Zhou, 2005). As a result, the concept has attracted a great deal of attention in the field of geotechnical engineering and has been discussed from various points of view in many publications. These include the three-dimensional (3D) and two-dimensional (2D) hydraulic conductivity, the damage coefficient, the geological strength index, and the REV (Wang et al., 2002; Ni et al., 2017; Wang et al., 2018; Huang et al., 2020). The REV method can describe a threshold of a rock mass property, such as hydraulic conductivity (Li and Zhang, 2011). Typical rock masses are formed under the influence of blocks with different domain sizes (Shahami et al., 2019). In this study, the REV of a rock mass was explored from the viewpoint of the block.

The stability of rocks has always been a focus of concern. Wang et al. estimated the effect of five indexes on the stability of slop by numerical and statistical methods (Wang et al., 2022c). The study of blockiness level is of great significance to avoid geological disasters such as rockfalls and tailings pond failures (Wang et al., 2019; Wang et al., 2021; Wang et al., 2022a; Lin et al., 2022; Ma and Liu, 2022). Blockiness is defined as the percentage of the volume of isolated blocks formed by fractures to the total volume of the rock (Xia et al., 2016). It is used to quantitatively describe the fragility level of a rock mass (Aler et al., 1996; Chen et al., 2021). A rock mass with a higher blockiness level tends to be more fragmented. Conversely, a rock mass with a lower blockiness level has a stronger integrity. In recent years, blockiness has been adopted by some researchers as an index of rock mass quality classification. In a paper by Xia et al. (2016), 77 types of fractured rock mass models were developed based on seven classes of fracture size and 11 spacing categories recommended and classified by the International Society for Rock Barton (1979). The rock block was identified and its B was investigated. For each domain size, nine implementations were performed to reduce the effects of randomness. The results indicated that 76 REV sizes ranged from 2 to 20 times the fracture spacing.

It is well known that the influence of fractures on the blockiness level is considerable, especially in the spacing, size, and statistical distribution of fractures (Elmouttie and Poropat, 2011; Zhu et al., 2014; Ajayi et al., 2018). The sizes and distributions of fractures in rock masses are diverse (Hu et al., 2022; Yang et al., 2022). Fracture spacing and size control the volume, quantity, and stability of a block. In this study, the fracture sizes of each model were constant. The quantitative relationship between B, fracture spacing, and size was explored, assuming equal fracture sizes (Xia and Yu, 2020). In this study, a relationship between B and normally distributed fracture size was obtained. The coefficient of variation (C_v) was now used to indicate the dispersion degree of fracture size. A more practical model was established by GeneralBlock (GB) software, and the influence of the statistical dispersion of fracture size on B and REV was investigated. To decrease the random error of this relationship, the number of calculations was increased from 5 to 100. This process includes the following: 1) based on the 77 models by Xia et al. (2016), the statistical distribution of fracture size was changed while the other parameters were kept constant; 2) five types of fracture networks were constructed under different statistical dispersions of fracture size; 3) rock blocks in each model were identified, and the fluctuation in B with the size of the model area was calculated; and 4) the REV sizes in these models were determined by the convergence or the C_v of B, and an analytical function describing the relationship between B and the distribution dispersion of fracture size was developed.

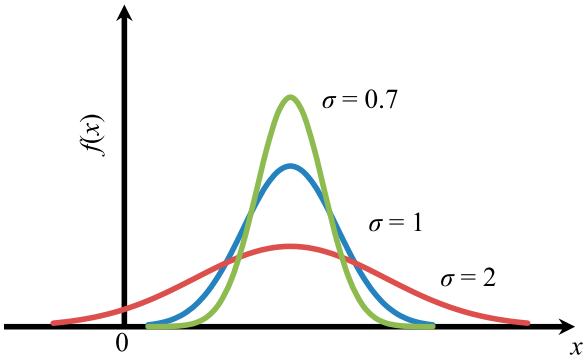

FIGURE 1
Probability density function $f(x)$ for σ = 0.7, σ = 1, and σ = 2.

2 Statistical distribution of fracture size

2.1 Fracture shape and size

The complex fractures in rock have a great influence on the quality and safety of rock in geological engineering projects such as dam foundations, underground tunnels, or caverns. A scheme for modeling fracture networks was proposed (Neuman, 1989). However, for this model, the fracture geometry and distribution must be determined first. In past research, the fractures have been hypothesized to be disc-shaped, ellipsoidal, or polygonal (Baecher and Lanney, 1978; Dershowitz and Einstein, 1988; Kalenchuk et al., 2006). Polygonal and ellipsoidal models, which incorporate more geometric coefficients than the disc model, may describe the fracture shape more accurately. However, it is not easy to determine these coefficients (such as the directions of the major and minor axes of an ellipse). The more coefficients there are, the greater the uncertainty of the model. In this study, the disk assumption was adopted, so only its diameter or radius was needed to describe the fracture size. The spatial location of fractures was determined by the Poisson model (Priest and Hudson, 1976). Among all fracture parameters, fracture size directly and critically affects the characteristics of rock masses such as fracture closure, permeability, and rock instability (La Pointe et al., 1993; Giwelli et al., 2009; Lang et al., 2014; Zhang et al., 2020). A normal distribution and dispersion level are concerns in this study.

TABLE 1 Spacing, size, and 3D density (d_3) of the fractures in the 77 fractured rock models. (*Xia et al., 2016*).

Spacing (C) size (D)	Extremely close (ECS) C=0.02 m	Very close (VCS1) C=0.04 m	Very close (VCS2) C=0.06 m	Close (CS1) C=0.13 m	Close (CS2) C=0.2 m	Moderate (MS1) C=0.4 m	Moderate (MS2) C=0.6 m	Wide (WS1) C=1.3 m	Wide (WS2) C=2 m	Very wide (VWS) C=4 m	Extremely wide (EWS) C=6 m
Very high (VHP) D=20.0 m	0.1592	0.0796	0.0531	0.0245	0.0159	0.0080	0.0053	0.0024	0.0016	0.0008	0.0005
High (HP) D=15.0 m	0.2829	0.1415	0.0943	0.0435	0.0283	0.0141	0.0094	0.0044	0.0028	0.0014	0.0009
Medium (MP2) D=10 m	0.6366	0.3183	0.2122	0.0979	0.0637	0.0318	0.0212	0.0098	0.0064	0.0032	0.0021
Medium (MP1) D=6.5 m	1.5068	0.7534	0.5023	0.2318	0.1507	0.0753	0.0502	0.0232	0.0151	0.0075	0.0050
Low (LP2) D=3.0 m	7.0736	3.5368	2.3579	1.0882	0.7074	0.3537	0.2358	0.1088	0.0707	0.0354	0.0236
Low (LP1) D=2.0 m	15.9155	7.9577	5.3052	2.4485	1.5915	0.7958	0.5305	0.2449	0.1592	0.0796	0.0531
Very low (VLP) D=1.0 m	63.6620	31.8310	21.2207	9.7942	6.3662	3.1831	2.1221	0.9794	0.6366	0.3183	0.2122

2.2 Statistical dispersion of fracture size

The statistical distribution of the fracture size is an important parameter for characterizing fractures. Although there are many distribution forms of fracture size, the Gaussian distribution (the normal distribution) is the most commonly applied distribution in the statistical analysis of geotechnical engineering. A simple form of the normal distribution is another reason for applying it. It only requires the parameters of mean and standard deviation. The discrete level of stochastic variables can be described by the standard deviation. Moreover, a normal distribution is generally adopted for fracture size. The standard deviation of the fracture size can be calculated by estimating the maximum value and the minimum value. In this study, the effect of the discrete level of fracture size on blockiness and REV was explored. The normal distribution of fracture size has been adopted by many authors, which is an important distribution in theory and application (Pahl, 1981; Min and Jing, 2003; Priest, 2004; Song et al., 2022; Zhang et al., 2022). According to the criterion of normal distribution, the probability density function, denoted as $f(x)$, was defined as (Wilson, 1927)

$$f(x) = 1/\left(\sqrt{2\pi}\sigma\right) \times \exp\left[-(x-\mu)^2/\left(2\sigma^2\right)\right], \quad -\infty < x < +\infty \tag{1}$$

where μ is the mean, σ is the standard deviation, and $\sigma > 0$. As demonstrated in Figure 1, the shape of the curve is determined by the parameter σ. The coefficient of variation (C_v) is defined as the ratio of the standard deviation (σ) to the mean (μ). To avoid the effect of the mean, C_v can be used to represent the statistical dispersion degree of fracture size.

3 Blockiness and REV of rock masses

3.1 Fracture network modeling

Xia et al. (2016) developed 77 types of fractured rock mass models and calculated the 3D fracture density (d_3) of these models (as illustrated in Table 1). On this basis, five types of models are selected to discuss the influence of fracture size dispersion with a normal distribution on the B and REV of rock masses. The five representative models were as follows: model I with moderate spacing and moderate persistence (MS1-MP1); model II with moderate spacing and low persistence (MS2-LP2); model III with wide spacing and high persistence (WS1-HP); model IV with wide spacing and medium persistence (WS1-MP1); and model V with wide spacing and low persistence (WS1-LP2). The domain sizes of these cubic models have side lengths ranging from 2 to 20 times the fracture spacing.

Using the principle of 3σ to measure the probability of a normal distribution within $\mu \pm 3\sigma$, the probability is approximately 99.7%, as given in Figure 2. That is, the probability of random numbers out of this range is negligible. Normal random variables range in value from positive to negative, whereas the fracture size cannot take negative values. We defined $\mu - 3\sigma > 0$ to ensure that the value is

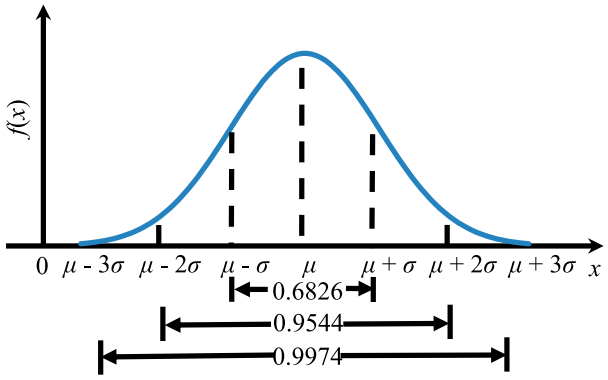

FIGURE 2
The areas under the normal density function within the ranges of $\mu \pm \sigma$, $\mu \pm 2\sigma$, and $\mu \pm 3\sigma$.

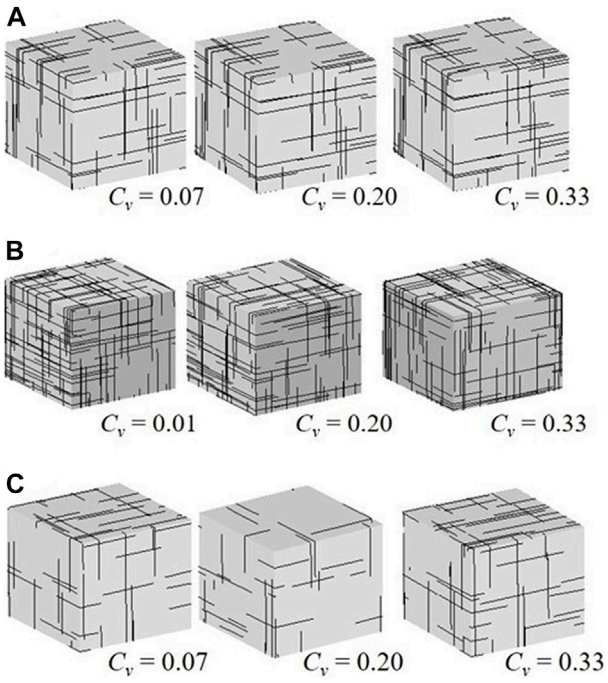

FIGURE 3
The fracture networks with different dispersions of fracture size: **(A)** model II, **(B)** model III, **(C)** model V; the domain size of **(A)** to **(C)** is 3.6 × 3.6 × 3.6 m^3, 18.2 × 18.2 × 18.2 m^3, 2.6 × 2.6 × 2.6 m^3.

positive. For each model, five different standard deviations were selected. The parameters of the discrete fracture networks are provided in Table 2, containing the fracture orientation, fracture occurrence, and standard deviations of fracture size. The representative fracture networks were obtained by statistical dispersions of different fracture sizes, as shown in Figure 3.

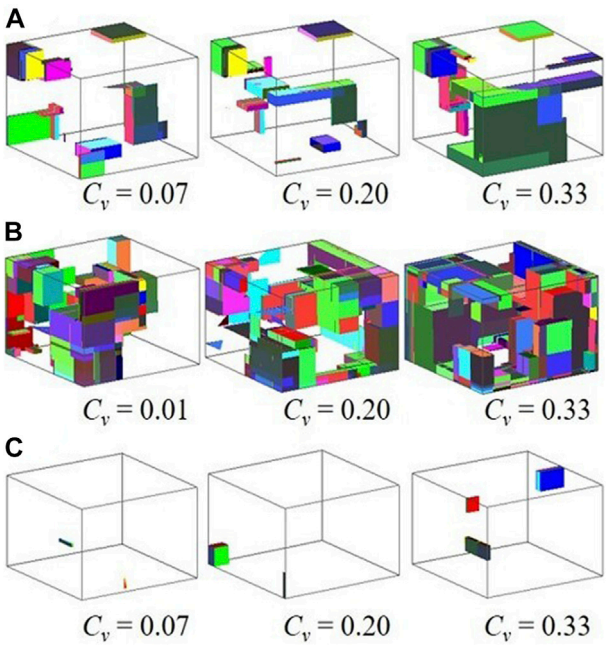

FIGURE 4
The models of rock masses produced by adopting different dispersions of fracture size: **(A)** model II, **(B)** model III, **(C)** model V; the domain size of **(A)**-**(C)** is 3.6 m^3 × 3.6 m^3 × 3.6 m^3, 18.2 m^3 × 18.2 m^3 × 18.2 m^3, 2.6 m^3 × 2.6 m^3 × 2.6 m^3.

3.2 Calculation of the blockiness and REV

In this study, fractures with five different standard deviations of normal distribution were considered in the simulation analysis. According to the parameters of fracture in Table 2, the domain size ranges from 2 to 20 times the spacing. A total of 4,525 fractured rock models were established. The method of multiple simulations was applied to reduce randomness. A comparison of the theoretical and simulated fracture radii of each model is presented in Table 3, for the number, mean, and standard deviation of the fractured radii. The results show that the models adopted in this work, which allow a more realistic consideration of fracture size dispersion than previous models, can capture the blockiness level well. These fractured rock models were considered reasonable. The rock model based on the fracture networks of the three models is shown in Figure 4. The number of blocks increases with the distribution dispersions of fracture size. To ignore random errors, simulations are performed 9 times at every domain size, and random values of B with 10 domain sizes of five models are obtained. The results reveal the behavior of B with domain size.

A rock mass has volumetric properties. When the volume of the rock mass reaches a certain range, the rock parameters tend to be stable; this threshold volume (the REV) can be used to

TABLE 2 Parameters of the discrete fracture network models with different means (μ), standard deviations (σ), and coefficients of variation (C_v).

Model	Orientation distribution	κ for Fisher	Average dip-directions of the three groups (°)	Average dips of the three groups (°)	Radius mean (μ)	Radius standard deviation(σ)	Coefficient of variation (C_v)
I	Fisher	20	180/90/360	89/89/1	3.25	0/0.1/0.25/0.5/0.75/1	0/0.03/0.08/0.15/0.23/0.31
II	Fisher	20	180/90/360	89/89/1	1.5	0/0.1/0.2/0.3/0.4/0.5	0/0.07/0.13/0.2/0.27/0.33
III	Fisher	20	180/90/360	89/89/1	7.5	0/0.1/1/1.5/2/2.5	0/0.01/0.13/0.2/0.27/0.33
IV	Fisher	20	180/90/360	89/89/1	3.25	0/0.1/0.25/0.5/0.75/1	0/0.03/0.08/0.15/0.23/0.31
V	Fisher	20	180/90/360	89/89/1	1.5	0/0.1/0.2/0.3/0.4/0.5	0/0.07/0.13/0.2/0.27/0.33

TABLE 3 Comparison between theoretical and simulated fracture radii in each model.

Model	Theoretical μ (m)	Theoretical σ (m)	Simulated μ (m)	Simulatedσ (m)	Maximum radius(m)	Minimum radius(m)	Number of simulated fractures
I	3.25	0.10	3.26	0.10	3.572	2.908	1107
	3.25	0.25	3.27	0.25	4.054	2.395	1107
	3.25	0.50	3.29	0.51	4.859	1.54	1107
	3.25	0.75	3.31	0.76	5.663	0.6843	1107
	3.25	1.00	3.32	0.99	6.188	0.3942	1107
II	1.50	0.10	1.51	0.10	1.846	1.205	624
	1.50	0.20	1.52	0.21	2.192	0.9104	624
	1.50	0.30	1.53	0.31	2.537	0.6156	624
	1.50	0.40	1.54	0.41	2.883	0.3207	624
	1.50	0.50	1.54	0.50	2.961	0.02592	624
III	7.50	0.10	7.50	0.10	7.838	7.151	1476
	7.50	1.00	7.54	1.03	10.88	4.009	1476
	7.50	1.50	7.56	1.54	12.56	2.263	1476
	7.50	2.00	7.50	2.10	13.8	0.5092	1476
	7.50	2.50	7.58	2.50	14.84	0.3604	1476
IV	3.25	0.10	3.26	0.10	3.596	2.955	624
	3.25	0.25	3.27	0.26	4.115	2.513	624
	3.25	0.50	3.30	0.52	4.979	1.776	624
	3.25	0.75	3.32	0.77	5.844	1.039	624
	3.25	1.00	3.34	1.02	6.467	0.3018	624
V	1.50	0.10	1.50	0.10	1.886	1.14	456
	1.50	0.20	1.51	0.21	2.727	0.7804	456
	1.50	0.30	1.51	0.31	2.658	0.4206	456
	1.50	0.40	1.51	0.42	2.831	0.06087	456
	1.50	0.50	1.51	0.51	2.894	0.02592	456

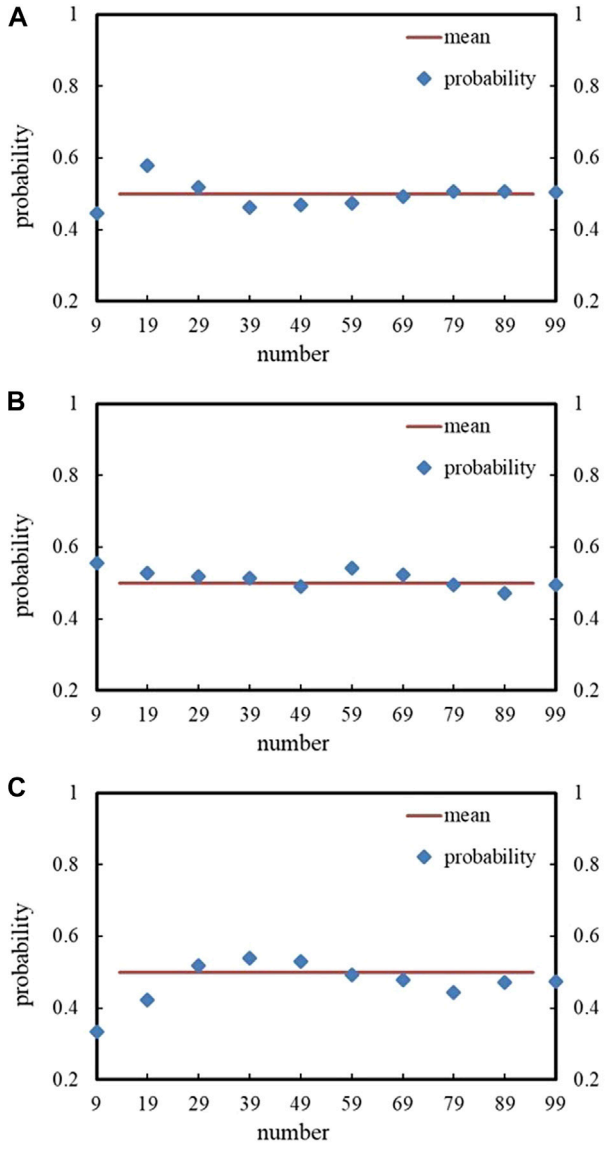

FIGURE 5
The 3 trials of random coin tossing from **(A–C)**.

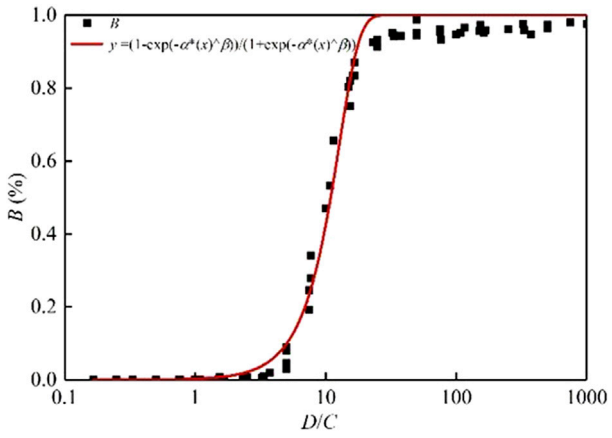

FIGURE 6
The function between blockiness, fracture diameter, and fracture spacing.

represent the whole rock. When the fluctuation in B is stable, the volume of rock is defined as the REV size. In this study, the C_v and the convergent mean with multiple simulations are used to investigate the REV volume (Min et al., 2004; Song et al., 2017; Chwała and Kawa, 2021). A point was proposed that 20 realizations were sufficient for the convergence of the factor of safety (Li et al., 2022). To obtain the value of B in the rock mass, 100 random realizations were performed at the REV size of the rock models.

The convergent mean with multiple simulations was used to estimate the fragile behavior of rock (Xia and Yu, 2020). For the 77 types of models, blocks were identified by GB, and the variation in B with domain size was investigated. Every domain size of the models was realized 5 times by Xia and Yu (2020). Then, a curve that represents the average of five random realizations was drawn to show the fluctuation in B with the domain size. In this way, the REV size of these models can be calculated by the convergence level of the mean B. The B of these fractured rock masses can be determined by the REV size. Based on block theory, the analytical function relating B, C, and D can be expressed (Yu et al., 2009; Xia and Yu, 2020; Cheng et al., 2021)

$$B = \left[1 - \exp\left(-\alpha L^{\beta}\right)\right] / \left[1 + \exp\left(-\alpha L^{\beta}\right)\right] \quad (2)$$

where L is the ratio of D to C; D is the fracture diameter, m; C is the fracture spacing, m; and α and β were calculated as $\alpha = -0.000176$ and $\beta = 3.42$. The value of B in this equation is simulated under the circumstances that the fracture size is equal. It is worth considering how many random simulations of models can bring the random results close to a true value (Liu et al., 2019). To explore this issue, the experiment involved tossing a coin *via* a computer simulation. As shown in Figure 5, a coin tossed multiple times can land on either side with equal probability until 69 coins have been tossed. Only then will the coin have a 90% within the range from 0.4 to 0.6. To obtain an accurate B value, 100 random operations were performed in 10 different volume domains of 77 rock models. Then, this equation has new factors: $\alpha = -0.00656$ and $\beta = 2.15509$.

The value of B was determined by the coefficient of variation and the convergent mean method with multiple simulations. The B value for 100 calculations of the 77 types of models is shown in Table 4 when the fracture size is constant. A total of 77,000 calculations are performed. The detailed data is contained in Supplementary Data S2 of the supplementary material. The value of B with 100 calculations slightly changed, compared with the findings by Xia and Yu (2020). The S-shaped curve of B with 100 calculations of the 77 models is shown in Figure 6, which is consistent with the simulated results.

TABLE 4 The calculated blockiness results of 77 fractured rock models.

Spacing size	ECS C=0.02 m (%)	VCS1 C=0.04 m (%)	VCS2 C=0.06 m (%)	CS1 C=0.13 m (%)	CS2 C=0.2 m	MS1 C=0.4 m (%)	MS2 C=0.6 m	WS1 C=1.3 m	WS2 C=2 m	VWS C=4 m	EWS C=6 m
VHP D=20.0 m	97.60	96.40	96.01	97.30	94.80%	95.10	94.4 0%	72.96%	56.52%	8.93%	0.92%
HP D=15.0 m	98.10	94.80	96.18	96.60	96.10%	94.30	93.20%	65.60%	27.70%—19.30%	1.9%	0.68%
MP2 D=10 m	97.40	96.10	95.90	93.20	94.96%	92.00	83.30%	27.90%—10.80%	9.70%—3.70%	0.71%	0.065%
MP1 D=6.5 m	97.06	95.10	95.10	94.79	95.15%	83.30	55.70%—53.20%	9.20%—4%	0.46%	0.057%	9.05E-03%
LP2 D=3.0 m	95.70	95.40	94.60	92.50	77.90%—80.30%	24.60	6.5%—3.0%	0.23%	0.071%	2.09E-03%	5.41E-04%
LP1 D=2.0 m	94.80	98.8	94.2	81.89	47.06%	4.6	0.97%—0.4%	0.7%	0.009%	4.43E-04%	1.75E-04%
VLP D=1.0 m	94.50	91.30	87.10	34.13	7.97%	0.7	0.17%	0.004%	6.76E-04%	1.19E-04%	6.02E-05%

4 Relationship between distribution dispersion of fracture size and blockiness and REV

4.1 Relationship between the distribution dispersion of fracture size and REV

There are some errors in the construction of stochastic discrete fracture networks, which can be reduced by multiple realizations (Wei et al., 2020). For the fracture network model, 10 ranges of rock volumes were considered to investigate the blockiness level. Nine simulations of the models were carried out within each rock volume, and nine blockiness values were obtained. The average of the nine blockiness results was taken as the blockiness level of the rock masses. There exists a size effect for the blockiness level of the rock mass. The blockiness level gradually becomes stable when the volume size of the rock masses reaches a certain condition. The coefficient of variation method is currently used to evaluate the stability of multiple stochastic simulations (Min and Jing, 2003; Wei et al., 2020; Wang et al., 2022c; Wu et al., 2022). The calculated data from random simulations are considered more reliable when the coefficient of variation of the multiple simulations keeps less than 10%, 5%, or 2%. Alternatively, visual observation of the mean value of multiple simulations is a way to evaluate the stability. In this study, the B value was determined with the coefficient of variation and the convergent mean with multiple simulations. When the simulation results of the rock model are stable with the volume of the rock, the minimum volume is considered to be the REV volume of the rock. The size of the rock volume can be represented by a multiple of the fracture spacing. In this study, the multiple of the fracture spacing was used to describe the REV size of the rock masses. For different distribution dispersions of fracture size, the diagram of the B value within the domain size is drawn in Figure 7. The horizontal coordinate is the ratio of the length of the rock side to the fracture spacing, representing the size of the rock volume. The vertical coordinate is the blockiness, representing the fragmentation degree of the rock. As can be seen, the fluctuations of the curves are largely unaffected by the distribution dispersion of fracture size. REV size is the rock volume when B tends to be stable with the increase in domain size. The lengths of models I–V have REV sizes varying from 10, 6, 14, 6, and 4 times the fracture spacing, respectively.

4.2 Relationship between distribution dispersion of fracture size and blockiness

The B value of these fractured rock masses can be decided at the REV size. When the distribution of fracture size is normal, the length of models I–V at REV size is correspondingly 10, 6, 14, 6, and 4 times the fracture spacing. Thus, we take 100 random realizations at REV size. The detailed data is contained in Supplementary Data S1 of the supplementary material. The fluctuation in B with the coefficient of variation of fracture size is shown in Figure 8. The curve represents the average of 100 random realizations. The B value increases with the C_v of the fracture size. As shown in Figure 8A, the B of model I increases

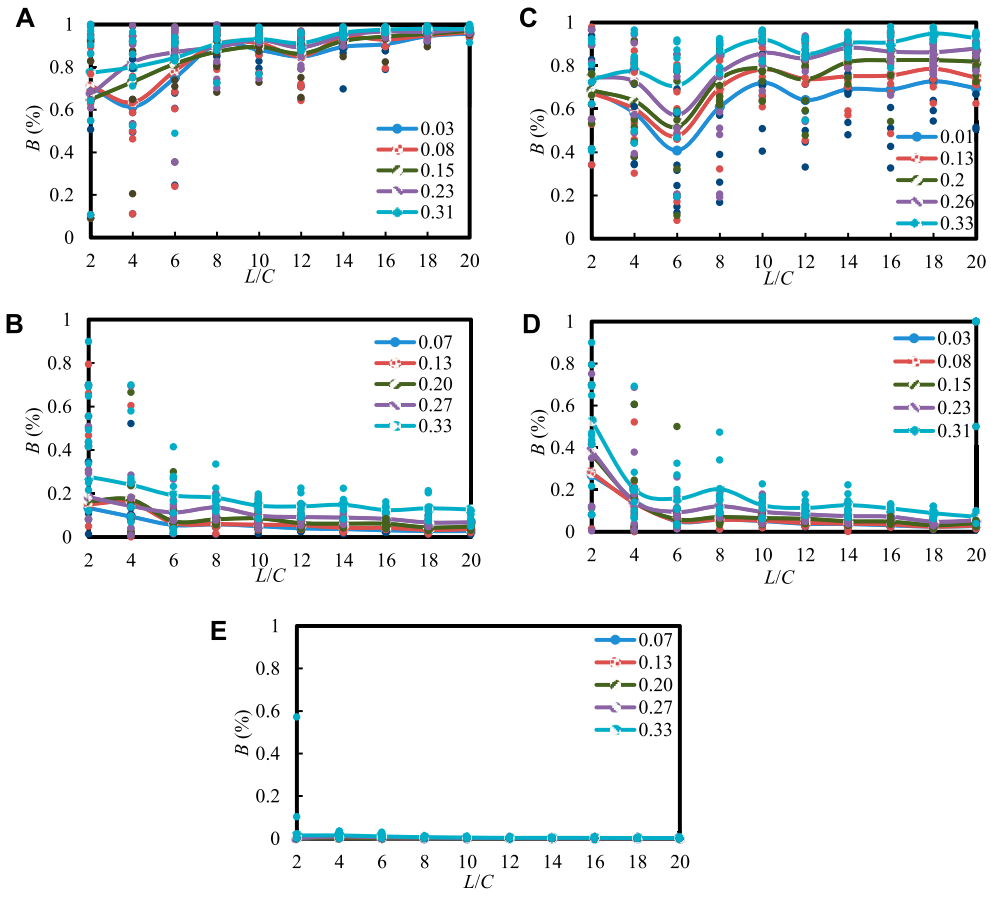

FIGURE 7
The relationships between *B* and the domain size of the five models: models of **(A–E)** is I to V.

from 84.69% to 91.14%. As shown in Figure 8B, the *B* of model II increases from 9.39% to 29.17%. As shown in Figure 8C, the *B* of the model III increases from 63.51% to 89.70%. As shown in Figure 8D, the *B* of the model IV increases from 9.24% to 27.49%. As shown in Figure 8E, the *B* of the model V increases from 0.52% to 2.04%.

If the distribution dispersion of the fracture size is higher, the rock has a higher blockiness level. The distribution dispersion of fracture size is important to influence the *B* of rock. As shown in Figure 8, the relationship between *B* and C_v is a linear curve. To explore the simulated relationship, the calculated results were fitted by computer tools. The equations describing the relationship between *B* and the distribution dispersion of fracture size corresponding to models I to V were

$$B = 0.1628C_v + 0.8599, R^2 = 0.8244 \quad (3-1)$$

$$B = 0.5797C_v + 0.0802, R^2 = 0.9604 \quad (3-2)$$

$$B = 0.7599C_v + 0.6442, R^2 = 0.9931 \quad (3-3)$$

$$B = 0.5535C_v + 0.0872, R^2 = 0.9462 \quad (3-4)$$

$$B = 0.0424C_v + 0.0033, R^2 = 0.8641 \quad (3-5)$$

where C_v is the coefficient of variation of fracture size; and R^2 is the relative coefficient. The R^2 of these expressions ranges from 0.8 to 1, which means that the abovementioned functions match the data and trend change closely. Moreover, all of these equations can be summarized by

$$B = k \times C_v + B_0 \quad (4)$$

where *k* is the slope, C_v is the coefficient of variation of fracture size, and B_0 is the intercept. Among these values, *k* represents the growth rate of increase in *B* with the distribution dispersion of fracture size, and B_0 is the blockiness when the fractured dispersion equals 0. The B_0 value in this equation can be determined by calculated data corresponding to equal fracture sizes. Namely, B_0 can be obtained from Table 4, and it is fairly consistent with these models. Equation 4 indicates that this function has a non-deterministic parameter. The C_v of the fracture size is defined as the ratio of standard deviation to the mean fracture size. Namely, it interprets the fracture size and relates it to the fracture diameter. As provided in Table 3, the value of B_0 can be effectively computed, whereas the relationship between *k* and the distribution dispersion of fracture size needs to be further validated. Since *k* can be assumed to capture the effects of fracture size and spacing, the 2D relationship among *k*, fracture diameter, and fracture spacing is depicted in Figure 9:

$$k = -0.01531(L)^2 + 0.29023L - 0.52239, R^2 = 0.99273 \quad (5)$$

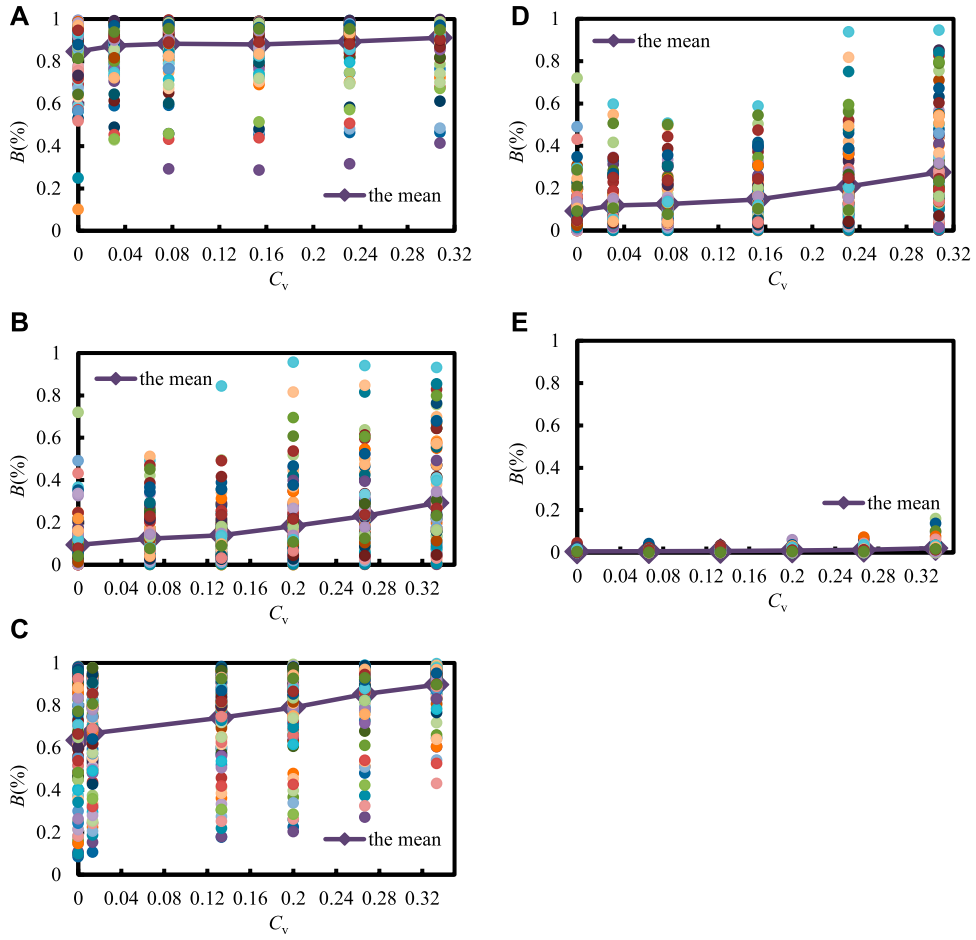

FIGURE 8
The relationships between B and the dispersion of fracture size (C_v): **(A–E)** is model I–V, the domain size of model I to V is 4 m³ × 4 m³ × 4 m³, 3.6 m³ × 3.6 m³ × 3.6 m³, 18.2 m³ × 18.2 m³ × 18.2 m³, 7.8 m³ × 7.8 m³ × 7.8 m³, 2.6 × 2.6 × 2.6 m³.

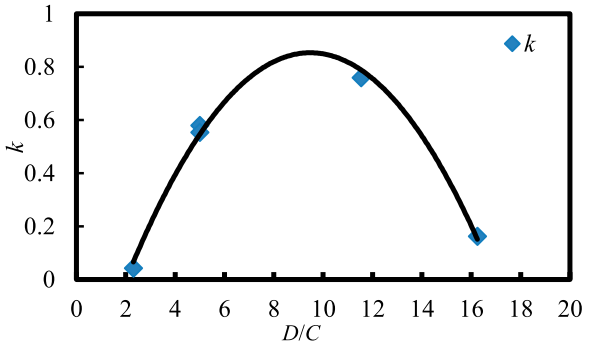

FIGURE 9
The 2D curve among k, fracture diameter (D), and fracture spacing (C).

where L is the ratio of D to C; and R^2 is the relative coefficient. Equation 5 is a standard quadratic polynomial function. Here, R^2 can reach 0.99273, which means that k has a reasonably high correlation with fracture spacing and diameter *via* this function. Combining Eqs 2, 4, 5, a new function between B, C_v, and L capturing the effect of fracture spacing and fracture diameter can be determined:

$$B = \left[-0.01531\,(L)^2 + 0.29023L - 0.52239\right] \times C_v - 2\Big/\left[1 + \exp\left(\alpha L^{\beta}\right)\right] + 1 \quad (6)$$

where L is the ratio of D to C; $\alpha = -0.00656$ and $\beta = 2.15509$.

5 Conclusion

The size and statistical distribution of fractures are key factors that determine the structural integrity and blockiness level of a rock mass. To discuss the influence of the distribution dispersion of fracture size on the B and REV of fractured rock masses, five standard deviations of fracture size with a normal distribution were considered. Based on 77 rock models, five typical fractured rock models were built. To take into account randomness, 10 volume domains of each model were studied and

nine random operations were performed. To obtain an accurate *B* value, 100 random operations were carried out in the REV size domain. The main research results are as follows:

(1) The blockiness converges gradually with increasing rock volume when the fracture size is normally distributed. The simulated results show that the REV size of these models remains constant with the increasing dispersion level of fracture size. Namely rock REV is insensitive to the distribution dispersion of fracture size when the fracture diameter is constant.
(2) The blockiness increases slightly with the distribution dispersion of fracture size. The numerical analysis shows that there is a positive linear correlation between *B* and the coefficient of variation of fracture size. The relationship between the growth rate of increase in *B* (*k*) and the ratio of fracture size to fracture spacing (*L*) is a parabolic curve. This formula for the fracture spacing, fracture diameter, and dispersion of fracture size in relation to the blockiness level provides a means of calculating the blockiness level of a rock mass. The blockiness level of 77 fractured rock masses provides data to support the study of rock masses.
(3) Note that the proposed extended equation is generally applicable only when the fracture size of the five models satisfies the normal distribution, and its exact relationship needs to be further verified by constructing more fractured rock models. In addition, there is more than one commonly distributed form of fracture size. The influence of the distributed forms of fracture size on the rock masses is subject to further study.

Data availability statement

The original contributions presented in the study are included in the article/Supplementary Material, further inquiries can be directed to the corresponding author.

Author contributions

LX and TM contributed to the methodology, validation, analysis, and investigation of this study. TM was responsible for resources, and data of the work. Supervision and project administration were performed by LX. Both authors contributed to the writing and editing of the manuscript. All the authors have read and agreed to submit the manuscript.

Funding

This study was financially supported by the National Natural Science Foundation of China (Nos. 41802248 and 40772208).

Conflict of interest

The authors declare that the research was conducted in the absence of any commercial or financial relationships that could be construed as a potential conflict of interest.

Publisher's note

Supplementary material

The Supplementary Material for this article can be found online at: https://www.frontiersin.org/articles/10.3389/feart.2023.1128167/full#supplementary-material

References

Ajayi, K. M., Shahbazi, K., Tukkaraja, P., and Katzenstein, K. (2018). A discrete model for prediction of radon flux from fractured rocks. *J. Rock Mech. Geotechnical Eng.* 10 (5), 879–892. doi:10.1016/j.jrmge.2018.02.009

Aler, J., DuMouza, J., and Arnould, M. (1996). Measurement of the fragmentation efficiency of rock mass blasting and its mining applications. *Int. J. Rock Mech. Min. Sci.* 33 (2), 125–139. doi:10.1016/0148-9062(95)00054-2

Baecher, G., and Lanney, N. (1978). Trace length biases in joint surveys. *Int. J. Rock Mech. Min. Sci. Geomechanics Abstr.* 16 (1), 56–65. doi:10.1016/0148-9062(79)90799-X

Barton, N. (1979). Suggested methods for the quantitative description of discontinuities in rock masses: International society for rock mechanics, commission for standardisation of laboratory and field tests int J rock mech Min sci. *Int. J. Rock Mech. Min. Sci. Geomechanics Abstr.* 15, 319–368. doi:10.1016/0148-9062(78)91472-9

Bear, T. (1972). *Dynamics of fluids in porous media*. Amsterdam: Elsevier.

Chen, Q., Wang, S., Yin, T., and Niu, W. (2021). Improvement of the concept of the blockiness level of rock masses. *Arabian J. Geosciences* 14 (2), 84. doi:10.1007/s12517-020-06374-8

Cheng, X. L., Liu, L. P., Xiao, J., Zhang, Q. H., Xue, J., and Wang, Y. (2021). A general block stability analysis algorithm for arbitrary block shapes. *Front. Earth Sci.* 9. doi:10.3389/feart.2021.723320

Chwała, M., and Kawa, M. (2021). Random failure mechanism method for assessment of working platform bearing capacity with a linear trend in undrained shear strength. *J. Rock Mech. Geotechnical Eng.* 13 (6), 1513–1530. doi:10.1016/j.jrmge.2021.06.004

Dershowitz, W. S., and Einstein, H. H. (1988). Characterizing rock joint geometry with joint system models. *Rock Mech. Rock Eng.* 21 (1), 21–51. doi:10.1007/BF01019674

Elmouttie, M. K., and Poropat, G. V. (2011). A method to estimate *in situ* block size distribution. *Rock Mech. Rock Eng.* 45 (3), 401–407. doi:10.1007/s00603-011-0175-0

Giwelli, A. A., Sakaguchi, K., and Matsuki, K. (2009). Experimental study of the effect of fracture size on closure behavior of a tensile fracture under normal stress. *Int. J. Rock Mech. Min. Sci.* 46 (3), 462–470. doi:10.1016/j.ijrmms.2008.11.008

Hu, H., Xia, B., Luo, Y., and Gao, Y. (2022). Effect of crack angle and length on mechanical and ultrasonic properties for the single cracked sandstone under triaxial stress loading-unloading. *Front. Earth Sci.* 10, 900238. doi:10.3389/feart.2022.900238

Huang, H., Shen, J., Chen, Q., and Karakus, M. (2020). Estimation of REV for fractured rock masses based on Geological Strength Index. *Int. J. Rock Mech. Min. Sci.* 126, 104179. doi:10.1016/j.ijrmms.2019.104179

Kalenchuk, K. S., Diederichs, M. S., and McKinnon, S. (2006). Characterizing block geometry in jointed rockmasses. *Int. J. Rock Mech. Min. Sci.* 43 (8), 1212–1225. doi:10.1016/j.ijrmms.2006.04.004

La Pointe, P. R., Wallmann, P. C., and Dershowitz, W. S. (1993). Stochastic estimation of fracture size through simulated sampling. *Int. J. Rock Mech. Min. Sci. Geomechanics Abstr.* 30 (7), 1611–1617. doi:10.1016/0148-9062(93)90165-A

Lang, P. S., Paluszny, A., and Zimmerman, R. W. (2014). Permeability tensor of three-dimensional fractured porous rock and a comparison to trace map predictions. *J. Geophys. Res. Solid Earth* 119 (8), 6288–6307. doi:10.1002/2014jb011027

Lei, Z., Wu, B., Wu, S., Nie, Y., Cheng, S., and Zhang, C. (2022). A material point-finite element (MPM-FEM) model for simulating three-dimensional soil-structure interactions with the hybrid contact method. *Comput. Geotechnics* 152, 105009. doi:10.1016/j.compgeo.2022.105009

Li, J. H., and Zhang, L. M. (2011). Connectivity of a network of random discontinuities. *Comput. Geotechnics* 38 (2), 217–226. doi:10.1016/j.compgeo.2010.11.010

Li, X., Liu, J., Gong, W., Xu, Y., and Bowa, V. M. (2022). A discrete fracture network based modeling scheme for analyzing the stability of highly fractured rock slope. *Comput. Geotechnics* 141, 104558. doi:10.1016/j.compgeo.2021.104558

Lin, S.-Q., Wang, G.-J., Liu, W.-L., Zhao, B., Shen, Y.-M., Wang, M.-L., et al. (2022). Regional distribution and causes of global mine tailings dam failures. *Metals* 12 (6), 905. doi:10.3390/met12060905

Liu, Y., Wang, Q., Chen, J., and Song, S. (2019). Identification of the representative volume element at the maji dam site based on a multisample nonparametric test. *Rock Mech. Rock Eng.* 52 (5), 1287–1301. doi:10.1007/s00603-018-1664-1

Long, J. C. S., and Billaux, D. M. (1987). From field data to fracture network modeling: An example incorporating spatial structure. *Water Resour. Res.* 23 (7), 1201–1216. doi:10.1029/WR023i007p01201

Ma, K., and Liu, G. (2022). Three-dimensional discontinuous deformation analysis of failure mechanisms and movement characteristics of slope rockfalls. *Rock Mech. Rock Eng.* 55 (1), 275–296. doi:10.1007/s00603-021-02656-z

Min, K.-B., and Jing, L. (2003). Numerical determination of the equivalent elastic compliance tensor for fractured rock masses using the distinct element method. *Int. J. Rock Mech. Min. Sci.* 40 (6), 795–816. doi:10.1016/S1365-1609(03)00038-8

Min, K.-B., Jing, L., and Stephansson, O. (2004). Determining the equivalent permeability tensor for fractured rock masses using a stochastic REV approach: Method and application to the field data from Sellafield, UK. *Hydrogeology J.* 12 (5), 497–510. doi:10.1007/s10040-004-0331-7

Neuman, S. (1989). Stochastic continuum representation of fractured rock permeability as an alternative to the REV and fracture network concepts. *Int. J. Rock Mech. Min. Sci.* 26 (2), 331–362. doi:10.1016/0148-9062(89)90133-2

Ni, P., Wang, S., Wang, C., and Zhang, S. (2017). Estimation of REV size for fractured rock mass based on damage coefficient. *Rock Mech. Rock Eng.* 50 (3), 555–570. doi:10.1007/s00603-016-1122-x

Pahl, P. J. (1981). Estimating the mean length of discontinuity traces. *Int. J. Rock Mech. Min. Sci.* 18 (3), 221–228. doi:10.1016/0148-9062(81)90976-1

Priest, S. D. (2004). Determination of discontinuity size distributions from scanline data. *Rock Mech. Rock Eng.* 37 (5), 347–368. doi:10.1007/s00603-004-0035-2

Priest, S. D., and Hudson, J. A. (1976). Discontinuity spacings in rock. *Int. J. Rock Mech. Min. Sci. Geomechanics Abstr.* 13 (5), 135–148. doi:10.1016/0148-9062(76)90818-4

Shahami, M. H., Bafghi, A. Y., and Marji, M. F. (2019). Investigating the effect of external forces on the displacement accuracy of discontinuous deformation analysis (DDA) method. *Comput. Geotechnics* 111, 313–323. doi:10.1016/j.compgeo.2019.03.025

Song, K., Yang, H., Xie, J., and Karekal, S. (2022). An optimization methodology of cutter-spacing for efficient mechanical breaking of jointed rock mass. *Rock Mech. Rock Eng.* 55 (6), 3301–3316. doi:10.1007/s00603-022-02806-x

Song, S., Sun, F., Chen, J., Zhang, W., Han, X., and Zhang, X. (2017). Determination of RVE size based on the 3D fracture persistence. *J. Eng. Geol. Hydrogeology* 50 (1), 60–68. doi:10.1144/qjegh2016-127

Wang, G., Hu, B., Tian, S., Ai, M., Liu, W., and Kong, X. (2021). Seepage field characteristic and stability analysis of tailings dam under action of chemical solution. *Sci. Rep.* 11 (1), 4073. doi:10.1038/s41598-021-83671-6

Wang, G., Tian, S., Hu, B., Xu, Z., Chen, J., and Kong, X. (2019). Evolution pattern of tailings flow from dam failure and the buffering effect of debris blocking dams. *Water* 11 (11), 2388. doi:10.3390/w11112388

Wang, G., Zhao, B., Lan, R., Liu, D., Wu, B., Li, Y., et al. (2022a). Experimental study on failure model of tailing dam overtopping under heavy rainfall. *Lithosphere* 2022 (10), 5922501. doi:10.2113/2022/5922501

Wang, G., Zhao, B., Wu, B., Wang, M., Liu, W., Zhou, H., et al. (2022b). Research on the macro-mesoscopic response mechanism of multisphere approximated heteromorphic tailing particles. *Lithosphere* 2022 (10), 1977890. doi:10.2113/2022/1977890

Wang, G., Zhao, B., Wu, B., Zhang, C., and Liu, W. (2022c). Intelligent prediction of slope stability based on visual exploratory data analysis of 77 *in situ* cases. *Int. J. Min. Sci. Technol.* 33, 47–59. doi:10.1016/j.ijmst.2022.07.002

Wang, L. G., Yamashita, S., Sugimoto, F., Pan, C., and Tan, G. (2003). A methodology for predicting the *in situ* size and shape distribution of rock blocks. *Rock Mech. Rock Eng.* 36 (2), 121–142. doi:10.1007/s00603-002-0039-8

Wang, M., Kulatilake, P. H. S. W., Um, J., and Narvaiz, J. (2002). Estimation of REV size and three-dimensional hydraulic conductivity tensor for a fractured rock mass through a single well packer test and discrete fracture fluid flow modeling. *Int. J. Rock Mech. Min. Sci.* 39, 887–904. doi:10.1016/S1365-1609(02)00067-9

Wang, Z., Li, W., Bi, L., Qiao, L., Liu, R., and Liu, J. (2018). Estimation of the REV size and equivalent permeability coefficient of fractured rock masses with an emphasis on comparing the radial and unidirectional flow configurations. *Rock Mech. Rock Eng.* 51 (5), 1457–1471. doi:10.1007/s00603-018-1422-4

Wei, X., Guo, Y., Cheng, H., Wei, J., Zhang, L., Huo, L., et al. (2020). Estimation of fracture geometry parameters and characterization of rock mass structure for the beishan area, China. *Acta Geol. Sin. - Engl. Ed.* 94 (5), 1381–1392. doi:10.1111/1755-6724.13824

Wilson, E. B. (1927). Probable inference, the law of succession and statistical inference. *J. Am. Stat. Assoc.* 22 (158), 209–212. doi:10.1080/01621459.1927.10502953

Wu, S., Zhao, G., and Wu, B. (2022). Real-time prediction of the mechanical behavior of suction caisson during installation process using GA-BP neural network. *Eng. Appl. Artif. Intell.* 116, 105475. doi:10.1016/j.engappai.2022.105475

Xia, L., and Yu, Q. (2020). Numerical investigations of blockiness of fractured rocks based on fracture spacing and disc diameter. *Int. J. Geomechanics* 20 (3). doi:10.1061/(asce)gm.1943-5622.0001596

Xia, L., Zheng, Y., and Yu, Q. (2016). Estimation of the REV size for blockiness of fractured rock masses. *Comput. Geotechnics* 76, 83–92. doi:10.1016/j.compgeo.2016.02.016

Xiang, W. F., and Zhou, C. B. (2005). Advances in investigation of representative elementary volume for fractured rock mass. *Chin. J. Rock Mech. Eng.* 24 (2), 5686–5692.

Yang, Y., Wang, S., Zhang, M., and Wu, B. (2022). Identification of key blocks considering finiteness of discontinuities in tunnel engineering. *Front. Earth Sci.* 10.794936. doi:10.3389/feart.2022.794936

Yu, Q., Ohnishi, Y., Xue, G., and Chen, D. (2009). A generalized procedure to identify three-dimensional rock blocks around complex excavations. *Int. J. Numer. Anal. Methods Geomechanics* 33 (3), 355–375. doi:10.1002/nag.720

Zhang, B., Mu, J., Zheng, J., Lv, Q., and Deng, J. (2022). A new estimation method and an anisotropy index for the deformation modulus of jointed rock masses. *J. Rock Mech. Geotechnical Eng.* 14 (1), 153–168. doi:10.1016/j.jrmge.2021.06.005

Zhang, L., Sherizadeh, T., Zhang, Y., Sunkpal, M., Liu, H., and Yu, Q. (2020). Stability analysis of three-dimensional rock blocks based on general block method. *Comput. Geotechnics* 124, 103621. doi:10.1016/j.compgeo.2020.103621

Zhu, H., Zuo, Y., Li, X., Deng, J., and Zhuang, X. (2014). Estimation of the fracture diameter distributions using the maximum entropy principle. *Int. J. Rock Mech. Min. Sci.* 72, 127–137. doi:10.1016/j.ijrmms.2014.09.006

frontiers | Frontiers in Earth Science

TYPE Original Research
PUBLISHED 01 March 2023
DOI 10.3389/feart.2023.1138018

OPEN ACCESS

EDITED BY
Wenzhuo Cao,
Imperial College London,
United Kingdom

REVIEWED BY
Jingbo Zhao,
China Jingye Engineering Technology Co., Ltd., China
Wang Liang,
Zi Jin (changsha) Engineering Technology Co., Ltd., China
Reza Derakhshani,
Utrecht University, Netherlands

*CORRESPONDENCE
Chunfang Ren,
478832857@qq.com

SPECIALTY SECTION
This article was submitted to Environmental Informatics and Remote Sensing, a section of the journal Frontiers in Earth Science

RECEIVED 05 January 2023
ACCEPTED 15 February 2023
PUBLISHED 01 March 2023

CITATION
Chen J, Chen M, Ren C and Song J (2023), Calculation and optimization of slope reinforcement at tunnel entrances—taking manyanpo tunnel as an example.
Front. Earth Sci. 11:1138018.
doi: 10.3389/feart.2023.1138018

Calculation and optimization of slope reinforcement at tunnel entrances—taking manyanpo tunnel as an example

Junzhi Chen, Mingqing Chen, Chunfang Ren* and Jia Song

Faculty of Land and Resources, Kunming University of Science and Technology, Kunming, China

Slope reinforcement is a common method to solve the problem of slope instability, and reasonable optimization of the corresponding support parameters is crucial for practical engineering. In this paper, the slope support method of Manyanpo tunnel entrance section is taken as an example, and the theoretical calculation method is used to optimize the project cost. Combined with the orthogonal test, the sensitivity analysis of the influencing factors of the stability of the support system and the selection of the optimal parameter combination scheme are carried out. Then, based on flac3d software, the optimization scheme is compared with the original design scheme. The results show that the safety factor of the optimized scheme is increased from 1.32 to 1.43 compared with the actual project. The optimized support parameters have better control effect on the displacement of the slope, especially in the *Z* direction. The optimized parameters have better support effect. This study can provide reference for the optimization design of slope engineering support.

KEYWORDS

slope support optimization, orthogonal test, bending moment of frame beam, FLAC3D, support parameter calculation

1 Introduction

The stability of rock slope is essential in the construction of housing, transportation links, water conservancy, and hydropower projects in mountainous areas (Zhao et al., 2022). Slope reinforcement is an important method to solve the problem of slope instability, and it is important to reasonably optimize the support parameters. In recent years, many researchers have done a lot of research on the optimization of slope support parameters and slope numerical modeling, and achieved fruitful results. Based on the limit equilibrium method and finite element method, Liao et al. (2021) optimized the reinforcement scheme of a reinforced high fill slope at an airport. Li et al. (2014) obtained the optimal design slope angle of fill slopes at different heights and the minimum expected cost of unit projects through analysis of the optimal design model. He and Lin (2010) discussed the influence of different bolt parameters on the stability of jointed slope based on FLAC3D software to realize optimization of slope anchorage. Lou and Zhou (2004) adjusted the support parameters, excavation depth, and support time of the slope in time; thus, effectively controlled the deformation of a slope in the construction process; and ensured the overall stability of a high soft rock slope based on monitoring of the horizontal displacement slope in the construction process. Li et al. (2018) considering the high cutting slope of the fast section of Yingbin West Road in Jiangmen City, Guangdong Province, proposed an optimization design of the key supporting parameters in

the anchor cable support scheme and obtained numerical values for the optimal anchor cable length, anchorage length, and anchor cable inclination angle. In addition, the stability and deformation characteristics of the slope after the installation of anchor cables were numerically simulated and analyzed. Qin (2015) employed numerical simulation to conduct a stability analysis and realize optimization design of related parameters of a slope reinforced by prestressed anchor anti-slide pile using finite element analysis software ABAQUS. Yi et al. (2013) determined the optimal combination of anchorage length and anchorage spacing of a specific slope *via* numerical simulation. Nengpan et al. (2009), based on TangTun highway in southern Anhui mountainous area, introduced a set of operable highway high-slope optimization design research methods. Wang et al. (2011) proposed the response surface test design method and applied it to the parameter selection of anchorage protection structure. The influence of anchor cable support parameters on the stability coefficient was studied, and the quantitative relationship model between the stability coefficient and the influencing factors was established. The residual distribution of the stability coefficient, the stability coefficient contour map, and the response surface three-dimensional map between different operating variables were provided. The test conditions were optimized, and the optimal value scheme of each anchor cable support parameter was obtained. Wang et al. (2014) proposed the method of pre-support and layer-by-layer excavation in a reserved excavation area. Accordingly, the optimal horizontal angle of anchor cable pre-support under different angles between rock strike and slope strike was evaluated, the support calculation model considering the angle of strike was established, and the corresponding relationship was derived. An et al. 2020 conducted a three-dimensional optimization design of the anchor cable reinforcement direction angle of the wedge-shaped rock slope. Finally, they verified the effectiveness and advancement of the method through examples and engineering examples. Zhang (2021) analyzed the protective effect of four kinds of bolt arrangement in a red layer slope by Flac3d software, and finally obtained the best bolt arrangement scheme. Liu et al. (2022) carried out a numerical simulation of the excavation process of the right bank slope group of Lawa, and on this basis, combined with the actual situation of the site, an optimization scheme of anchor cable support was proposed. Li et al. (2021) studied the influence of bolt length, anchorage angle, bolt spacing and layout on slope stability for a bedding rock slope, and then proposed an anchorage optimization scheme through orthogonal test. Lin et al., (2013) used NURBS technology to carry out three-dimensional geological modeling of the study area, and carried out secondary development of VisualGeo modeling software, and finally realized the automatic subdivision and data extraction of three-dimensional slope. Based on GIS and numerical simulation software, Han et al. (2019) proposed a set of three-dimensional slope modeling and simulation calculation schemes with strong applicability and smooth operation.

In summary, most scholars mainly measure the advantages and disadvantages of the support scheme from the perspective of cost and slope stability. Few scholars measure the advantages and disadvantages of the support scheme from the change of the bending moment of the support material. The main innovation of this paper is to introduce the bending moment index as the evaluation index to measure the effect of slope support before and after optimization. At the same time, the original support scheme of the slope at the entrance of Manyanpo tunnel is optimized by orthogonal experiment, and then the numerical simulation of the support scheme before and after optimization is carried out based on FLAC3D software. Finally, the safety factor, displacement data and bending moment data before and after optimization are compared, thus comprehensively verifying the rationality of the optimization scheme. This study can provide a new idea and method for the selection of optimization schemes and the comparative study of support schemes before and after optimization, and provide a reference for the optimization of slope support engineering.

2 Project profile

The slope cover of a tunnel entrance in Yunnan is quaternary residual silty soil, which mainly comprises gneiss. The surface water system in the area is relatively developed and the rock is broken. A diagram of the slope protection is provided in Figure 1. The slope height is 24–56 m, and excavation is the main method. A bench is set every 8 m, and the width of each bench is 1 m, with a maximum of 7 grade slope. According to the local geological conditions and weathering degree of rock mass, the slope reinforcement method includes prestressed anchor cable frame beam support (the composite structure of the prestressed anchor cable and concrete frame beam can give full play to the anchoring effect of anchor cable and frame beam, which is widely used in slope reinforcement (Yao et al., 2006)), and the area is approximately 4,500 m^2. Slope excavation slope is 1:0.75–1, prestressed anchor cable frame beam arrangement slope rate is consistent with the slope rate, frame beam classification arrangement. Table 1 presents specific settings.

3 Calculation method of slope stability

In 1975, Zienkiewicz et al. (1975) first introduced the strength reduction method into the calculation of slope stability. In the development of slope engineering in recent years, with the development of the computer industry, the strength reduction method (Cai et al., 2015; Li et al., 2015; Li et al., 2017; Liu et al., 2017; Shi et al., 2019; Fang et al., 2020) is widely used in various projects, and has made great progress and breakthroughs. Compared with other analysis methods, this method has the following advantages: (Chen and Xu, 2013):

(1) The core idea of SRM is consistent with engineering practice.
(2) All the data of the internal force of soil and structure can be obtained.
(3) It is not necessary to presuppose the sliding surface, and automatically output the potential sliding surface.
(4) Simulating the progressive development of slope stability in the whole process of slope construction.
(5) It can simulate more complex formation conditions, and is not limited by slope shape, material properties, *etc.*, and has wider applicability.

Therefore, this method was used to calculate the slope stability. The principle is to make the slope just reach the critical failure state.

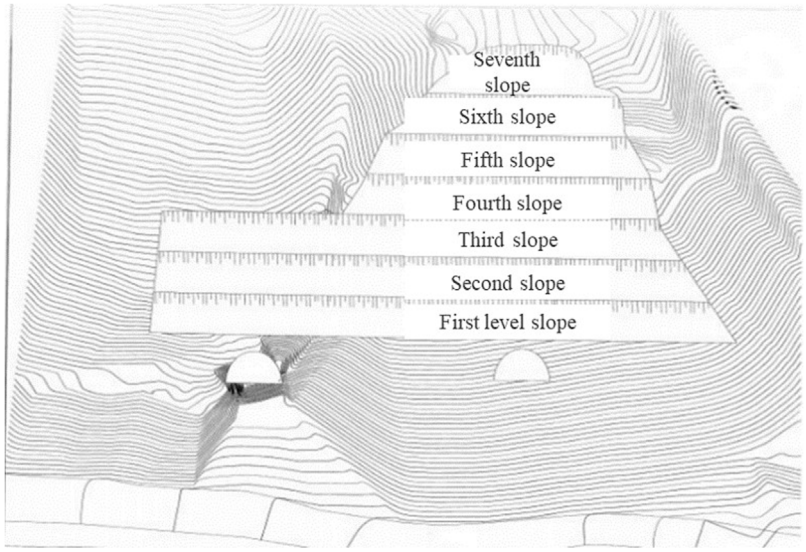

FIGURE 1
Schematic diagram of slope protection.

TABLE 1 Setting Information of prestressed anchor cable frame beam.

Length of anchor cable/m	Bonding length/m	Free segment length/m	Anchor cable (prestressed steel strand)/mm	Hole grouting	Framed girder	Anchor cable spacing (horizontal and vertical)/m	Section of frame beam/m
25	12	13	4φs15.2	M30	C25	3.5	0.5×0.5

TABLE 2 Slope rock mass parameters.

Rock and soil mass	Soil layer thickness (m)	Bulk density (kN•m^{-3})	Elastic modulus (GPa)	Poisson ratio	Cohesion (MPa)	Internal friction angle (°)
artificial fill	2	18	0.010	0.3	0.020	17.85
Silty clay	6	21	0.025	0.3	0.020	19.55
Gneiss V_1	6–14	26	1.0	0.22	0.2	40
Gneiss V_2	24–55	26	1.0	0.22	0.2	40
Gneiss V_3	24–55	26	1.0	0.22	0.2	40

The safety factor is defined as the ratio of the actual shear strength of rock and soil mass to the reduced shear strength at critical failure (Chen and Xu, 2013). The calculation formula is as follows:

$$c_F = \frac{c}{F_s} \quad (1)$$

$$\varnothing_F = tan^{-1}\left((tan\varnothing)/F_s\right) \quad (2)$$

c —Cohesion before reduction;
c_F— Cohesion after reduction;
$\varnothing$ —Internal friction angle before reduction;
$\varnothing_F$ —Internal friction angle after reduction;
F_s—Reduction coefficient;

4 Numerical calculation model and parameter selection

4.1 Selection of parameters

4.1.1 Selection of mechanical parameters

The mechanical parameters of each rock and soil mass are listed in Table 2.

4.1.2 Selection of anchor cable and frame beam parameters

Specific values of the calculation parameters for the anchor cable frame beam are provided in Tables 3, 4.

TABLE 3 Anchor parameters.

Length (m)	Elastic modulus (GPa)	Cross sectional area (m^2)	Grouting perimeter (m)	Tensile strength (kN)	The stiffness of cement slurry per unit length ($N\cdot m^{-2}$)	Bond strength of cement slurry per unit length ($N\cdot m^{-1}$)
25	195	0.007254656	0.4082	1985	1.7×106	1.3×105

TABLE 4 Parameters of frame beams.

Elastic modulus (GPa)	Poisson ratio	Cross sectional area (M^2)	Polar moment of inertia (M^4)	Y-axis moment of inertia (M^4)	*Z*-axis moment of inertia (M^4)
28	0.2	0.25	0.01042	0.00521	0.00521

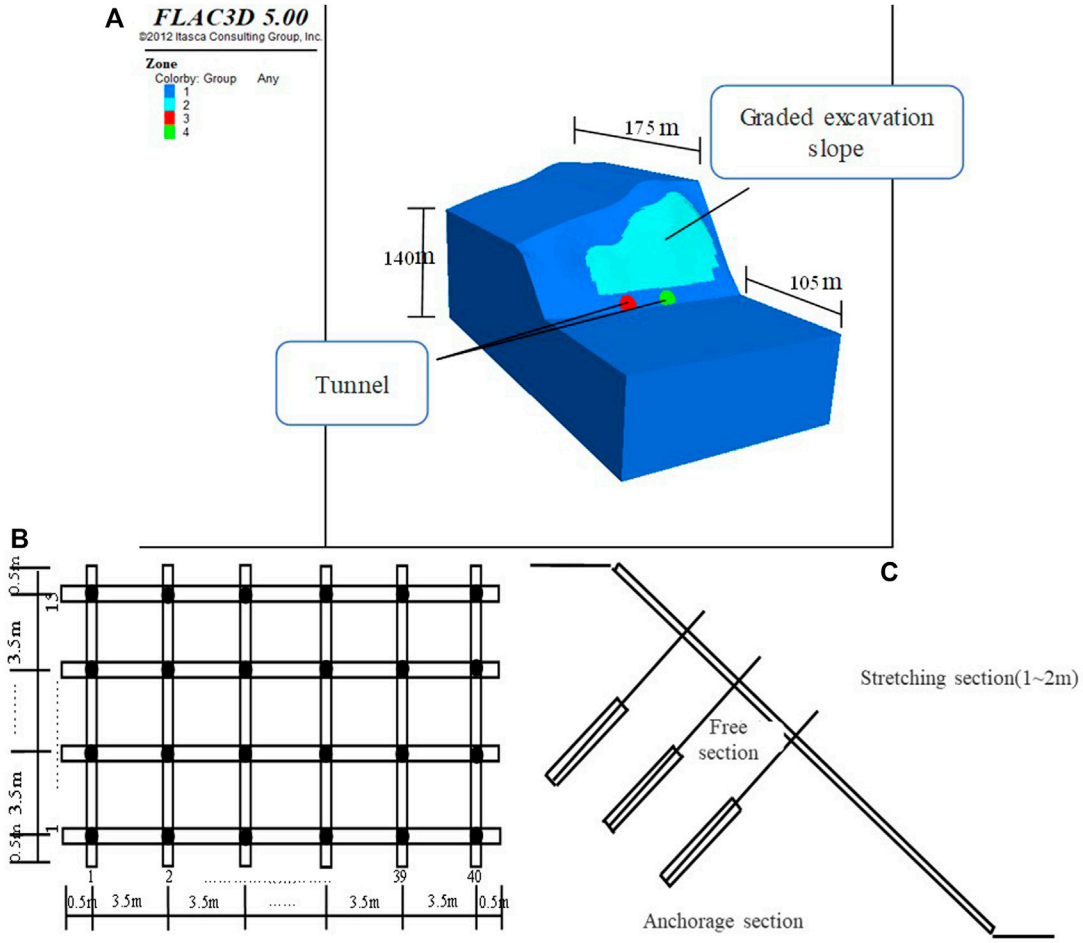

FIGURE 2
(A) Calculation of slope map; **(B)** Anchor cable and frame beam layout diagram; **(C)** Anchor cable layout.

4.2 Numerical calculation model of slope

The model size is based on the actual slope size. According to the rock mass parameters of the slope in Table 2, the material properties of the slope were defined. Other parameters and anchor cable arrangement are displayed in Figures 2A–C. The Drucker Prager criterion (D-P criterion) was selected as the constitutive model. The upper boundary is set as free boundary, and the other boundaries are fixed.

4.3 Calculation scheme of slope grading excavation

The slope was constructed in the order of excavating the first level of protection, and the construction sequence of the next level of slope was repeated after the stability of the upper level of slope. The monitoring points were set up using FISH language in FLAC to analyze the state of anchor cable of frame beam during excavation.

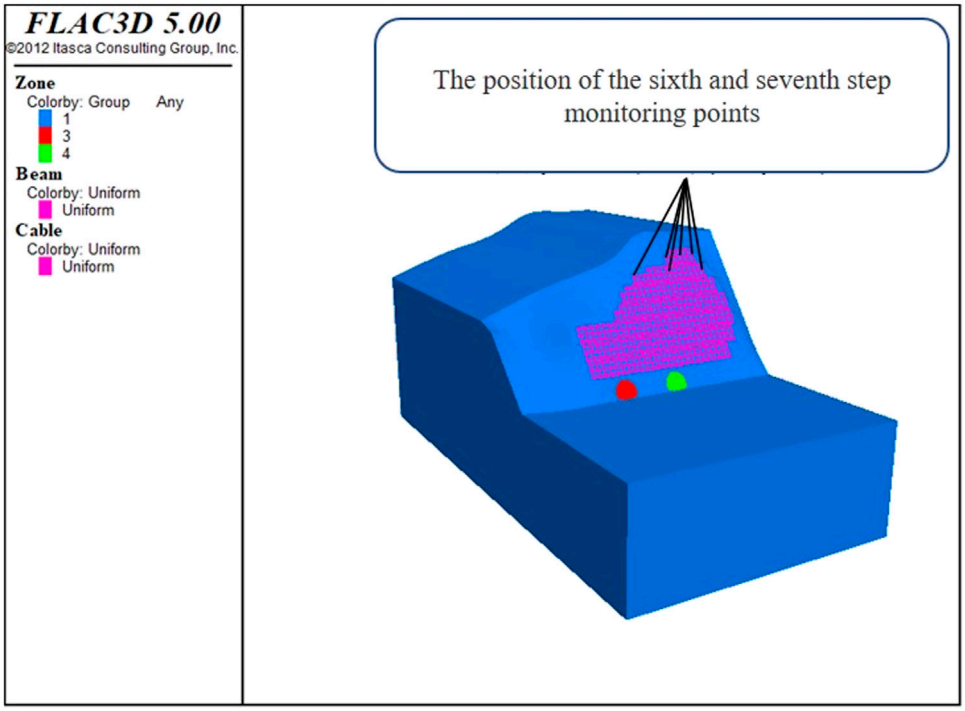

FIGURE 3
Layout schematics of monitoring points for sixth and seventh steps.

After the excavation of the slope, the intersection point of the anchor cable frame beam in the left, middle and right positions of each grade slope were considered as the monitoring points, resulting in the total of 21 monitoring points. A schematic of the layout of the sixth and seventh step monitoring points is presented in Figure 3. The arrangement of the monitoring points below is consistent with the arrangement of the sixth and seventh steps.

5 Parameter setting and optimization of prestressed anchor cable (Xue, 2016)

5.1 Optimization of anchorage force and anchorage angle

Various setting parameters of prestressed anchor cable frame beams exist, therefore, it is difficult to conduct a comprehensive analysis. Several research results (Zhang, 2011; Chen, 2015; Pan, 2017) demonstrate that anchoring force, anchorage angle, and anchorage spacing are the main setting parameters; and based on these, other parameter values are calculated. Therefore, this study considers these three factors as the research objects for calculation and optimization.

The anchoring force is determined by the sliding force of the slope, as shown in Figure 4. Assuming that the sliding force is f, then:

$$P = \frac{P_1}{\sin(\theta+\beta)\tan\varphi + \cos(\theta+\beta)} \tag{3}$$

$$N_t = p \times \frac{N_1}{N_2} \tag{4}$$

P_1—Anti-sliding force, in equilibrium, the value is equal to the sliding force F (kN); P—Anchoring force (kN); θ—Angle of slide (°); β—Anchorage angle (°); φ—Angle of internal friction (°); N_1—Interval of anchors (m); N_2—Number of anchor cables; When the slope angle is 53°, the anti-sliding force of the slope calculated *via* Lizheng software is 6,762 kN, and the prestress design value of a single anchor cable is 718 kN, from Formula 4.

As shown in Figure 4:

$$P_1 = P(\sin(\theta+\beta)\tan\varphi + \cos(\theta+\beta) \tag{5}$$

The purpose of the design value of the anchorage angle is to provide the maximum anti-sliding force, and the extreme value of Formula 5 above can be obtained. Let $\partial P/\partial\beta = 0$, then:

$$\beta = \theta - \varphi \tag{6}$$

According to the limit equilibrium theory of earth pressure, the following can be determined: θ∈(45°-φ/2,45°+φ/2) The anchorage angle can be determined as: β=15–35°. To save construction costs, the anchor cable can be re-optimized. The anchoring force determines the length of the anchorage section. The value of the tension section is generally 0.5–1 m, so the length of the free section can be adjusted, If the anchor cable can bear a large anti sliding force in a short length, the anchor cable has the best effect. Assuming that the vertical distance from the sliding surface to the slope is l, the length of the free section of the anchor cable is:

$$L_1 = \frac{L}{\sin(\beta+\gamma)} \tag{7}$$

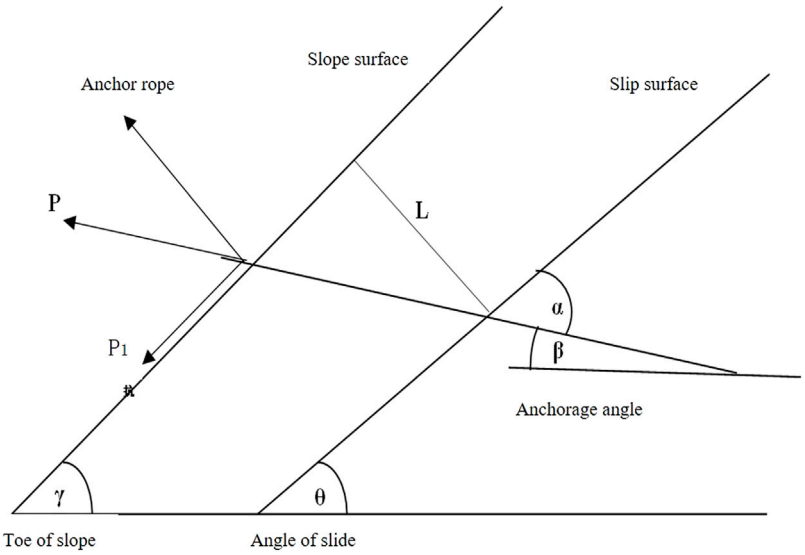

FIGURE 4
The stress diagram of slope.

$$Q' = \frac{p_1}{L_1} = \frac{P(\sin(\theta+\beta)\tan\varphi + \cos(\theta+\beta))}{\frac{L}{\sin(\beta+\gamma)}} \quad (8)$$

$$= \frac{P\sin(\beta+\gamma)((\sin(\theta+\beta)\tan\varphi + \cos(\theta+\beta))}{L}$$

$$\frac{\partial q'}{\partial \beta} = \frac{p(\cos(\gamma+\theta+2\beta) + \sin(\gamma+\theta+2\beta)\tan\varphi}{L} \quad (9)$$

L_1—Length of free end of anchor cable (m); L—Vertical distance from sliding surface to slope (m); γ—Slope angle (°);

5.2 Optimization of anchorage spacing

According to the elastic foundation model, the spacing of the frame beam should satisfy $L < \pi/2\lambda$ (λ = 0.3–0.5), where λ is the elastic characteristic of beam, then the value of beam is 3–5 m. If the economic cost is considered, the cost of material lengths of 3, 4, and 5 m can be compared. Assuming that there is a square slope of 22 m × 22 m, the number of anchor cables required for the frame beam from large to small is 7, 5, 4. According to Formula 10 ~ 12, the required steel strands are 3, 4, and 6, and the required anchorage lengths are 7, 13, 19.5 m. The material cost of a 15.24-mm steel strand is 6,737 yuan per ton, cement mortar is 573 yuan per ton, and frame beam concrete is 527 yuan per cubic meter. If the price of frame beam concrete is K, the mortar is 2.5K, and the steel strand is 31.2 K. The corresponding calculation results are shown in Table 5.

$$A_S \geq \frac{K_t N}{f} \quad (10)$$

$$L_{锚固} = \frac{K \times N}{\pi \times n \times d \times \tau_a} = \frac{K \times N}{\pi \times D \times \tau_b} \quad (11)$$

TABLE 5 Cost table of different anchor cable spacing.

Interval of anchors	3 m (K)	4 m (K)	5 m (K)
Fabrication cost	13,167	12,554	15,025

$$n = \frac{A_S}{\frac{\pi d d}{4}} \quad (12)$$

A_S—Rod area (m^2); N—Axial tension value of single anchor cable (kN); f—Standard tensile strength of steel strand (MPa);

d—Diameter of steel strand (mm); D—Anchorage body diameter (mm); n—Number of strands;

τ_a—Bond strength between mortar and steel strand (KPa); K—Factor of safety, Take 1.8; It can be observed from the table that the cost is the smallest when the anchor cable spacing is 4 m, and the frame beam meets the design requirements. It is not excluded that there is a small value between the anchor cables of 3–4 m. Therefore, it is better to optimize the anchor cable spacing in 3–4 m.

6 Selection of parameter optimization scheme based on orthogonal experiment

Based on the above calculations and optimizations, the anchor force is 460 kN, the anchor angle is 20–27°, and the anchor cable spacing is 3–4 m. The prestress value applied to each anchor cable in the No. One tunnel of the slope is 460 kN, and the calculated anchorage force is 718 kN. Therefore, 400–800 kN is considered in the prestress level value, and the specific scheme is introduced in detail in the following contents.

TABLE 6 Factor level table.

Level factor	1	2	3
Prestress(A)	400	600	800
Anchorage angle(B)	20	25	30
Anchor spacing(C)	3	3.5	4

TABLE 7 Test scheme Table.

	A	B	C	Factor of safety
	1	2	3	
1	1 (400)	1 (20)	1 (3)	0.85
2	1	2 (25)	2 (3.5)	1.25
3	1	3 (30)	3 (4)	1.26
4	2	1	2	1.26
5	2	2	3	1.43
6	2	3	1	1.21
7	3	1	3	1.27
8	3	2	1	1.25
9	3	3	2	1.38

6.1 Design of orthogonal test

An orthogonal experiment (Zhuang and He, 2006; Zhong et al., 2015; Chai, 2017; Yang et al., 2017; Liu et al., 2021; Peng et al., 2021) is a combination of various factors and horizontal numerical permutations to form multiple schemes. The permutation and combination can be a comprehensive test or a few special representative combinations. The calculation is basically unbiased. The optimal scheme of various schemes is obtained *via* probability calculation. Its advantage is that it can reduce the number of tests while ensuring the reliability of test results through orthogonal design for the tests with long test cycle, high test cost and difficult test.

This experiment involves three factors and three levels; the levels of experimental parameters are shown in Table 6.

Considering the overall safety factor of the slope after tunnel excavation as the standard to measure the slope stability, the solution process was as detailed in Table 7.

6.2 Analysis of test results

The data in Tables 8, 9 were obtained according to the standard calculation method of an orthogonal table in the orthogonal experiment. It can be observed from the values of S^2_j and F that among the factors in the test, the influence degree of the factor is C > A = B. By comparing the above K_{ji} values, $K_{13} > K_{12} > K_{11}$ in factor A, $K_{22} > K_{21} > K_{23}$ in factor B, and $K_{33} > K_{32} > K_{31}$ in factor C, it is concluded that under such mountain conditions, the optimal scheme is prestressed at 600 kN, anchor cable spaced at 4 m, and maintained at an anchorage angle of 20°.

TABLE 8 Calculation Table.

	A	B	C	Vacant column
	1	2	3	4
1	1	1	1	1
2	1	2	2	2
3	1	3	3	3
4	2	1	2	3
5	2	2	3	1
6	2	3	1	2
7	3	1	3	2
8	3	2	1	3
9	3	3	2	1
K_{j1}	3.36	3.38	3.66	3.35
K_{j2}	3.9	3.90	3.89	3.74
K_{j3}	3.9	3.85	3.96	3.82
Q_j	14.12897	14.11097	14.88777	13.26750
S^2_j	0.06647	0.04847	0.82527	0.72230

7 Results and discussion

The numerical simulation of the slope before and after the optimization of the support parameters is carried out, and the numerical simulation results are compared. The comparison includes three aspects, safety factor, displacement and frame beam bending moment.

7.1 Comparison of safety factors

The safety factor of slope is an important parameter to evaluate the safety of slope (Azadi et al., 2022; Nanehkaran et al., 2022; Nanehkaran et al., 2023). The safety factor of the slope before the optimization of the support parameters is 1.32, and the safety factor of the slope after the optimization of the support parameters is 1.43, which is 8.3% higher than that before the optimization of the support parameters. It greatly improves the stability of the slope.

7.2 Comparison of monitoring points increment on slope

Figures 5A–C present comparison charts of *X*, *Y*, *Z*-direction displacement curves before and after optimization. According to the data curves of the left, middle, and right monitoring points in Figures 5A–C, it can be observed that the general trend of the displacement-excavation times curves in the X, Y, and Z directions before and after the optimization is basically the same, however, the fluctuation of the optimized displacement-excavation times curve is smaller, indicating that the optimized supporting parameters indicate better control effect on the deformation of the slope in the X, Y, and Z directions. At the same

TABLE 9 Analysis of variance table.

Source of variance	Quadratic sum	Degree of freedom	Mean square deviation	F ratio	Significance
Factor A	0.06648	2	0.03324	0.00369	(*)
Factor B	0.05887	2	0.02943	0.00327	(*)
Factor C	0.89803	2	0.44902	0.04989	*
Error	0.72230	2	0.36115		
Summation	1.74568	8			

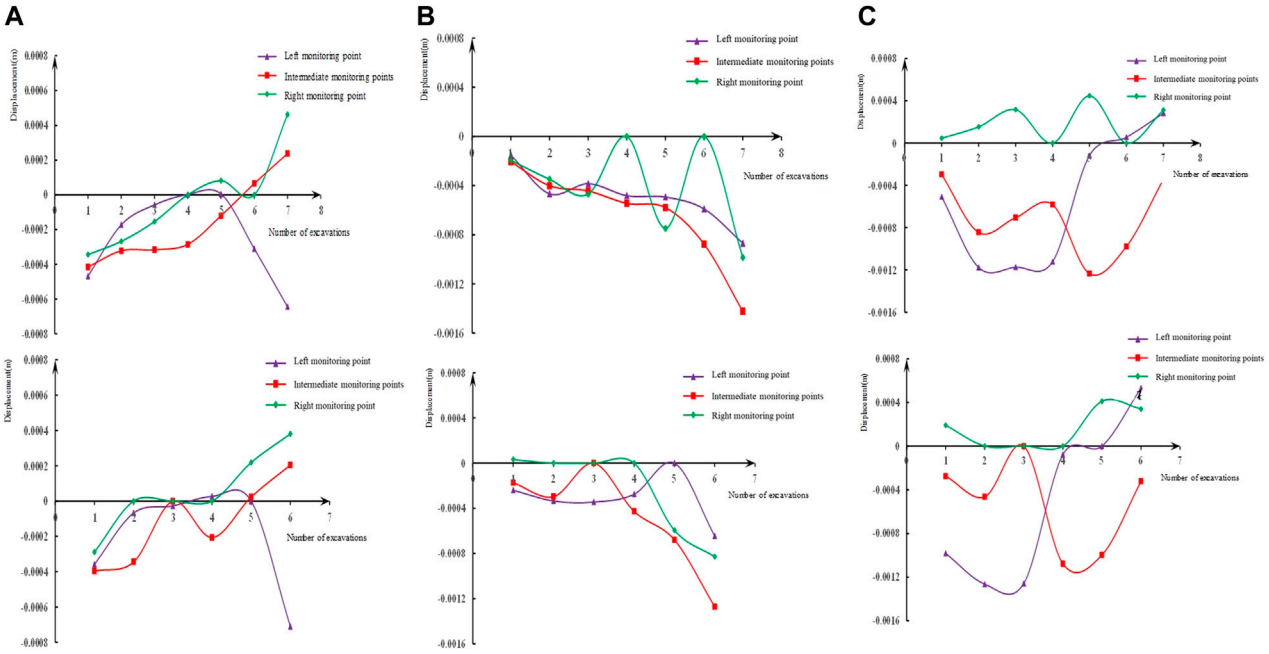

FIGURE 5
(A) X-direction displacement map before and after optimization; **(B)** Y-direction displacement map before and after optimization; **(C)** *Z*-direction displacement map before and after optimization (The first line of pictures is before optimization, and the second line of pictures is after optimization.)

time, the maximum displacement of the slope in the three directions of X, Y and Z after optimizing the parameters is 0.00027, 0.00047, and 0.00058 m respectively, which is about 30% of the maximum displacement increment of the monitoring points in each direction. This shows that the parameter optimization effect is better.

According to the comparative analysis of displacement in three directions, the optimized supporting parameters have better control effect on slope displacement, particularly on the displacement in the *Z* direction, which can effectively prevent the occurrence of landslide disasters.

7.3 Comparison of bending moments of frame beams

The bending moment data of the middle frame beams of some slopes were considered, as shown in Figures 6A–C. By comparing and analyzing the bending moment diagrams before and after optimization, the following results were obtained.

(1) Compared with the bending moment data of the cross beam of the middle frame beam of the slope before optimization, the bending moment fluctuation after optimization is relatively stable, and the bending moment values of most beams are maintained at a low level, and fluctuate greatly, indicating that the optimized supporting parameters demonstrate a good control effect on the slope deformation.
(2) After optimization, the maximum bending moment of the cross beam of the middle frame beam at all levels of the slope is approximately 7.5×10^5 kN M, while the maximum value before optimization is approximately 4.2×10^4 kN M, which is tens of times higher than that before optimization, indicating that the optimized bending moment beam exhibits better material properties and improved supporting effect.

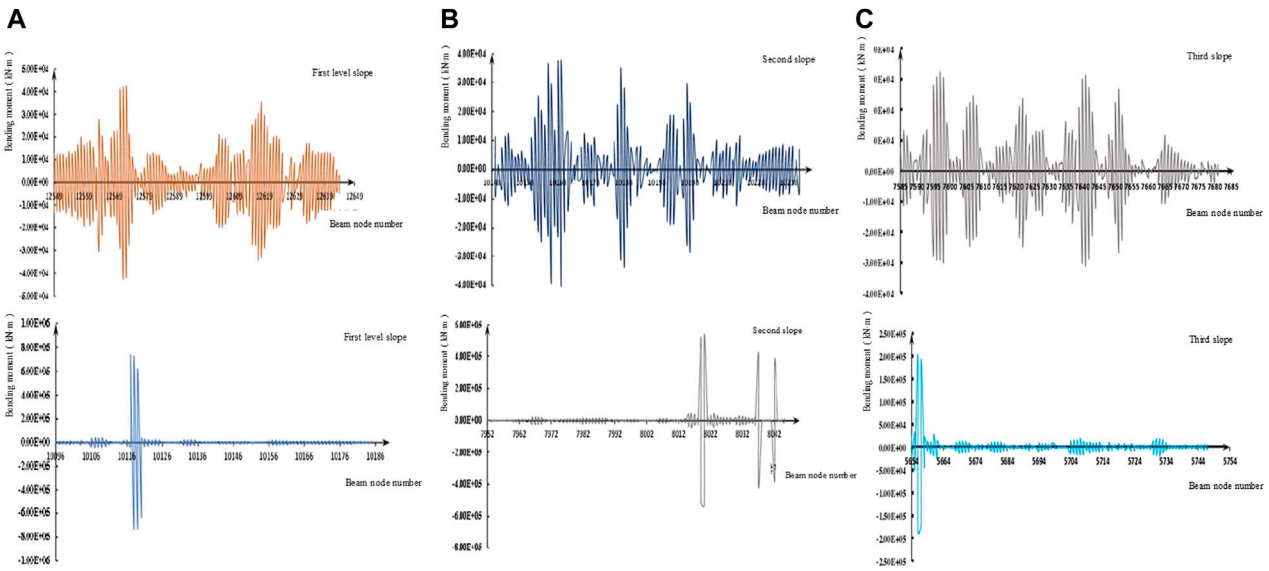

FIGURE 6
(A) Bending Moment Diagram of Frame Beam of the First Slope before and after Structural Parameter Optimization; **(B)** Bending Moment Diagram of Frame Beam of the Second Slope before and after Structural Parameter Optimization; **(C)** Bending Moment Diagram of Frame Beam of the Third Slope before and after Structural Parameter Optimization (The first line of pictures is before optimization, and the second line of pictures is after optimization.)

7.4 Discussion

When evaluating the optimized support effect, most scholars use the safety factor and displacement cloud map as the standard to evaluate the optimization effect. However, this evaluation standard is not comprehensive, and it cannot reveal whether the support material fully exerts its material characteristics, which may cause excessive waste of materials. In this study, a series of monitoring points were set up through the preparation of fish language, and finally the change curve of the bending moment value of the frame beam at each monitoring point during the operation of the support system was obtained. The curve can clearly show the stress of the frame beam, and it is easier to judge whether the frame beam fully exerts its material characteristics, thereby reducing the excessive surplus of materials, which has a great help to control the cost of slope support. However, in the face of large-scale slope support projects, this method needs to design more monitoring points to monitor the stress of frame beams, which will increase the workload. Therefore, it is necessary to further study which parts of the monitoring point data are more important, thereby reducing the layout of monitoring points to reduce the workload.

8 Conclusion

In this paper, the original support parameters of the slope at the entrance of the Manyanpo tunnel are optimized, and the slope before and after the optimization of the support parameters is numerically simulated. Then the results of the numerical simulation are analyzed and compared. Finally, the following conclusions are drawn.

(1) The optimized support parameter combination is: prestress is 600 kN, anchorage angle is 20°, and anchor cable spacing is 4 m. The order of the influence degree of these parameters on the stability of the support system from large to small is prestress, anchoring angle and anchor cable spacing.
(2) The slope safety factor after optimizing the support parameters is 8.3% higher than that before optimization, which improves the stability of the slope. The optimized support parameters have better control effect on the displacement of slope in *X*, *Y*, and *Z* directions, especially in *Z* direction.
(3) The maximum bending moment value of the frame beam after parameter optimization is tens of times of the maximum bending moment value of the frame beam before optimization, which indicates that the optimized bending moment beam can exert better material properties while ensuring slope stability.

Data availability statement

The original contributions presented in the study are included in the article/Supplementary Material, further inquiries can be directed to the corresponding author.

Author contributions

Conceptualization: JC, MC, CR, and JS methodology: JC, MC, CR, and JS writing—original draft preparation: MC and JS writing—review and editing: JC and CR.

Conflict of interest

The authors declare that the research was conducted in the absence of any commercial or financial relationships that could be construed as a potential conflict of interest.

Publisher's note

References

An, C., Ye, L., Wang, L., Deng, S., Sun, P., Fan, B., et al. (2020). Three-dimensional optimization design of anchor cable reinforcement direction angle of rock slope wedge [J]. *Geotech. Mech.* 41 (08), 2765–2772.

Azadi, A., Esmatkhah Irani, A., Azarafza, M., Hajialilue Bonab, M., Sarand, F. B., and Derakhshani, R. (2022). Coupled numerical and analytical stability analysis charts for an earth-fill dam under rapid drawdown conditions. *Appl. Sci.* 12 (9), 4550. doi:10.3390/app12094550

Cai, D., Wu, C., Chen, F., Yao, J., and Ye, Y. (2015). Stability analysis of subgrade slope of heavy haul trains on existing lines [J]. *J. Civ. Eng.* 48 (S2), 252–256.

Chai, H. (2017). *Engineering mathematics[M]*. Shanghai: East China University of Technology Press.

Chen, K. (2015). Optimum design of slope support based on strength reduction and orthogonal test[J]. *Fujian Build.* (04), 66–69. + 109.

Chen, Y., and Xu, D. (2013). *FLAC/FLAC3D foundation and engineering examples*. 2nd edition. Beijing: China Water Conservancy and Hydropower Press, 265–275.

Fang, W., Wang, R., and Du, Z. (2020). Multi-field coupling strength reduction method for RCC gravity dam on deep overburden [J]. *J. Appl. Basic Eng. Sci.* 28 (01), 40–49.

Han, T., Lin, B., and Lu, H. (2019). Three-dimensional slope modeling method and its stability based on GIS and numerical simulation software coupling [J]. *Geotech. Mech.* 40 (07), 2855–2865.

He, Z., and Lin, H. (2010). Impact analysis of bolt support on slope stability of jointed rock mass [J]. *Highw. traffic Technol.* 27177 (11), 8–12. + 19.

Li, H., Tan, H., Yuan, W., Huang, Q., Han, Z., Wang, H., et al. (2021). Optimization of bolt anchorage parameters considering lateral restraint [J]. *Sci. Technol. Eng.* 21 (18), 7731–7738.

Li, J., Geng, W., and Pan, J. (2018). Stability analysis and support parameter optimization design of high cutting slope[J]. *Chin. foreign Highw.* 38 (05), 31–34.

Li, J., Junling, S., Zhong, H., and Zhao, R. (2017). Study on stability of surrounding rock of double-hole long-span tunnel based on strength reduction method [J]. *J. Civ. Eng.* 50 (S2), 198–202.

Li, X., Yang, S., Zhang, Y., and Miao, C. (2015). Study on the safety and stability of subsea tunnels under hydrostatic pressure [J]. *J. Water Conservancy* 46 (S1), 101–106.

Li, Y., Tang, Z., and Liu, Z. (2014). Optimal design model of filling slope in construction site based on expected cost [J]. *Hydrogeol. Eng. Geol.* 41256 (02), 79–84. + 110.

Liao, H., Xu, C., and Yang, Y. (2021). Optimization design of geogrid reinforced high slope in an airport flight area [J]. *Hydrogeol. Eng. Geol.* 48302 (06), 113–121. doi:10.16030/j.cnki.issn.1000-3665.202012015

Lin, D., Li, M., and Tong, D. (2013). Three-dimensional geological modeling and stability analysis and application of spillway excavation slope [J]. *Rock Mech. Eng. J.* 32 (S2), 3878–3887.

Liu, D., Wang, Q., Wei, W., and Jiang, Q. (2022). Three-dimensional numerical analysis and support scheme optimization of excavation of right bank slope group of Lawa hydropower station [J]. *Hydropower Energy Sci.* 40 (03), 153–157.

Liu, H., Zuo, J., Liu, D., Li, C., Xu, F., and Lei, B. (2021). Optimization of roadway bolt support based on orthogonal matrix analysis [J]. *J. Min. Saf. Eng.* 38 (01), 84–93.

Liu, L., Liang, S., Jiao, Y., Wang, H., Zhang, X., and Xie, B. (2017). Study on the stability of 1 ~ # landslide accumulation body near the river on loess slope under reservoir water level fluctuation [J]. *Geotech. Mech.* 38 (S1), 359–366.

Lou, G., and Zhou, D. (2004). Monitoring and design optimization of soil-nailing support for high weak rock slope[j]. *Chin. J. Rock Mech. Eng.* 23 (16), 2734–2738.

Nanehkaran, Y. A., Licai, Z., Chengyong, J., Chen, J., Anwar, S., Azarafza, M., et al. (2023). Comparative analysis for slope stability by using machine learning methods. *Appl. Sci.* 13 (3), 1555. doi:10.3390/app13031555

Nanehkaran, Y. A., Pusatli, T., Chengyong, J., Chen, J., Cemiloglu, A., Azarafza, M., et al. (2022). Application of machine learning techniques for the estimation of the safety factor in slope stability analysis. *Water* 14 (22), 3743. doi:10.3390/w14223743

Nengpan, J., Zhao, J., and Deng, H. (2009). Stability evaluation and support optimization design of highway high slope[J]. *J. Rock Mech. Eng.* 28 (06), 1152–1161.

Pan, T. (2017). Prestressed anchor frame slope support design parameter optimization analysis[J]. *Low. carbon world* (10), 95–97.

Peng, P,, Zhang, D., and Sun, Z. (2021). Design method of surrounding rock deformation characteristics and reinforcement parameters of tunnel with weak interlayer [J]. *Rock Mech. Eng.* 40 (11), 2260–2272.

Qin, X. (2015). *Prestressed anchor anti-slide pile reinforcement slope optimization design research[D]*. Beijing): China University of Geosciences.

Shi, L., Ni, D., Yan, Z., Chen, J., and Hu, M. (2019). Study on the strength reduction method for the safety factor of anti-uplift stability of bias foundation pit in soft soil area [J]. *J. Geotechnical Eng.* 41 (S1), 13–16.

Wang, Y., Wei, X. Z., and Shao, L. F. (2011). *Response surface optimization design for cutting slope anchoring parameter[J]*. Journal of Yangtze River Scientific Research Institute.

Wang, Z., Xia, Y., and Xiong, Z. (2014). Study on pre-supporting excavation of bedding rock slope and anchor optimization design[J]. *Chin. J. Undergr. Space Eng.*

Xue, G. (2016). Design scheme and optimization analysis of landslide control in a project [J]. *Shanxi Traffic Sci. Technol.* (02), 10–12. + 26.

Yang, N., Li, W., and Xuan, C. (2017). FLAC3D can break the improvement of bolt unit and the application of deep coal roadway [J]. *J. Min. Saf. Eng.* 34 (02), 251–258. doi:10.13545/j.cnki.jmse.2017.02.008

Yao, L., Zhou, D., and Zhao, G. (2006). Prestressed anchor frame beam supporting structure design[J]. *Rock Mech. Eng.* (02), 318–322.

Yi, G., Tong, L., and Zhang, X. (2013). Optimum design of slope excavation support for Zhuziba yard[J. *J. Civ. Environ. Eng.* 35 (S2), 12–17.

Zhang, L. (2011). *Application of bolt parameter optimization in excavation slope reinforcement[J]*. Resource environment and engineering, 248–251.

Zhang, Y. (2021). Optimization design of anchorage parameters for dip red bed slope [J]. *Railw. Build.* 61 (02), 67–70.

Zhao, M., Liu, J., and Zhao, H. (2022). Stability analysis of rock slope based on MSDP criterion[J/OL]. *J. Rock Mech. Eng.* 1 (9).

Zhong, Z., Li, X., Yao, Q., Ju, M., and Li, D. (2015). Based on orthogonal test of coal rock interbedded roof roadway instability factors [J]. *J. China Univ. Min. Technol.* 44 (02), 220–226.

Zhuang, C., and He, C. (2006). *Application of mathematical statistics[M]*. Guangzhou: South China University of Technology Press.

Zienkiewiez, O. C., Humpheson, C., and Lewis, R. W. (1975). Associated and non-associated visco-plasticity and plasticity in soil mechanics. *J.* 25 (4), 671–689. doi:10.1680/geot.1975.25.4.671

frontiers | Frontiers in Earth Science

TYPE Original Research
PUBLISHED 13 March 2023
DOI 10.3389/feart.2023.1121618

OPEN ACCESS

EDITED BY
Guangjin Wang,
Kunming University of Science and Technology, China

REVIEWED BY
Zheng Zhi,
Guangxi University, China
Rui Li,
Chongqing University, China

*CORRESPONDENCE
Jiabing Zhang,
zjb22@mails.jlu.edu.cn
Yingchun Li,
751789319@qq.com

SPECIALTY SECTION
This article was submitted to Environmental Informatics and Remote Sensing, a section of the journal Frontiers in Earth Science

RECEIVED 12 December 2022
ACCEPTED 21 February 2023
PUBLISHED 13 March 2023

CITATION
Hu N, Zhang J, Teng L, Lu Y, Li Y, Li X and Zhu C (2023), Analysis of displacement evolution characteristics of reverse-dip layered rock slope based on geological geometric partition.
Front. Earth Sci. 11:1121618.
doi: 10.3389/feart.2023.1121618

Analysis of displacement evolution characteristics of reverse-dip layered rock slope based on geological geometric partition

Nanxiang Hu[1,2,3,4], Jiabing Zhang[2,3,5]*, Lin Teng[1], Yiping Lu[4], Yingchun Li[1]*, Xiaoshuang Li[1] and Chun Zhu[1,2,3,4]

[1]College of Civil Engineering, Qilu Institute of Technology, Jinan, China, [2]Key Laboratory of Geohazard, Fujian Province, Fuzhou, China, [3]Key Laboratory of Geohazard Prevention of Hilly Mountains, Ministry of Natural Resources of China, Fuzhou, China, [4]School of Earth Science and Engineering, Hohai University, Nanjing, China, [5]College of Construction Engineering, Jilin University, Changchu, China

To investigate the toppling displacement evolution characteristics of anti-dip rock slopes, the Xiaodongcao-Zhengjiadagou bank slope is taken as an engineering case, and firstly, the geological geometric distribution characteristics of the slope are obtained by superimposing the lithology, slope, and elevation raster layers of the slope through ArcGIS, and the geological partition with the largest area is the Lower Triassic Daye Formation, bottom elevation, and medium slope; based on the actual surface displacement monitoring data, the spatio-temporal evolution nephogram of toppling displacement of bank slope every half year is interpolated by Inverse Distance Weight method, and then the last displacement nephogram is assigned to the thousandth and superimposed with the geological geometric partition to obtain the displacement superposition characteristics. The results show that: the obvious zone of horizontal displacement deformation mainly occurs in the front and middle of the bank slope, mainly shear deformation, vertical displacement is primarily in the front and the back edge of the bank slope and the total displacement deformation is more similar to the horizontal displacement; the horizontal displacement value is larger than the vertical displacement value, the horizontal displacement deformation controls the overall deformation of the bank slope; through the analysis of the geometric superposition evolution of the anti-dip rock slope, the displacement superposition strong deformation zone is located at the boundary between the Triassic Jialingjiang Formation (T1j) and the Triassic Daye Formation (T1d).

KEYWORDS

anti-dip slope, displacement nephogram, evolution characteristics, strong deformation zone, geological partition

1 Introduction

Southwest China is a region where landslide geological disasters occur frequently, and the analysis of the deformation characteristics of landslides is one of the essential aspects of landslide control (Bao et al., 2023). Especially when encountering complex geological conditions such as broken structural surface, weak interlayer and fault, the stability of landslide is greatly reduced (Wang et., 2022a; Wang et., 2022b; He et al., 2022).

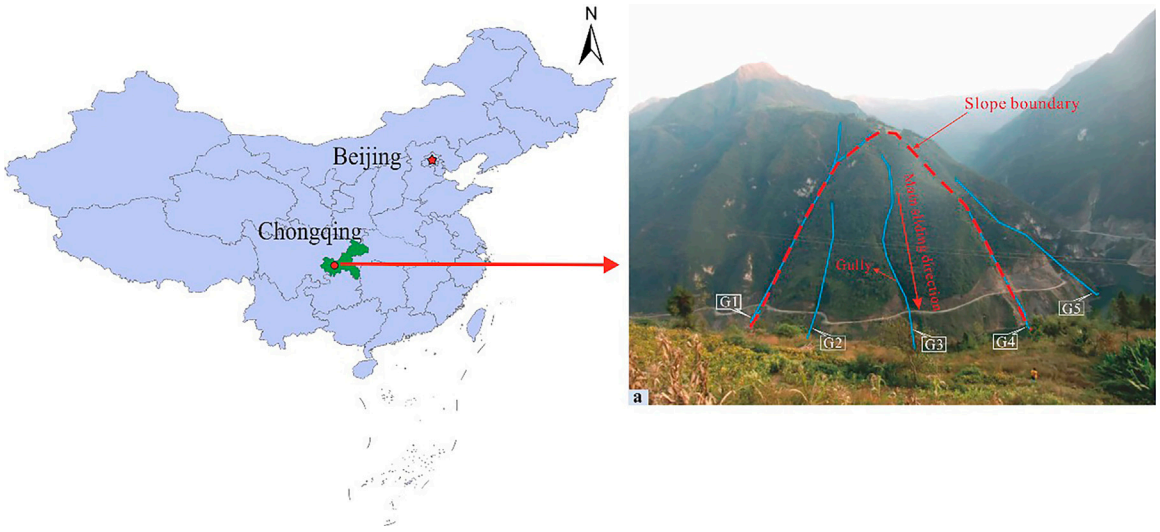

FIGURE 1
The whole landscape of the bank slope.

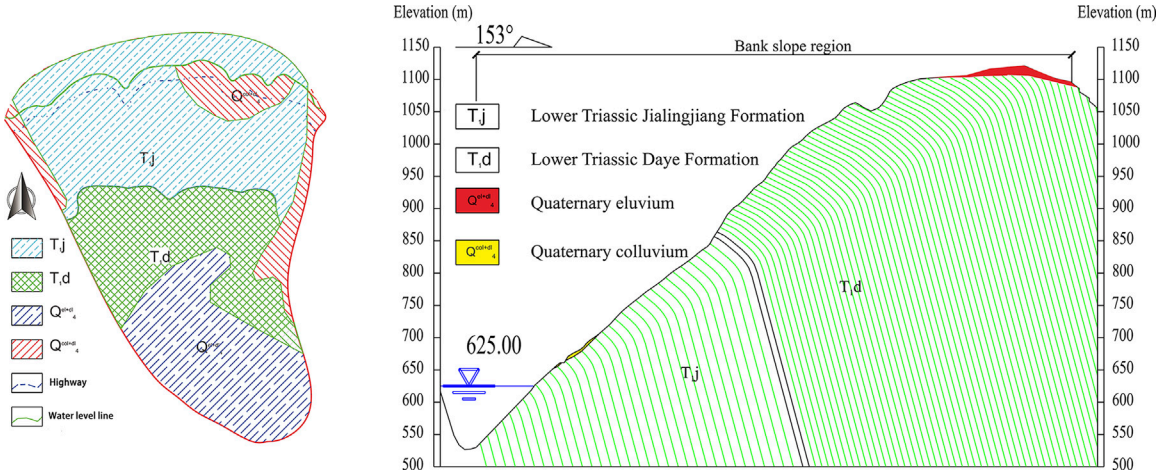

FIGURE 2
Distribution and geological section of exposed rock and soil on bank slope.

Huang. (2012) studied some typical large-scale landslides in mainland China in the 20th century and developed a geomechanical model for large-scale toppling in anti-dip strata. Goodman and Bray. (1976) classified the damage mode of anti-dip slopes into three main types: bending damage, block damage, and bending-block damage. Liu et al. (2009), Liu et al. (2010) conducted a more in-depth study on overturning damage of rock slopes based on Goodman's theory of rock slope damage. Chen et al. (2016) established a mechanical model and stability analysis method for bending and tipping damage of anti-dip rock slopes based on limit equilibrium theory. Shen et al. (2010) studied the rheological properties of red soft rock, and their results have important reference values for the design of anti-dip red soft rock slopes. Adhikary et al. (1997) conducted a series of model centrifugal tests to study the bending and tipping damage mechanism of jointed rock slopes. Alejano et al. (2010) used numerical analysis to analyze the damage mechanism of open pit mine. They interpreted the anti-dip stratified slope as a complex combination of tipping and cyclic damage. Bowa and Xia. (2018) proposed a technique for angular analysis of counter-tilted failure surfaces applicable to block tipping failure mechanisms, which can provide an accurate application for evaluating the instability of rock slopes with counter-tilted failure surfaces. Li et al. (2019) analyzed the width, and ridge number variation characteristics of the fast Fourier transform spectrum along the slope surface to reveal the internal damage characteristics of anti-dip rock slopes. Ning et al. (2019) conducted a simulation study on the evolutionary characteristics of toppling failure of anti-dip rock slopes and revealed the relationships between the surface peak ground

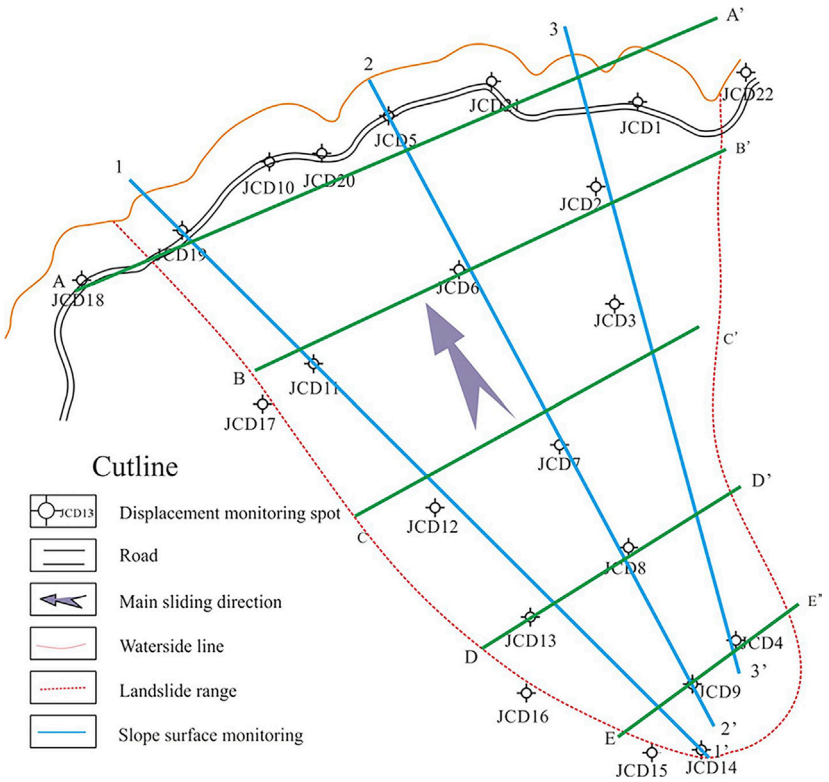

FIGURE 3
Plane layout of surface displacement monitoring.

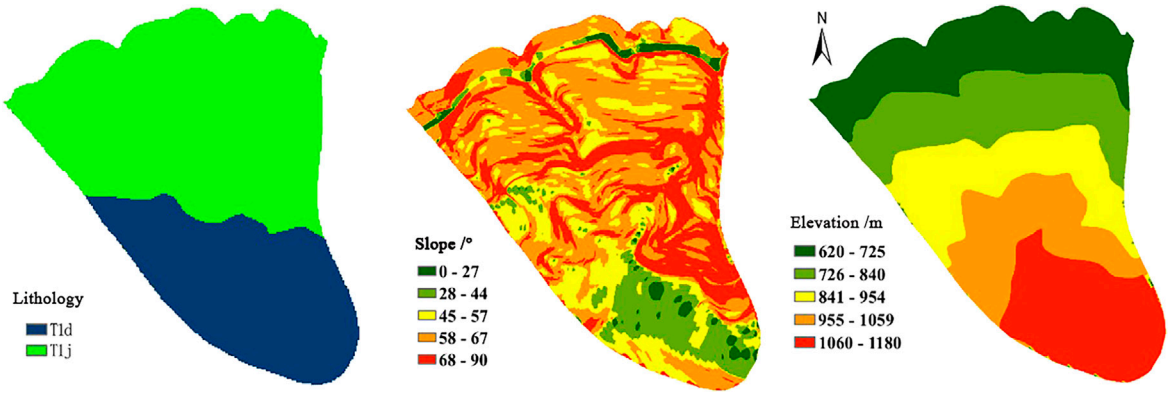

FIGURE 4
Lithology, slope, and elevation distribution map.

acceleration, the horizontal depth of the failure plane, and slope displacement. Tao et al. (2019) used the superimposed cantilever beam theory and the maximum tensile stress strength criterion for brittle damage to derive a formula for calculating the vertical crack extension depth in reverse slope overturning damage by studying and analyzing the unstable damage mode of massive overturning damage of the southwest slope of the Changshanhao open-pit gold mine. Based on the similarity ratio theory, Zhu et al. (2020) developed a physical model to investigate in depth the damage mechanism of anti-dip layered slopes during excavation. Weng et al. (2020) proposed an innovative failure criterion for assessing the stability of anti-dip rock slopes, which outperforms the Mohr-Coulomb criterion at low normal stresses and is more relevant to reality. Xie et al. (2020) analyzed the evolution characteristics of toppling deformation of rock slopes from the perspective of the energy field. Dong et al. (2020); Dong et al. (2022) combined field

TABLE 1 Bank slope geological zoning basis.

Type	Lithology	Slope/°	Elevation/m
Grade	1: Lower Triassic Daye Formation (*T1d*)	1: 0–27	1: 620–725
	2: Lower Triassic Jialingjiang Formation (*T1j*)	2:28–44	2: 726–840
		3:45–57	3: 841–954
		4:58–67	4: 955–1,059
		5: 68–90	5: 1,060–1,180
Partition number	Hundreds digit	Tens digit	Single digit

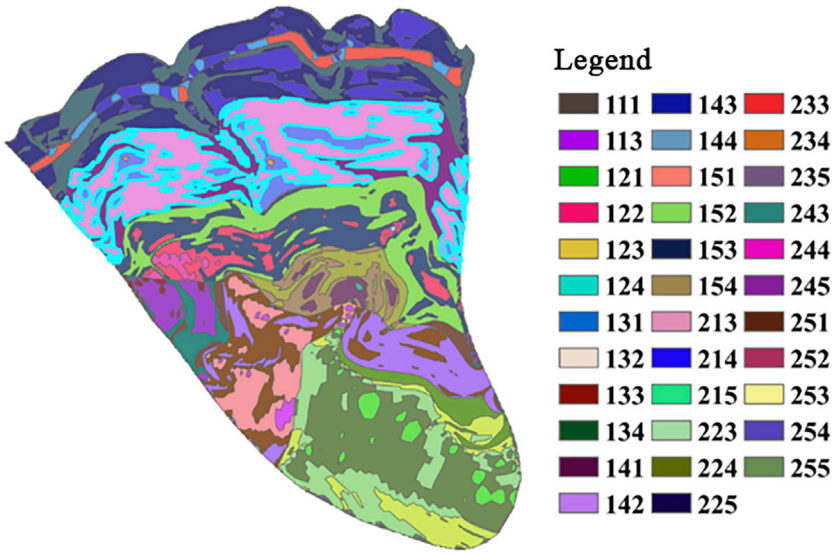

FIGURE 5
Geologic geometric displacement superimposed partition map.

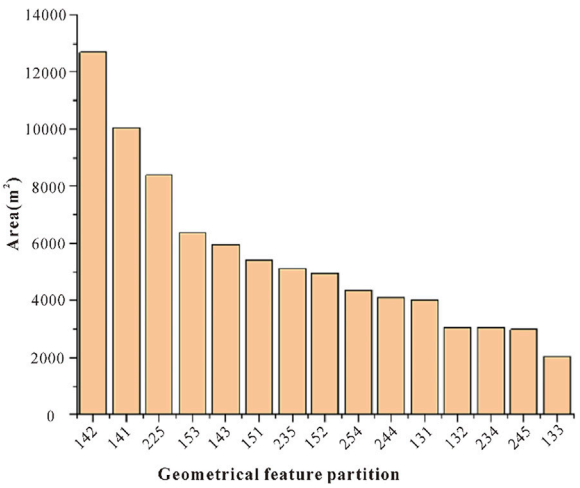

FIGURE 6
Bank slope geological geometric partitioning unit area of statistical results.

monitoring data to simulate the excavation process of anti-dip rock slopes with the discrete element method and analyzed the influence of different factors on the slope. The results show that the scale and stability of the deformation zone of the anti-dip rock slope have a specific influence, and the lithology determines the failure mode of the toppling failure. Cheng et al. (2021) used a digital camera to take high-speed images of real-time deformation behavior of overturn-resistant rock slopes under external loads, analyzed the entire damage process of anti-dip rock slopes, and discussed in detail the ultimate damage modes of the anti-dip rock slopes with different joint angles. Ding et al. (2021) studied the characteristics and process of the flexural toppling of anti-dip rock slopes. They obtained the characteristics and mechanical mechanism of flexural toppling, as well as the zoning of the slope. Xu et al. (2022) used the discrete element method (DEM) to explore the failure of earthquake-induced large-scale anti-dip rock landslides. Ren et al. (2022) used the three-dimensional discrete element method to analyze the dynamic response to the seismic dynamic of the anti-dip rock slopes. Nie et al. (2022)

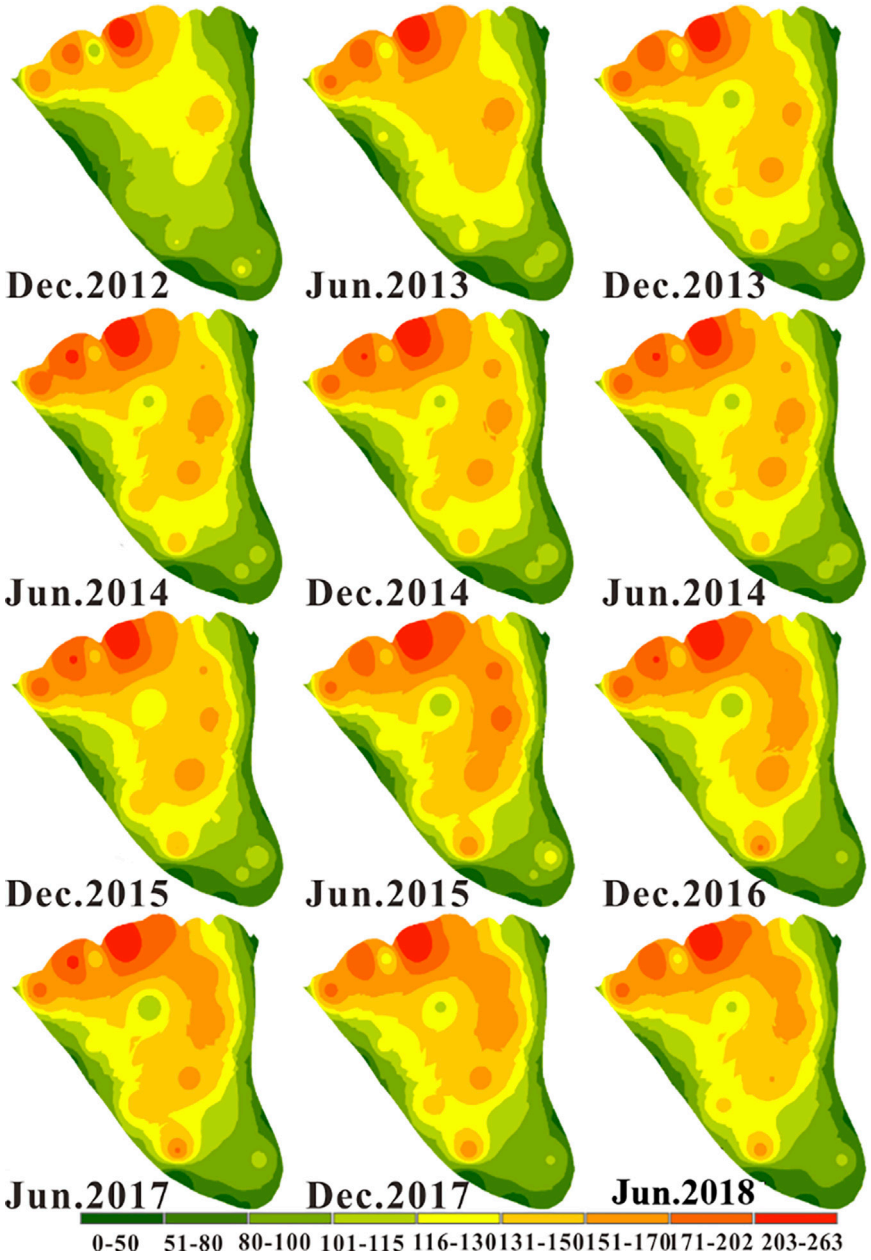

FIGURE 7
Spatial and temporal evolution nephogram of horizontal displacement (mm).

conducted a study on the control of deformation damage of NPR structural cables on rocky slopes under excavation by using numerical simulation method, and revealed the control mechanism of NPR structural cables on rocky slope tipping deformation. They studied the amplification effect, the change in the Fourier spectrum, the failure mechanism, and the permanent displacement of the slopes under seismic action.

As this project is a typical anti-dip layered rock slope, it has attracted the attention of many experts and scholars. Cai et al. (2014) established the cantilever beam limit equilibrium calculation model and verified its correctness with the numerical software UDEC, and obtained that the damage zone of anti-dip stratified rock slope is determined by the foot of the slope, dip angle of the rock layer, and slope height. Gao et al. (2015) considered the Goodman-Bray method of calculating the stability of anti-dip rock slopes under the action of groundwater. Wei. (2015) used numerical software (UDEC) to study the variation rule of toppling deformation of anti-dip slopes with the thickness ratio of adjacent rock strata. Jiang et al. (2016) divided the damage of anti-dip rock slopes into three main stages: bending, bending cracking, and fracture cracking.

Many factors affect the tipping deformation of rocky slopes, and the research results also have specific reference values. Most scholars

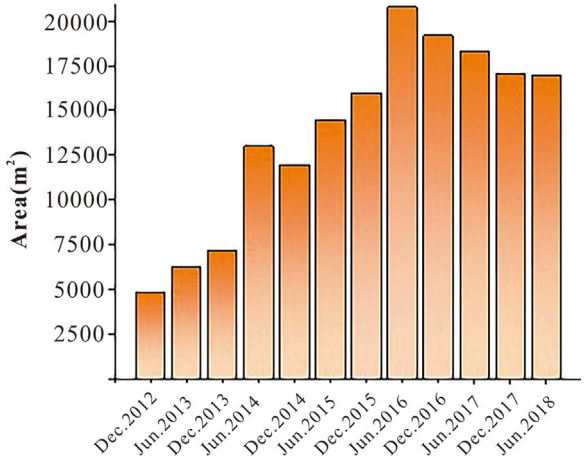

FIGURE 8
Area of horizontal displacement strong deformation zone.

mainly analyze the overall stability of anti-dip rock slopes through theoretical analysis, physical model tests, and numerical simulation, and analyze the deformation evolution characteristics of rocky slopes as a whole (Gschwind et al., 2019; Martino et al., 2020; Wang et al., 2020; Tang et al., 2022; Liang et al., 2022; Zheng et al., 2022; Lei et al., 2022; Wang et al., 2020; Wang et al., 2023; Ren et al., 2023). However, the actual monitoring data show that the deformation evolution characteristics of anti-dip rock slopes vary significantly in different areas and have different geological geometric characteristics. Therefore, this paper takes the typical anti-dip rock slope as the research object. Based on field investigation, it takes the lithology, slope, and elevation of the rock slope as the characteristic geological factors and analyzes its spatial distribution characteristics (Wang et al., 2022; Wu et al., 2022). Based on the discrete actual displacement monitoring data, the evolution nephogram of toppling displacement of rock slope is obtained by Inverse Distance Weight method, and the Spatiotemporal evolution nephogram of displacement is superimposed with geological and geometric characteristics. This study explores the geometric characteristics of the anti-dip rock slope and its displacement superposition evolution characteristics, which can provide a reference for similar engineering examples.

2 Project overview

Xiaodongcao-Zhengjiadagou bank slope is located on the right bank of the upper reaches of Xixi River, Zhongliang Township, Wuxi County, Chongqing (Figure 1), 1.2 km from Zhongliang Reservoir (Figure 1), with the elevation of the bank slope ranging from 540 m to 1,183 m and the width of 700 m; the overall topography of the bank slope is steep, the slope aspect is 345°, the vegetation in the area is developed, the front part of the topography is steep, the topography slope angle is 45°–68°, and the back part of the topography is relatively gentle, the topography slope angle is 11°–18°, and the local section can reach 37°. The topographic characteristics of the bank slope are mainly controlled by lithology and geological structure. According to the field geological survey and engineering investigation, it is revealed that the rock mass of the bank slope is mainly composed of the Lower Triassic Jialingjiang Formation (T1j) and Daye Formation (T1d); among them, Jialingjiang Formation (T1j) is a medium-thick laminated dolomitic tuff, mainly distributed in the middle and front part of the bank slope, mainly subject to shear stress. The rock structure is relatively complete, but the local weathering is substantial. The Daye Formation (T1d) is a thin and medium-thick laminated marl tuff, mainly distributed in the middle and posterior part of the bank slope, which is in the area of obvious tensile stress during the bending and tipping deformation, so the rock structure is broken, and the bending and tipping deformation of the rock layer is obvious (Figure 2).

The surface displacement monitoring system mainly consists of 22 surface displacement monitoring points evenly distributed throughout the study area, including 17 monitoring points on the bank slope body and five outside the bank slope boundary; the surface displacement monitoring time was from December 2012 to December 2016. The monitoring system was divided into five transverse and three longitudinal profiles based on their arrangement characteristics. After the reservoir completion, the water level was raised by nearly 100 m compared with the original, and the deformation of the front and trailing edge of the bank slope was more pronounced. The surface of the trailing edge showed obvious pulling cracks, which seriously threatened the life safety of the downstream residents (Figure 3).

3 Analysis of bank geometric characteristics zoning

3.1 Analysis of geometric characteristics factor

The geometric characteristics of the bank slope area were analyzed by ArcGIS, and the distribution characteristics of stratigraphic lithology, slope, and elevation in the bank slope area were obtained. As can be seen from Figure 4, the front part of the bank slope is steep, except for the rear part, which is relatively gentle (0°–27°); most of the other areas have a slope angle greater than 44°, the slope body gully is developed, the gully is “V"-shaped, with significant differences in topographic relief. The Lower Triassic Jialingjiang Formation (T1j) is located in the front to the middle of the bank slope, and the Daye Formation (T1d) is located at the rear edge of the bank slope.

3.2 Geometric characteristics superposition

The lithology, slope, and elevation raster layers were reclassified, and the lithology was assigned to the hundreds digit, slope to the tens digit, and elevation to the single digit by the Spatial Analyst tool of GIS. The geological geometry of the bank slope was performed according to the Jenks Natural Breaks Classification (Table 1), and the bank slope was finally divided into 35 characteristic partitions (Figure 5).

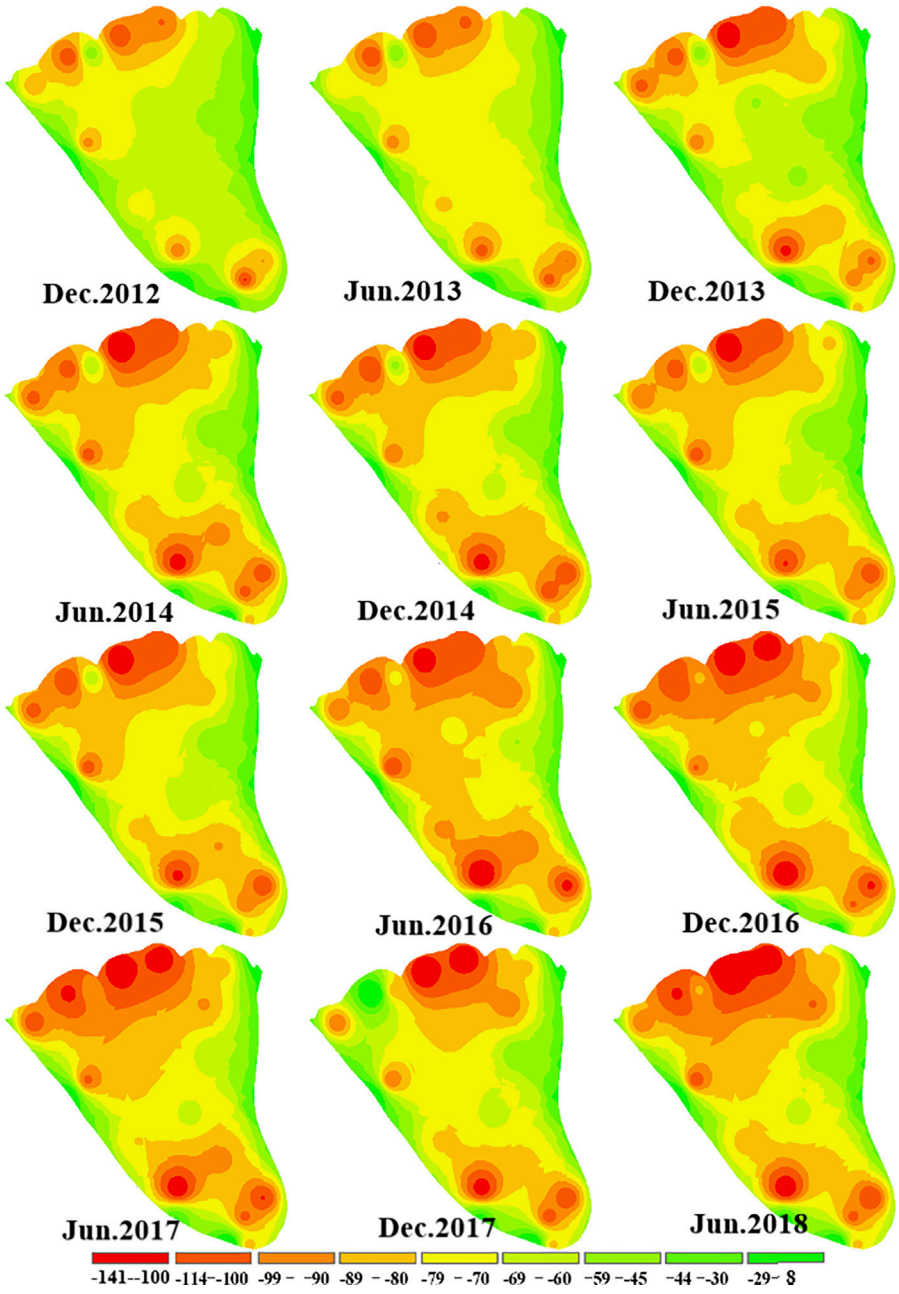

FIGURE 9
Spatial and temporal evolution nephogram of vertical displacement.

3.3 Analysis of geometric superposition characteristics

The geological geometric displacement superposition partition map can be divided into 35 characteristic partitions by GIS raster calculation, with a total area of 97039.01 m^2. Among them, the characteristic partition area with an area greater than 2000 m^2 accounts for 85.04% of the total area, and the largest characteristics partition is the 142nd (Figure 6).

4 Analysis of the evolutionary characteristics of displacement nephogram

The Inverse Distance Weight method was used to interpolate the displacement deformations of the bank slope surface monitoring points. The displacements were classified into nine categories by the Jenks Natural Breaks Classification. The horizontal displacement deformation nephogram, vertical displacement deformation nephogram, and total displacement deformation nephogram were interpolated every 6 months.

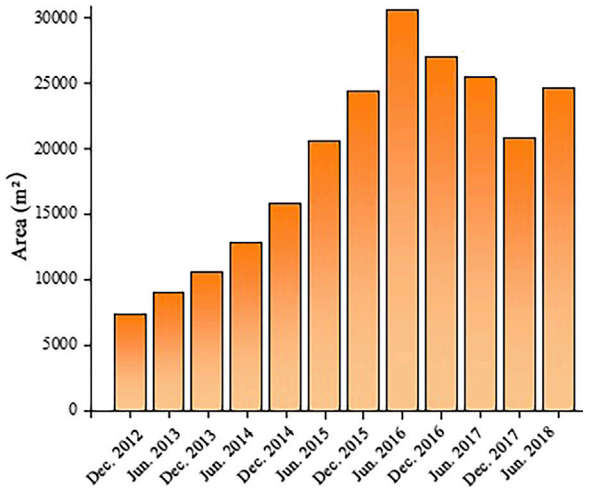

FIGURE 10
Area of strong deformation zone in the vertical direction.

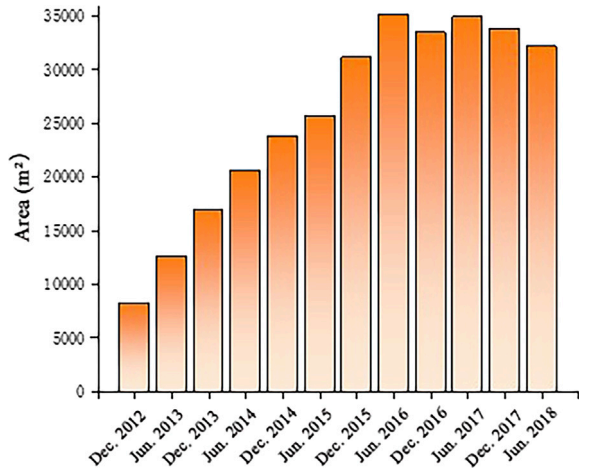

FIGURE 11
Spatial and temporal evolution nephogram of total displacement.

4.1 Analysis of the evolution of horizontal displacement nephogram

The temporal and spatial evolution nephogram of the horizontal displacement of the bank slope below (Figure 7) shows that the bank slope's obvious area of horizontal displacement deformation mainly appears in the front and middle of the bank slope. The maximum horizontal displacement appears in the front of the bank slope, mainly distributed in a dotted shape and a strip distribution in the middle. With time, it can be seen from the evolution nephogram that the horizontal displacement deformation in the middle increases significantly and gradually expands to the right side, and the horizontal displacement on the right side of the middle is significantly larger than that on the left side. The area with horizontal displacement deformation greater than 150 mm is the obvious area of horizontal displacement deformation. As shown in Figure 8, the obvious area of horizontal displacement deformation increases and decreases with time, reaching a maximum of 20780.38 m^2 in June 2016, and then the deformation of the middle displacement gradually weakens and changes to the right side of the front, gradually fading to point. The horizontal displacement of the middle strip deformation area and the front point deformation area alternately control the evolutionary law of tipping deformation of the anti-dip rock slope, where shear deformation mainly occurs.

4.2 Analysis of the evolution of vertical displacement nephogram

The temporal and spatial evolution nephogram of the vertical displacement of the bank slope below (Figure 9) shows that the obvious area of vertical displacement deformation mainly occurs in the front of the bank slope and the back edge of the bank slope. The maximum vertical displacement occurs in the middle area of the front of the bank slope and the trailing edge of the bank slope and is dotted. The vertical displacement change in the middle of the bank slope is the smallest. With time, the deformation of the front and back edges became more pronounced and gradually increased. The trailing edge of the bank slope mainly occurs in vertical deformation, corresponding to the evolution law of toppling deformation.

The vertical displacement of the front of the bank slope gradually increases overall. It gradually expands from the middle to the left and right sides, and the front middle of the bank slope and the change of vertical displacement on the left side is more evident than on the right side. The change of vertical displacement in the middle and rear part of the bank slope and the rear edge is more pronounced, with a point-like distribution, and gradually increases with time. The area with vertical displacement less than −80 mm is defined as the obvious area of vertical displacement deformation (Figure 10). In June 2016, the area of the strong deformation zone reached a maximum of 30592.39 m^2. The evolutionary characteristics of the vertical displacement in the middle of the bank slope were not prominent, and the change in the right side of the middle was small; it showed the anti-dip evolutionary characteristics of the bank slope.

4.3 Analysis of the evolution of the total displacement nephogram

The temporal and spatial evolution nephogram of the total displacement of the bank slope below (Figure 11) shows that the total displacement and horizontal displacement deformation are relatively similar, with the maximum total displacement mainly occurring in the front of the bank slope, with a point-like distribution. With time, the total displacement deformation in the middle gradually increases. As can be seen from Figure 12, the area of the total displacement strong deformation zone reached a maximum of 35057.62553 m^2 in June 2016 and expanded from the front to the middle of the bank slope, and the deformation of the right side of the middle was significantly more significant than the left side; the tipping deformation was dominated by horizontal displacement changes, and the horizontal displacement deformation was significantly more significant than the vertical displacement changes.

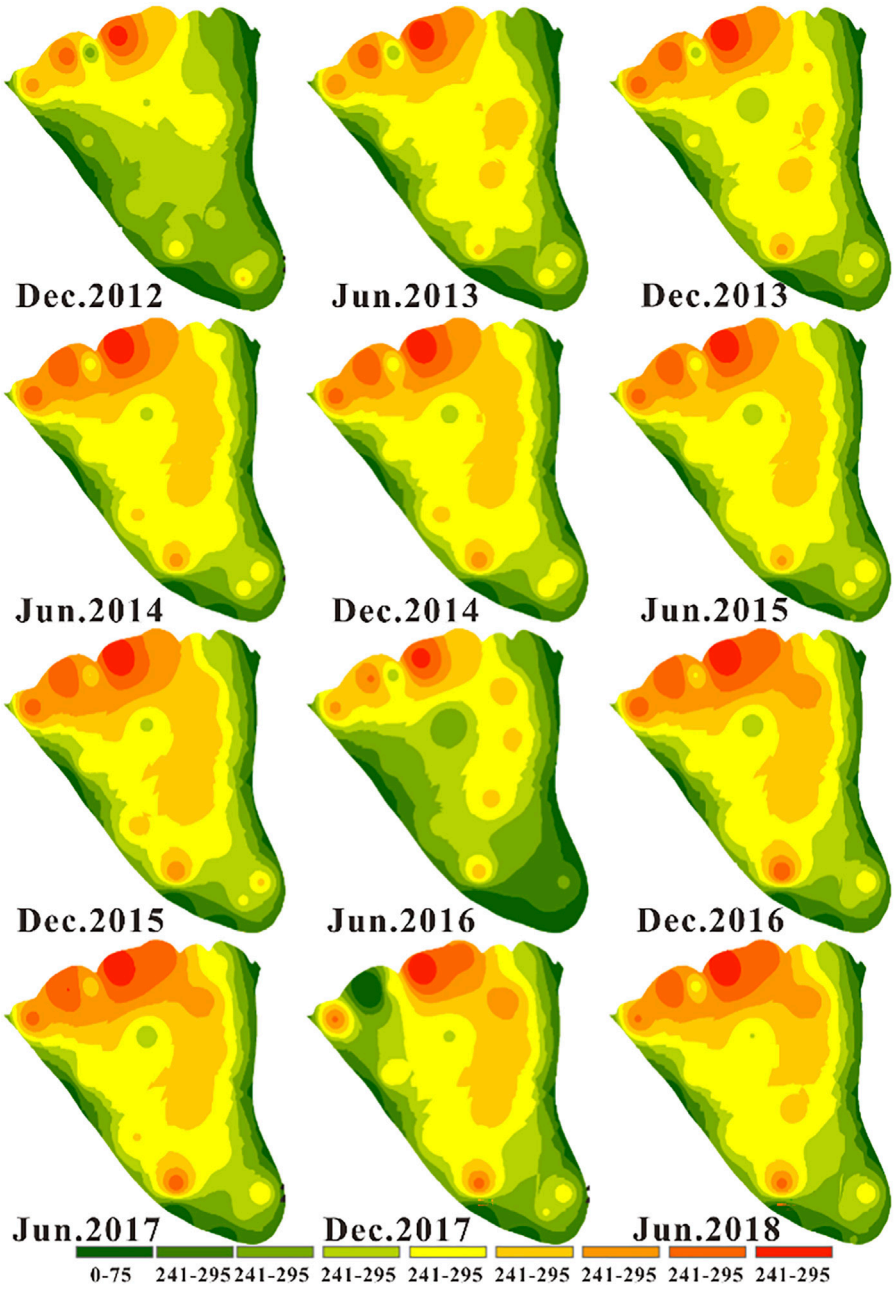

FIGURE 12
Area of strong deformation zone in total direction.

5 Analysis of displacement superposition characteristics

Based on geological geometric superposition, the horizontal displacement nephogram, vertical displacement nephogram, and total displacement nephogram of the later interpolation are assigned to the thousands digit, and the displacement geometric superposition characteristics partition based on the geological geometric partition is obtained. The displacement strong deformation zone and the most prone area of the bank slope are analyzed.

5.1 Analysis of geometric superposition characteristics of horizontal displacement

The horizontal displacement is reclassified into three categories 17 mm–103 mm as the weak deformation zone, 104–146 mm as the medium deformation zone, 147 mm–255 mm as the strong deformation zone, and the horizontal displacement is superimposed with geological geometry to get the horizontal displacement geometry superimposed characteristics zone, which is divided into 88 characteristics partitions (Figure 13).

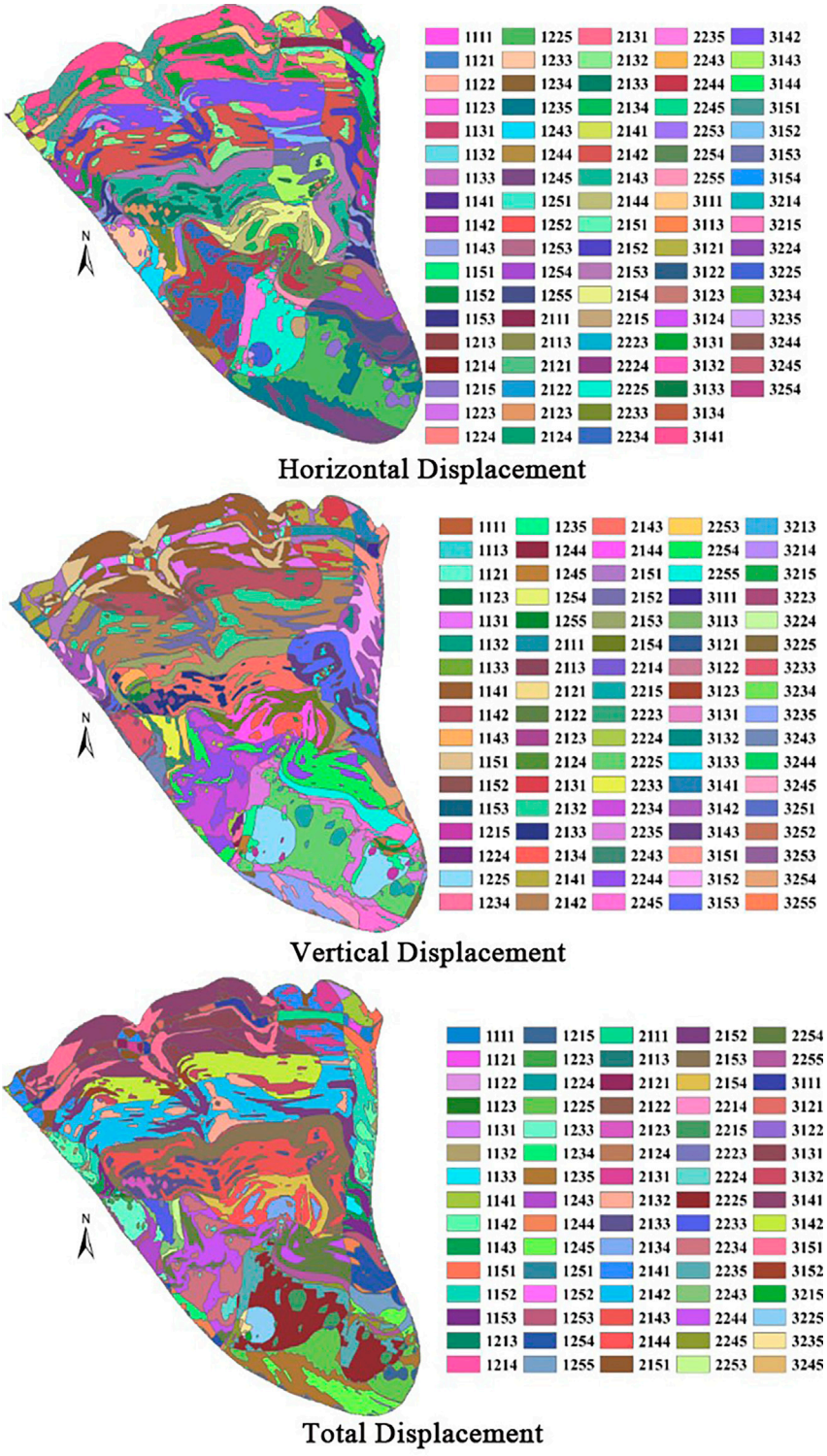

FIGURE 13
Superposition of displacement geometric characteristics.

The area of each horizontal displacement geometric superposition characteristics partition was counted by GIS (Figure 14). The characteristics partition with a strong deformation area larger than 1,500 m^2 was selected as the horizontal displacement strong deformation partition. Among them, the horizontal displacement strong deformation partition with the largest strong deformation area is the 141th partition, whose strong deformation area is 7,311.724 m^2, accounting for

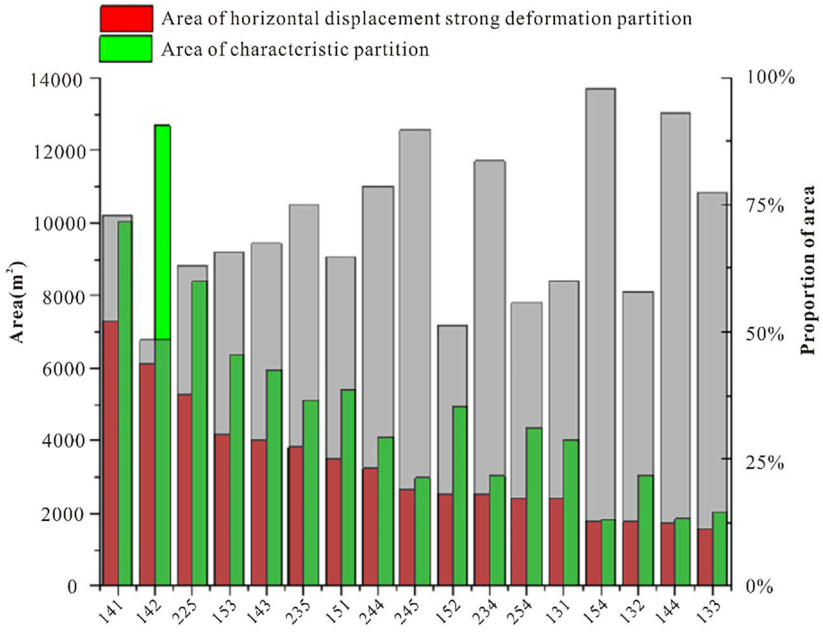

FIGURE 14
The ratio of the area of strong deformation of horizontal displacement and its characteristic area.

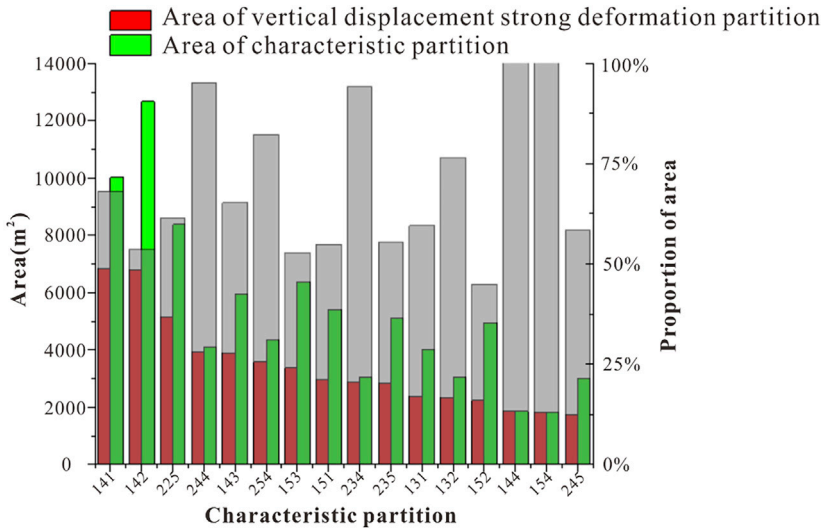

FIGURE 15
The ratio of the area of strong deformation of vertical displacement and its characteristic area.

72.29% of the 141th partition. This characteristic partition is located in the Jialingjiang Formation (T1j), medium slope, and bottom elevation. The horizontal displacement-prone partition is the 154th partition, 97.95% of which is the strong deformation zone, and the strong deformation area is 1779.01 m^2. This characteristic partition is located at the boundary between Jialingjiang Formation (T1j) and Daye Formation (T1d), high slope and medium elevation.

5.2 Analysis of geometric superposition characteristics of vertical displacement

The area of each vertical displacement geometric superposition characteristics partition was counted by GIS (Figure 15). The characteristics partition with a strong deformation area larger than 1,500 m^2 was selected as the vertical displacement strong deformation partition. Among them, the vertical displacement strong deformation

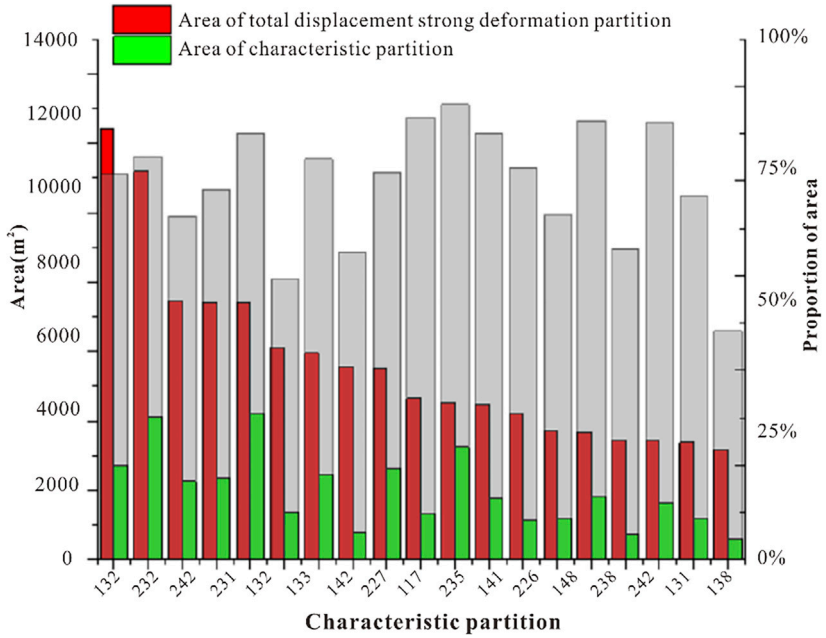

FIGURE 16
The ratio of the area of strong deformation of total displacement and its characteristic area.

partition with the largest strong deformation area is the 141th partition, whose strong deformation area is 6,832.61 m^2, accounting for 68.16% of the 141th partition. This characteristic partition is located in the Jialingjiang Formation (T1j), medium slope, and bottom elevation. The vertical displacement-prone partitions are the 154th and 14fourth, 100% of which are strong deformation zones. They are located at the boundary between Jialingjiang Formation (T1j) and Daye Formation (T1d), with a high slope and medium elevation.

5.3 Analysis of geometric superposition characteristics of total displacement

The area of each total displacement geometric superposition characteristics partition was counted by GIS (Figure 16). The characteristics partition with a strong deformation area larger than 1,500 m^2 was selected as the total displacement strong deformation partition. Among them, the total displacement strong deformation partition with the largest strong deformation area is the 132nd partition, whose strong deformation area is 6,832.61 m^2, accounting for 81.61% of the 132nd partition. This characteristic partition is located in the Jialingjiang Formation (T1j), medium slope, and bottom elevation. The total displacement-prone partition is the 235th partition, 96.21% of which is the strong deformation zone. This characteristic partition is located at the boundary between Jialingjiang Formation (T1j) and Daye Formation (T1d), high slope and medium elevation.

6 Conclusion

Based on the analysis of typical anti-dip layered rock slope cases, based on discrete surface displacement monitoring data and combined with different geological zones, this paper explores the real evolution law of toppling deformation in each zone. It can reference similar anti-dip slope monitoring, early warning, and prevention. The main results are as follows.

(1) The geometric characteristics overlay was obtained by superimposing geometric factors such as lithology, slope, and elevation of the bank slope strata through ArcGIS raster calculation. It was divided into 35 characteristics partitions with an area of 97039.01 m^2. The characteristics partition with the largest superimposed area is the 142nd partition, located in the Lower Triassic Daye Formation, bottom elevation, medium slope.
(2) The analysis of evolution characteristics of horizontal displacement nephogram, vertical displacement nephogram, and total displacement nephogram shows that the obvious zone of horizontal displacement deformation mainly occurs in the front and middle of the bank slope and is dominated by shear deformation, the vertical displacement is mainly in the front of the bank slope and the back edge, the total displacement deformation is more similar to the horizontal displacement, the horizontal displacement value is larger than the vertical displacement value, and the horizontal displacement deformation controls the overall toppling deformation of the bank slope.
(3) Based on the geological geometric superposition, the displacement nephogram of the last interpolation is overlaid with it. The results show that: the strong deformation partition of horizontal and vertical displacement is the 141th partition, and the strong deformation zone of total displacement is the 132nd partition. The horizontal displacement-prone area is the 154th partition, the vertical displacement-prone area is the

154th and fourth partition, and the total displacement-prone area is the 235 partition.

Data availability statement

The original contributions presented in the study are included in the article/supplementary material, further inquiries can be directed to the corresponding authors.

Author contributions

JZ and NH participated in the design of this study, and they both performed the statistical analysis. NH carried out the study and collected important background information. YLi drafted the manuscript. All authors read and approved the final manuscript. JZ and LT carried out the concepts, design, definition of intellectual content, literature search, data acquisition, data analysis and manuscript preparation. YLu, XL and CZ provided assistance for data acquisition, data analysis and statistical analysis. JZ and YLi carried out literature search, data acquisition and manuscript editing. XL and CZ performed manuscript review. All authors have read and approved the content of the manuscript. All authors have made substantial contributions to all of the following: (1) The conception and design of the study, or acquisition of data, or analysis and interpretation of data, (2) drafting the article or revising it critically for intellectual content, (3) final approval of the version to be submitted.

Funding

This study was supported by the Young creative talents introduction and culturing program of universities in Shandong Province (Grant No. [2021]51), the National Natural Science Foundation of Shandong Province of China (NSFC) (Grant No. ZR2022ME188), the project of Slope safety control and disaster prevention technology innovation team of "Youth Innovation Talent Introduction and Education Plan" of Shandong Colleges and universities (Grant No. Lu Jiao Ke Han [2021] No. 51), and the opening fund of Key Laboratory of Geohazard Prevention of Hilly Mountains, Ministry of Natural Resources (Grant No. FJKLGH2023K001).

Conflict of interest

The authors declare that the research was conducted in the absence of any commercial or financial relationships that could be construed as a potential conflict of interest.

Publisher's note

All claims expressed in this article are solely those of the authors and do not necessarily represent those of their affiliated organizations, or those of the publisher, the editors and the reviewers. Any product that may be evaluated in this article, or claim that may be made by its manufacturer, is not guaranteed or endorsed by the publisher.

References

Adhikary, D. P., Dyskin, A. V., Jewell, R. J., and Stewart, D. P. (1997). A study of the mechanism of flexural toppling failure of rock slopes. *Rock Mech. Rock Eng.* 30 (2), 75–93. doi:10.1007/bf01020126

Alejano, L. R., Gomez-Marquez, I., and Martinez-Alegria, R. (2010). Analysis of a complex toppling-circular slope failure. *Eng. Geol.* 114 (1-2), 93–104. doi:10.1016/j.enggeo.2010.03.005

Bao, Y. D., Chen, J. P., Su, L. J., Zhang, W., and Zhan, J. W. (2023). A novel numerical approach for rock slide blocking river based on the cefdem model: A case study from the samaoding paleolandslide blocking river event. *Eng. Geol.* 312, 106949. doi:10.1016/j.enggeo.2022.106949

Bowa, V. M., and Xia, Y. Y. (2018). Stability analyses of jointed rock slopes with counter-tilted failure surface subjected to block toppling failure mechanisms. *Arabian J. Sci. Eng.* 43 (10), 5315–5331. doi:10.1007/s13369-018-3168-4

Cai, J. S., Yan, E. C., Wang, Z. Q., Yang, J. G., and Tang, R. X. (2014). Study of cantilever beam limit equilibrium model of anti-dip layered rock slopes. *Rock Soil Mech.* 35 (S1), 15–18. doi:10.16285/j.rsm.2014.s1.003

Chen, C., Zheng, Y., and Sun, C. (2016). An analytical approach on flexural toppling failure of counter-tilt slopes of layered rock. *Chin. J. Rock Mech. Eng.* 35 (11), 2174–2187. doi:10.13722/j.cnki.jrme.2016.1001

Cheng, H., Han, L. Y., Wu, Z. J., and Zhou, X. P. (2021). Experimental study on the whole failure process of anti-dip rock slopes subjected to external loading. *Bull. Eng. Geol. Environ.* 80 (8), 6597–6613. doi:10.1007/s10064-021-02311-5

Ding, B. D., Han, Z. Y., Zhang, G. C., Beng, X. T., and Yang, Y. C. (2021). Flexural toppling mechanism and stability analysis of an anti-dip rock slope. *Rock Mech. Rock Eng.* 54 (8), 3721–3735. doi:10.1007/s00603-021-02435-w

Dong, M. L., Zhang, F. M., Lv, J. Q., Fei, Y., and Li, Z. N. (2020). Study of stability influencing factors of excavated anti-dip rock slope. *Ksce J. Civ. Eng.* 24 (8), 2293–2303. doi:10.1007/s12205-020-1412-4

Dong, M. L., Zhang, F. M., Yu, C., Lv, J. Q., Zhou, H. X., Li, Y. K., et al. (2022). Influence of a dominant fault on the deformation and failure mode of anti-dip layered rock slopes. *Ksce J. Civ. Eng.* 26 (8), 3430–3439. doi:10.1007/s12205-022-1852-0

Gao, L. T., Yan, E. C., and Xie, L. F. (2015). Improved goodman-bray method in consideration of groundwater effect. *J. Yangtze River Sci. Res. Inst.* 32 (2), 78–83. doi:10.3969/j.issn.1001-5485.2015.02.017

Goodman, R. E., and Bray, J. W. (1976). Toppling of rock slopes, specialty conference on rock engineering for foundations and slopes. *Am. Soc. Civ. Eng.* 2, 201–234.

Gschwind, S., Loew, S., and Wolter, A. (2019). Multi-stage structural and kinematic analysis of a retrogressive rock slope instability complex (Preonzo, Switzerland). *Eng. Geol.* 252, 27–42. doi:10.1016/j.enggeo.2019.02.018

He, M. C., Sui, Q. R., Li, M. N., Wang, Z. J., and Tao, Z. G. (2022). Compensation excavation method control for large deformation disaster of mountain soft rock tunnel. *Int. J. Min. Sci. Technol.* 32 (5), 951–963. doi:10.1016/j.ijmst.2022.08.004

Huang, R. Q. (2012). Mechanisms of large-scale landslides in China. *Bull. Eng. Geol. Environ.* 71 (1), 161–170. doi:10.1007/s10064-011-0403-6

Jiang, X. N., Fan, L. G., Zhou, Y. L., and Zhu, T. Y. (2016). Research on the deformation failure mechanism and influence factors of large dipping steeply anti-dip rock landslide. *Chin. J. Undergr. Space Eng.* 12 (2), 356–361.

Lei, Z. D., Wu, B. S., Wu, S. S., Nie, Y. X., Cheng, S. Y., and Zhang, C. Y. (2022). A material point-finite element (MPM-FEM) model for simulating three-dimensional soil-structure interactions with the hybrid contact method. *Comput. Geotechnics* 152, 105009. doi:10.1016/j.compgeo.2022.105009

Li, L. Q., Ju, N. P., Zhang, S., Deng, X. X., and Sheng, D. C. (2019). Seismic wave propagation characteristic and its effects on the failure of steep jointed anti-dip rock slope. *Landslides* 16 (1), 105–123. doi:10.1007/s10346-018-1071-4

Liang, X., Tang, S. B., Tang, C. A., Hu, L. H., and Chen, F. (2022). Influence of water on the mechanical properties and failure behaviors of sandstone under triaxial compression. *Rock Mech. Rock Eng.* 56, 1131–1162. doi:10.1007/s00603-022-03121-1

Liu, C. H., Jaksa, M. B., and Meyers, A. G. (2009). A transfer coefficient method for rock slope toppling. *Can. Geotechnical J.* 46 (1), 1–9. doi:10.1139/t08-094

Liu, C. H., Jaksa, M. B., and Meyers, A. G. (2010). Toppling mechanisms of rock slopes considering stabilization from the underlying rock mass. *Int. J. Rock Mech. Min. Sci.* 47 (2), 348–354. doi:10.1016/j.ijrmms.2009.11.008

Martino, S., Cercato, M., Della Seta, M., Esposito, C., Hailemikael, S., Iannucci, R., et al. (2020). Relevance of rock slope deformations in local seismic response and microzonation: Insights from the Accumoli case-study (central Apennines, Italy). *Eng. Geol.* 266, 105427. doi:10.1016/j.enggeo.2019.105427

Nie, W., Wang, W. Q., Tao, Z. G., Zhu, C., and Chen, Y. (2022). Numerical modeling of the NPR-cable and its applications for analysis of a slide-toe-toppling failure. *Comput. Geotechnics* 149, 104852. doi:10.1016/j.compgeo.2022.104852

Ning, Y. B., Zhang, G. C., Tang, H. M., Shen, W. C., and Shen, P. W. (2019). Process analysis of toppling failure on anti-dip rock slopes under seismic load in southwest China. *Rock Mech. Rock Eng.* 52 (11), 4439–4455. doi:10.1007/s00603-019-01855-z

Ren, D. Z., Wang, X. Z., Kou, Z. H., Wang, S. C., Wang, H., Wang, X. G., et al. (2023). Feasibility evaluation of CO2 eor and storage in tight oil reservoirs: A demonstration project in the ordos basin. *Fuel* 331, 125652. doi:10.1016/j.fuel.2022.125652

Ren, Z. H., Chen, C. X., Sun, C. Y., and Wang, Y. (2022). Dynamic analysis of the seismo-dynamic response of anti-dip bedding rock slopes using a three-dimensional discrete-element method. *Appl. Sciences-Basel* 12 (9), 4640. doi:10.3390/app12094640

Shen, Q., Chen, C. X., Lu, H. F., and Zhao, Y. Y. (2010). Experimental research on the rheology characterisic of the red soft rock of badong group. *Disaster Adv.* 3 (4), 210–213. doi:10.1155/2021/6615379

Tang, S. B., Li, J. M., Ding, S., and Zhang, L. T. (2022). The influence of water-stress loading sequences on the creep behavior of granite. *Bull. Eng. Geol. Environ.* 81 (11), 482. doi:10.1007/s10064-022-02987-3

Tao, Z. G., Geng, Q., Zhu, C., He, M. C., Cai, H., Pang, S. H., et al. (2019). The mechanical mechanisms of large-scale toppling failure for counter-inclined rock slopes. *J. Geophys. Eng.* 16 (3), 541–558. doi:10.1093/jge/gxz020

Wang, G. J., Tian, S., Hu, B., Kong, X. Y., and Chen, J. (2020a). An experimental study on tailings deposition characteristics and variation of tailings dam saturation line. *Geomechanics Eng.* 23 (1), 85–92. doi:10.12989/gae.2020.23.1.085

Wang, G. J., Zhao, B., Wu, B. S., Wang, M. L., Liu, W. L., Zhou, H. M., et al. (2022a). Research on the macro-mesoscopic response mechanism of multisphere approximated heteromorphic tailing particles. *Lithosphere* 2022 (10), 1977890. doi:10.2113/2022/1977890

Wang, G. J., Zhao, B., Wu, B. S., Zhang, C., and Liu, W. L. (2023). Intelligent prediction of slope stability based on visual exploratory data analysis of 77 *in situ* cases. *Int. J. Min. Sci. Technol.* 33 (1), 47–59. doi:10.1016/j.ijmst.2022.07.002

Wang, H., Li, H., Tang, L., Ren, X., Meng, Q., and Zhu, C. (2022b). Fracture of two three-dimensional parallel internal cracks in brittle solid under ultrasonic fracturing. *J. Rock Mech. Geotechnical Eng.* 14 (3), 757–769. doi:10.1016/j.jrmge.2021.11.002

Wang, Q., Xu, S., Xin, Z. X., He, M. C., Wei, H. Y., and Jiang, B. (2022c). Mechanical properties and field application of constant resistance energy-absorbing anchor cable. *Tunn. Undergr. Space Technol.* 125, 104526. doi:10.1016/j.tust.2022.104526

Wang, Z. Y., Gu, D. M., and Zhang, W. G. (2020b). Influence of excavation schemes on slope stability: A DEM study. *J. Mt. Sci.* 17 (6), 1509–1522. doi:10.1007/s11629-019-5605-6

Wei, M. H. (2015). Anti-dip layered slope deformation and failure mode of formation thickness and other properties. *Sci. 'Technology Eng.* 15 (31), 141–146. doi:10.3969/j.issn.1671-1815.2015.31.026

Weng, M. C., Chang, C. Y., Jeng, F. S., and Li, H. H. (2020). Evaluating the stability of anti-dip slate slope using an innovative failure criterion for foliation. *Eng. Geol.* 275, 105737. doi:10.1016/j.enggeo.2020.105737

Wu, S. S., Zhao, G. F., and Wu, B. S. (2022). Real-time prediction of the mechanical behavior of suction caisson during installation process using GA-BP neural network. *Eng. Appl. Artif. Intell.* 116, 105475. doi:10.1016/j.engappai.2022.105475

Xie, L. F., Zhu, Q. Y., Qin, Y. J., Wang, J. H., and Qian, J. G. (2020). Study on evolutionary characteristics of toppling deformation of anti-dip Bank Slope based on energy field. *Sustainability* 12 (18), 7544. doi:10.3390/su12187544

Xu, W. J., Wang, L., and Cheng, K. (2022). The failure and river blocking mechanism of large-scale anti-dip rock landslide induced by earthquake. *Rock Mech. Rock Eng.* 55 (8), 4941–4961. doi:10.1007/s00603-022-02903-x

Zheng, Z., Su, G. S., Jiang, Q., Pan, P. Z., Huang, X. H., and Jiang, J. Q. (2022). Mechanical behavior and failure mechanisms of cylindrical and prismatic rock specimens under various confining stresses. *Int. J. Damage Mech.* 31 (6), 864–881. doi:10.1177/10567895221083997

Zhu, C., He, M. C., Karakus, M., Cui, X. B., and Tao, Z. G. (2020). Investigating toppling failure mechanism of anti-dip layered slope due to excavation by physical modelling. *Rock Mech. Rock Eng.* 53 (11), 5029–5050. doi:10.1007/s00603-020-02207-y

frontiers | Frontiers in Earth Science

TYPE Methods
PUBLISHED 23 March 2023
DOI 10.3389/feart.2023.1163187

OPEN ACCESS

EDITED BY
Guangjin Wang,
Kunming University of Science and Technology, China

REVIEWED BY
Peng Shoujian,
Chongqing University, China
Wang Xueb-bin,
Liaoning Technical University, China

*CORRESPONDENCE
Ke-gang Li,
106146135@qq.com

SPECIALTY SECTION
This article was submitted to Environmental Informatics and Remote Sensing, a section of the journal Frontiers in Earth Science

RECEIVED 10 February 2023
ACCEPTED 03 March 2023
PUBLISHED 23 March 2023

CITATION
Lou Y-h and Li K-g (2023), A rockburst grade evaluation method based on principal component analysis and the catastrophe progression method. *Front. Earth Sci.* 11:1163187. doi: 10.3389/feart.2023.1163187

A rockburst grade evaluation method based on principal component analysis and the catastrophe progression method

Ying-hao Lou[1,2] and Ke-gang Li[2,3]*

[1]Faculty of Public Safety and Emergency Management, Kunming University of Science and Technology, Kunming, China, [2]Yunnan Key Laboratory of Sino-German Blue Mining and Utilization of Special Underground Space, Kunming, China, [3]School of Land and Resources Engineering, Kunming University of Science and Technology, Kunming, China

Rockburst disasters always have a great influence on engineering practice. In order to accurately predict the occurrence of rockburst hazards, this paper proposes a rockburst rating evaluation method based on principal component analysis (PCA) and the catastrophe progression method, taking into account several influencing factors. In this paper, 15 indicators, such as strength brittleness factor (R), stress factor (P), and rock quality index (RQD) (reflecting the strength and fragmentation degree of rock mass), were selected from seven samples and were analyzed and downscaled by principal component analysis. Combined with the catastrophe progression method, each layer index was dimensionless and normalized to determine the mutation level value of each layer. Based on the principle of complementarity or non-complementarity, to determine the total mutation level value, the layer index was used to divide the rockblast-level interval and predict the rockblast level. The results show that the method proposed in this paper can be used to not only distinguish the importance of each of the same level of indicators but also avoid the impact of superimposed factor correlations between the same level of indicators, making the results more objective. This paper presents accurate rock explosion assessment results and an actual engineering situation. The number of factors affecting the assessment of the rock explosion level provides new insights.

KEYWORDS

principal component analysis, catastrophe progression method, rockburst classification, prediction, multi-factor, predictive models

1 Introduction

Many engineering geological disasters have been encountered in modern engineering, such as tailings dam break (Wang et al., 2022a; Wang et al., 2022b; Wang et al., 2019; Lin et al., 2022) and rockburst. A rockburst is a complex rock destabilization phenomenon affected by a variety of factors. A rockburst occurs with a strong destructive force, and rockburst hazards occur with sudden changes. During underground excavation, in a high-stress environment, the sudden unloading of energy from hard rocks can lead to the ejection of peripheral rocks, causing serious damage to equipment and engineers (Rehman et al., 2021). The severity of damage caused by rockbursts can be affected by factors such as excavation depth and stress levels (Naji et al., 2019), and the prediction of rockburst hazards becomes particularly important.

Rockburst hazard predictions can be broadly divided into two types—single-indicator and multiple-indicator—while the prediction of indicators of multiple factors can determine various factors of rockburst occurrence, making the discrimination more comprehensive. Using the maximum shear stress in the surrounding rock, uniaxial compressive strength and six other indicators were combined with the principles of the principal component analysis and probabilistic neural network analysis of multiple rockburst cases to predict the level of rock bursts (WU et al., 2018). Considering the fuzzy nature of rockburst grading predictions, combined with an SOFM (self-organizing feature mapping) neural network, a rockburst prediction model was established (YANG et al., 2021). CNNs (convolutional neural networks) were combined with LSTM (long short-term memory) to first predict the future state of the rockburst indicator eigenvolume, and this was then combined with the particle swarm algorithm to optimize the generalized neural network to predict the future state of the rockburst level (LIU et al., 2021a). Principal component analysis and the fuzzy integrated evaluation method were used for rockburst prediction (PU et al., 2018). These methods are multi-indicator rockburst comprehensive evaluation methods that take into account uncertainties in rockburst predictions, and they include the interval fuzzy comprehensive evaluation method (WANG et al., 2019), fuzzy object element model (WANG et al., 2015), and attribute recognition model (He et al., 2020). There are also some better but not used methods for rockburst prediction such as real-time prediction using GA-BP neural networks (Wu et al., 2022).

In summary, numerous researchers have refined the theory of rockburst predictions from different perspectives. However, most of the existing literature on rockburst predictions only takes into account a few factors affecting the occurrence of rockbursts or only takes into account the random nature of the occurrence of rockbursts and does not combine this irregularity and the occurrence of a variety of factors affecting rockburst hazards, so rockburst predictions are limited. As the occurrence of rockbursts is usually irregular and uncertain, and there is a certain degree of ambiguity and randomness in the process of taking and evaluating rockburst indicators (LIANG and Guoyan, 2021), rockburst predictions should be combined with the conditions of rockburst occurrences and the problem of non-linearity of data between samples and indicators. The catastrophe progression method cited in this paper does not need to assign weights to the indicators, which greatly reduces the subjectivity of the judging system and makes the results more scientific; but the catastrophe progression method does need to differentiate the importance of indicators at the same level, so this paper uses principal component analysis to assist in the evaluation. The catastrophe progression method mostly uses a low-dimensional data model, and under the influence of multiple indicators, the dimensionality of indicators is reduced by principal component analysis, and the dimensionality is reduced to several composite variables to replace the original multiple variables, so as to meet the needs of the catastrophe progression method model, ensuring more objective results.

2 Principle of the method

2.1 Principal component analysis

The occurrence of rock blasts is subject to a variety of factors acting together. As a result, the impact of rock blast occurrences is far-reaching. In order to eliminate the impact of superimposed factors between the same level of indicators, so that they are independent of each other while reflecting the information contained in the original data, the number of variables is reduced, but the main information is also highlighted, simplifying the relationship between indicators. Principal component analysis is widely used to reduce the dimensionality of data, mainly using linear algebra methods and theories to discover the most important parts of the data, and is used to replace the original data, so that the original data are moved into a new independent comprehensive dataset (LIU et al., 2021b). That is, a small number of uncorrelated quantities relative to the original data sample carry enough information to reflect the information about the process operating conditions contained in a large number of process variables (LIANG et al., 2016). That is, the potential data aggregation of the predictors can be analyzed by principal component analysis (Wang et al., 2023), as in the following equation:

$$\begin{aligned} y_1 &= p_{11}x_1 + p_{12}x_2 + \ldots + p_{1m}x_m = {p_1}^{T}x, \\ y_2 &= p_{21}x_1 + p_{22}x_2 + \ldots + p_{2m}x_m = {p_2}^{T}x, \\ &\vdots \\ y_m &= p_{m1}x_1 + p_{m2}x_2 + \ldots + p_{mm}x_m = {p_m}^{T}x. \end{aligned} \tag{1}$$

The basic steps of principal component analysis are as follows:

(1) For the matrix X:

$$X = \begin{bmatrix} X_{12}X_{12}\cdots X_{1m} \\ X_{21}X_{22}\cdots X_{2m} \\ \cdots\cdots\cdots\cdots \\ X_{n1}X_{n2}\cdots X_{nm} \end{bmatrix} = \left(X_{ij}\right)_{n\times m}. \tag{2}$$

Normalization of the input sample data:

$$X_{ij}' = \left(X_{ij} - \bar{X}_j\right)/S_j, \tag{3}$$

where

$$X_j = \frac{1}{n}\sum_{i=1}^{n} X_{ij}. \tag{4}$$

$$S_j = \sqrt{\frac{1}{n-1}\sum_{i=1}^{n}\left(X_{ij} - \overline{X_j}\right)^2}. \tag{5}$$

(2) Calculation of the symmetric matrix of correlation coefficients after normalization:

$$R = \begin{bmatrix} r_{12}r_{12}\cdots r_{1m} \\ r_{21}r_{22}\cdots r_{2m} \\ \cdots\cdots\cdots\cdots \\ r_{n1}r_{n2}\cdots r_{nm} \end{bmatrix}. \tag{6}$$

Calculation of correlation coefficients between variables r_{jk}:

$$r_{jk} = \frac{\sum_{k=1}^{n}\left(x_{ki}' - \overline{x_i}'\right)\left(x_{kj}' - \overline{x_j}'\right)}{\sqrt{\sum_{k=1}^{n}\left(x_{ki}' - \overline{x_i}'\right)^2\sum_{k=1}^{n}\left(x_{kj}' - \overline{x_j}'\right)}}. \tag{7}$$

(3) Finding the eigenvalues and eigenvectors of R: $\lambda_1, \lambda_2, \cdots, \lambda_m$, $p_1, p_2, \cdots, p_m$

(4) Calculation of the main element:

$$t_i = Xp_i. \tag{8}$$

TABLE 1 Common mutation models.

Mutation model	Control variable	Potential function	Normalization formula
Fold	1	$F(x) = x^3 + ax$	$x_a = a^{1/2}$
Cusp	2	$F(x) = x^4 + ax^2 + bx$	$x_a = a^{1/2}, x_b = b^{1/3}$
Swallow-tail	3	$F(x) = x^5 + ax^3 + bx^2 + cx$	$x_a = a^{1/2}, x_b = b^{1/3}, x_c = c^{1/4}$
Butterfly	4	$F(x) = x^6 + ax^4 + bx^3 + cx^2 + dx$	$x_a = a^{1/2}, x_b = b^{1/3}, x_c = c^{1/4}, x_d = d^{1/5}$
Wigwam	5	$F(x) = x^7 + ax^5 + bx^4 + cx^3 + dx^2 + ex$	$x_a = a^{1/2}, x_b = b^{1/3}, x_c = c^{1/4}, x_d = d^{1/5}, x_e = e^{1/6}$

[a]F(x) is the potential function, and (a,b,c,d,e) is the control variable for the state variable.

(5) Calculation of the contribution rate and cumulative contribution rate of each principal component:

$$\text{Contribution rate} = \frac{\lambda_i}{\sum_{k=1}^{m}\lambda_k} (i = 1, 2, \cdots, m). \quad (9)$$

$$\text{Cumulative contribution rate} = \frac{\sum_{s=1}^{i}\lambda_s}{\sum_{k=1}^{m}\lambda_k} (i = 1, 2, \cdots, m). \quad (10)$$

2.2 Catastrophe progression method

The catastrophe progression method is a comprehensive evaluation method developed on the basis of mutation theory. Mutation types exist in theory in many ways, but for reasons such as normalization, the values are too small to be ignored when the number of control variables exceeds five (CUI and Shasha, 2022). The catastrophe progression method is based on the potential function, and the evaluation indexes are dimensionless. Each index is then integrated from a low level to a high level, and for the same index, the principle of integrated evaluation is adopted to find out the value of each level affiliation function separately. The total affiliation value is calculated using a normalization formula.

(1) Determination of the mutation model:

The selected target is analyzed to determine the desired mutation model. There are five main models of mutation that are commonly used (Zhang et al., 2018a; Zhang et al., 2018b; LUO et al., 2018), which are shown in Table 1.

(2) Dimensionless processing of parameter indicators:

The comprehensive evaluation indicators can be divided into two types: positive indicators and negative indicators. With positive indicators, the larger the data, the better the predictions will be; with negative indicators, the smaller the data, the better the predictions will be. Positive and negative indicators are calculated as shown in Eqs 11, 12, respectively:

$$x_i' = \frac{x_i - x_{min}}{x_{max} - x_{min}}, \quad (11)$$

$$x_i' = \frac{x_{max} - x_i}{x_{max} - x_{min}}. \quad (12)$$

Here, x_i' is the dimensionless processed data, x_i is the original parameter, and x_{max} and x_{min} are the maximum and minimum values in the sample data of a single variable, respectively.

(3) Calculation of mutation-level values.

The values obtained using the normalization formula for different indicators of the same control variable can take three principles: the principle of complementarity, the principle of non-complementarity, and the principle of complementarity after over-queuing. The first two principles are used in this paper, and the formulas for the principle of complementarity and the principle of non-complementarity are as follows:

$$x = \frac{(x_1 + x_2 + x_3 + \cdots x_i)}{i} (i = 1, 2, 3, 4, \cdots), \quad (13)$$

$$x = \min\{x_1, x_2, x_3, \cdots, x_i\}. \quad (14)$$

Here, X is the state variable and $(x_1, x_2, x_3, \ldots x_i)$ is the controlling variable.

2.3 The rockburst evaluation index system

In this paper, 15 variable indicators and seven sets of data are selected from three aspects of lithology conditions, stress conditions, and surrounding rock conditions to construct an evaluation model (LIANG, 2004; JIANG et al., 2010; Qi-tao et al., 2014; Yu, 2016; LI et al., 2020), as shown in Figure 1.

The main steps of the rockburst evaluation are as follows:

(1) Principal component analysis is used at the same level to reduce the dimensionality of the impact factor indicators while dividing several principal components.
(2) Dimensionless processing of the data is performed, and the desired mutation model is selected according to the number of indicators.
(3) The reduced-dimensional indicators are ranked according to the absolute value of the coefficients of the principal component score matrix and then brought into the mutation model for calculation.
(4) Mutation-level values for each level are calculated to determine the total mutation-level values according to the principles of complementarity and non-complementarity.
(5) The resulting value of the total mutation level is used to divide the rockburst grade interval and compare it with the actual project.

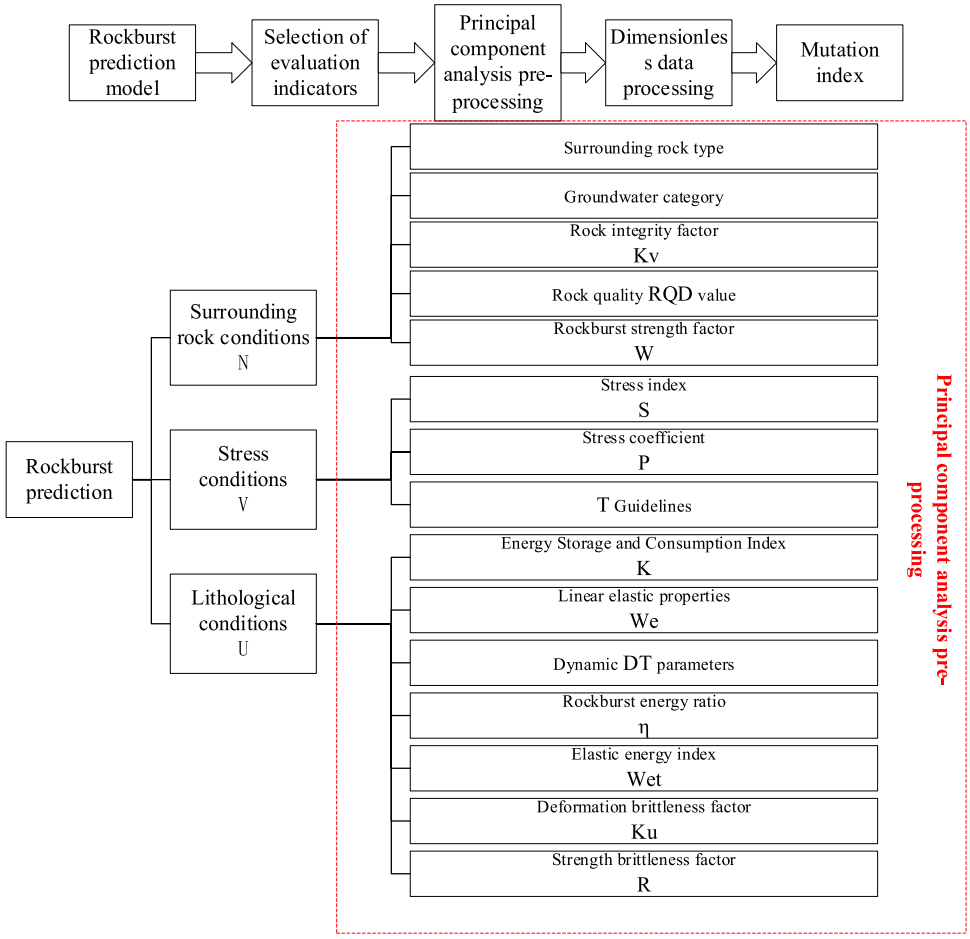

FIGURE 1
Overall evaluation system.

Lithological conditions mainly include strength brittleness factor R, deformation brittleness factor Ku, elastic energy index Wet, rockburst energy ratio η, dynamic DT parameters, linear elastic properties We, and energy storage and consumption index K. Stress conditions mainly include T guidelines, stress coefficient P, and stress index S. Surrounding rock conditions mainly include rockburst strength factor W, rock quality RQD value, rock integrity factor Kv, groundwater category, and surrounding rock type (where the types of surrounding rock were I, II, III, IV, and V, and the groundwater categories were gushing water, line flow, dripping water, and no groundwater).

3 Rockburst prediction model based on the PCA–catastrophe progression method

To validate the model, the data of selected indicators are shown in Table 2.

3.1 Rockburst prediction index division and ranking

Taking the stress condition as an example for principal component analysis, the original data were standardized before conducting the principal component analysis. The results are shown in Table 3.

Two principal components, F2 and F3, were extracted, generally taking indicators with loadings greater than 0.7, from which it can be concluded that the extracted principal component F2 includes T guidelines and stress index S. Principal component F3 includes stress coefficient P. The ranking of the indicators under the principal components by the magnitude of the absolute value of the coefficients of the principal component score matrix is derived from the principal component F1: T guidelines > stress index S. The numerical results are shown in Tables 4, 5.

Principal component F3 has only one indicator, so sorting is not necessary. The rockburst evaluation system is shown in Figure 2.

TABLE 2 Rockburst evaluation indexes of each project.

Project name	R	Ku	Wet	η	DT	We	K	T	P	S	W	RQD	Kv	Surrounding rock type	Groundwater category
Diversion tunnel of the Tianshengqiao II Hydropower Station	23.97	7.8	6.6	0.043	89	134.12	105.23	0.63	0.34	0.18	0.92	0.6	0.63	3.5	4.02
Yuzi River Hydropower Station diversion tunnel	15.04	9.5	9	0.048	78	123.03	110.56	0.6	0.53	0.24	1.6	0.68	0.69	4	4.2
Jinping II Hydropower Station diversion tunnel	18.46	3.56	3.8	0.037	279	56.23	36.77	0.45	0.82	0.23	1.62	0.62	0.62	3.38	3.89
Ertan Hydropower Station 2# branch hole	29.73	2.56	7.3	0.036	356	48.67	25.45	0.32	0.41	0.13	0.32	0.28	0.59	3	2.03
Taipingyi Hydropower Station diversion tunnel	17.55	8.36	9	0.045	69	120.56	125.67	0.69	0.38	0.24	0.99	0.63	0.61	4	3.95
Pubugou Hydropower Station underground refuge	20.5	2.48	5	0.034	278	78.35	36.26	0.36	0.35	0.13	0.89	0.26	0.58	2.64	1.56
Underground plant of the Laxiwa Hydropower Station	24.11	2.63	9.3	0.035	296	49.67	23.36	0.47	0.32	0.16	0.78	0.29	0.54	2.36	1.89

TABLE 3 Total variance interpretation.

Ingredient	Initial eigenvalue		Extraction of the sum of squares of loads				Sum of squared rotating loads		
	Total	Percentage of variance	Cumulative %	Total	Percentage of variance	Cumulative %	Total	Percentage of variance	Cumulative %
1	1.887	62.904	62.904	1.887	62.904	62.904	1.678	55.941	55.941
2	1.083	36.086	98.990	1.083	36.086	98.990	1.291	43.049	98.990
3	0.030	1.010	100						

TABLE 4 Component matrix.

Indicator	Ingredient	
	1	2
T	0.992	0.031
S	0.788	−0.608
P	0.531	0.844

TABLE 5 Component score coefficient matrix.

Indicator	Ingredient	
	1	2
T	0.645	−0.271
P	−0.155	0.814
S	0.438	0.292

3.2 Determination of the sudden change level of rockburst predictors

(1) Determination of third-level catastrophe-level values

The determination of the catastrophe-level values first requires dimensionless processing of the raw data. The original data is dimensionless and processed according to Eqs 11, 12. Due to the limited space of the article, this paper selects the indicators of the Tianshengqiao II Hydropower Station Diversion Tunnel to specify the catastrophe-level value method. The processed data are shown in Table 6.

Normalization of dimensionless processed data: Taking the stress condition as an example, two indicators, T and S, under F2 are used to select the normalized formula for the cusp, and one variable, P, under F3 is used to select the fold:

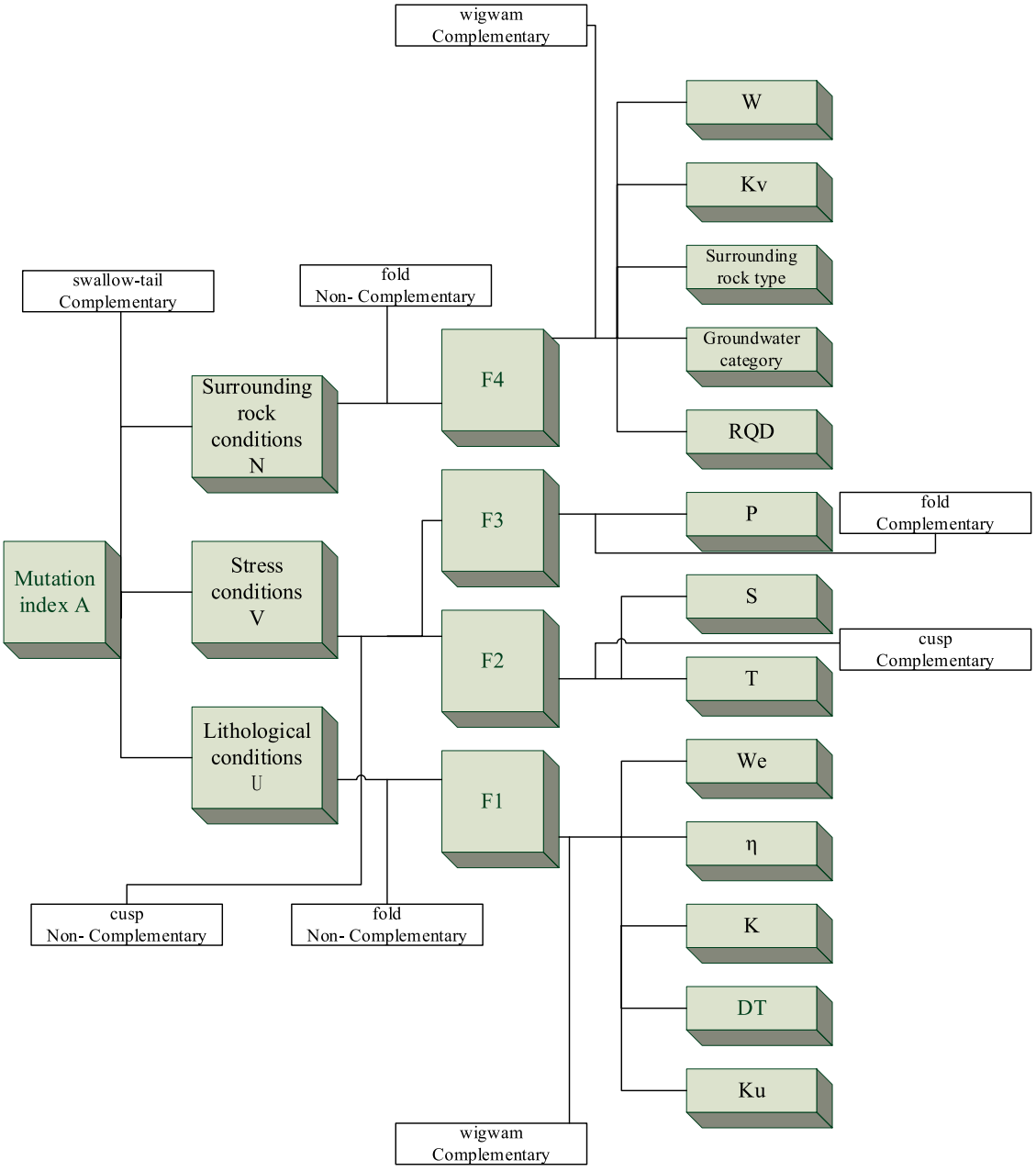

FIGURE 2
Rockburst evaluation system of the principal component analysis–catastrophe progression method.

$x_T = 0.837838^{1/2} = 0.915335, x_s = 0.454545^{1/3} = 0.768881.$

The complementarity principle is satisfied under the F2 condition, and catastrophe-level values of F2 are calculated according to Eq. 13:

$$V_{F2} = \frac{x_T + x_S}{2} = 0.842108.$$

Only one indicator exists under the F3 condition, from which the mutation level can be derived:

$$V_{F3} = 0.04^{1/2} = 0.02.$$

Similarly, calculated under the lithology condition, five indicators exist under the F1 condition, and the normalized formula for the Wigwam is calculated in turn as follows:

$x_{Ku} = 0.757835^{1/2} = 0.870537, x_{DT} = 0.930314^{1/3} = 0.97621,$
$x_K = 0.800215^{1/4} = 0.945804, x_\eta = 0.5625^{1/5} = 0.891301, x_{We} = 1^{1/6} = 1.$

The F1 condition satisfies the principle of complementarity, and the catastrophe-level values in F1 are calculated:

TABLE 6 Data after dimensionless processing.

Indicator	Diversion tunnel of the Tianshengqiao II Hydropower Station
R	0.607897
Ku	0.757835
Wet	0.597615
η	0.5625
DT	0.930314
We	1
K	0.800215
T	0.837838
P	0.04
S	0.454545
W	0.461538
RQD	0.809524
Kv	0.6
Surrounding rock type	0.695122
Groundwater category	0.931818

TABLE 7 Third-level catastrophe-level values of each project.

Project name	Third-level catastrophe-level values			
	U_{F1}	V_{F2}	V_{F3}	N_{F4}
Diversion tunnel of the Tianshengqiao II Hydropower Station	0.936771	0.842108	0.2	0.914308
Yuzi River Hydropower Station diversion tunnel	0.980203	0.934959	0.648074	0.999484
Jinping II Hydropower Station diversion tunnel	0.604381	0.780739	1	0.93099
Ertan Hydropower Station 2# branch hole	0.228913	0	0.424264	0.474778
Taipingyi Hydropower Station diversion tunnel	0.962924	1	0.34641	0.932001
Pubugou Hydropower Station underground refuge	0.41641	0.164399	0.244949	0.456423
Underground plant of the Laxiwa Hydropower Station	0.358102	0.642607	0	0.321655

$$U_{F1} = \frac{x_{KU} + x_{DT} + x_K + x_\eta + x_{We}}{5} = 0.936771.$$

Calculated under the surrounding rock conditions and under the same lithological conditions, there are five indicators, according to the complementary principle, used to calculate the mutation level of F4:

$$N_{F4} = \frac{x_{RDQ} + x_{Groundwater\ category} + x_{Surrounding\ rock\ type} + x_{Kv} + x_W}{5} = 0.914308.$$

The calculated data for all the indicators of the seven projects are shown in Table 7.

(2) Determination of the second-level catastrophe-level values and first-level catastrophe-level values.

According to the aforementioned calculation process, the second-level catastrophe-level values can be calculated, and the specific data are shown in Table 8.

Under the stress condition, there are two variables, F2 and F3, that need to be accounted for, according to the principle of non-complementarity. The second-level catastrophe-level values are derived according to Eq. 14:

$$V' = \min\{V_{F2}, V_{F3}\}.$$

TABLE 8 Second-level catastrophe-level values and first-level catastrophe-level values of each project.

Second-level catastrophe-level values and first-level catastrophe-level values of each project				
Project name	U	V	N	A
Diversion tunnel of the Tianshengqiao II Hydropower Station	0.967869	0.584804	0.956194	0.936306
Yuzi River Hydropower Station diversion tunnel	0.990052	0.865383	0.999742	0.982633
Jinping II Hydropower Station diversion tunnel	0.777419	0.883594	0.964878	0.944134
Ertan Hydropower Station 2# branch hole	0.478448	0	0.689041	0.534263
Taipingyi Hydropower Station diversion tunnel	0.981287	0.702312	0.965402	0.956905
Pubugou Hydropower Station underground refuge	0.645299	0.405461	0.675591	0.816687
Underground plant of the Laxiwa Hydropower Station	0.598417	0	0.567146	0.547127

TABLE 9 Sample rockburst actual grade.

Project name	Rockburst actual grade
Diversion tunnel of the Tianshengqiao II Hydropower Station	III
Yuzi River Hydropower Station diversion tunnel	III~IV
Jinping II Hydropower Station diversion tunnel	II~III
Ertan Hydropower Station 2# branch hole	II
Taipingyi Hydropower Station diversion tunnel	III
Pubugou Hydropower Station underground refuge	II
Underground plant of the Laxiwa Hydropower Station	II

The second-level catastrophe-level values are calculated in the same way for the surrounding rock conditions and lithology conditions. The first-level catastrophe-level values are calculated by applying swallow-tail to lithological conditions, stress conditions, and envelope conditions and can be calculated according to the principle of complementarity:

$$U = U_{F1}^{1/2}, V = V'^{1/3}, N = N_{F4}^{1/4}.$$

The first-level catastrophe-level values are calculated by satisfying the complementarity principle:

$$A = \frac{U + V + N}{3}.$$

Table 9 shows the actual grade of the project rock explosion. According to Tables 8, 9, the sample rockburst total mutation-level value (A) is the horizontal coordinate and the actual occurrence level of rockburst is the vertical coordinate. The scatter plot is shown in Figure 3.

As shown in Figure 3, rockbursts are divided into four intervals: level I [0, 0.5], level II [0.5, 0.82], level III [0.82, 0.96], and level IV [0.96, 1.00].

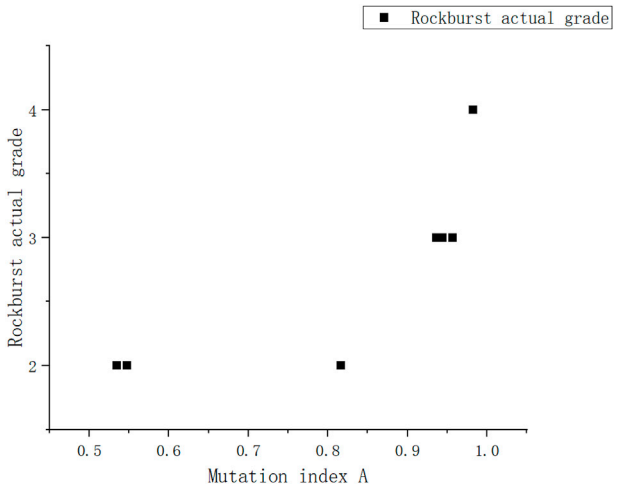

FIGURE 3
Mutation value and rockburst level relationship.

4 Model testing

In order to verify the accuracy of the model, the actual rockblast data on the Baihetan Hydropower Station from the literature (Dong et al., 2018) were brought into the model for verification, and the results are shown in Table 10. It can be seen that the actual rockblast level compared with the sample is consistent.

TABLE 10 Rockburst level prediction.

	Project name	Baihetan Hydropower Station
Third-level catastrophe-level values	U_{F1}	0.655874
	V_{F2}	0.626008
	V_{F3}	0.860233
	N_{F4}	0.680269
Second-level catastrophe-level values and first-level catastrophe-level values	U	0.809861
	V	0.791207
	N	0.824784
	A	0.925937
Rockburst actual grade		II~III
Prediction level		III

5 Comparison and discussion

1 According to the literature (LI et al., 2022), compared to the matter–element extension model rockburst prediction method, although the results of the actual rockburst level of the Baihetan Hydropower Station were validated to be consistent, the method proposed in this paper based on principal component analysis does not use subjective assignment to give the appropriate weight to the influencing factors, but rather a number of variables to reduce the dimensionality of the variables in line with the basic model of the catastrophe progression method. It overcomes subjective thinking and is more convincing.

2 To a certain extent, the method proposed in this paper requires more accurate engineering practice data and data on various factors affecting rock bursts in actual engineering. If the data are incomplete, variations in results arise, so this method has some limitations. In addition to relying on accurate data, it is also necessary to process a large number of data, which will also affect the accuracy of the results in engineering practice.

6 Conclusion

1 In this paper, considering various factors affecting rockbursts, the variable dimension reduction based on the principal component analysis method meets the basic model requirements of the catastrophe progression method, and through the combination of the two methods, the defects of general fuzzy algorithm are reduced, the accuracy of calculation results is satisfied objectively, and the subjectivity in data processing is overcome.

2 The seven typical rockburst engineering examples based on this analysis and a comprehensive dataset of rockburst engineering examples to test the feasibility of the improved sudden change level method model for rockburst predictions show that it can be used for rockburst ratings. Finally, the accuracy of the model can be illustrated by establishing four rockburst grade intervals (level I [0, 0.5], level II [0.5, 0.82], level III [0.82, 0.96], and level IV [0.96, 1.00]) based on total mutation grade A.

Data availability statement

The original contributions presented in the study are included in the article/Supplementary Material; further inquiries can be directed to the corresponding author.

Author contributions

Y-hL: writing—original draft, data curation, and methodology. K-gL: writing—review and editing.

Conflict of interest

The authors declare that the research was conducted in the absence of any commercial or financial relationships that could be construed as a potential conflict of interest.

The handling editor GW declared a shared affiliation with the authors YL and KL.

Publisher's note

References

Cui, Tiejun, and Shasha, L. I. (2022). Method of determining system fault state level based on catastrophe progression and im-proved ahp. *Saf. Environ. Eng.* 03, 23–28. doi:10.1016/S1674-5264(09)60080-6

Dong, Y., Pei, X., Zhang, Y., Liang, Y., and Xi, Z. (2018). Prediction of rock burst-based on combination weighting and cloud model theory. *Chin. J. Undergr. Space Eng.* 14 (S1), 409–415. doi:10.1016/S1003-6326(16)64313-3

He, Y. F., Li, T. B., and Cao, H. Y. (2020). Attribute recognition model of fatalness assessment of rockburst in tunnel construction and its application. *Hydrogeology Eng. Geol.* 47 (2), 102–111. doi:10.16030/j.cnki.issn.1000-3665.201908002

Jiang, Q., Feng, X., Su, G., and Chen, G. (2010). Stability analysis of large underground caverns in Laxiwa hydropower plant under high crustal stress. *J. Hydroelectr. Eng.* 29 (5), 132–140.

Li, J., Zhou, Z. H., and Ding, W. J. (2022). Prediction of rock burst proneness based on principal component matter-element extension model. *Industrial Minerals Process.* 51 (5), 7–12. doi:10.1016/j.ijrmms.2015.02.004

Li, M., Li, K., Qin, Q., Wang, T., Zhang, X., and Liu, Y. (2020). Judgment model of rock burst tendency based on improved combination weighting-TOPSIS method. *J. Saf. Sci. Technology* 16 (03), 74–80. doi:10.11779/CJGE201806013

Liang, Q., Han, H., Cui, X., and Gu, B. (2016). Fault diagnosis for refrigeration system based on PCA-PNN. *CIESC J.* 67 (03), 1022–1031. doi:10.11949/j.issn.0438-1157.20151301

Liang, W., and Guoyan, Z. H. A. O. (2021). A review of research on long-term and short-term rockburst risk evaluation in deep hard rock. *Chin. J. Rock Mech. Eng.* 29, 1–21. doi:10.1007/s11053-020-09664-w

Liang, Zhiyong (2004). *Study on the prediction and prevention of rockburst in the diversion tunnel of JinPing 1 hydropower*. Chengdu, China: Chengdu University of Technology.

Lin, S., Wang, G., Liu, W., Zhao, B., Shen, Y., Wang, M., et al. (2022). Regional distribution and causes of global mine tailings dam failures. *Metals* 12 (6), 905. doi:10.3390/met12060905

Liu, H., Xu, F., and Liu, B. (2021). Time-series prediction method for risk level of rockburst disaster based on CNN-LSTM. *J. Central South Univ. Technol.* 52 (3), 659–670. doi:10.1155/2019/7343784

Liu, X., Zhang, X., and Yang, W. (2021). Rockburst prediction based on pca-svm. *China Min. Mag.* 2021 (07), 176–180. doi:10.1155/2021/7968730

Luo, Z., Kui, L. I., An, Y., Li, H., and Fu, W. (2018). Risk assessment of gas explosion based on improved catastrophe progression method. *Saf. Coal Mines* 49 (06), 246–250. doi:10.3390/pr11020554

Naji, A. M., Rehman, H., Emad, M. Z., Ahmad, S., Kim, J., and Yoo, H. (2019). Static and dynamic influence of the shear zone on rockburst occurrence in the headrace tunnel of the neelum jhelum hydropower project, Pakistan. *Energies* 12, 2124. doi:10.3390/en12112124

Pu, Y., Apel, D., and Xu, H. (2018). A principal component analysis/fuzzy comprehensive evaluation for rockburst potential in kimberlite. *Pure Appl. Geophys.* 175 (6), 2 141–142 151. doi:10.1007/s00024-018-1790-4

Qi-tao, P. E. I., Hai-bo, L. I., Liu, Y. Q., and Guo-kai1, Z. H. A. N. G. (2014). A grey evaluation model for predicting rockburst proneness based on combination weight and its application. *Rock Soil Mech.* 35 (S1), 49–56. doi:10.1155/2019/3453614

Rehman, H., Naji, A. M., Nam, K., Ahmad, S., Muhammad, K., and Yoo, H. K. (2021). Impact of construction method and ground composition on headrace tunnel stability in the neelum–jhelum hydroelectric project: A case study review from Pakistan. *Appl. Sci.* 11, 1655. doi:10.3390/app11041655

Wang, C. L., Wu, A., Xiaohui, L., Lu, H., and Liu, X. (2015). Predicting rockburst tendency based on fuzzy matter-element model. *Int. J. Rock Mech. Min. Sci.* 75, 224–232. doi:10.1016/j.ijrmms.2015.02.004

Wang, G., Tian, S., Hu, B., Xu, Z., Chen, J., and Kong, X. (2019a). Evolution pattern of tailings flow from dam failure and the buffering effect of debris blocking dams. *Water*, 11, (11), 2388–2401. doi:10.3390/w11112388

Wang, G., Zhao, B., Lan, R., Liu, D., Wu, B., Li, Y., et al. (2022). Experimental study on failure model of tailing dam overtopping under heavy rainfall. *Lithosphere*, 2022, 5922501. doi:10.2113/2022/5922501

Wang, G., Zhao, B., Wu, B., Wang, M., Liu, W., Zhou, H., et al. (2022). Research on the macro-mesoscopic response mechanism of multisphere approximated heteromorphic tailing particles. *Lithosphere* 2022 (10), 1977890. doi:10.2113/2022/1977890

Wang, G., Zhao, B., Wu, B., Zhang, C., and Liu, W. (2023). Intelligent prediction of slope stability based on visual exploratory data analysis of 77 *in situ* cases. *Int. J. Min. Sci. Technol.* 33 (1), 47–59. doi:10.1016/j.ijmst.2022.07.002

Wang, X., Li, S., Xu, Z., Hu, J., Li, Z., and Zhang, B. (2019b). An interval fuzzy comprehensive assessment method for rock burst in underground caverns and its engineering application. *Bull. Eng. Geol. Environ.*, 78(7):5161–5176. doi:10.1007/s10064-018-01453-3

Wu, S., Zhao, G., and Wu, B. (2022). Real-time prediction of the mechanical behavior of suction caisson during installation process using GA-BP neural network. *Eng. Appl. Artif. Intell.* 116, 105475. doi:10.1016/j.engappai.2022.105475

Wu, S., Zhang, C., and Chengzi, Q. (2018). Prediction of intensity classification of rockburst based on PCA-PNN principle. *J. China Coal Soc.* 44 (09), 2767–2776. doi:10.13225/j.cnki.jccs.2018.1519

Yang, Xiaobin, Pei, Yanyu, Cheng, Hongming, Hou, Xin, and Lv, Jiaqi (2021). Prediction method of rockburst intensity grade based on SOFM neural network model. *Chin. J. Rock Mech. Eng.* 40 (S1), 2708–2715.

Yu, Qun (2016). *Study on rockburst Nucleation process and Early Warning method of Deep-buried Tunnels*. Dalian, China: Dalian University of Technology.

Zhang, H., Qiu, B., Tang, M., and He, M. (2018). Risk assessment model of agricultural products cold chain logistics based on the improved catastrophe progression method. *J. Syst. Eng.* 33 (03), 412–421. doi:10.1108/imds-03-2016-0098

Zhang, T., Li, J., and Liao, W. (2018). The mutation progression method is applied in the prediction of tunnel rock burst level. *Highway* 63 (09), 316–320. doi:10.1155/2021/8248443

frontiers | Frontiers in Earth Science

TYPE Original Research
PUBLISHED 30 March 2023
DOI 10.3389/feart.2023.1156114

OPEN ACCESS

EDITED BY
Wenzhuo Cao,
Imperial College London,
United Kingdom

REVIEWED BY
Chun Zhu,
Hohai University, China
Mohammad Azarafza,
University of Tabriz, Iran

*CORRESPONDENCE
Gang Deng,
dgang@iwhr.com

SPECIALTY SECTION
This article was submitted to Environmental Informatics and Remote Sensing,
a section of the journal
Frontiers in Earth Science

RECEIVED 01 February 2023
ACCEPTED 20 March 2023
PUBLISHED 30 March 2023

CITATION
Hou W, Wen Y, Deng G, Zhang Y and Wang X (2023), A multi-target prediction model for dam seepage field.
Front. Earth Sci. 11:1156114.
doi: 10.3389/feart.2023.1156114

A multi-target prediction model for dam seepage field

Weiya Hou, Yanfeng Wen, Gang Deng*, Yanyi Zhang and Xiangnan Wang

State Key Laboratory of Simulation and Regulation of Water Cycle in River Basin, China Institute of Water Resources and Hydropower Research, Beijing, China

Prediction of dam behavior based on monitoring data is important for dam safety and emergency management. It is crucial to analyze and predict the seepage field. Different from the mechanism-based physical models, machine learning models predict directly from data with high accuracy. However, current prediction models are generally based on environmental variables and single measurement point time series. Sometimes point-by-point modeling is used to obtain multi-point prediction values. In order to improve the prediction accuracy and efficiency of the seepage field, a novel multi-target prediction model (MPM) is proposed in which two deep learning methods are integrated into one frame. The MPM model can capture causal temporal features between environmental variables and target values, as well as latent correlation features between different measurement points at each moment. The features of these two parts are put into fully connected layers to establish the mapping relationship between the comprehensive feature vector and the multi-target outputs. Finally, the model is trained for prediction in the framework of a feed-forward neural network using standard back propagation. The MPM model can not only describe the variation pattern of measurement values with the change of load and time, but also reflect the spatial distribution relationship of measurement values. The effectiveness and accuracy of the MPM model are verified by two cases. The proposed MPM model is commonly applicable in prediction of other types of physical fields in dam safety besides the seepage field.

KEYWORDS

seepage field, multi-target prediction model (MPM), temporal features, latent correlation features, soft parameter sharing

1 Introduction

A dam is a complex and important water retaining structure in the field of hydraulic engineering. Because the dam possesses huge amounts of hydraulic energy, once it is broken, the flood will cause immeasurable damage to the lives and properties of people downstream. It is of great practical importance to know the operational behavior of the dam and predict its development through dam safety monitoring (Wu and Su, 2005; Jeon et al., 2009; Gu et al., 2016).

Two types of methods can be used to establish dam behavior prediction models: physics-driven methods and data-driven methods. Physics-driven methods mainly use finite element method to predict and analyze the physical field of the dam according to the constitutive model based on the physical and mechanical relationships of materials (Gu et al., 2011; Huang and Chen, 2012). The physics-driven methods essentially reveal the operational behavior of the main physical fields of the dam. However, these approaches place high demands on constitutive models, which limits the applicability of such approaches. Data-

TABLE 1 A summary of deep learning in dam behavior prediction.

Deep learning (DL) model	Application	Advantage	Limitations
Based on rough set theory and LSTM (Qu et al., 2019)	Concrete dam Deformation	Highest value based on accuracy, robustness, externality, and generalization; multipoint prediction	Result depend upon choice of inputs, and is noise sensitive
LSTM-based deep learning technique (Yang D. S. et al., 2020)	Concrete double-curved arch dam Deformation	Evaluated operation behavior of dams under different environmental factors; high accuracy	The suitable inputs are difficult to determine; single point prediction
Using a mixed attention mechanism and LSTM model (Ren et al., 2021)	Concrete gravity dam Displacement	Flexible and capable for adapting to highly complex interactions between the variables; accurately predicted the displacement behavior	Can result in inaccurate prediction due to anomaly; over-fitting in some cases
Using various DL and transfer learning techniques (Li et al., 2022)	High concrete parabolic double-curvature arch dam; Deformation	Can be applied in case of missing data, can model complex non-linear relationships; high accuracy and robustness	The input environment variables are excessive
Based on the CNN-GRU Model (Hua et al., 2023)	Concrete gravity dam; Uplift pressure	Improves the utilization rate of dam safety monitoring results	Over-fitting and single point prediction
Based on combined CNN and LSTM in parallel (This paper)	Earth dam and rockfill dam Seepage field	Multi-target prediction with high accuracy and efficiency, avoiding over-fitting; Simple operation and reliable precision	Suitable for normal operation period, other periods need to reverify

driven methods, which are based on regression analysis of historical monitoring data and influencing factors can be subdivided into two categories: One is the traditional statistical model (Fanelli, 1975; Bonelli and Royet, 2001; Deng et al., 2007), which is the most frequently used data-driven method in practical engineering applications due to its definite physical meaning and simple application. The statistical model physically explains and predicts dam behavior rules. However, this model needs to establish a functional relationship between effect variables (dependent variables) and influencing factors (independent variables) (Zhu et al., 2019; Liang et al., 2022; Tang et al., 2022) based on mathematical statistics theory. The selection of appropriate independent variables is difficult to determine because the operational behavior of the dam is affected by many complex factors and the influence of different factors on the behavior of the dam is unstable. All these factors lead to low prediction accuracy of the statistical model. The other is the most advanced machine learning method (Su et al., 2000). A more typical method is to use neural networks to establish complex non-linear and time-varying input-output relationships between effect variables and influencing factors. For example, Su et al. (2001) used the fuzzy neural network to establish the functional relationship between the horizontal displacement of the dam crest and water level, temperature, and time effect. Shi et al. (2020) used the radial basis function neural network optimized by the genetic algorithm to predict the seepage discharge of the concrete face rockfill dam. Hou et al. (2022) combined time series decomposition and deep learning to predict the deformation of high embankment dams. Azarafza et al. (2021), Azarafza et al. (2022), and Nikoobakht et al. (2022) have also done much research work based on deep learning to verify its advantages in landslide susceptibility assessment, landslide susceptibility mapping, and prediction of geotechnical features of rock materials. To give a brief summary, Table 1 is presented to describe about deep learning models, along with the application in dam behavior prediction, as well as their advantages and disadvantages. More information can be found in the literatures (Xu et al., 2019; Ren et al., 2021). From these studies, we can conclude that neural networks have a high potential for dam behavior prediction. However, due to the large amount of noise interference in the monitoring data, the prediction accuracy of the model is likely to be low due to overfitting. Moreover, the above data-driven methods are all for the prediction of single measurement point, which cannot well predict the main physical fields of dam behavior with multiple measurement points.

The single measurement point prediction model plays an important role in explaining the operation rules of the dam and implementing safety monitoring, but it does not involve the interconnection between multiple measurement points. It only reflects the structural state of the location of single measurement point, which has limitations. Even if multiple single measurement point prediction models are used to obtain predictions of multiple measurement points, the rules described by them are often not consistent and coordinated. Multiple target learning (MTL) (Caruana, 1993) is a modeling method that accounts for latent correlation between target values at multiple measurement points by sharing parameters and simultaneously predicts multiple target values in the physical field by training a model. Training multiple targets in parallel is equivalent to implicitly increasing the amount of training data, which reduces the risk of overfitting and improves the prediction accuracy and efficiency. The main parameter of sharing patterns in MTL models include hard parameter sharing (Caruana, 1993) and soft parameter sharing (Misra et al., 2016; Gao et al., 2019). Hard parameter sharing means that multiple target-specific output layers are maintained and all target values are forced to use the same parameters to obtain a common parameter model. Soft parameter sharing is simpler and more flexible than hard parameter sharing because each target is assigned its own set of parameters and the parameters are partially shared through some mechanism. The main difficulty in developing MTL models is the need to exploit correlations and differences between targets. The initial applications of MTL models for dam behavior prediction include: Yao et al. (2022) performed an improved multi-output support vector machine, and the

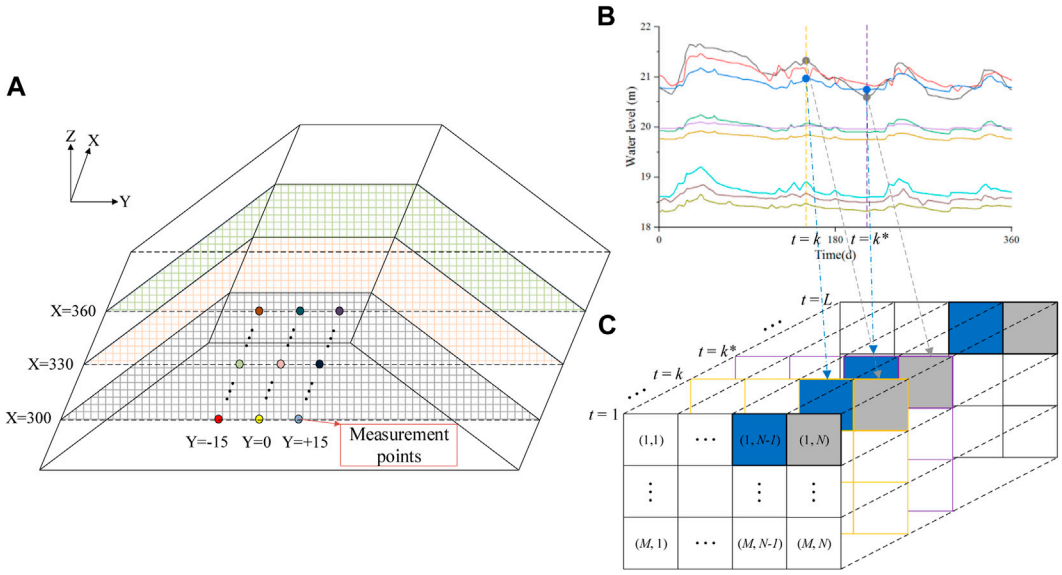

FIGURE 1
Similar trends and differences of target values. **(A)** Mesh. **(B)** Time series. **(C)** Data grids.

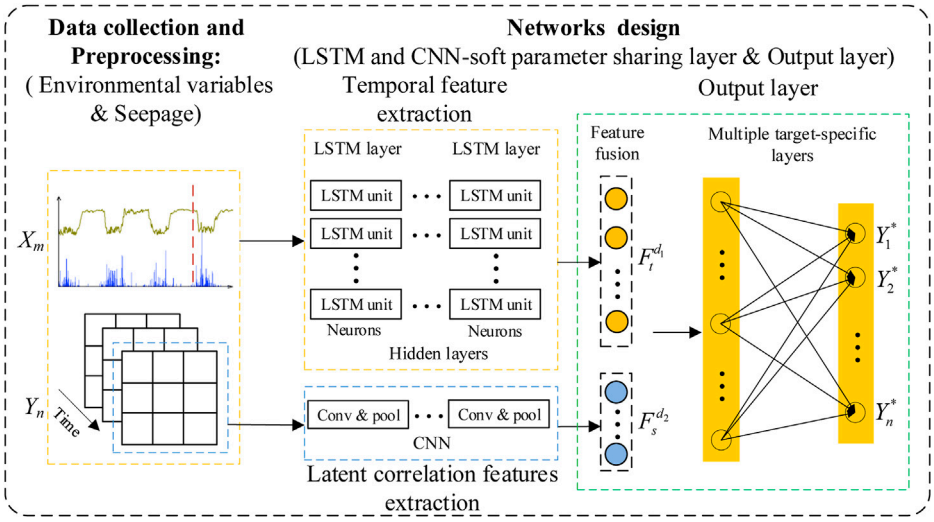

FIGURE 2
The framework of the MPM model.

improved model considered chaos and similarity of displacement series to simultaneously predict displacements of multiple measurement points with the same trend. Chen et al. (2022) proposed a serial model composed of convolutional neural networks and convolutional long short-term memory networks to extract spatial features from multiple measurement values and temporal features in time series in turn, and then simultaneously predict displacements of multiple measurement points. This method focused on statistical rules for target series without environmental variables.

In summary, there is a wealth of theoretical research results for dam behavior prediction models, but less research on the seepage field prediction based on deep learning. Seepage failure is one of the major causes of dam failure (Foster et al., 2000). The analysis and prediction of the seepage field has important implications for dam safety (Deng et al., 2020). The objective of this study is to establish an efficient and accurate the seepage field prediction model for the simultaneous prediction of seepage at multiple measurement points. It is well known that the response of dam seepage field to changes in environmental variables is non-synchronous, and the rules for the

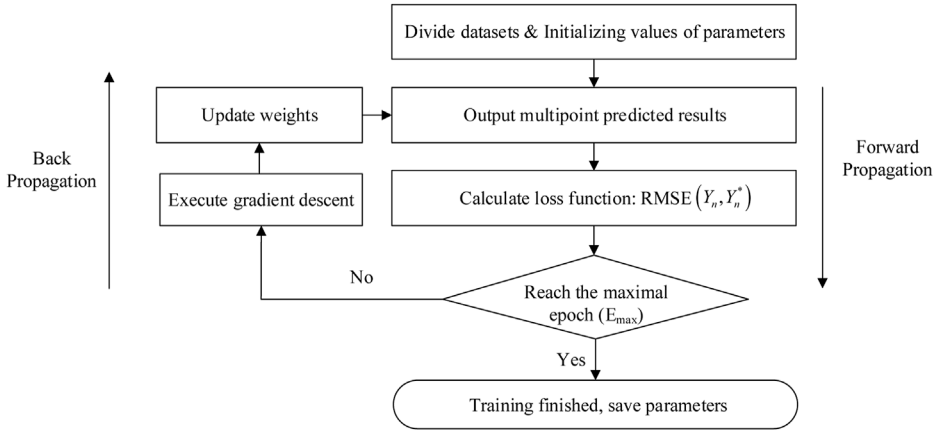

FIGURE 3
Flow chart of the MPM training process.

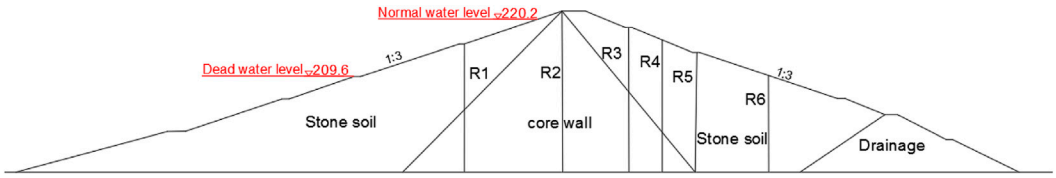

FIGURE 4
Piezometric tubes distribution of the Naban earth dam.

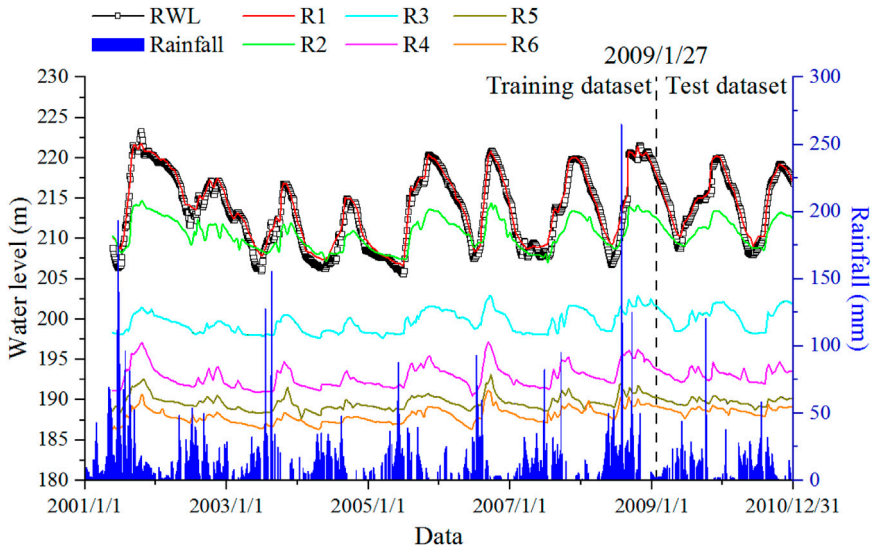

FIGURE 5
Time series of monitoring data.

TABLE 2 Setting of hyperparameters.

Parameters		Values
CNN Architecture	Convolutional layer 1	8
		Kernel: 2
		Stride: 1
		Padding: 1
	Convolutional layer 2	8
		Kernel: 3
		Stride: 1
		Padding: 1
	Maxpool	Kernel: 3×3
		Stride: 2×2
		Padding: 1
	Fully connect nodes	512
	Time step	1
	Activation function	Relu
LSTM Architecture	Hidden layers nodes	16
	Hidden layers	2
	Time step	12
	Activation function	Softmax
Output layer	Hidden layers	2
	Dropout rate	0.1
Training	Optimizer	Adam
	Loss function	RMSE
	Batch size	64
	Epochs	1,000
	Learning rate	0.001

temporal development of target values at different measurement points are related to the location of the measurement points. The longer the period and the smaller the variation of target values of points closer to the downstream, while those closer to the upstream are not (i.e., the variation trend of target values at different measurement points is similar but not the same at any one time). When multi-target prediction is performed and hard parameter sharing is applied, it forces the regularity of each measurement point at any time to be consistent, affecting prediction accuracy. Applying soft parameter sharing to learn the differences between target values can effectively improve the learning capacity of the model. Given its strong ability to capture local features for adjacent target values (Krizhevsky et al., 2012), the convolutional neural networks (CNN) model is introduced as the soft parameter sharing layer. Since the temporal variation trends of target values at different measurement points are highly similar and both target values and environmental variables have strong time series characteristics, the long short-term memory networks (LSTM) model, which is superior in processing sequential data, is introduced to extract causal temporal features between environmental variables and target values. For dam seepage prediction, no evidence has been found at present for using a combination of CNN and LSTM in parallel. Therefore, based on the causal relationship between external loads and seepage field distribution, this study combines CNN and LSTM in parallel to establish a novel multi-target prediction model (MPM) for simultaneous predictions at multiple measurement points. The MPM model can not only describe the variation regulation of measurement values with the change of load and time, but also reflect the spatial distribution relationship of measurement values by considering the correlation information among multiple measurement points, which is undoubtedly more comprehensive and real for correctly mastering the structural condition and variation rules of the whole dam. The MPM model improves prediction accuracy and efficiency while also achieving seepage field prediction. It is of great importance to effectively and safely manage reservoir operation, as well as to improve future planning for dam seepage problems.

2 The novel prediction model

2.1 The existing models adopted

2.1.1 Long-short term memory model

Long short-term memory networks (LSTM) (Hochreiter and Schmidhuber, 1997) are an extension of recurrent neural network designed to solve the problem of long-term dependencies and vanishing gradients. In LSTM, it can continuously learn short-term time changes and long-periodic variation rules (Hochreiter, 1998) due to its connection to hidden nodes. LSTM has a stronger temporal feature extraction capability and a faster training speed for time series (Zhao et al., 2021). Because of these characteristics, LSTM produced good performance in predicting dam behavior series (Zhao et al., 2021; Hou et al., 2022). LSTM is also one of the most widely adopted models for MTL models (Wan et al., 2021; Zong et al., 2022). For non-linear regression, LSTM can be used to obtain highly-accurate predictions, and its governing equation can be simplified as follows:

$$h_t, c_t = LSTM\left(x_t, h_{t-1}, c_{t-1}\right) \tag{1}$$

where $\boldsymbol{x}_t$ is the input vector, c is the memory cell, and h is the hidden layer.

The LSTM model in this paper contains multiple hidden layers (Luo et al., 2022) to extract deep causal temporal features. The output of the last hidden layer of LSTM is recorded as $F_t^{d_1}$ after flattening so as to facilitate feature fusion and connect fully connected layers.

2.1.2 Convolutional neural networks

Convolutional neural networks (CNN) (Hubel and Wiesel, 1959; LeCun and Bengio, 1995) are mainly used to process variables in Euclidean space (Hakim et al., 2021). The convolutional layer, the pooling layer, and the activation function of the CNN model are the core steps of feature extraction. The convolutional layers extract the different non-linear interaction

TABLE 3 Evaluation results of prediction models.

Measurement points	Metrics	LSTM-M	MPM	Relative improvement: P/%
R1	MSE/m	0.796	**0.201**	74.7
	RMSE/m	0.892	**0.448**	49.7
	MAE	0.638	**0.292**	54.2
	R^2	0.925	**0.981**	—
	MAPE/%	0.297	**0.136**	54.2
R2	MSE/m	0.202	**0.017**	91.5
	RMSE/m	0.449	**0.131**	70.9
	MAE	0.354	**0.102**	71.3
	R^2	0.910	**0.992**	—
	MAPE/%	0.168	**0.048**	71.3
R3	MSE/m	0.738	**0.023**	96.9
	RMSE/m	0.859	**0.151**	82.4
	MAE	0.723	**0.101**	86.0
	R^2	0.581	**0.987**	—
	MAPE/%	0.360	**0.050**	86.0
R4	MSE/m	0.501	**0.037**	92.6
	RMSE/m	0.708	**0.193**	72.7
	MAE	0.597	**0.124**	79.2
	R^2	−0.121	**0.917**	—
	MAPE/%	0.309	**0.064**	79.2
R5	MSE/m	0.166	**0.009**	94.8
	RMSE/m	0.407	**0.093**	77.2
	MAE	0.344	**0.063**	81.8
	R^2	−0.132	**0.941**	—
	MAPE/%	0.181	**0.033**	81.8
R6	MSE/m	0.627	**0.014**	97.8
	RMSE/m	0.792	**0.118**	85.1
	MAE	0.699	**0.087**	87.6
	R^2	−3.676	**0.896**	—
	MAPE/%	0.370	**0.046**	87.6

Note: the boldface indicates better performance.

relationship features of the input data by setting different convolution kernels. The pooling layer reduces redundant features by taking the maximum or average value of the data in the convolution kernel. The activation function reflects the mapping relationship between input and output in two adjacent layers, which provides neural networks with non-linearity capability.

In this paper, the CNN model is introduced to extract latent features between adjacent target values. The input is a data grid with multiple measurement values at each moment that is regularly arranged, and high-dimensional feature extraction is performed using a series of convolutions and maximum pooling subsampling. The activation function is the rectified linear unit (Relu). Finally, it is flattened into a one-dimensional feature vector $F_s^{d_2}$ to facilitate feature fusion and to connect fully connected layers.

2.2 The framework of the MPM model

The seepage field contains multiple measurement points that can be meshed at each moment to produce a series of data grids (Figure 1A). The position of the measurement points is indexed by coordinates, and there is at most one measurement value in each

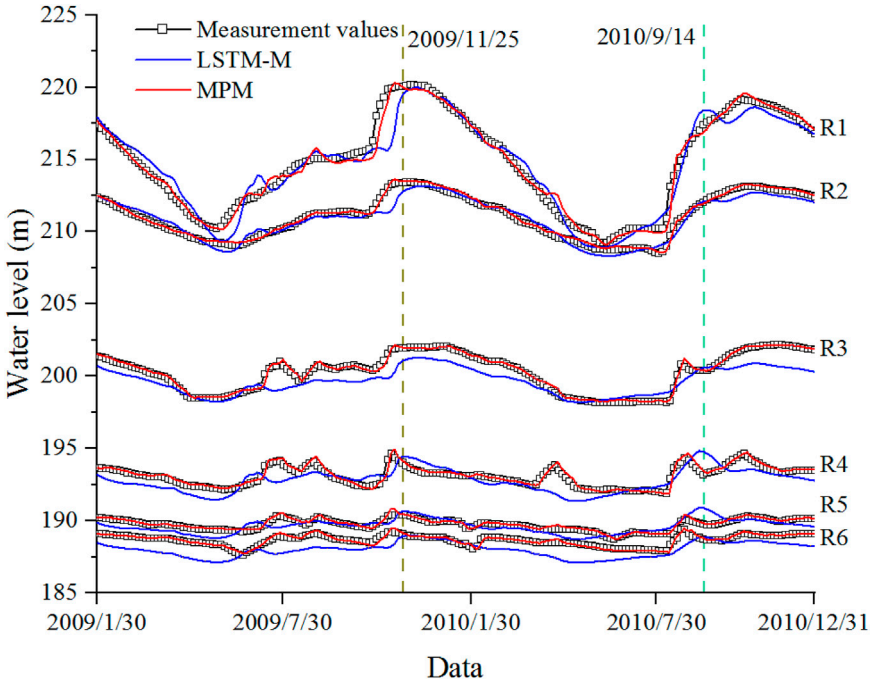

FIGURE 6
Measurement and predicted values from LSTM-M and MPM.

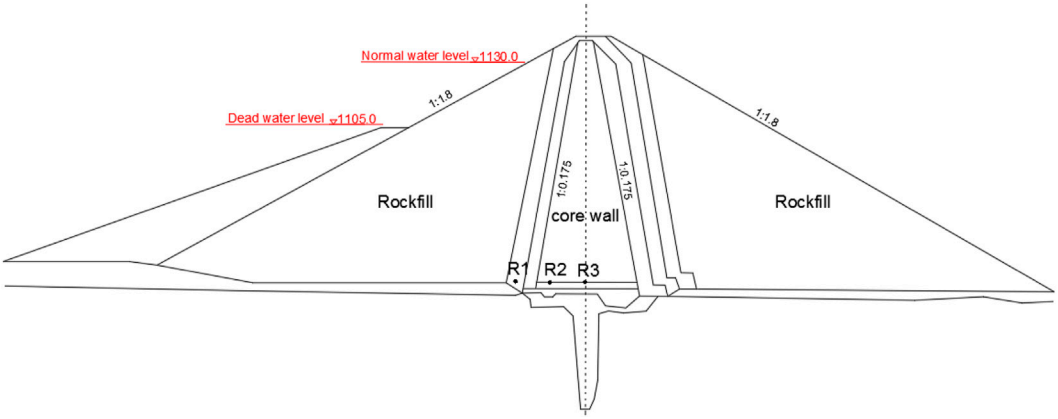

FIGURE 7
Osmometers distribution of the Lubuge rockfill dam.

small square, and no measurement value is assigned 0. The data grid at each moment is similar to the images that CNN usually processes. The measurement value of each point in the data grid is typical time series data, which is suitable for analysis by LSTM. Similar trends and differences can be seen among time series (Figures 1B, C).

The MPM model consists of two different parallel networks, CNN and LSTM (the framework is shown in Figure 2). The LSTM model efficiently captures causal temporal features. By constructing a data grid with multiple target values at each moment, the CNN model with local feature extraction capability adaptively deep mines latent features from the data grid to optimize the multi-target model. Latent correlation features between target values learned by CNN are fused with causal temporal features extracted by LSTM, and the final multi-target predictions are obtained by fully connected layer mapping.

For specific data processing, preprocessed environmental variables and monitoring history data are fed into the MPM model, the temporal features are extracted by the LSTM model, correlation features between target values are extracted by the CNN-soft parameter sharing layer, flattened feature vectors are obtained

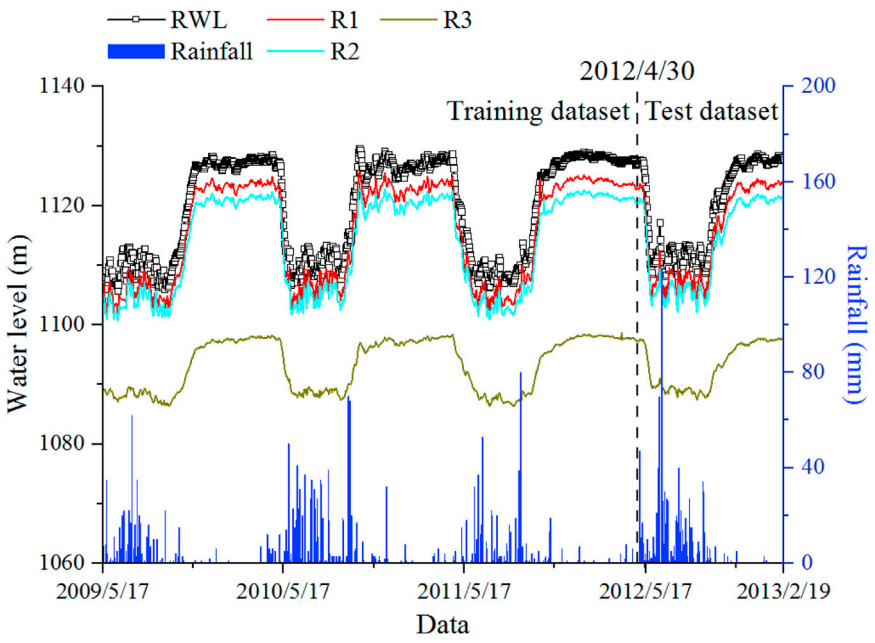

FIGURE 8
Time series of monitoring data.

for feature fusion at the same time, and the respective outputs of multiple target values are connected by fully connected layers. The MPM model integrates CNN and LSTM into a unified framework for jointly training one loss function. In addition, since the MPM model has multiple outputs, back propagation is carried out in parallel. A standard back propagation algorithm propagates errors from the output layer to the feature fusion layer and then to the parallel network layer and updates parameters.

The parts are described below:

(1) Data collection and preprocessing: abnormal data were eliminated, and data format conventions and normalization were carried out for environmental variables and target values (Yang D. S. et al., 2020) to make them suitable for the MPM model. Inputs are $\boldsymbol{X}_m$ and $\boldsymbol{Y}_n$, where $\boldsymbol{X}$ is a matrix of m environmental variables and $\boldsymbol{Y}$ is a matrix of n target values.

(2) Soft parameter sharing layer: Soft parameter sharing layer is built by CNN with local perception and weight sharing features. The CNN model is introduced to mine latent correlation features between target values of adjacent measurement points.

(3) Feature fusion layer: There are two main feature fusion methods in hybrid neural networks: addition (Yang J et al., 2020) and concatenation (Zhang et al., 2022). Feature addition requires the same dimension of feature vectors, while concatenation is more flexible. Moreover, feature fusion through concatenation has the effect of reinforcing and interconnecting features (Zhang et al., 2017; Zhang et al., 2022). Therefore, concatenation is used to fuse feature vectors in MPM.

(4) Output layer: Fully connected layers are performed to connect the final multi-target outputs, which consist of an input layer, hidden layers, and an output layer. The input to this module is the comprehensive feature vector. Full connection between adjacent layers is used to integrate local information, and the corresponding activation function is set to achieve non-linearity. Due to data regression, the activation function is sigmoid. For neural networks, when the input data is not very large, the 2- to 3-layer structure can fit any function (Yan et al., 2019).

2.3 The detailed calculation method

2.3.1 Model training

Details of the MPM model are presented in Algorithm 1.

Input: Environmental variables $\boldsymbol{X_m}$ and target values $\boldsymbol{Y_n}$
1. Data preprocessing
2. Get training and test datasets
3. Randomly initialize model parameters
4. Set loss function: RMSE
5. **Begin training**:
6. Forward propagation
7. Calculate loss function
8. Calculate gradient descent
9. Backpropagation and update model parameters
10. **End training**
11. Save model parameters
12. Begin testing
13. Inverse standardization

Output: The predictions of $\boldsymbol{Y_n^*}$

Algorithm 1: The MPM model.

TABLE 4 Setting of hyperparameters.

Parameters		Values
CNN Architecture	Convolutional layer 1	16
		Kernel: 2
		Stride: 1
		Padding: 1
	Convolutional layer 2	8
		Kernel: 2
		Stride: 1
		Padding: 1
	Maxpool	Kernel: 2×2
		Stride: 2×2
		Padding: 1
	Convolutional layer 3	8
		Kernel: 3
		Stride: 1
		Padding: 1
	Maxpool	Kernel: 3×3
		Stride: 2×2
		Padding: 1
	Fully connect nodes	64
	Time step	1
	Activation function	Relu
LSTM Architecture	Hidden layers nodes	128
	Hidden layers	2
	Time step	12
	Activation function	Softmax
Output layer	Hidden layers	2
	Dropout rate	0.1
Training	Optimizer	Adam
	Loss function	RMSE
	Batch size	32
	Epochs	1,000
	Learning rate	0.001

The specific training process is as follows (Figure 3):

Step 1: Obtain the initial training dataset and initialize the model parameters.

Step 2: Enter the training data into the networks to start the training. According to the output predictions and target values, the error of multiple measurement points on the output layer is calculated and then propagated forward to the feature fusion layer and the parallel layer, where the error is calculated.

Step 3: Update the weights according to the error on the output layer and calculate the total error of the multi-target results. If the maximum number of iterations is reached, proceed directly to Step 4. Otherwise, Step 2 is returned.

Step 4: Model training is completed, and the configuration of the entire network is saved for prediction.

2.3.2 Hyperparameter optimization

The goal of hyperparameter optimization is to make the model perform better on both training and test datasets. At present, there is no perfect theoretical guidance for the selection of hyperparameters of deep neural networks, which need to be constantly adjusted according to the learning effect of the model. In order to obtain the optimal structure of the deep learning model, this study adopts the variable control approach to select hyperparameters such as the number of network layers, the number of neurons, and the number of iterations, taking into account the prediction accuracy and complexity of the model.

2.4 Comparison model and evaluation metrics

To verify the effectiveness of the MPM model, it is compared and analyzed with the traditional multi-target benchmark model based on hard parameter sharing (Zhou et al., 2018; Sun et al., 2021). For convenience, the benchmark model is denoted LSTM-M in this paper. Hard parameter sharing layer of the LSTM-M model is built by LSTM neural networks, and the output results are target-specific and built by fully connected layers. The LSTM-M model based on hard parameter sharing can share complementary knowledge between various time series and capture temporal features between environmental variables and target values. For fair comparison, the hyperparameters and inputs of the LSTM-M model are consistent with those of the MPM model.

In order to examine the superiority of the MPM model from different perspectives, mean square error (MSE), root mean square error (RMSE), mean absolute error (MAE), coefficient of determination (R^2), and mean absolute percentage error (MAPE) are five commonly used metrics to fully compare and evaluate predictive performance. Among them, R^2 reflects fit performance, ranging from 0 to 1, and a more significant R^2 represents a better fit. MSE and RMSE are sensitive to outliers and can measure deviations between predictions and target values. MAE is the mean of the absolute value of the error, and MAPE measures the absolute difference between predictions and target values, with a smaller value representing better prediction performance. The equations are as follows:

$$MSE = \frac{1}{M \cdot N} \sum_{j=1}^{M} \sum_{i=1}^{N} \left(\hat{y}_{j,i} - y_{j,i} \right)^2 \tag{2}$$

$$RMSE = \frac{1}{M} \sum_{i=1}^{M} \sqrt{\frac{1}{N} \sum_{j=1}^{N} \left(\hat{y}_{j,i} - y_{j,i} \right)^2} \tag{3}$$

TABLE 5 Evaluation results of prediction models.

Measurement points	Metrics	LSTM-M	MPM	Relative improvement: P/%
R1	MSE/m	1.604	**0.786**	51.0
	RMSE/m	1.267	**0.887**	30.0
	MAE	0.827	**0.566**	31.5
	R^2	0.972	**0.986**	—
	MAPE/%	0.074	**0.051**	31.6
R2	MSE/m	1.055	**0.402**	61.9
	RMSE/m	1.027	**0.634**	38.2
	MAE	0.676	**0.421**	37.7
	R^2	0.980	**0.992**	—
	MAPE/%	0.061	**0.038**	37.7
R3	MSE/m	0.240	**0.054**	77.4
	RMSE/m	0.490	**0.233**	52.5
	MAE	0.368	**0.166**	54.9
	R^2	0.983	**0.996**	—
	MAPE/%	0.034	**0.015**	54.9

Note: the boldface indicates better performance.

$$MAE = \frac{1}{M}\sum_{i=1}^{M}\left(\frac{1}{N}\sum_{j=1}^{N}\left|\hat{y}_{j,i} - y_{j,i}\right|\right) \tag{4}$$

$$R^2 = \frac{1}{M}\sum_{i=1}^{M}\left(1 - \frac{\sum_{j=1}^{N}\left(\hat{y}_{j,i} - y_{j,i}\right)^2}{\sum_{j=1}^{N}\left(y_{j,i} - \bar{y}_{j,i}\right)^2}\right) \tag{5}$$

$$MAPE = \frac{100\%}{M \cdot N}\sum_{i=1}^{M}\sum_{j=1}^{N}\left|\frac{\hat{y}_{j,i} - y_{j,i}}{y_{j,i}}\right| \tag{6}$$

where $\hat{y}$ is the predicted value, y is the measurement value, $\bar{y}_i$ is the mean value of target values, N is the number of samples, and M is the number of measurement points.

In addition, to directly analyze the prediction performance of two models, the promotion percentages of MSE, RMSE, MAE, and MAPE are applied. The index can be expressed as Eq. 7, where EM represents different evaluation metrics and the positive value represents that the second model has better performance than the first. The higher the ratio, the greater the performance improvement of the model.

$$P = \frac{EM_1 - EM_2}{EM_1} \cdot 100\% \tag{7}$$

3 Applications and result analysis

3.1 The first model application

3.1.1 Project status and monitoring data profile

Naban (Sun, 2012) is an earth dam with a clay core wall, a crest elevation of 231.5 m, a maximum height of 78.5 m, a crest width of 8.0 m, a normal reservoir water level of 220.2 m, and a dead water level of 209.6 m. Reservoir water level (RWL) and rainfall are environmental variables. Given the low downstream water level and little fluctuation, the influence of the downstream water level is not considered in this case. The total water head measured by six piezometer tubes in the maximum height section is selected as the representative measurement value, denoted R1–R6. The position of multiple piezometer tubes is shown in Figure 4.

3.1.2 Training and prediction

There were 969 observations from 24 May 2001, to 31 December 2010. The time series of monitoring data is shown in Figure 5.

The dataset from 24 May 2001 to 27 January 2009, is used as training data for optimizing and adjusting parameters, and the dataset from 30 January 2009 to 31 December 2010, is used as test data for prediction and performance evaluation.

In this case, the CNN model has two convolutional layers with 8 neurons and 2 and 3 convolution kernels, respectively. The LSTM model has 16 neurons in the two hidden layers, and the fully connected layers have two hidden layers. The batch size is 64, the number of iterations (epoch) is set to 1,000, Adam is the optimizer, the initial learning rate is set to 0.001, and the dropout rate is set to 0.1. The details are shown in Table 2.

3.1.3 Results and comparison

The evaluation results for LSTM-M and MPM are shown in Table 3, and the boldface indicates better performance.

The intuitive comparison results are shown in Figure 6. It can be seen from the figure that both models can achieve simultaneous predictions of multiple parallel targets, but the MPM model performs better, and the prediction accuracy is greatly improved compared to the LSTM-M model. From the

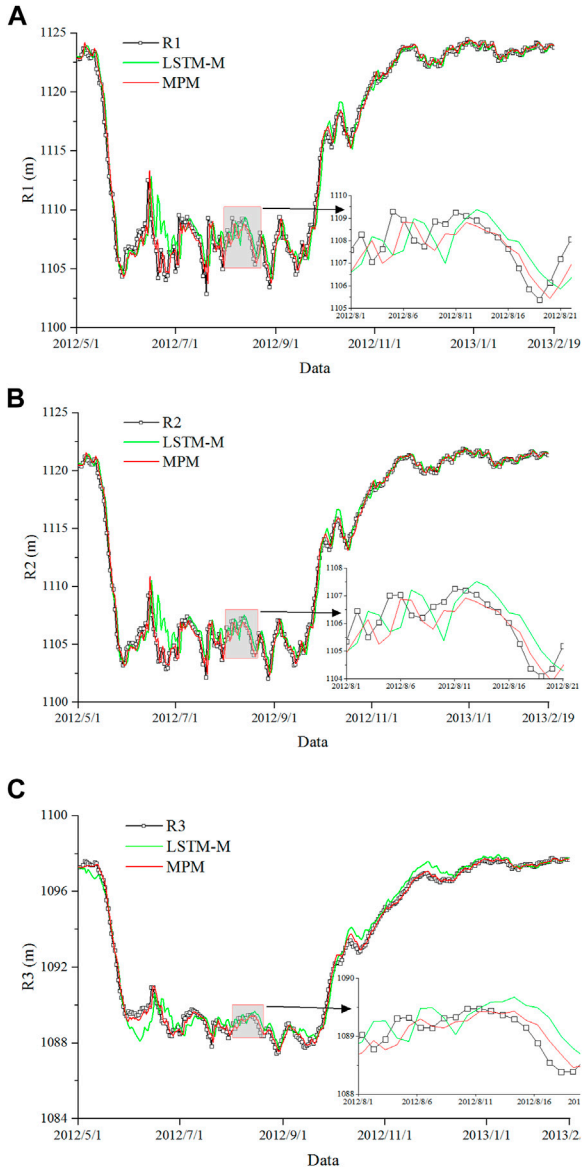

FIGURE 9
Measurement and predicted values from LSTM-M and MPM. **(A)** R1. **(B)** R2. **(C)** R3.

MAPE, MSE, RMSE, and MAE, it can be seen that the MPM model improves on average by 76.7%, 91.4%, 73.0%, and 76.7%, respectively, compared to the LSTM-M model. According to R^2, the MPM model has a good fit between predictions and target values, and the average R^2 for the six measurement points is 0.952. The results show that the prediction accuracy has been remarkably improved by introducing the CNN model. It is very important to consider latent correlation features between target values based on the benchmark LSTM-M model.

In addition, it can be seen from the predictions that the errors of the two models are mainly reflected at the time when the inflection point fluctuates greatly and the MPM model has more ideal feature sensitivity. For example, in Figure 6, the data at both times of the dashed lines indicate that the rules learned by the LSTM-M model are approximately the same, which is the delayed peak, especially at R1, R4, and R5 on 14 September 2010, where the predicted values differ significantly from target values. As can be seen, it is difficult to guarantee the accuracy of LSTM-M predictions when there are differences in the correlation between environmental variables and various target values. In addition, during the training process, because the same parameters are used for each measurement value of the LSTM-M model, the parameters are adjusted by errors and back propagation of multiple measurement points. When the error of one measurement point is large, the prediction accuracy of other measurement points will be sacrificed to balance the overall error. The CNN model is introduced to extract latent correlation features between adjacent target values, consider correlations and differences between target values, and adopt different parameters accordingly, thus improving the learning effect of the model and effectively enhancing the prediction performance.

3.2 The second model application

3.2.1 Project status and monitoring data profile

Lubuge is a weathered rockfill dam, with the top elevation of the dam, the maximum dam height, the width of the dam crest, and the length of the dam crest being 1138.0, 103.8, 10.0, and 217.0 m, respectively. The normal reservoir water level is 1130.0 m, the corresponding storage capacity is 111.0 million m^3, the dead water level is 1105.0 m, the storage capacity is 75.0 million m^3, and the reservoir presents an incomplete capacity for seasonal regulation. Given the low downstream water level and little fluctuation, the influence of the downstream water level is not considered in this case. Three osmometers from the largest section were selected for analysis and were denoted R1–R3. The position of multiple osmometers is shown in Figure 7.

3.2.2 Training and prediction

There were 1,375 observations from 17 May 2009 to 19 February 2013. The time series of monitoring data is shown in Figure 8.

The dataset from 17 May 2009 to 30 April 2012, is used as training data for optimizing and adjusting parameters, and the dataset from 1 May 2012 to 19 February 2013, is used as test data for prediction and performance evaluation.

In this case, the CNN model has three convolutional layers with 16, 8, and 8 neurons and 2, 2, and 3 convolution kernels, respectively. The LSTM model has three hidden layers with 128 neurons. The batch size is 32, and the other parameters are the same as those above. The details are shown in Table 4.

3.2.3 Results and comparison

The evaluation results for LSTM-M and MPM are shown in Table 5, and the boldface indicates better performance.

The intuitive comparison results are shown in Figure 9. When LSTM-M and MPM are compared, it is clear that the prediction accuracy of MPM has improved significantly, and MSE, RMSE, MAE, and MAPE have improved by 63.4%, 40.2%, 41.4%, and 41.4%

on average, at the three measurement points, respectively. The average R^2 at the three measurement points is 0.992, which is higher than that of LSTM-M (0.978).

3.3 Result analysis

The MPM model has achieved better prediction results in practical applications, and possible reasons for this include: 1. The LSTM model can deeply learn the non-linear temporal features between environmental variables and target values. 2. The introduction of the CNN model can effectively obtain latent correlation features between target values, and when the causal relationship between target values and environmental variables is different, the latent correlation features can be effectively used to reduce the prediction error and better fit the variation trend. 3. Feature fusion can act as feature reinforcement and intercorrelation, allowing data features to be extracted and identified from various aspects. 4. Multi-target joint training implicitly increases the amount of training data and prevents model over-fitting.

4 Conclusion

In this study, the MPM model is proposed, which considers causal temporal features between environmental variables and target values, as well as correlations and differences between target values.

The MPM model integrates CNN and LSTM into a unified framework. The LSTM model is introduced to efficiently learn the causal temporal features of short-term time changes and long-periodic variation rules in time series, while the CNN model is introduced to build the soft parameter sharing layer to efficiently mine latent correlation features of the data grid at each moment. After integrating causal temporal features and latent multi-target correlation features, fully connected layers are used to establish the mapping relationship between the comprehensive feature vector and the multi-target outputs. The MPM model allows data features to be extracted and identified from various aspects. Monitoring data of two embankment dams are used to show the prediction performance. Compared with the traditional benchmark model based on hard parameter sharing, the MPM model has better fitting effect and prediction accuracy.

The main advance of the MPM model is that CNN and LSTM are combined parallelly. Parallel networks do not depend on each other, which improves the prediction the performance of the model without consuming too much time. Although the monitoring data at multiple points in this paper are the same type, the proposed MPM model is still applicable in prediction of multiple types of physical fields in safety monitoring.

It should be noted that the model performance is inspected on the basis of the training data, which is during the normal operation period of the embankment dams. Further studies are needed to test the model performance based on the data of other types of dams and on the data of different periods of monitoring data, such as the initial operation data or long-term operation data.

Data availability statement

The original contributions presented in the study are included in the article/supplementary material, further inquiries can be directed to the corresponding author.

Author contributions

YW, GD, WH, YZ, and XW conceived of the presented idea. GD and WH set up the prediction model and performed the computations. GD analyzed the data. YW supervised the study. WH and GD wrote the first version of the manuscript. All authors contributed to manuscript revision, read, and approved the submitted version.

Funding

This work was supported by the National Key Research and Development Program of China (Grant No. 2022YFC3005501), the IWHR Research and Development Support Program (Grant No. GE0145B032021), and the Independent Research Fund of State Key Laboratory of Simulation and Regulation of Water Cycle in River Basin (Grant No. SKL2020ZY09).

Conflict of interest

The authors declare that the research was conducted in the absence of any commercial or financial relationships that could be construed as a potential conflict of interest.

Publisher's note

All claims expressed in this article are solely those of the authors and do not necessarily represent those of their affiliated organizations, or those of the publisher, the editors and the reviewers. Any product that may be evaluated in this article, or claim that may be made by its manufacturer, is not guaranteed or endorsed by the publisher.

References

Azarafza, M., Azarafza, M., Akgün, H., Atkinson, P. M., and Derakhshani, R. (2021). Deep learning-based landslide susceptibility mapping. *Sci. Rep.* 11 (1), 24112. doi:10.1038/s41598-021-03585-1

Azarafza, M., Hajialilue Bonab, M., and Derakhshani, R. (2022). A deep learning method for the prediction of the index mechanical properties and strength parameters of marlstone. *Materials* 15 (9), 6899. doi:10.3390/ma15196899

Bonelli, S., and Royet, P. (2001). "Delayed response analysis of dam monitoring data [C]," in *Proceedings of ICOLD European symposium* (Oxfordshire: Taylor and Francis Press), 91–99.

Caruana, R. A. (1993). Multitask learning: A knowledge-based source of inductive bias[J]. *Mach. Learn. Proc.* 10 (1), 41–48. doi:10.1016/b978-1-55860-307-3.50012-5

Chen, Y., Ma, G., Zhou, W., Wu, J. Y., and Zhou, Q. C. (2022). Rockfill dam deformation prediction model based on deep learning extracting spatiotemporal features[J]. *J. Hydroelectr. Eng.* 2022, 1–13.

Deng, G., Cao, K., Chen, R., Wen, Y. F., Zhang, Y. Y., and Chen, Z. K. (2020). A new method for dynamically estimating long-term seepage failure frequency for high concrete faced rockfill dams. *Environ. Earth Sci.* 79 (10), 247. doi:10.1007/s12665-020-08962-z

Deng, N. W., Chen, Z., and Ye, Z. R. (2007). Modeling of partial least-squared regression and genetic algorithm in dam safety monitoring analysis[J]. *Dam Saf.* 4, 33–35. doi:10.3969/j.issn.1671-1092.2007.04.011

Fanelli, M. (1975). Control of dam displacements. *Energ. Elettr.* 52, 125–139.

Foster, M., Fell, R., and Spannagle, M. (2000). The statistics of embankment dam failures and accidents. *Rev. Can. De. Géotechnique.* 37 (5), 1000–1024. doi:10.1139/t00-030

Gao, Y., She, Q., Ma, J., Zhao, M., and Yuille, A. L. (2019). "Nddr-cnn: Layer-wise feature fusing in multi-task cnn by neural discriminative dimensionality reduction[C]," in Proceedings of the IEEE Conference on Computer Vision and Pattern Recognition, Long Beach, CA, USA, 3205–3214. doi:10.48550/arXiv.1801.08297

Gu, C. S., Su, H. Z., and Wang, S. W. (2016). Advances in calculation models and monitoring methods for long-term deformation behavior of concrete dams[J]. *J. Hydroelectr. Eng.* 35 (5), 1–14. doi:10.11660/slfdxb.20160501

Gu, C. S., Wang, Y. C., Peng, Y., and Xu, B. S. (2011). Ill-conditioned problems of dam safety monitoring models and their processing methods. *Sci. China Technol. Sci.* 54 (12), 3275–3280. doi:10.1007/s11431-011-4573-z

Hakim, W. L., Rezaie, F., Nur, A. S., Panahi, M., Khosravi, K., Lee, C. W., et al. (2021). Convolutional neural network (CNN) with metaheuristic optimization algorithms for landslide susceptibility mapping in Icheon, South Korea. *J. Environ. Manag.* 305, 114367. doi:10.1016/j.jenvman.2021.114367

Hochreiter, S., and Schmidhuber, J. (1997). Long short-term memory. *Neural Comput.* 9 (8), 1735–1780. doi:10.1162/neco.1997.9.8.1735

Hochreiter, S. (1998). The vanishing gradient problem during learning recurrent neural nets and problem solutions. *Int. J. Uncertain. Fuzziness Knowledge-Based Syst.* 6 (2), 107–116. doi:10.1142/S0218488598000094

Hou, W. Y., Wen, Y. F., Deng, G., Zhang, Y. Y., and Chen, H. (2022). Deformation prediction of high embankment dams by combining time series decomposition and deep learning[J]. *J. Hydroelectr. Eng.* 41 (3), 123–132. doi:10.11660/slfdxb.20220312

Hua, G. W., Wang, S. J., Xiao, M., and Hu, S. H. (2023). Research on the uplift pressure prediction of concrete dams based on the CNN-gru model. *J. Water.* 15 (2), 319. doi:10.3390/w15020319

Huang, H., and Chen, B. (2012). Dam seepage monitoring model based on dynamic effect weight of reservoir water level. *Energy Procedia* 16, 159–165. doi:10.1016/j.egypro.2012.01.027

Hubel, D. H., and Wiesel, T. N. (1959). Receptive fields of single neurones in the cat's striate cortex. *J. Physiology* 148 (3), 574–591. doi:10.1113/jphysiol.1959.sp006308

Jeon, J., Lee, J., Shin, D., and Park, H. (2009). Development of dam safety management system. *Adv. Eng. Softw. [J]* 40 (8), 554–563. doi:10.1016/j.advengsoft.2008.10.009

Krizhevsky, A., Sutskever, I., and Hinton, G. E. (2012). ImageNet classification with deep convolutional neural networks[J]. *Adv. neural Inf. Process. Syst.* 52, 1097–1105. doi:10.1145/3065386

LeCun, Y., and Bengio, Y. (1995). Convolutional networks for images, speech, and time series[J]. *Handb. Brain Theory Neural Netw.* 3361 (10).

Li, Y. T., Bao, T. F., Gao, Z. X., Shu, X. S., Zhang, K., Xie, L. C., et al. (2022). A new dam structural response estimation paradigm powered by deep learning and transfer learning techniques. *Struct. Health Monit.* 21 (3), 770–787. doi:10.1177/14759217211009780

Liang, X., Tang, S. B., Tang, C. A., Hu, L. H., and Chen, F. (2022). Influence of water on the mechanical properties and failure behaviors of sandstone under triaxial compression. *Rock Mech. Rock Eng.* 56, 1131–1162. doi:10.1007/s00603-022-03121-1

Misra, I., Shrivastava, A., and Gupta, A. (2016). "Hebert M. Cross-stitch networks for multi-task learning[C]," in Proceedings of the 2016 IEEE Conf on Computer Vision and Pattern Recognition, Las Vegas, 3994–4003. IEEE. doi:10.1109/CVPR2016.433

Nikoobakht, S., Azarafza, M., Akgün, H., and Derakhshani, R. (2022). Landslide susceptibility assessment by using convolutional neural network. *Appl. Sci.* 12, 5992. doi:10.3390/app12125992

Qu, X. D., Yang, J., and Chang, M. (2019). A deep learning model for concrete dam deformation prediction based on RS-LSTM. *J. Sensors* 1, 1–14. doi:10.1155/2019/4581672

Ren, Q., Li, M., Li, H., and Shen, Y. (2021). A novel deep learning prediction model for concrete dam displacements using interpretable mixed attention mechanism. *Adv. Eng. Inf.* 50 (3), 101407. doi:10.1016/j.aei.2021.101407

Shi, Z. W., Gu, C. S., Zhao, E. F., and Xu, B. (2020). A novel seepage safety monitoring model of CFRD with slab cracks using monitoring data. *Math. Problems Eng.* 12, 1–13. doi:10.1155/2020/1641747

Su, H. Z., Gu, C. S., and Wu, Z. R. (2000). Application of artificial intelligence theory to dam safety monitoring[J]. *Dam Observation Geotechnical Tests* 24 (3), 7–9. doi:10.3969/j.issn.1671-3893.2000.03.003

Su, H. Z., Wu, Z. R., Wen, Z. P., and Gu, C. S. (2001). Dam safety monitoring model based on fuzzy neural network and genetic algorithm[J]. *Dam Observation Geotechnical Tests* 25 (1), 10–12+22. doi:10.3969/j.issn.1671-3893.2001.01.004

Sun, L. C. (2012). *Study on the seepage flow prediction of earth-rock dam [D]*. Nanning: Guangxi university. (in Chinese).

Sun, Q. K., Wang, X. J., Zhang, Y. Z., Zhang, F., Zhang, P., and Gao, W. Z. (2021). Multiple load prediction of integrated energy system based on long short-term memory and multi-task learning[J]. *Automation Electr. Power Syst.* 45 (5), 63–70.

Tang, S. B., Li, J. M., Ding, S., and Zhang, L. (2022). The influence of water-stress loading sequences on the creep behavior of granite. *Bull. Eng. Geol. Environ.* 81, 482. doi:10.1007/s10064-022-02987-3

Wan, C., Li, W. Z., Ding, W. X., Zhang, Z. J., Lu, Q. N., Qian, L., et al. (2021). Multi-task sequence learning for performance prediction and KPI mining in database management system. *Inf. Sci.* 568, 1–12. doi:10.1016/j.ins.2021.03.046

Wu, Z. R., and Su, H. Z. (2005). Dam health diagnosis and evaluation. *Smart Mater. Struct.* 14 (3), S130–S136. doi:10.1088/0964-1726/14/3/016

Xu, D., Shi, Y. X., Tsang, I. W., Ong, Y. W., Gong, C., and Shen, X. B. (2019). Survey on multi-output learning. *IEEE Trans. Neural Netw. Learn. Syst.* 31, 2409–2429. doi:10.1109/TNNLS.2019.2945133

Yan, R., Geng, G. C., Jiang, Q. Y., and Li, Y. L. (2019). Fast transient stability batch assessment using cascaded convolutional neural networks. *IEEE Trans. Power Syst.* 34 (4), 2802–2813. doi:10.1109/TPWRS.2019.2895592

Yang, D. S., Gu, C. S., Zhu, Y. T., Dai, B., Zhang, K., Zhang, Z. D., et al. (2020). A concrete dam deformation prediction method based on LSTM with attention mechanism. *IEEE Access* 8, 185177–185186. doi:10.1109/access.2020.3029562

Yang, J., Qu, J., Mi, Q., and Li, Q. (2020). A CNN-LSTM model for tailings dam risk prediction. *IEEE Access* 8, 206491–206502. doi:10.1109/ACCESS.2020.3037935

Yao, K. F., Wen, Z. P., Yang, L. P., Chen, J., Hou, H. W., and Su, H. Z. (2022). A multipoint prediction model for nonlinear displacement of concrete dam. *Computer-Aided Civ. Infrastructure Eng.* 37 (14), 1932–1952. doi:10.1111/mice.12911

Zhang, J. B., Zheng, Y., and Qi, D. K. (2017). "Deep spatio-temporal residual networks for citywide crowd flows prediction[C]," in *Proceedings of the thirty-first AAAI conference on artificial intelligence (AAAI'17)* (Palo Alto, California, U.S. AAAI Press), 1655–1661. doi:10.48550/arXiv.1610.00081

Zhang, L., Cai, Y. Y., Huang, H. L., Li, A. Q., Yang, L., and Zhou, C. H. (2022). A CNN-LSTM model for soil organic carbon content prediction with long time series of MODIS-based phenological variables. *Remote Sens.* 14 (18), 4441. doi:10.3390/rs14184441

Zhao, M. D., Jiang, H. F., Zhao, M. D., and Bie, Y. J. (2021). Prediction of seepage pressure based on memory cells and significance analysis of influencing factors. *Complexity* 12, 1–10. doi:10.1155/2021/5576148

Zhou, Y., Chang, F. J., Chang, L. C., Kao, I. F., and Wang, Y. S. (2018). Explore a deep learning multi-output neural network for regional multi-step-ahead air quality forecasts. *J. Clean. Prod.* 209 (1), 134–145. doi:10.1016/j.jclepro.2018.10.243

Zhu, C., Xu, X. D., Wang, X. T., Xiong, F., Tao, Z. G., Lin, Y., et al. (2019). Experimental investigation on nonlinear Flow anisotropy behavior in fracture media. *Geofluids* 9, 1–9. doi:10.1155/2019/5874849

Zong, M., Wang, R. L., Ma, Y. J., and Ji, W. T. (2022). Spatial and temporal saliency based four-stream network with multi-task learning for action recognition. *Appl. Soft Comput.* 132, 109884. doi:10.1016/j.asoc.2022.109884

frontiers | Frontiers in Earth Science

TYPE Original Research
PUBLISHED 18 April 2023
DOI 10.3389/feart.2023.1147129

OPEN ACCESS

EDITED BY
Wenzhuo Cao,
Imperial College London,
United Kingdom

REVIEWED BY
Kang Bian,
Chinese Academy of Sciences (CAS),
China
Yi-Xiang Song,
Hebei University of Technology, China

*CORRESPONDENCE
Yunlei Tian,
tianyunlei1234@163.com

RECEIVED 18 January 2023
ACCEPTED 05 April 2023
PUBLISHED 18 April 2023

CITATION
Li B, Tian Y, Tian J, Zuo S and Chen S (2023), Bending-damaged fracture criterion and numerical implementation of limestone beam under three-point bending test.
Front. Earth Sci. 11:1147129.
doi: 10.3389/feart.2023.1147129

Bending-damaged fracture criterion and numerical implementation of limestone beam under three-point bending test

Benyun Li[1], Yunlei Tian[2]*, Jiao Tian[1], Shuangying Zuo[2,3] and Shiwan Chen[2,3]

[1]Guizhou Transportation Planning Survey and Design Academic Co.,Ltd., Guiyang, China, [2]The College of Resources and Environmental Engineering, Guizhou University, Guiyang, China, [3]Key Laboratory of Karst Georesources and Environment, Ministry of Education, Guizhou University, Guiyang, China

To study the characteristics of tensile cracking by rock-bending damage, the bending stress–strain curves and the cumulative ringing counts were obtained by a three-point bending test and acoustic emission (AE) monitoring of limestone beams. Based on the Lemaitre strain equivalent principle and the continuous damage theory, the bending damage variable D was defined by the AE cumulative ringing counts, and the bending crack damage evolution equation was established according to the Weibull distribution of the rock element strength. To realize the numerical test of the bending deformation, the damage variable *D* was used as the intermediate variable, and the specific process of damage bending stress transformation and the realization of the tensile crack criterion were secondary developed by FISH language in FLAC^{3D}. According to the results, the central part of rock beam deforms downward under the action of bending stress, and both ends tilt up. Therefore, the bending failure begins with the tensile crack at the bottom of the rock beam and gradually extends to the compression zone. The maximum damage value is about 0.402 before the peak stress. The compressive stress in the *x* direction increases from the neutral layer to the top of the rock beam, and the tensile stress in the *x* direction increases from the neutral layer to the bottom of the rock beam. The maximum tensile stress is distributed in the center of the bottom of the specimen, where the bending effect is obvious. The stress–time curve was divided into the (I) compaction stage, (II) expansion stage, and (III) penetration stage, accordingly, and the evolution of damage equation was divided into three stages: initial damage stage, slow damage stage, and accelerated damage stage. The curves of the experimental result, theoretical model prediction result, and numerical simulation result were in good agreement with each other, which indicates that the numerical simulation based on the criterion of rock damaged fracture can better reflect the bending process of rock beams under three-point bending stress.

KEYWORDS

limestone, three point bending test, damaged fracture criterion, numerical simulation, AE

Highlights

- The bending damage variable D was defined by the AE cumulative ringing counts, which can be divided into three stages during the whole loading and increases rapidly after 80% peak stress.
- The element stress of the section of the rock beam was converted into the bending stress, used to establish the damaged fracture criterion.
- The damage zone and bending stress distribution were obtained by FISH language in FLAC^{3D} for secondary development of the numerical test.

1 Introduction

Rock is usually placed in a compressive state as a kind of geotechnical engineering material, which attracts research attention of many scholars to the rock compressive strength (Liao et al., 2019). However, in some cases, the bending tensile failure of rock is the dominating mode of engineering instability and failure (Andreev, 1991; Zhang, 1994; Cai et al., 2001; Pine et al., 2007), such as the bending failure in the horizontal roof plate of underground cavities and tunnels (Guan et al., 2012), the slide-bending failure in the bedding rock slope (Yang et al., 2022), the crooked-toppling failure in the anti-dip layered rock slope, and a buckling failure in the vertical rock slope (Zhang, 1994). Because of the important engineering application value of bending tensile failure of rock, much research has been conducted. ASTM International (2008) proposed some methods, including compact tension and three-point bending, to test the bending strength of materials. ISRM (1978) proposed the test standards of direct tension and Brazilian splitting. Pandey and Singh (1986) studied deformation of rock in different tensile tests. Meanwhile, the acoustic emission (AE) technique, a kind of useful means to monitor the development and evolution of microcracks during rock deformation, is widely used in rock damage analysis (Liu B. X. et al., 2009; Tian et al., 2022). Extensive information can be reflected by AE signals, including the evolution process (Pei et al., 2013), the mechanism of failure (Aggelis et al., 2013; Zhou et al., 2019; Gan et al., 2020), and the quantification and location of damage (Liu Y. M. et al., 2009; Tian et al., 2020). Therefore, many scholars have studied the evolution of microcracks in rock during bending failure through AE monitoring. Zeng (2015) studied the AE characteristics of sandstone under three-point bending and analyzed the influencing factors of damage. Deng et al. (2016) studied the influence of grain size and AE characteristics through a three-point bending test. Lacidogna et al. (2018) conducted a three-point bending test on pre-slotted concrete beam specimens and used the AE technique to monitor the crack growth process. Prem and Murthy (2016) applied the AE technique to study the damage mechanism of the reinforced concrete beams under a bending test.

Some theories have also been proposed regarding bending tensile failure, along with deeper research. One of them is the fracture mechanics theory, which focuses on the change laws of crack propagation, damage characteristics, stress intensity factor, and the fracture toughness of rock beams with prefabricated cracks under vertical load. Atkinson (1992) published the first monograph on rock fracture mechanics in 1987, which expanded a new direction for rock mechanics. Lu et al. (2021) conducted a three-point bending test on granite and marble with different prefabricated crack methods and lengths. Li et al. (2018) conducted a three-point bending test on a sandstone specimen with a perpendicular crack surface. Zuo et al. (2017) studied the influence of temperature, buried depth, and offset notch on the tensile fracture characteristics of rock mass through a three-point bending test. The other theory is about material mechanics or structural mechanics, and it focuses on the influencing factors of the bending strength and tensile modulus of rock materials and the bending failure mechanism. Yao et al. (2018) proposed a two-parameter tensile strength model for rocks based on the successful application of the non-local theory and the three-point bending test. Francesco et al. (2019) combined the AE monitoring and the non-local integral plastic damage constitutive theory to simulate and analyze the bending fracture process of Adelaide black granite. Zuo et al. (2013), Zuo et al. (2015) established an anisotropic model of layered rock mass reflecting transverse isotropy and a criterion for bending failure mode.

However, the previous research was mainly based on the plat and beam model or basic theories of fracture mechanics and material mechanics, focusing on the research of crack propagation, energy accumulation, and dissipation, etc., and explaining the phenomenon mechanism in the process of testing. It gave little consideration to the damage and parameter deterioration in the deformation process of rock beam, and the mechanical theory is not strong in guiding the numerical simulation. Therefore, in this work, based on the Weibull distribution function of micro-element strength, the bending damage evolution equation of limestone beam is established, and the damage and parameter deterioration in the deformation process of rock beam are considered. Then, the bending stress yield criterion is used as the damage and bending crack criterion of the rock beam, and the damage variable D is used as the intermediate variable to conduct the bending numerical test of the rock beam. The specific process of the calculation of damage bending stress and the realization of the tension crack criterion is compiled with the inbuilt FISH language of FLAC^{3D}. The research results are helpful to understand the bending deformation characteristics and failure mechanism of limestone beam.

2 Experimental work

2.1 Specimens and instruments

As shown in Figure 1A, the limestone beam specimens were taken from the same site and were made into six rectangular solid beams of 60 cm in length, 10 cm in width, and 10 cm in height. The testing system, as shown in Figure 1, included an electro-hydraulic servo universal mechanics testing system (Figure 1B), AE monitoring system (Figure 1C), and strain monitoring system (Figure 1D).

2.2 Test methods

1) The rock beams were wiped with fine sandpaper to polish their surfaces, and the strain gauges were pasted on the side and bottom of the rock beams smoothly. As shown in Figure 1D,

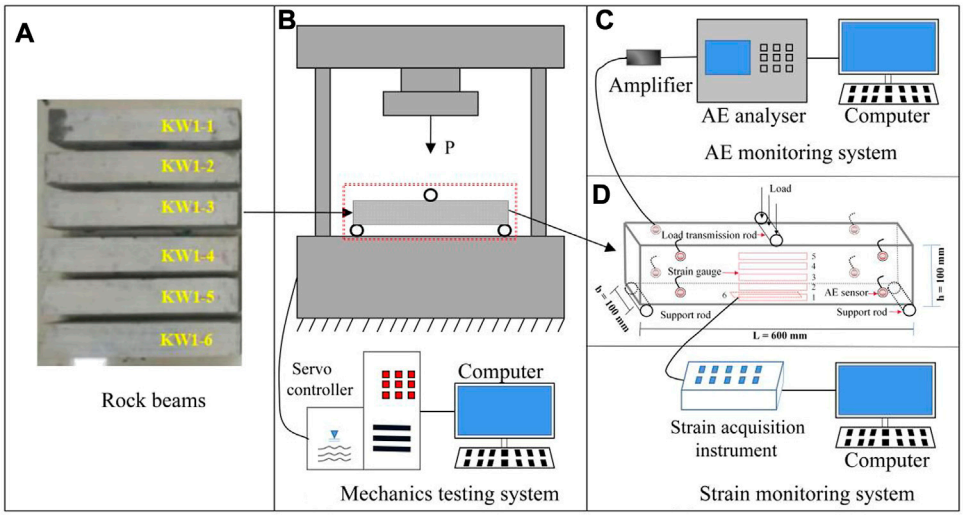

FIGURE 1
Testing system: **(A)** rock beams specimens, **(B)** universal mechanics testing system, **(C)** AE monitoring system, **(D)** strain monitoring system.

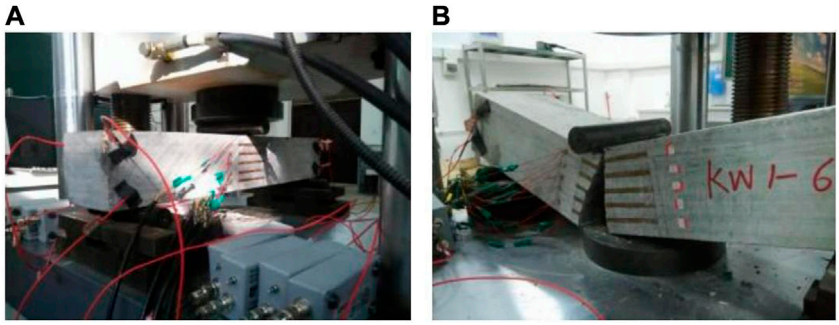

FIGURE 2
(A) The prepared limestone beam, **(B)** the fractured limestone beam.

strain gauge 3 was located at the side central axis of the rock beams, and the intervals among strain gauges 1 to 5 were 15 mm. Strain gauge 6 was located at the middle bottom of the beams. The beams with strain gauges were left in a ventilated environment for 4–5 h.

2) The six strain gauges were connected to the corresponding channels of the static strain data acquisition instrument, and at the same time, another strain gauge located on the spare rock was connected to the temperature compensation channel of the strain acquisition instrument to make a temperature compensation for the test.
3) Fixing the eight AE sensors at the selected point on the rock beams with rubber bands, the vacuum silicone grease was used to couple the rock beams and the AE sensor. The location of the strain gauges and AE sensors are shown in Figure 2A. The peak definition time (PDT), hit definition time (HDT), and hit locking time (HLT) were set as 50, 200, and 300 μs, respectively. The threshold for AE detection was set to 40 dB.
4) After the preparatory work was completed, the limestone beams were loaded to failure with a rate of 0.002 mm/s under AE and strain monitoring. The fractured limestone beam is shown in Figure 2B.

3 Results and analysis

3.1 Test result

3.1.1 Load–displacement curve

Figure 3 shows the relationship between the load and mid-span vertical displacement of the rock beam. As can be directly seen in Figure 3, the load–displacement curves are convex.

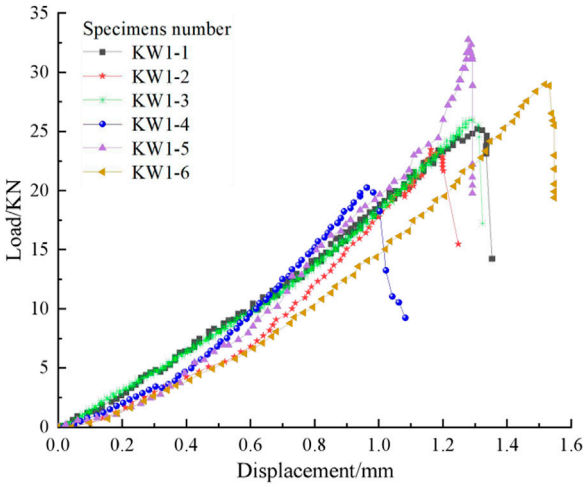

FIGURE 3
Load–displacement curves in three-point bending test.

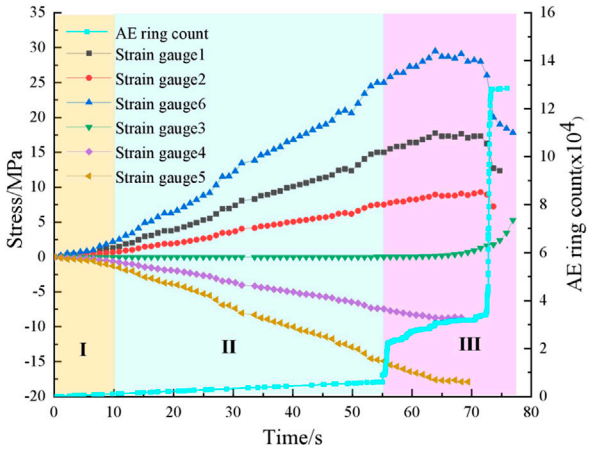

FIGURE 4
Stress-cumulative ringing counts–time curve of specimen KW1-5.

Because the failure of rock is closely related to the evolution of internal microcracks, the load–displacement curves can be divided into three stages from the analysis of the evolution of internal microcracks: (I) microcracks compaction stage, (II) microcracks expansion stage, and (III) microcracks penetration stage. Taking the curve of KW1-5 as an example from Figure 3, the microcracks compaction stage (I) occurs at the initial loading period of the rock beam. At this stage, the original microcracks in the rock beam are compacted; however, the load on the rock beam is too small to produce new microcracks, causing the displacement changes slowly with the increase of the load. With the load continues to increase, the microcracks in the upper part of the rock beam are dramatically compacted, and at the same time, the microcracks in the lower part of the rock beam are in a tension state. New microcracks begin to appear and expand in the lower part of the rock beam, but they are not connected yet. At this period, the curve is approximate to a straight line, called the microcracks expansion stage (II). When the load further increases, the load–displacement curve turns down sharply after the peak value, and the rock beam breaks suddenly. At this time, the vertical displacement of the rock beam is almost unchanged, and the bearing capacity of the rock beam drops sharply due to the complete penetration of the microcracks. This period is identified as the microcracks penetration stage (III), which reflects the characteristics of the bending brittle fracture of limestone beam.

3.1.2 Stress-cumulative ringing–time curve

The maximum bending stress located at the lower edge of the mid-span section was calculated from Eq. 1:

$$\sigma = \frac{3PL}{2bh^2} \tag{1}$$

Where P is the load (N), L, b, *and* h are, respectively the length, width, and height of the rock beam (m). The results calculated according to Eq. 1 are shown in the Figure 4.

According to the stress-cumulative ringing number–time curves of Figure 4, we can find that the bending stress of limestone beam changes with time in three stages: the slow growth stage, linear growth stage, and sharp decline stage after the peak. This is in accordance with the analysis results in subsection 3.1.1. Accordingly, the AE signals show different evolution characteristics with different loading stages.

At the microcracks compaction stage (I), the source of AE signals is inactive, corresponding to the compression of the original microcracks in the rock beam, which causes the cumulative ringing number at a low level.

At the microcracks expansion stage (II), the source of the AE signals changes from compression of the original microcracks to production of new microcracks with the increase of the load, which causes the cumulative number of AE rings to increase with the stress; the specimen is still at a stable stage.

At the microcracks penetration stage (III), the cumulative number of AE rings increases dramatically because of the unstable expansion of the microcracks. The increase rate is faster than that of stages I and II, and there are two sudden growth points. The first point is located at the point of 80% peak stress, because of the large number of microcracks that are generated, expanded, and connected. The second point occurs at the moment when the stress drops rapidly, and it is mainly caused by the complete destruction of the rock beam, which can be taken as a sign of rock beam failure.

3.2 Analysis

3.2.1 Bending damage analysis

3.2.1.1 Definition and monitoring method of bending damage variables

Based on the continuous damage theory and Lemaitre strain equivalent principle, the stress–strain constitutive relationship of the tensile zone in the bending damage

process can be expressed as Eq. 2:

$$\sigma_t = E(1 - D)\varepsilon \tag{2}$$

Where σ_t is the tensile stress, $\varepsilon$is the strain, E is Young's modulus, and D is the damage variable. According to the research by Zhang et al. (2006), the relationship between the damage variable and the AE cumulative rings can be directly defined as:

$$D = \frac{N}{N_m} \tag{3}$$

Where N is the real-time AE ringing during the bending damage process, which represents the microcracks generated by the stress on the specimen at this moment, and where Nm is the cumulative ringing number of complete failure at the end of the test, which represents all the microcracks generated by the stress on the specimen.

The relationship between strain and time collected by different strain gauges in Figure 4 was fitted, and it was found that the relationship between strain and time in the different parts is linear, and the expression is:

$$\varepsilon = kt + \varepsilon_0 \tag{4}$$

According to the study by Wu et al. (2015), when the rock specimen is brittle or undergoes brittle–ductile failure, exponential function can be considered to express the functional relationship between the AE cumulative rings count N and time t:

$$N = A_1 \exp(B_1 t) + C \tag{5}$$

The value of A_1, B_1, and C can be determined by experimental data. Substituting Eq. 4 into Eqs 5, 6 can be derived:

$$N = A_1 \exp\left[\frac{B(\varepsilon - \varepsilon_0)}{k}\right] + C \tag{6}$$

Tang et al. (2003) and Jiang and Wen (2011) established the constitutive model of the rock stress–strain curve based on the Weibull distribution model as follows:

$$D = 1 - \exp\left(-\frac{\varepsilon^m}{\alpha}\right) \tag{7}$$

$$\sigma = E\varepsilon \exp\left(-\frac{\varepsilon^m}{\alpha}\right) \tag{8}$$

Yang et al. (2005) established a new method to determine the parameters of a rock damage model:

$$m = 1/\ln(E\varepsilon_e/\sigma_e) \tag{9}$$

$$\alpha = m{\varepsilon_e}^m \tag{10}$$

Where $m$is the shape factor of the distribution function and σ_e and ε_e are, respectively, the tensile stress and tensile strain at the lower edge of the rock beam at the end of the test.

The relationship among the AE cumulative ring numbers N, stress σ, and damage variable D can be obtained by combining Eqs 6–8 as follows:

$$D = 1 - \exp\left[-\frac{1}{\alpha}\left(\frac{k}{B_1}\ln\frac{N-C)}{A_1} + \varepsilon_0\right)^m\right] \tag{11}$$

$$\sigma = E\varepsilon \exp\left[-\frac{1}{\alpha}\left(\frac{k}{B_1}\ln\frac{N-C)}{A_1} + \varepsilon_0\right)^m\right] \tag{12}$$

In the process of large-scale rock beam bending, the neutral layer between the compression zone and the tension zone will gradually shift from the middle of the rock beam to the upper part with the gradual bending failure. However, because the scale of this test was small and the tensile fracture process was very short, the upward displacement distance of the intermediate layer was small, so it was not considered in the calculation. Taking the deformation at the bottom of each rock beams as the calculation point, the calculation parameters are shown in Table 1.

According to the AE accumulated ringing number collected during the test, as shown in Figure 5, the damage variable D of the rock beam was calculated by Eqs 3, 11.

According to the analysis in Figures 4, 5, and subsection *3.1.1, 3.1.2*, the bending damage of limestone beam can be divided into the initial damage stage, slow damage stage, and accelerated damage stage. The initial damage stage corresponds to the microcracks compaction stage (I), and the value of damage variable D tends to 0. The slow damage stage corresponds to the microcracks expansion stage (II), and the growth rate of the damage variable D is slow. The accelerated damage stage corresponds to the microcracks penetration stage (III). At this stage, the damage variable D starts to increase rapidly when the stress increases to 80% of the peak stress. When the stress reaches the peak, the damage variable D increases rapidly until the sample is fully damaged, which shows that during the process of bending deformation, the ductility of the rock is not obvious, and the rock shows transient brittle tensile fracture. The analysis results show that the damage variable correction theory conforms to the actual test situation.

3.2.1.2 Damage stress correction

The evolution of stress growth with strain after the damage correction of each strain gauge can be calculated according to Eq. 2. Taking strain gauge 6 of rock beam specimen kw1-5 as an example, the stress–strain relationship curve after damage correction is shown in Figure 6.

The black scattered points in Figure 6 are the test data, and the red line is the damage correction curve. The two curves fit well, which shows that the damage evolution model can well reflect the bending stress deformation process of limestone beam.

3.2.2 Fracture criterion of bending damage of rock mass

When the rock beam is bent under the action of torque, the upper part is compressed, and the lower part is tensioned. With the increase of bending torque, the tensile stress on the tensile side gradually increases. When the tensile stress exceeds the ultimate tensile strength, the rock beam begins to crack. The bending failure can be judged by the tensile stress yield criterion:

$$f_r{}^t = \sigma_b - R_r^t \tag{13}$$

Where σ_b is the edge bending stress in the x direction of the rock beam and R_r^t is the ultimate tensile strength. The calculation formula of σ_b under normal compressive stress is:

$$\sigma_b = \frac{M \cdot y}{Iz} \tag{14}$$

$$M = \frac{P \cdot l}{4} \tag{15}$$

$$I_Z = \frac{b \cdot h^3}{12} \tag{16}$$

TABLE 1 Parameter fitting of damage evolution equation of six samples.

Specimens	σ_e/MPa	ε_e	E/GPa	m	$A_1/10^{-5}$	B_1	C	k (E)	ε_0
kw1-1	32.5	4.25e-3	8.06	10.69	2.08	0.12	0	0.82–6	0
kw1-3	22.5	3.3e-3	7.35	13.31	3.14	0.33	0	0.90–6	0
kw1-4	17.8	4.6e-3	4.35	8.54	5.59	0.43	0	0.85–6	0
kw1-5	32.5	4.25–3	8.69	7.82	4.41	0.29	0	0.65–6	0

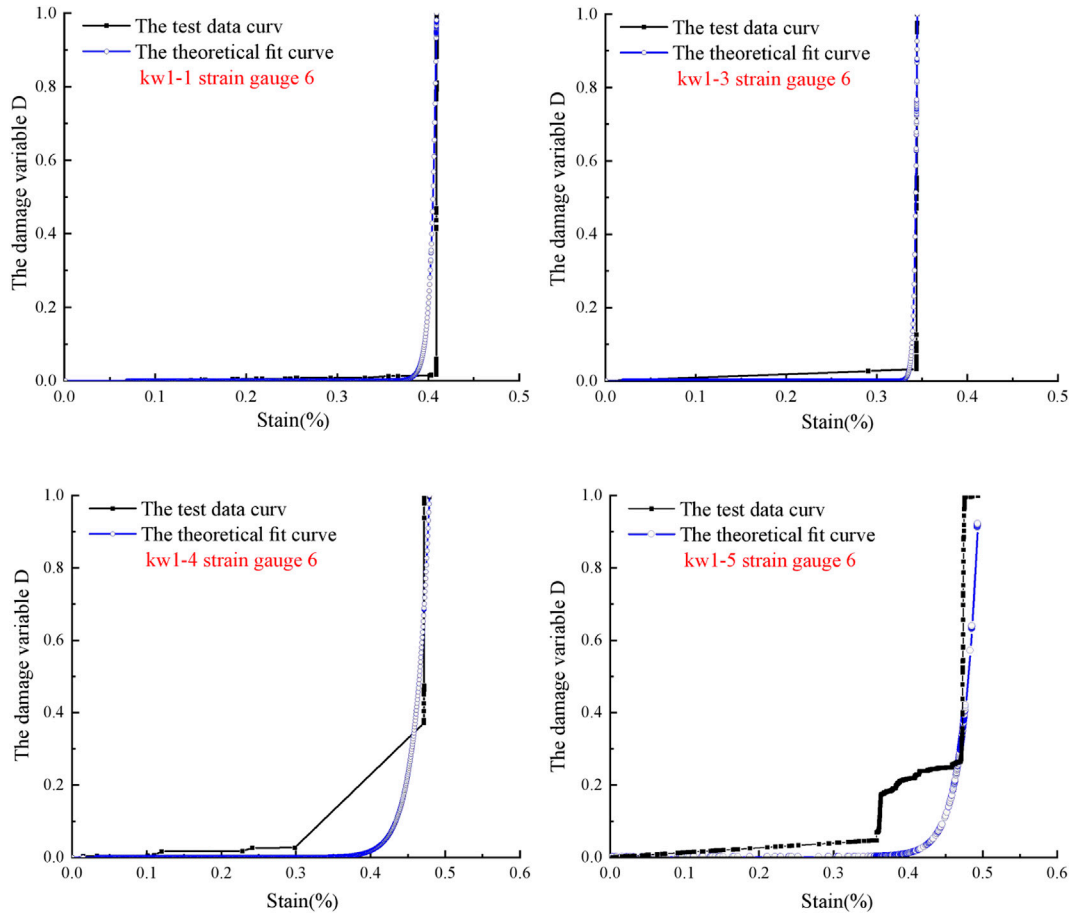

FIGURE 5
Evolution law of damage variables with time.

where M is the maximum bending moment, P is the vertical compressive load, l is the length of the limestone sample, b is the width of the section, h is the height of the section, Iz is the moment of inertia of the cross-section to the bending neutral layer, and y is the distance from the stress location to the bending neutral layer.

The stress essentially represents the central stress of the block element during numerical calculation, but the maximum principal stress under the bending failure progress is located at the tensile side edge of the rock beam. Therefore, it is necessary to convert the stress (block element stress contained in any section perpendicular to the neutral axis) to the bottom edge bending stress σ_b. The method is shown in the following steps:

1) Assuming the normal stress along the x direction at any block element center in the rock beam is $\sigma_{x(ij)}$, by using the Lagrangian interpolation method for the center stress of each block element of a section that is perpendicular to the horizontal beam, the value of the normal stress distribution along the x direction of the section can be obtained. The calculative method is showed as Eq. 17:

$$\sigma_x'(r) = \sum_{i=1}^{m} \sigma_{x(ij)} l_i(r) \tag{17}$$

Where $l_i(r)$ is the Lagrange interpolation basis function, the calculation equation is shown as follows:

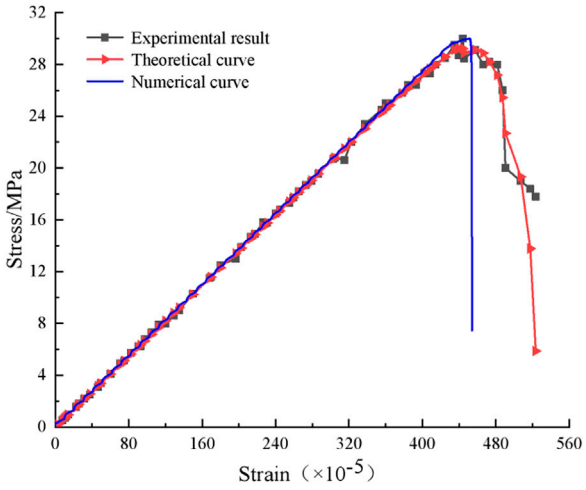

FIGURE 6
Comparison of σ-ε curves at strain gauge 6 of specimen KW1-5.

$$l_i(r) = \frac{(r-r_1)\cdots(r-r_{i-1})(r-r_{i+1})\cdots(r-r_m)}{(r_i-r_1)\cdots(r_i-r_{i-1})(r_i-r_{i+1})\cdots(r_i-r_m)} \quad (18)$$

Where r_i is the distance from the center of each block element in column j to the neutral axis, and r is the distance from each point of column j unit to the neutral axis.

2) The bending torque (M) of the block element can be obtained by taking the torque from $\sigma_x'(r)$ to the block element center. Since the stress distribution of $\sigma_x'(r)$ is polynomial, the equation for obtaining M by integrating $\sigma_x'(r)$ is as follows:

$$M = -\int_0^{h'} \sigma_x'(r)dr \quad (19)$$

Where h' is the height of the block element.

After the bending torque M is obtained, the bending stress σ_b at the lower boundary of each block element of rock beam can be calculated by Eq. 20:

TABLE 2 Parameters in numerical tests.

Parameter	E/GPa	μ	c/MPa	φ/°	R_t/MPa
Limestone	6.83	0.24	3.5	38	33.0

$$\sigma_b = \frac{6\sum M}{bh'^2} \quad (20)$$

4 Three-point bending numerical test of rock beam

To verify the accuracy of the bending damage evolution model and the rationality of the damage tensile fracture criterion of the limestone beam under the action of a three-point bending load, the numerical test was carried out by using FLAC^{3D} software according to the indoor test data.

4.1 Compilation of damage constitutive model

Based on the self-contained Mohr-Coulomb model of FLAC^{3D}, the numerical simulation of the damage constitutive model of limestone beam under three-point bending test was realized by the built-in FISH language. For each element, the strain increment in x direction was accumulated at each calculation time step and used to calculate the damage variable (Eq. 11). The damage deterioration of the elastic modulus and damaged stress were corrected (Eq. 12). The bending stress was calculated according to Eqs 14–17, and it was judged whether bending failure occurred according to Eq. 13.

4.2 Model and parameters

The numerical test parameters are based on the indoor data of the three-point bending test (L=0.6 m, b=0.1 m, h=0.1 m). The numerical calculation model is shown in Figure 7, and the numerical calculation physical and mechanical parameters are shown in Table. 2.

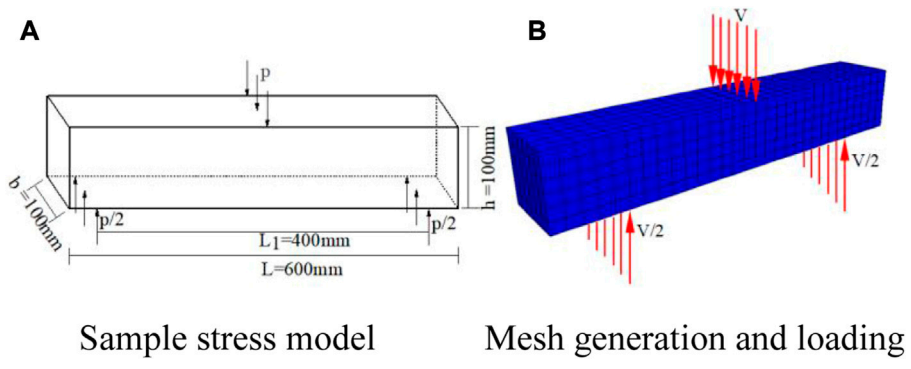

FIGURE 7
Calculation model diagram. **(A)** Sample stress model, **(B)** Mesh generation and loading.

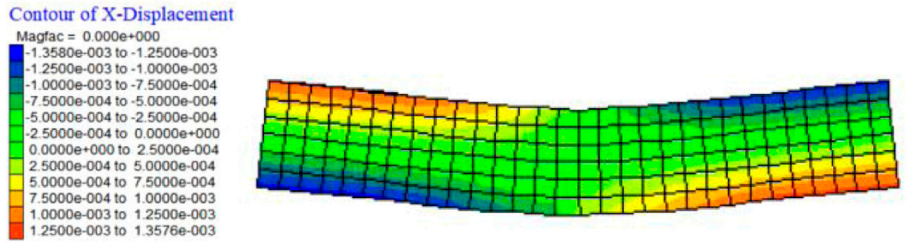

FIGURE 8
x-displacement distribution.

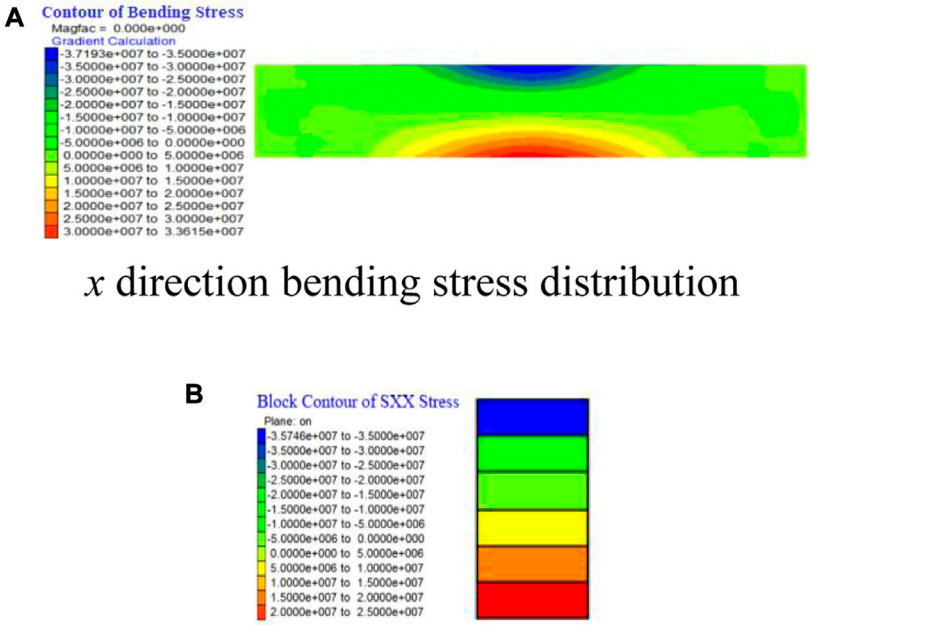

FIGURE 9
Distribution of bending stress and *x*-direction stress. **(A)** *x* direction bending stress distribution, **(B)** Stress distribution in x direction of section element *x*=0.

FIGURE 10
Distribution of bending zones.

4.3 Result analysis

As for the horizontal bottom of the rock beam, the stress–strain relationship at the section (*x*=0) during the numerical test is shown in the blue curve in Figure 6.

We can find that the bending stress of numerical calculation increases with the strain and drops sharply after the peak stress is about 30 MPa, which closely coincides with the test curve and theoretical curve. The displacement distribution along the *x* direction of the rock beam is shown in Figure 8. The

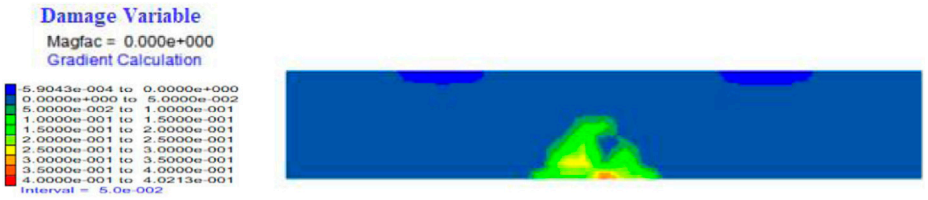

FIGURE 11
Distribution of damage variable.

displacement increases from the central section to both edges along x direction gradually. The maximum displacement. which is mainly distributed at the top and bottom of the specimen, is about 1.36 mm, and the minimum displacement is 0 mm, distributed near the neutral layer. The deformation process of the rock beam during three-point bending has been exhibited straightly by the numerical simulation test results. The rock beam deforms under the action of bending stress, the central part deforms downward, and both ends tilt up. At the same time, the bottom of rock beam is deformed towards both ends by tension, and the upper part is deformed towards the neutral layer by compression. Therefore, the bending failure begins with the tensile crack at the bottom of the specimen, and gradually extends to the compression zone. In the process, the neutral layer shifts upward. Since the tensile crack failure process is very short, the neutral layer shift is not considered in this work.

As shown in Figures 9A, B, the compressive stress in the x direction increases from the neutral layer to the top of the rock beam, and the maximum compressive stress is about 35.7 MPa, which is distributed in the area above the neutral layer. The tensile stress in the x direction increases from the neutral layer to the bottom of the rock beam, and the maximum tensile stress is about 25.0 MPa, which is distributed in the area below the neutral layer. The maximum compressive stress is greater than the maximum tensile stress. The maximum tensile stress is distributed in the central of the bottom of the specimen where the bending effect is most obvious, which is consistent with the deformation of the indoor test. At the same time, the bending stress distribution is close to the x-direction normal stress of the section element x=0, but the value is different. The bending stress at the bottom of the middle of the rock beam is 33.6 MPa, obviously greater than the stress in the x direction, which is also the reason why the unit center stress cannot replace the edge tensile stress.

The tensile fracture zone is shown in Figure 10, mainly distributed at the bottom of the beam. The damage starts from the tensile zone at the bottom of the beam, and the maximum damage value is about 0.402 before the stress reaches the peak value (Figure 11), which is close to the damage variable value caused by the same stress in Figure 5. The stress distribution of each section is consistent with the actual situation.

5 Conclusion

1) The bending failure progress of limestone beam can be divided into three stages from the analysis of stress-cumulative ringing–time curves: (I) the microcracks compaction stage, (II) microcracks expansion stage, and (III) microcracks penetration stage. Correspondingly, the evolution of the bending damage variable D is also divided into initial damage stage, slow damage stage, and accelerated damage stage. The damage variable D increases rapidly when the stress increases to 80% of the peak stress.
2) The damage variable D is corrected by the data of the three-point bending test, and the result conforms to the actual test situation. Under the conditions of damage variable D, the stress–strain constitutive model of three-point bending tensile zone of limestone rock beam is established based on the Lemaitre strain equivalent principle and continuous damage theory, and the obtained curve is in good agreement with the fitting curve of the test data.
3) The yield criterion of bending stress is selected as the bending failure criterion. The specific implementation process of stress damage deterioration, the calculation of bending stress at the lower edge of the limestone beam, and the bending failure criterion are programmed by FISH language to realize the secondary development of software FLAC^{3D}, thus programmatically realizing the calculation of the damage deterioration formula and bending criterion. The numerical simulation results show that: ① The stress–strain curve of the whole bending deformation progress is in good agreement with the fitting curve of the test results and the prediction curve of the theoretical model. ② According to the cloud diagram of displacement distribution in the x direction, the rock beam deforms under the action of bending stress, the central part deforms downward, and both ends tilt up. Therefore, the bending failure begins with the tensile crack at the bottom of the specimen and gradually extends to the compression zone. The maximum damage value is about 0.402 before the peak stress. ③ The compressive stress in the x direction increases from the neutral layer to the top of the rock beam, and the tensile stress in the x direction increases from the neutral layer to the bottom of the rock beam. The maximum tensile stress is distributed in the center of the bottom of the specimen where the bending effect is most obvious, which is consistent with the deformation of the indoor test.

Data availability statement

The original contributions presented in the study are included in the article/supplementary material, further inquiries can be directed to the corresponding author.

Author contributions

All authors listed have made a substantial, direct, and intellectual contribution to the work and approved it for publication.

Funding

This work was supported by Major Science and Technology Special Project of Guizhou Province, China [No. (2018)3011], Guizhou Provincial Science and Technology Foundation [(2020)1Z052].

Conflict of interest

Authors BL and JT were employed by company Guizhou Transportation Planning Survey and Design Academic Co., Ltd.

The remaining authors declare that the research was conducted in the absence of any commercial or financial relationships that could be construed as a potential conflict of interest.

Publisher's note

All claims expressed in this article are solely those of the authors and do not necessarily represent those of their affiliated organizations, or those of the publisher, the editors and the reviewers. Any product that may be evaluated in this article, or claim that may be made by its manufacturer, is not guaranteed or endorsed by the publisher.

References

Aggelis, D. G., Mpalaskas, A. C., and Matikas, T. E. (2013). Investigation of different fracture modes in cement-based materials by acoustic emission. *Cem. Concr. Res.* 48, 1–8. doi:10.1016/j.cemconres.2013.02.002

Andreev, G. E. (1991). A review of the Brazilian test for rock tensile strength determination. Part I: Calculation formula. *Min. Sci. Technol.* 13 (3), 445–456. doi:10.1016/0167-9031(91)91006-4

ASTM International (2008). *Standard test method for splitting tensile strength of intact rock core specimens[S]*. West Conshohocken: ASTM.

Atkinson, B. K. (1992). *Rock fracture mechanics*. Beijing: Earthquake Press.

Cai, M., Kaiser, P. K., and Martin, C. D. (2001). Quantification of rock mass damage in underground excavations from microseismic event monitoring. *Int. J. Rock Mech. Min. Sci.* 38 (8), 1135–1145. doi:10.1016/s1365-1609(01)00068-5

Deng, C. F., Liu, J. F., and Chen, L. (2016). Study on fracture mechanical behavior and acoustic emission characteristics of granites with different particle sizes. *Rock Soil Mech.* 37 (08), 2313–2320.

Gan, Y. X., Wu, S. C., Ren, Y., and Zhang, G. (2020). Evaluation indexes of granite splitting failure based on RA and AF of AE parameters. *Rock Soil Mech.* 41 (7), 2324–2332.

Guan, H., Huang, B. X., and Feng, H. (2012). Experimental study on three-point bending fracture characteristics of limestone sample. *Coal Sci. Technol.* 40 (07), 5–9.

International Society for Rock Mechanics (1978). Suggested methods for determining tensile strength of rock materials. *Int. J. Rock Mech. Min. Sciences&, Geomechanics Abstr.* 15 (3), 99–103.

Jiang, L. C., and Wen, Y. (2011). Damage constitutive model of sandstone during corrosion by AMD. *J. Central South Univ. Sci. Technol.* 42 (11), 3502–3506.

Lacidogna, G., Piana, G., and Carpinteri, A. (2018). Damage monitoring of three-point bending concrete specimens by acoustic emission and resonant frequency analysis. *Eng. Fract. Mech.* 210, 203–211. doi:10.1016/j.engfracmech.2018.06.034

Li, Y. F., Dong, S. M., and Pan, X. (2018). Experimental study of mixed-mode I/III fracture of sandstone. *Rock Soil Mech.* 39 (11), 4063–4070.

Liao, Z. Y., Zhu, J. B., and Tang, C. A. (2019). Numerical investigation of rock tensile strength determined by directtension, Brazilian and three-point bending tests. *Int. J. Rock Mech. Min. Sci.* 115, 21–32. doi:10.1016/j.ijrmms.2019.01.007

Liu, B. X., Huang, J. L., and Wang, Z. Y. (2009a). Study on damage evolution and acoustic emission character of coal-rock under unixial compression. *Rock Mech. Eng.* 28 (S1), 3234–3238.

Liu, Y. M., Wang, J., Cai, M. F., Wang, S. R., and Ke, D. (2009b). Study on disposal pit space for high-level radioactive waste in thermal mechanical coupling conditions. *Uranium Geol.* 25 (6), 373–379.

Lu, H., Feng, X. T., and Yang, C. X. (2021). Effect of different notch prefabricated methods and different notch length on three-point bending test of rock. *Rock Soil Mech.* 42 (4), 1115–1125.

Pandey, P., and Singh, D. P. (1986). Deformation of a rock in different tensile tests. *Eng. Geol.* 22 (3), 281–292. doi:10.1016/0013-7952(86)90029-3

Pei, J. L., Liu, J. F., Zuo, J. P., and Zhang, R. (2013). Investigation on dynamic evolution process of natural fractures based on acoustic emission position. *Chin. J. Rock Mech. Eng.* 32 (4), 696–704.

Pine, R. J., Owen, D. R. J., Coggan, J. S., and Rance, J. M. (2007). A new discrete fracture modelling approach for rock masses. *Geotechnique* 57 (9), 757–766. doi:10.1680/geot.2007.57.9.757

Prem, P. R., and Murthy, A. R. (2016). Acoustic emission monitoringof reinforced concrete beams subjected to four-pointbend-ing. *Appl. Acoust.* 117, 28–38. doi:10.1016/j.apacoust.2016.08.006

Tang, C. A., Wang, S. H., and Fu, Y. F. (2003). *Numerical test of rock failure process*. Beijing: Science Press.

Tian, Y. L., Chen, S. W., Zuo, S. Y., Yang, F. B., He, Q., and Zheng, K. X. (2022). Experimental study on thermo-mechanical properties of Beishan granite under mild temperature. *Case Stud. Therm. Eng.* 37, 102271. doi:10.1016/j.csite.2022.102271

Tian, Y., Yu, R. G., Zhang, Y., and Zhao, X. B. (2020). Application of acoustic emission characteristics in damage identification and quantitative evaluation of limestone. *Adv. Eng. Sci.* 52 (3), 115–122.

Wu, X. Z., Liu, J. W., and Liu, X. X. (2015). Study on the coupled relationship between AE accumulative ring-down count and damage constitutive model of rock. *J. Min. Saf. Eng.* 32 (1), 28–34.

Yang, M. H., Zhao, M. H., and Cao, W. G. (2005). Determination of parameters of statistical constitutive model for rock damage softening. *J. Hydraulic Eng.* 36 (03), 345–349.

Yang, X. F., Lu, Z. D., and Xing, C. (2022). Study on mechanical model of slip bending failure mechanism of bedding rock slope with plate crack structure. *Rock Soil Mech.* 43 (S1), 258–266.

Yao, W., Xia, K. W., and Li, X. (2018). Non-local failure theory andtwo-parameter tensile strength model for semi-circularbending tests of granitic rocks. *Int. J. Rock Mech. Min. Sci.* 110, 9–18. doi:10.1016/j.ijrmms.2018.07.002

Zeng, J. (2015). *Experimental study on influencing factors of acoustic emission characteristics of Chongqing sandstone under three-point bending test conditions[D]*. Chongqing: Chongqing University.

Zhang, M., Li, Z. K., and Yang, Q. (2006). Adamage model and statistical analysis of acoustic emission for quasi-brittle materials. *Rock Mech. Eng.* 25 (12), 2493–2501.

Zhang, Z. (1994). *Principles of engineering geology[M]*. Beijing: Geologic Press.

Zhou, Y. F., Zhu, X., and Liu, W. D. (2019). Identification of cracking characteristics of limestone under uniaxial compression conditions using acoustic emission and GMM, Water Resour. *Hydropower Eng.* 50 (11), 131–140.

Zuo, J. P., Wang, J. T., Sun, Y. J., Chen, Y., Jiang, G. H., and Li, Y. H. (2017). Effects of thermal treatment on fracture characteristics of granite from Beishan, a possible high-level radioactive waste disposal site in China. *Eng. Fract. Mech.* 182, 425–437. doi:10.1016/j.engfracmech.2017.04.043

Zuo, S. Y., Shi, W. B., and Liang, F. (2015). Numerical simulation and engineering application for failure modes and criterion of layered anisotropic rock mass. *Chin. J. Geotechnical Eng.* 37 (1), 191–196.

Zuo, S. Y., Ye, M. L., and Tang, X. L. (2013). Numerical model and validation of failure mode for underground caverns in layered rock mass. *Rock Soil Mech.* 34 (1), 458–465.

frontiers | Frontiers in Earth Science

TYPE Original Research
PUBLISHED 09 May 2023
DOI 10.3389/feart.2023.1182413

OPEN ACCESS

EDITED BY
Guangjin Wang,
Kunming University of Science and Technology, China

REVIEWED BY
Gengshuo Zhang,
The University of Queensland, Australia
Xiang Fan,
Chang'an University, China

*CORRESPONDENCE
Haijun Zheng,
zhangyan2020@cdut.edu.cn

RECEIVED 08 March 2023
ACCEPTED 21 April 2023
PUBLISHED 09 May 2023

CITATION
Liu S, Zheng H, Chen G, Hu Y and Meng K (2023), Acoustic emission precursor information of rock failure under true triaxial loading and unloading conditions. *Front. Earth Sci.* 11:1182413. doi: 10.3389/feart.2023.1182413

Acoustic emission precursor information of rock failure under true triaxial loading and unloading conditions

Sijie Liu, Haijun Zheng*, Guoqing Chen, Yitao Hu and Kai Meng

State Key Laboratory of Geohazard Prevention and Environment Protection, Chengdu University of Technology, Chengdu, China

Rock failure generally leads to serious consequences, and it is significant to obtain the precursor information prior to failure using associated techniques. Acoustic emission (AE) is one of the indispensable methods for disaster warning of hard and brittle rock. Acoustic emission detection technology can effectively monitor real-time information about changes in the rock interior and predict the process of rock damage failure. To probe the relationship among the AE precursor information of red sandstone under different intermediate principal stresses, an experimental study was conducted by us to examine the alterations in AE parameters during the failure of red sandstone under both loading and unloading circumstances. The study shows that the ringing count rate and absolute energy *versus* time curves are divided into four stages, namely, quiet, frequent, sudden increase and decline periods. The cumulative count curve is also divided into four phases: pre-unloading period, post-unloading period, sharp increase period, and decrease period. With the rise of the intermediate principal stress, the ringing count rate and energy exhibited during the frequent period of AE demonstrate a consistent increase, with a larger increase in the maximum value and a smaller increase in the average value. In addition, the peak value of AE signals during failure also increases accordingly. The occurrence moment and clarity of the frequent period determine the reliability and priority of the information related to the rock's failure precursor; moreover, the reliability and priority of the AE precursor information will increase with the increase of the intermediate principal stress. After comparison, it is found that the AE precursor information occurs prior to the thermal infrared precursor information.

KEYWORDS

loading and unloading, true triaxial test, acoustic emission, thermal infrared precursor information, failure

1 Introduction

Acoustic emission (AE) is a transient elastic wave within a material due to the rapid release of local strain energy. The generation and development of internal fractures in brittle rocks during failure is a good AE signal source, and since there are no obvious anomalies on the surface of hard brittle rocks before instability failure, it is often challenging to predict the occurrence of such type of failures. Therefore, as a concomitant phenomenon, AE produced during the rock failure process can provide effective information for predicting rock instability failure and provide significant evidence for predicting rock failure (Fortin

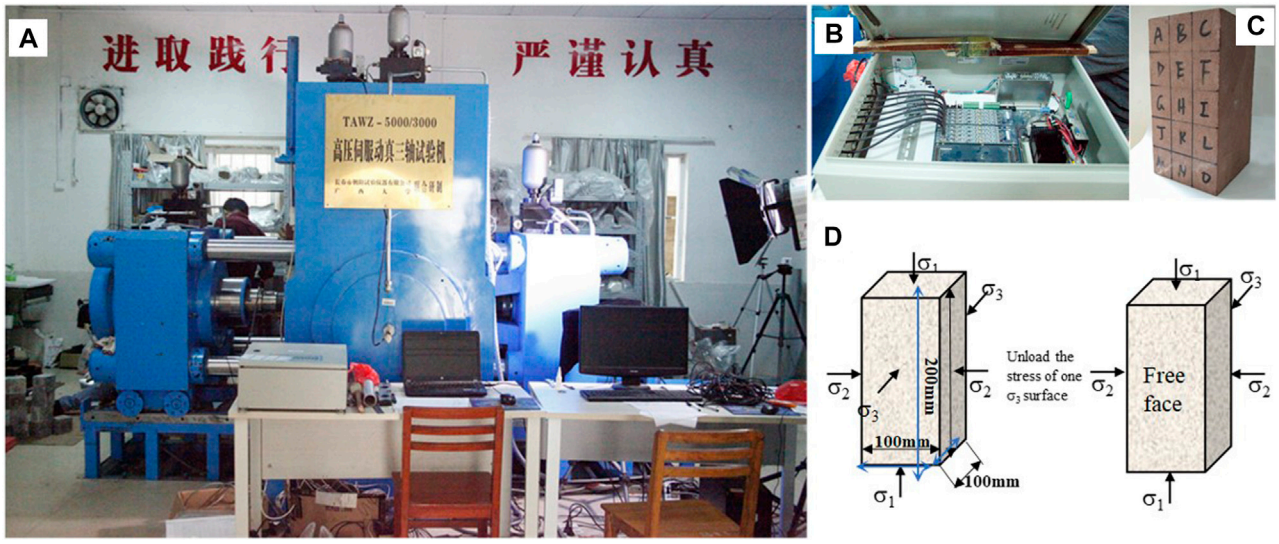

FIGURE 1
Diagram of test equipment, specimen and stress state. **(A)** High pressure servo-motion true triaxial tester. **(B)** Micro-II Digital AE System. **(C)** Red sandstone specimens. **(D)** Schematic diagram of the true triaxial loading and unloading stress state.

TABLE 1 Details of true triaxial load and unload tests.

Test group number	σ_1/MPa	σ_2/MPa	σ_3/MPa	Number of specimens
A-1	60	10	5→0	3
A-2	60	20	5→0	3
A-3	60	40	5→0	3
A-4	60	60	5→0	3

et al., 2009; Brantut et al., 2011; Zhang et al., 2019; Chen et al., 2020), thus better ensuring the safety of people's lives and property.

During rock failure, a large amount of elastic strain energy could be released, and monitoring changes in AE parameters has become a new direction in the study of rock failure. Through analysis of variations in AE parameters during rock failure, the alterations in the internal structural condition of the rock mass can be identified, thereby allowing for inference of the mechanism underlying rock mass failure. It has been proposed that the b-value of AE in rock failure exhibits a tendency to decrease as stress increases prior to failure and experiences a marked decrease at the moment of failure (Lei, 2006; Dong et al., 2022). The acoustic response and fractal dimension can reflect the evolution and expansion of fractures during loading, and the acoustic fractal values can be used to study the precursor information of rock failure (Kong et al., 2016; Xu et al., 2017). Furthermore, the spatial correlation length of acoustic emissions can be regarded as a precursor parameter for rock failure, which generally increases during the failure process (Tyupkin and Giovambattista, 2005; Li et al., 2010). The spatial AE localization technique enables the analysis of the internal fracture evolution of rock specimens over the loading process (Yang et al., 2012; Wang et al., 2022). The sharp increase in various parameters of AE is closely associated with the occurrence of rock fractures (Zhao et al., 2015; Moradian et al., 2016).

True triaxial stress paths can accurately reflect the deformation and failure patterns of rock masses caused by different excavation methods in engineering and can better simulate the mechanical response and deformation and failure characteristics of rock masses after excavation. Mogi (1971) successfully developed the world's first true triaxial test machine for rocks, proving the existence of intermediate principal stress effects on rocks. The effect of intermediate principal stresses on the strength characteristics of rocks has been confirmed by many scholars (Haimson and Chang, 2012; Ma et al., 2017). In addition, many studies based on true triaxial tests have shown that intermediate principal stresses have significant influence on the mechanical properties, failure mechanisms, and underground engineering stability of rocks (Ma et al., 2014; Feng et al., 2016; Vachaparampil and Ghassemi, 2017; Gao et al., 2018; Zhang et al., 2021; Zhao et al., 2022a; b; Xu et al., 2022).

In this study, the variation of AE parameters of red sandstone under different intermediate principal stresses are investigated, the similarities and differences among the acoustic emissions under different intermediate principal stresses are compared, and finally

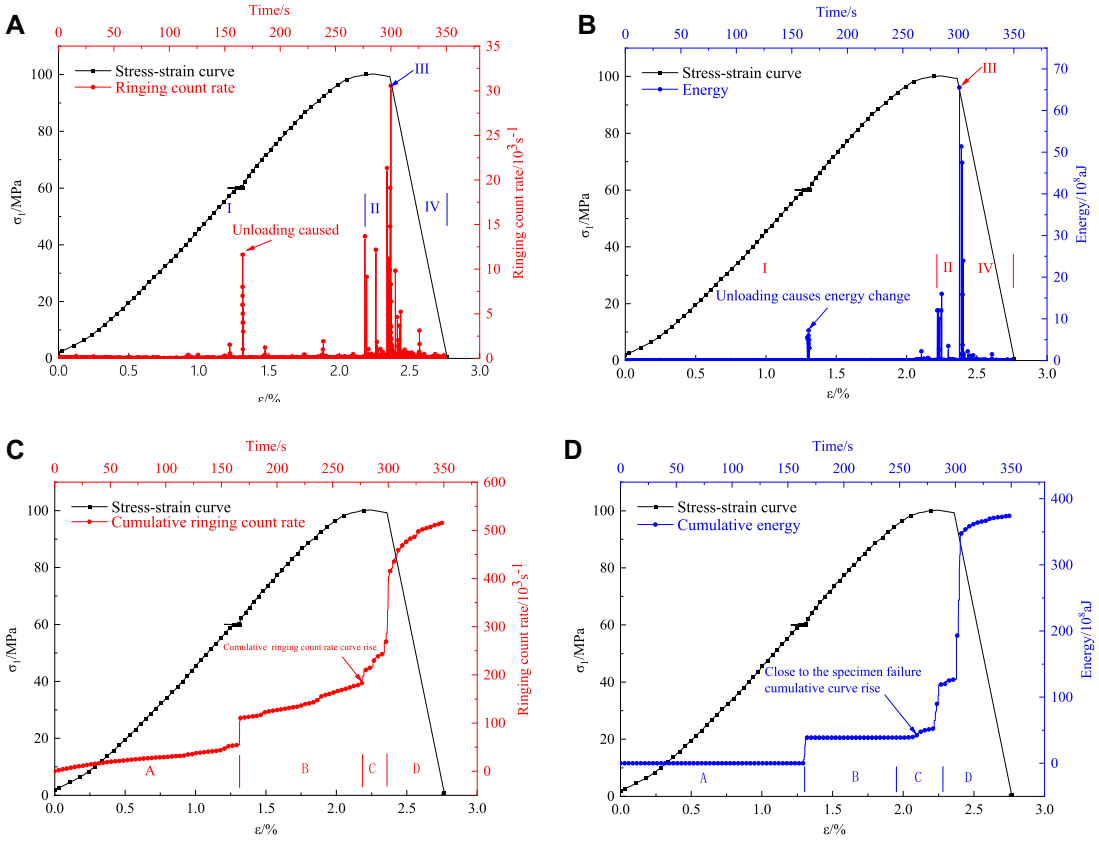

FIGURE 2
Relationship between AE parameters and time at 10 MPa. **(A)** Ringing count rate curve. **(B)** Absolute energy curve. **(C)** Cumulative ringing count rate curve. **(D)** Accumulated absolute energy curve.

the AE precursor information before rock failure through true triaxial tests under unloading conditions are analyzed. The temporal relationships among the various precursors were identified, for the purpose of better predicting and preventing excavation and unloading-induced rock instability failure.

2 Test methods

2.1 Test conditions and test equipment

The red sandstone specimens used are dense and tight, with a good integrity. The specimens are rectangular in shape and its dimensions are 100 mm × 100 mm × 200 mm with a flatness error of ± 0.05 on the end face and a verticality error of ± 0.25°C. The minimum principal stress in the true triaxial loading test is 5 MPa, and a total of 4 different intermediate principal stress conditions were set up. In each condition 3 specimens were tested, and a total of 12 specimens were used.

The true triaxial test was carried out using the new high-pressure servo-dynamic true triaxial rigidity tester TAW1-5000/3000 (Figure 1) (Su et al., 2017). The development, extension and penetration of fractures on the rock surface were captured using a high speed digital camera developed by SVSI, United States. The AE monitoring was conducted using the Micro-II Digital AE System from PAC company, United States. The FLIRSC305 infrared thermal imaging camera was also used to monitor the changes in the thermal image of the specimen's free face.

2.2 True triaxial loading and unloading test scheme

The initial ground stress is set before the test, where σ_1 represents the maximum principal stress, σ_2 represents the intermediate principal stress and σ_3 denotes the minimum principal stress, the direction of the minimum principal stress is the free face.

Test scheme: first, the stress of 0.5 MPa was applied to σ_1 using the displacement control method in order to connect the specimen end face with the face of the transfer column. Then, the load control method was employed to reach the design value σ_1 at a loading rate of 0.2 MPa/s. After that, using the same method, keep σ_1 unchanged and load σ_2 to the design value; keep σ_2 unchanged and load σ_3 to the design value and maintain this stress state for 10 s. After the initial stress loading was completed, one side was quickly unloaded, while the opposite side was adjusted to displacement control. Then, σ_1 was increased at a loading rate of 2 kN/s until the instability failure of the specimen. The stress state is shown in Figure 1D, and the stress path is the same as the true triaxial loading path. During this process, AE,

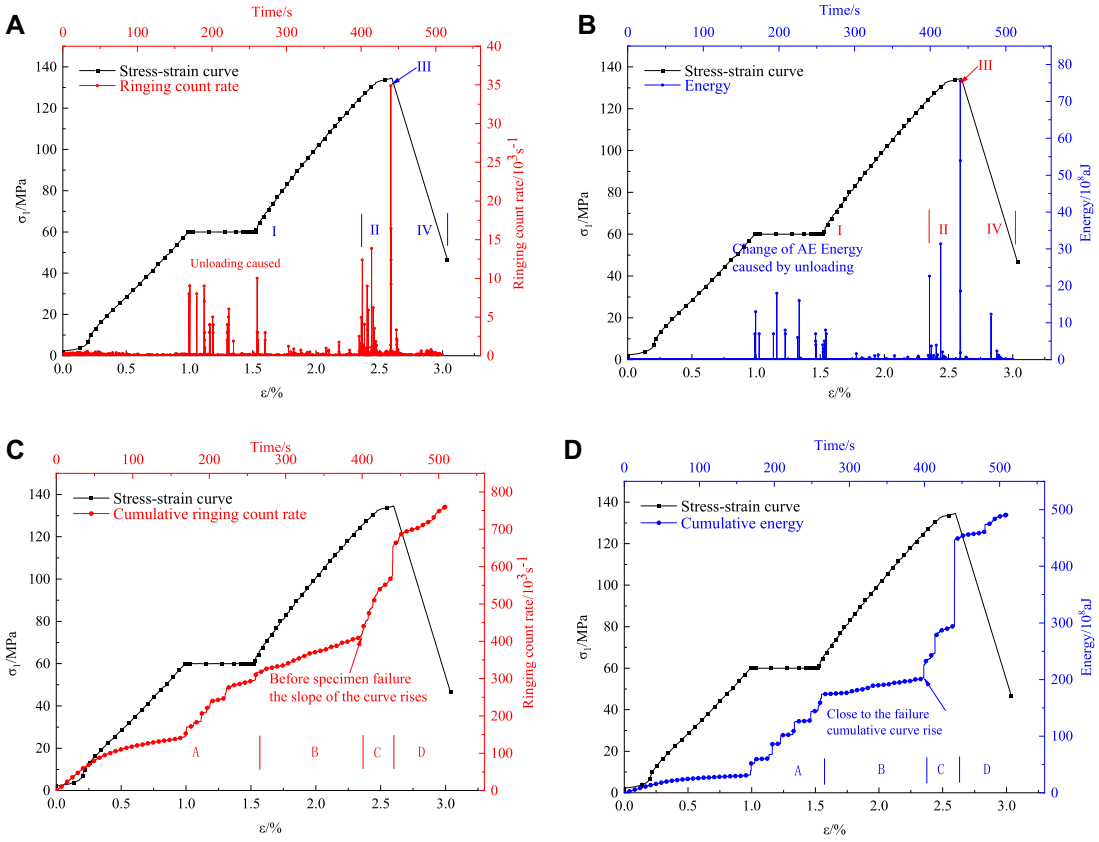

FIGURE 3
Relationship between AE parameters and time at 20 MPa. **(A)** Ringing count rate curve. **(B)** Absolute energy curve. **(C)** Cumulative ringing count rate curve. **(D)** Accumulated absolute energy curve.

high-speed camera and infrared thermal imaging camera collected data simultaneously. The true triaxial stress levels for this study were listed as follows: σ_1 was set at 60 MPa. σ_2 was set as 10 MPa, 20 MPa, 40 MPa, and 60 MPa, respectively; σ_3 was set as 5 MPa. The test details are shown in Table 1.

3 Experimental results and analysis

3.1 Characteristics of AE precursor information

The AE characteristics of rocks in true triaxial loading tests and the corresponding precursor information have been extensively studied in previous studies. On this basis, the AE signals in real triaxial loading and unloading tests were investigated to decode their characteristics under this stress path and the precursor information before rock failure. In particular, analyzing the AE characteristics under different intermediate principal stresses and comparing the similarities and differences.

Figure 2 shows the curves of each AE parameter *versus* time under the intermediate principal stress of 10 MPa. Which I is quiet period, II is frequent period, III is sudden increase period, IV is decrease period, A is pre-unloading period, B is post-unloading period, C is sudden increase period and D is decrease period. Figures 2A, B show the ringing count rate and absolute energy, respectively, and Figures 2C, D display the corresponding cumulative count curves. According to Figures 2A, B, the quiet period is the longest in the whole process. In general, the ring count rate remains in a low level but increases significantly when the specimen is disturbed during unloading. The frequent period accounts for about 7% of the whole process, and the overall level of ringing count rate and energy level is increased, and microcracks inside the specimen are pervasively developed. The sudden increase period is the shortest due to the specimen failure that makes the ringing count rate and energy rise steeply and then fall back in a short time. It is prominent that the rock failure process is extremely short. After the ringing count rate and energy fall back, they enter into the decrease period, during which the number of AE specimens gradually decreases. Based on the characteristics of the changes in AE ringing count rate and energy, it can be inferred that before the failure of the specimen, the levels and numbers of AE events will significantly increase. This indicates that internal micro-cracks have developed extensively and interconnected within the specimen, implying that the rock specimen is about to fail.

Figures 2C, D show the cumulative counting curves of AE ringing count rate and energy *versus* time. The cumulative curves are divided into four periods A, B, C, and D, which are named as pre-unloading period, post-unloading period, sharp increase period, and decrease period, respectively. Notably, there is a sudden jump in the

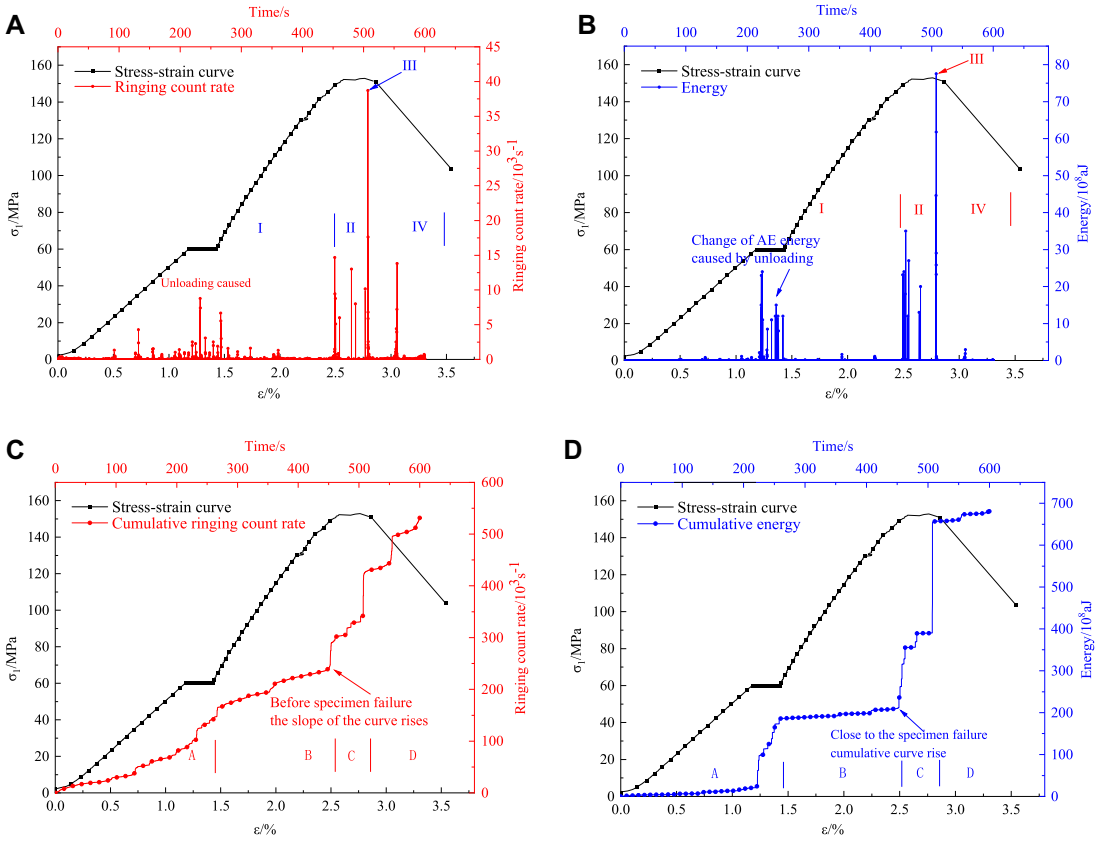

FIGURE 4
Relationship between AE parameters and time at 40 MPa. **(A)** Ringing count rate curve. **(B)** Absolute energy curve. **(C)** Cumulative ringing count rate curve. **(D)** Accumulated absolute energy curve.

cumulative curve of the ringing count rate, and the slope of the curve increases after the jump. 25 s before the steep increase, the curve enters the sudden increase period. During this period, the curve rises obviously, this information can serve as a precursor for rock failure. The cumulative curve increases sharply and steeply when the specimen is damaged and then returns to flat. The cumulative energy curve has only slight change in slope before and after unloading and enters the sudden increase period 36 s before specimen failure. In this period, the AE energy increases multiple times, resulting in a stair-stepping pattern.

Figure 3 shows the curves of each AE parameter *versus* time under an intermediate principal stress of 20 MPa. As shown in Figures 3A, B, the overall characteristics of the ringing count rate and energy curves are similar. In the quiet period, the overall AE signal level is low, and the signal appears to rise significantly during the unloading period. Around 44 s before the specimen failure, the AE enters a frequent period, during which the number of AE specimens and the signal level increase significantly, with abundant microcrack development inside the specimen. Then, specimen failure occurs. The AE signal increases steeply and then falls back, and finally declines gradually. The changing characteristics of ringing count rate and energy show that at the early stage of loading, there are no internal microcracks and the AE signal is less. During the unloading process, the rock specimen is disturbed both inside and outside, and the acoustic signal increases significantly. The quiet period accounts for the largest proportion of the entire process, reaching about 78%, and the frequent period accounts for 8%–9%, which can effectively warn the rock failure. Additionally, the rapid rock failure leads to a short period of sudden increase, accounting for only about 1% of the whole process.

The cumulative counting curve is clearly segmented, showing multiple periods. The slope of the curve after unloading is higher than that before unloading, and the curve rises faster during the unloading period, exhibiting a stair-stepping pattern. The curve enters the sudden increase period when 45 s before the specimen failure (Figures 3C, D).

Figure 4 shows the curves of each parameter of AE *versus* time under an intermediate principal stress of 40 MPa. As shown in Figures 4A, B, the overall level of both AE ringing count rate and energy increases as the intermediate principal stress increases, and the number of AE events during the unloading period increases significantly. The duration of the frequent period of AE increases by 51 s, and the number of AE events during this period fluctuates drastically. The overall change in AE ringing count rate and energy is similar, showing an abrupt increase at the unloading, pre-failure, and failure moments.

According to Figures 4C, D, the cumulative curve rises faster and the slope is relatively steeper during the unloading period. Furthermore, the slope of the post-unloading cumulative curve is larger than that before unloading. Stage C marks the sudden

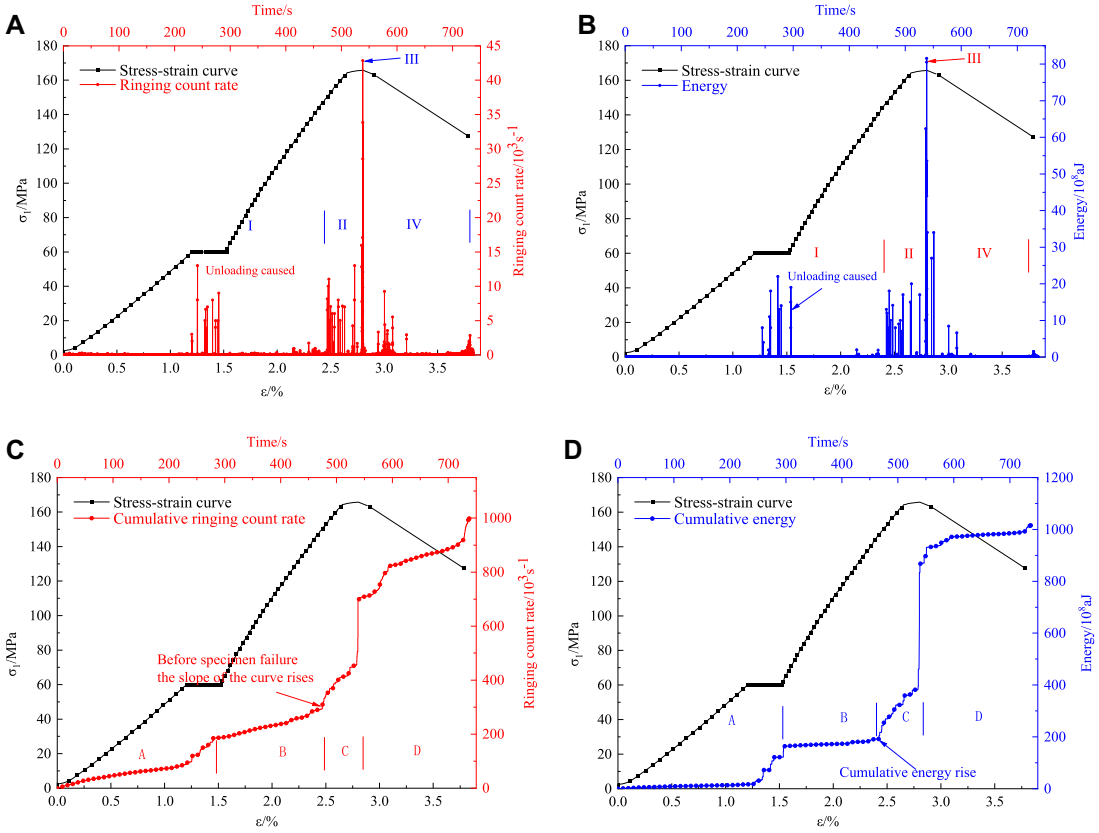

FIGURE 5
Relationship between AE parameters and time at 60 MPa. **(A)** Ringing count rate curve. **(B)** Absolute energy curve. **(C)** Cumulative ringing cumulative count rate curve. **(D)** Accumulated absolute energy curve.

increase period of the cumulative curve, which corresponds to the period of frequent AE the fluctuate AE characteristic in the frequent period, when manifested in the cumulative curve, shows a stair-stepping pattern. When the specimen is damaged, the cumulative curve rises steeply in a short time and then becomes approximately horizontal.

Similar to the above figures, Figure 5 shows the curves at an intermediate principal stress of 60 MPa. As shown in Figures 5A, B, the AE grows prominently during the unloading frequent periods. The first half of the frequent period is characterized by numerous increasing acoustic signals, indicating that the microcracks inside the rock specimen are highly developed. By comparison, the signals are sparse in the second half, which demonstrates that most of the internal microcracks are interconnected. This indicates that most of the micro-cracks inside the rock specimen have interconnected, and a large number of cracks hinder the propagation of acoustic signals within the rock, resulting in a decrease in AE signals. The starting point of the frequent period of the ringing count rate is 74 s away from the steep increase point, and the starting point of the frequent period of energy is 85 s away from the sudden increase point.

As shown in Figures 5C, D, in the period before unloading, the cumulative curve is approximately horizontal, with a slow increase in the AE signal. However, unloading leads to a sudden increase in the AE signal, and the curve shows a stair-stepping-shape increase. Then, the signal remains generally stable. About 76 s before the specimen failure, the curve again rises in steps, followed by a steep and sudden increase. There are similarities and differences between the ringing count rate and energy curves. For the similarities, there are two stair-stepping-shape increase in the curve, and the post-unloading curve slope is higher than that before unloading. For the differences, first, the sudden increase period of energy is 2 s less than that of the ringing count rate. In addition, the energy grows more significantly than the ringing count rate when the cumulative curve rises steeply. Comparatively, the cumulative curves of ringing count rate and energy are similar in overall changing characteristics and rising patterns.

After comparison, this can be seen that the cumulative AE curve is more obviously segmented, which can better reflect the growth of AE signal at each period. The ringing count rate and absolute energy reflect the actual acoustic signal changes during the loading process as well as the development of microcracks within the rock at each moment. Both the two forms of AE have precursor information. Specifically, the ringing count rate and absolute energy focus on full process monitoring, while the cumulative counting approach focuses on the segmentation of the AE. By presenting the AE ringing count rate and energy as cumulative forms, the curves not only show segmented, but also emphasize AE anomalies at each period.

TABLE 2 Comparative analysis of the duration time of each period of AE at different intermediate principal stresses.

Different periods of AE		Duration time				Changes in time
		10 MPa (s)	20 MPa (s)	40 MPa (s)	60 MPa (s)	
Ringing count rate	I quiet period	276	400	452	474	Periods I and II and IV become longer as σ_2 increases, and Period III changes discretely
	II frequent period	24	44	51	74	
	III sudden increase period	8	5	4	9	
	IV decrease period	40	59	93	180	
Absolute Energy	I quiet period	277	399	452	463	Periods I and II, IV all increase with σ_2, with no specific pattern in period III.
	II frequent period	23	45	51	85	
	III sudden increase period	8	6	3	15	
	IV decrease period	40	58	94	174	
Cumulative ringing count rate	A pre-unloading period	173	263	259	287	The sudden increase period C and decrease period D grow with increasing σ_2, and periods A and B show poor changing regularity
	B post-unloading period	102	136	193	183	
	C sudden increase period	25	45	52	78	
	D decrease period	48	64	96	189	
Accumulated absolute energy	A pre-unloading period	173	263	259	298	The sudden increase period and decrease period show an overall increase as σ_2 increases, and no specific changing pattern can be found in the pre- and post-unloading periods
	B post-unloading period	91	138	193	174	
	C sudden increase period	36	44	52	76	
	D attenuation section	48	65	96	189	

3.2 Comparative analysis of AE precursor information under different intermediate principal stresses

The characteristics of the AE during true triaxial loading and unloading of rock specimens under different intermediate principal stresses are analyzed in the above context. It is clear that the quiet, frequent and decrease periods of the ringing count rate and energy increase with the increase of intermediate principal stress, similar to the sudden increase and decrease periods in the cumulative counting curve.

Table 2 shows the comparative analysis of AE at various duration time periods under different intermediate principal stresses. This can be seen that the duration of the frequent periods of the AE ringing count rate and absolute energy both increase with the increase of the intermediate principal stress, and the duration of the sudden increase period of the cumulative count curve also increases with the increase of the intermediate principal stress. The detailed manifestations can be summarized as follows: the duration of the frequent periods of the ringing count rate is 24 s, 44 s, 51 s, 74 s, respectively, and that of the absolute energy is 23 s, 45 s, 51 s, 85 s, respectively. The duration of the sudden increase period of the cumulative ringing count curve is 25 s, 45 s, 52 s, 78 s, respectively, and that of the energy accumulation curve is 36 s, 44 s, 52 s, 76 s, respectively. Such regular variations in the AE frequency period and sudden increase period is due to the strength increase of the specimen associated with the increase of the intermediate principal stress. However, the stress threshold for the appearance of cracks within the specimen is unchanged; thus, the appearance time of the frequency period appears earlier with the increase of the intermediate principal stress. The sudden increase period in the cumulative count rate and cumulative energy curves corresponds to the AE frequency period, so that the earlier appearance of the sudden increase period is also observed with increasing intermediate principal stress. As the precursor information of rock failure, the occurrence of frequency period and sudden increase period become earlier with increasing intermediate principal stress.

Due to the fact that the quiet, frequent, and decrease periods of the ringing count rate become longer as σ_2 increases, the following equation was finally obtained by fitting the AE ringing count rate *versus* time curve (Figure 6):

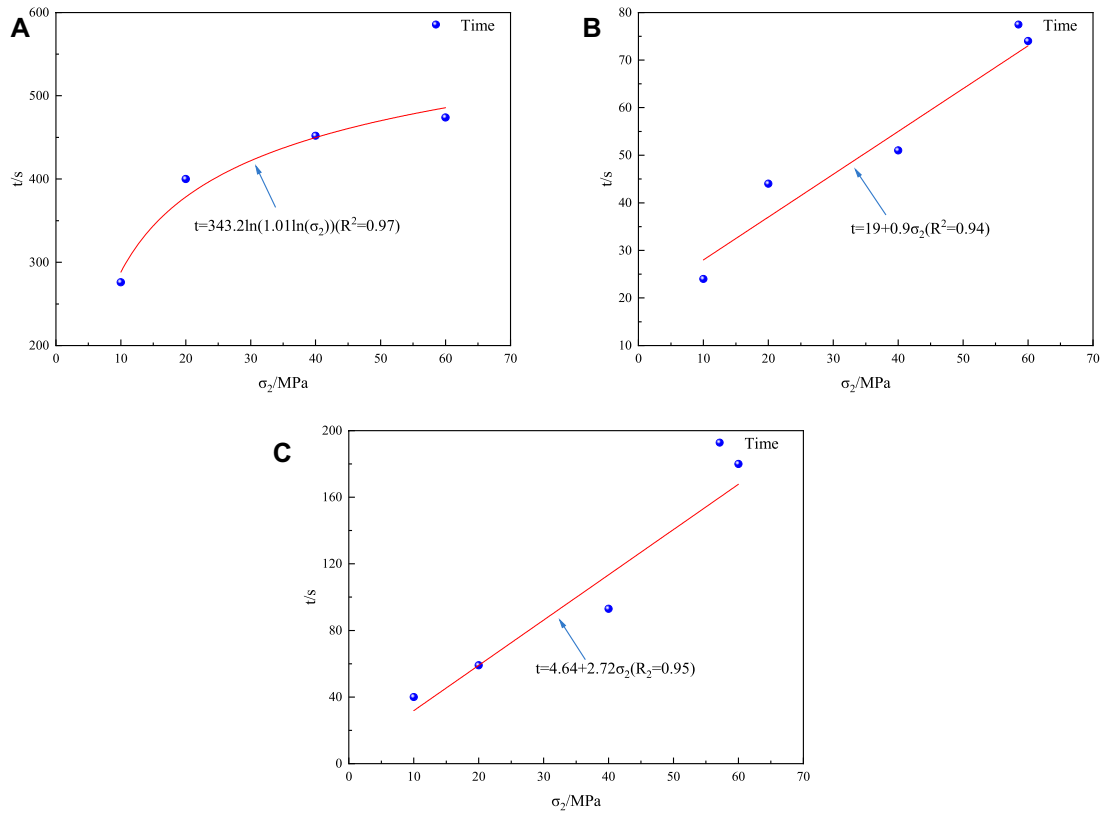

FIGURE 6
Fitted curve of σ_2 *versus* time for each period of the ringing count rate. **(A)** Fitted curve of quiet period. **(B)** Fitted curve of frequent period. **(C)** Fitting curve of decrease period.

$$t = 343.2 \ln\ (1.01 \ln(\sigma_2))\ (R^2 = 0.97) \quad (1)$$

$$t = 19 + 0.9\sigma_2\ (R^2 = 0.94) \quad (2)$$

$$t = 4.64 + 2.72\sigma_2\ (R^2 = 0.95) \quad (3)$$

Likewise, since the quiet, frequent, and decrease periods of absolute energy become longer as σ_2 increases, the absolute energy of AE *versus* time curve was fitted and the following equations were acquired (Figure 7):

$$t = 327.7 \ln(1.06 \ln(\sigma_2))\ (R^2 = 0.95) \quad (4)$$

$$t = 14.86 + 0.9\sigma_2\ (R^2 = 0.92) \quad (5)$$

$$t = 6.34 + 2.62\sigma_2\ (R^2 = 0.96) \quad (6)$$

In the similar fashion, the following equation was obtained by fitting the cumulative count rate of AE ringing *versus* time curve (Figure 8):

$$t = 18.93 + 0.96\sigma_2\ (R^2 = 0.94) \quad (7)$$

$$t = 3.09^{\sigma 2/16.87} + 3.09^{\sigma 2/20.62} + 37.48\ (R^2 = 0.98) \quad (8)$$

Similarly, the following equation was obtained by fitting the cumulative ringing count rate *versus* time curve (Figure 9):

$$t = 27.32 + 0.76\sigma_2\ (R^2 = 0.95) \quad (9)$$

$$t = 2.79^{\sigma 2/16.38} + 3.09^{\sigma 2/20.03} + 38.33\ (R^2 = 0.97) \quad (10)$$

Based on the result that the duration of the frequent and sudden increase periods of AE increases with increasing intermediate principal stress, a comparative study of the changes in the mean and maximum values of the corresponding signals was carried out to probe how they are affected by changes in intermediate principal stress and to compare the magnitude of the signal values during the sudden increase period.

Figure 10 shows the comparative analysis of the AE signals during the frequent and sudden increase periods at different intermediate principal stresses, and the following conclusions can be drawn: 1) As the intermediate principal stress increases, the ringing count rate and energy during the frequent period continue to increase, with a larger increase in the maximum value and a smaller increase in the average value. 2) As the intermediate principal stress increases, the peak value of the AE signal also increases when the rock specimen is damaged. These characteristics of the AE signal associated with the change in intermediate principal stress can be attributed to the following reasons. First, the increase in intermediate principal stress increases the compressive strength of the rock, thereby further increasing the acoustic signal threshold during the development of cracks and leading to the increase in the AE signal value. In addition, as the intermediate principal stress increases, the strength of the rock specimen also increases. This leads to higher peak stress during specimen failure

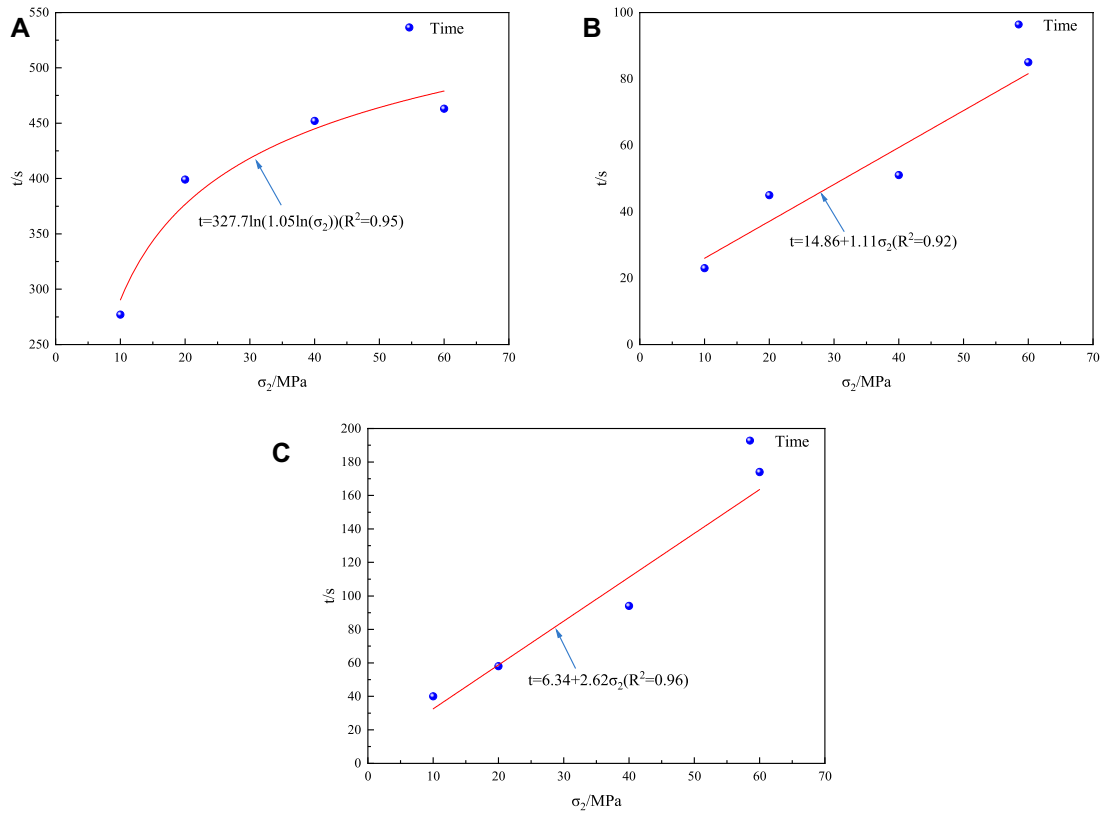

FIGURE 7
Fitted curve of σ_2 *versus* time for each period of the absolute AE energy. **(A)** Fitted curve of quiet period. **(B)** Fitted curve of frequent period. **(C)** Fitted curve of decrease period.

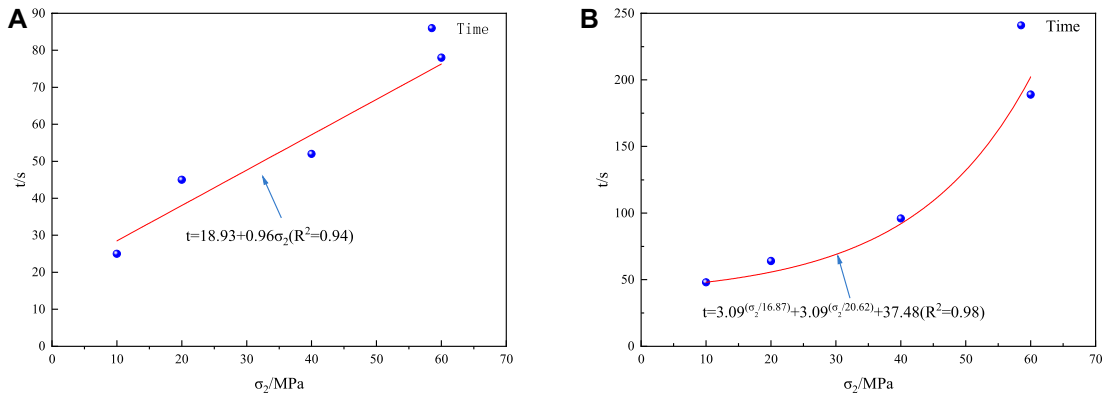

FIGURE 8
Fitted curve of σ_2 *versus* time for each period of the cumulative ringing count rate. **(A)** Fitted curve of sudden increase period. **(B)** Fitted curve of decrease period.

and a more vigorous failure process, resulting in a higher AE signal value.

The occurrence moment and clarity of the frequent period control the reliability and priority of the precursor information. The above analysis of AE periods shows that the duration of frequency period is influenced by the magnitude of the intermediate principal stress. The higher the intermediate principal stress, the longer the AE frequency period, indicating that the first occurrence of the AE frequency period is longer from the moment of specimen failure. When the intermediate

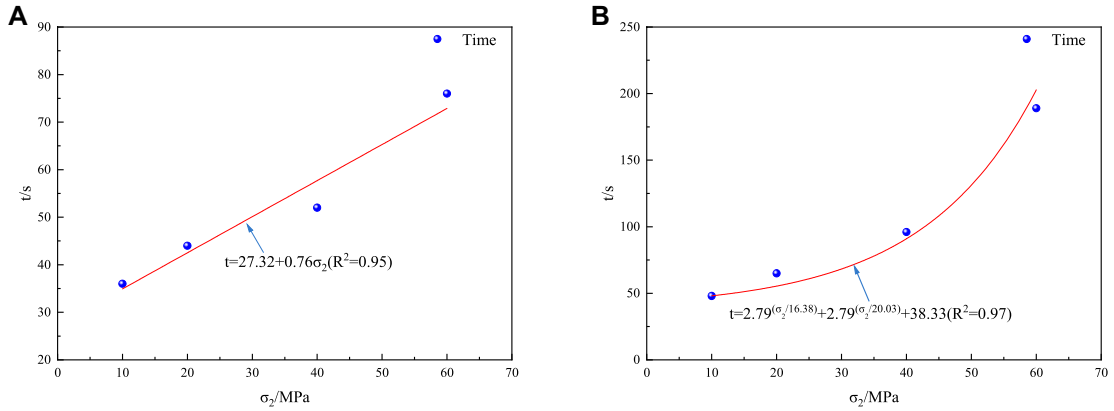

FIGURE 9
Fitted curve of σ_2 *versus* time for each period of cumulative AE energy. **(A)** Fitted curve of the sudden increase. **(B)** Fitted curve of decrease period.

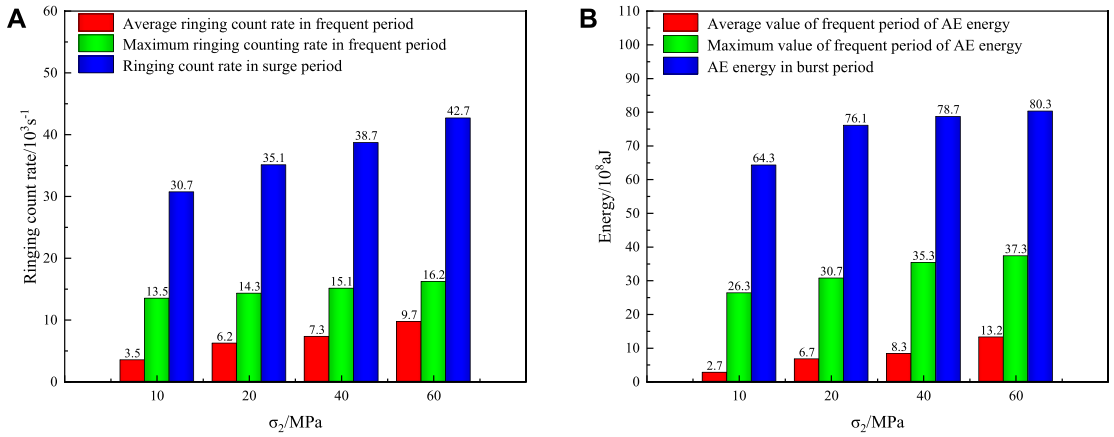

FIGURE 10
Comparison of signal values between frequent and sudden increase periods under different intermediate principal stresses. **(A)** Ringing count rate. **(B)** Absolute energy.

principal stress increases, both the average and maximum values of the AE signal during the frequency period increase, which greatly enhance the recognition effectiveness of AE precursor information. This shows that the reliability and priority of the AE precursor information increases with increasing intermediate principal stresses.

4 Discussion

The sudden increase in AE indicates that the rock specimen failure approaches, and the precursor information is obtained from the change in acoustic signal inside the rock. According to the theory of the thermoelastic effect, when an object is subjected to tensile stress, the object will release energy and its temperature will decrease. On the contrary, when it is subjected to compressive stress, the object will absorb energy with a temperature increase. Thermal infrared remote sensing technology can record thermal infrared information of specimens, which is utilized to explore and capture the characteristics of precursor information (Lou and He, 2018; Ma and Sun, 2018; Yin et al., 2021; Li et al., 2022). AE obtains precursor information from the interior of the rock, while thermal infrared imaging collects the information mainly from the rock surface. Therefore, this study investigates the precursor information of rock failure using both approaches.

Specifically, the AE monitoring of the true triaxial test was conducted and the FLIRSC305 infrared thermal imaging camera was also used to monitor the thermal image changes throughout the whole process. With these supports, the AE characteristics and thermal image anomaly evolution of the specimen failure process under different intermediate principal stress conditions were analyzed. The representative analysis results of red sandstone under 60 MPa are shown in Figure 11.

Figure 11A shows the evolution of the thermal infrared image on the unloading specimen free face when the intermediate principal stress is 60 MPa. It is clear that the first thermal abnormality that

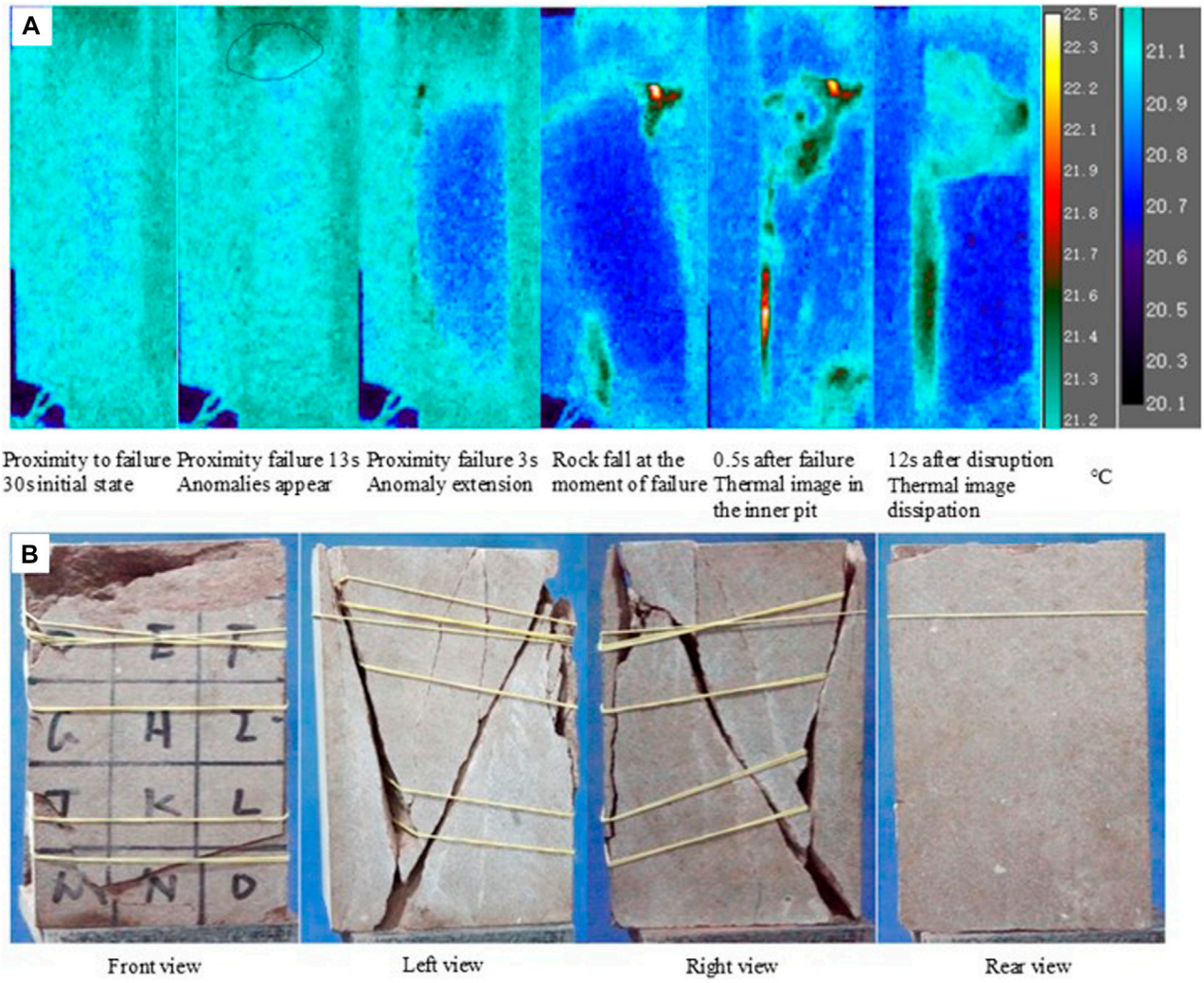

FIGURE 11
Morphological characteristics of rock fracture and the evolution of thermal infrared thermography of rock failure. **(A)** Thermal infrared image evolution under the unloading test on rock specimen. **(B)** Rock fracture morphology.

TABLE 3 Occurrence time analysis of AE precursors compared with thermal infrared precursors under different intermediate principal stresses.

σ_2/MPa	Occurrence time			Thermal infrared precursors *versus* AE
	Thermal imaging (s)	AE ringing (s)	AE energy (s)	
10	5.5	24	23	Thermal images are 18.5 s later than ringing and 17.5 s later than energy
20	7	44	45	Thermal images are 37 s later than ringing and 38 s later than energy
40	9	51	51	Thermal images are 42 s later than ringing and 42 s later than energy
60	13	74	85	Thermal image 61 s later than ringing and 72 s later than energy

covers an area of 1.8 cm^2 appears 13 s before the specimen failure, and then gradually expands to a maximum of about 45 cm^2 before failure. Compared to the bright high temperature patches appeared under the previous smaller intermediate principal stress condition, the area under 60 MPa stress is larger and longer, with a broader development area. Figure 11B shows the fracture morphology of the rock at an intermediate principal stress of 60 MPa. The whole of the free face is ejected, forming a rupture surface of comparable size to the free face. The shear fracture zones on the left and right sides of the rock specimen are mainly "V" shaped and diagonally penetrated,

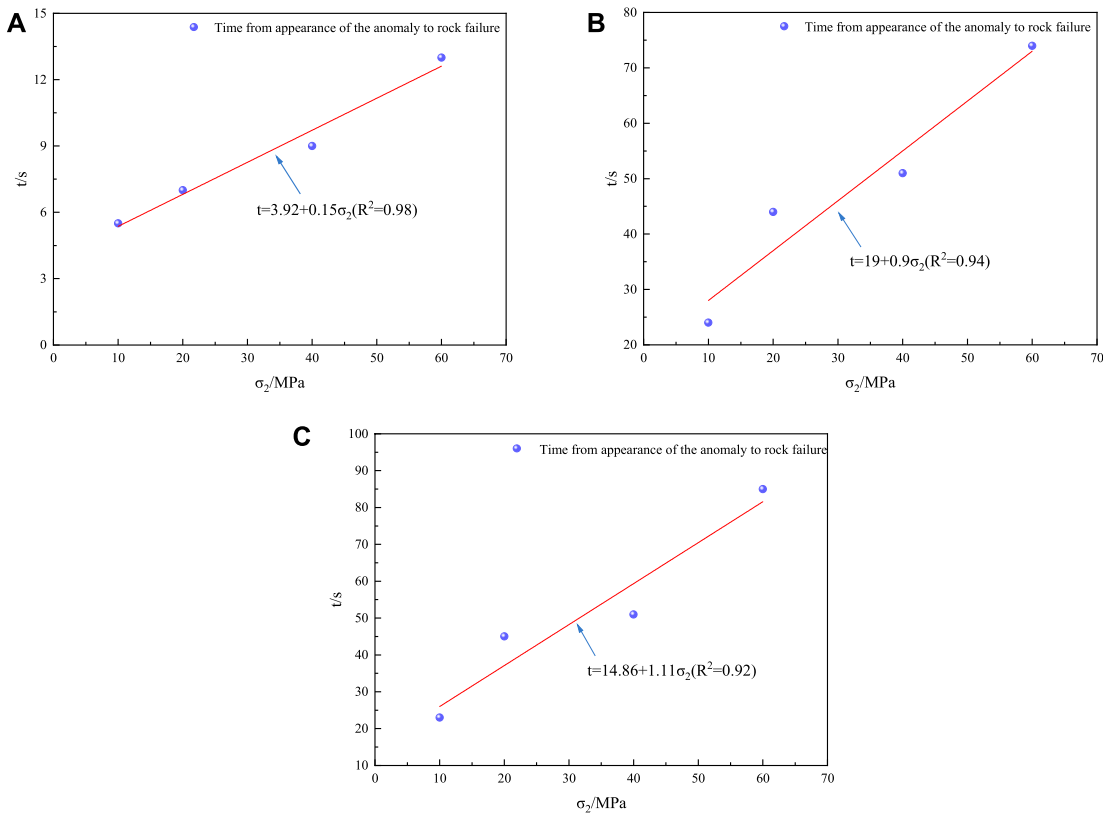

FIGURE 12
Fitting of AE and thermal infrared precursors for different intermediate principal stresses. **(A)** Thermal infrared imaging. **(B)** AE ringing count rate. **(C)** AE energy.

with feather cracks in the diagonally penetrated shear zone, which are distributed around the shear zone and are secondary to the extrusive friction that occurs in the shear zone. The integrity of the back of the specimen is good after failure.

The results show that as the intermediate principal stress increases, the thermal abnormality appears earlier, the pre-failure maximum thermal abnormality area increases, and the recognition effectiveness of the thermal image precursor information also increases accordingly. During the thermal abnormality expansion process, the thermal image abnormality spans a large area, indicating that the main factor leading to the differential change of the thermal image precursor information is the change of the intermediate principal stress, while the unloading is less dominant in the process.

Table 3 shows the comparative analysis of the occurrence time of the AE and thermal infrared precursors under different intermediate principal stresses. It is notable that the thermal infrared image precursors appear the latest and are the closest to the moment of specimen failure. By comparison, the AE precursors appear the earliest and are the first response to rock failure. Overall, AE precursors appear prior to the thermal infrared precursors. The energy and ringing count rates of AE are similar, without showing a clear order of occurrence time. The above time difference can be attributed to the following reasons: 1) Thermal infrared image anomalies are caused by temperature changes on rock surface, and only when the temperature change amount reaches the threshold will it result in visibly anomalous changes in the thermal image 2) The frequent period of AE is caused by the sudden increase of the acoustic signal inside the rock, suggesting that a large number of microcracks have already developed inside the rock. Compared with the thermal infrared precursors, the AE ones are closer to the moment of rock failure. 3) Due to the unloading-triggered disturbance, the occurrence time of the frequent periods of AE ring count rate and energy shows no clear regularity. Furthermore, the duration of the two frequent periods is highly similar under low intermediate principal stress conditions, while the duration of the energy frequent period is slightly earlier when the intermediate principal stress increases.

During the true triaxial loading and unloading test, the thermal imaging camera was used to monitor the temperature change-induced thermal abnormality on the unloading surface in order to warn rock failure. Meanwhile, AE instruments monitor the acoustic signal changes inside the rock to warn rock failure.

By fitting both AE and thermal infrared precursor information to the red sandstone at different intermediate principal stresses, linear relationships of time advanced and intermediate principal stresses for thermal infrared images, AE ringing count rate, and AE energy were obtained, and the final fitted equations were written as (Figure 12):

$$t = 3.92 + 0.15\sigma_2 \left(R^2 = 0.98\right) \quad (11)$$

$$t = 19 + 0.9\sigma_2 \left(R^2 = 0.94\right) \quad (12)$$

$$t = 14.86 + 1.11\sigma_2 \left(R^2 = 0.92\right) \quad (13)$$

where t is the time advanced and σ_2 denotes the intermediate principal stress.

5 Conclusion

In this study, true triaxial unloading tests were conducted on red sandstone specimens under different intermediate principal stresses to analyze their AE characteristics, focusing on deciphering the corresponding relationship between failure precursors and different AE signals during the failure process. Furthermore, the AE precursor information are compared with the thermal infrared precursor information, and the following conclusions were obtained.

The characteristic curve of AE parameters has obvious phased characteristics. Both AE ringing count rate and energy *versus* time curves show four periods (i.e., quiet, frequent, sudden increase and decline periods). In addition, the cumulative count curve is divided into four periods, that is, pre-unloading period, post-unloading period, sharp increase period and the final decrease period.

The AE precursor information is mainly manifested by the frequent period and the sharp increase period in the cumulative counting process. Notably, as the intermediate principal stress increases, the frequent period of AE appears earlier with increased AE signal values. The sharp increase period also occurs earlier with increasing intermediate principal stress.

As the intermediate principal stress increases, the area of the anomalous patches of thermal infrared image increases, the first occurrence time of thermal infrared image becomes earlier, and the pre-failure maximum anomalous area of the specimen also increases. By comparing the thermal infrared and AE precursor information, it is prominent that the latter occurs prior to the former.

Data availability statement

The original contributions presented in the study are included in the article/supplementary material, further inquiries can be directed to the corresponding author.

Author contributions

All authors listed have made a substantial, direct, and intellectual contribution to the work and approved it for publication.

Funding

This study is supported by the National Natural Science Foundation of China (Grant Nos 41972284 and 42107211). This study is also supported by the Natural Science Foundation of Sichuan Province (Grant Nos 2022NSFSC1063 and 2022NSFSC1112) and State Key Laboratory of Geohazard Prevention and Geoenvironment Protection Independent Research Project (No. SKLGP 2020Z005). The authors would also like to thank the journal editor and anonymous reviewers for their valuable suggestions.

Conflict of interest

The authors declare that the research was conducted in the absence of any commercial or financial relationships that could be construed as a potential conflict of interest.

Publisher's note

All claims expressed in this article are solely those of the authors and do not necessarily represent those of their affiliated organizations, or those of the publisher, the editors and the reviewers. Any product that may be evaluated in this article, or claim that may be made by its manufacturer, is not guaranteed or endorsed by the publisher.

References

Brantut, N., Schubnel, A., and Guéguen, Y. (2011). Damage and rupture dynamics at the brittle-ductile transition: The case of gypsum. *J. Geophys. Res. Solid Earth* 116 (B1), B01404. doi:10.1029/2010jb007675

Chang, C., and Haimson, B. (2012). "A failure criterion for rocks based on true triaxial testing," in *The ISRM suggested methods for rock characterization, testing and monitoring: 2007-2014* (Singaore, Singapore: Springer,Cham), 259–262.

Chen, G.-Q., Sun, X., Wang, J.-C., Wang, D., and Zhu, Z.-F. (2020). Detection of cracking behaviors in granite with open precut cracks by acoustic emission frequency spectrum analysis. *Arab. J. Geosci.* 13 (6), 258. doi:10.1007/s12517-020-5253-8

Dong, L., Zhang, L., Liu, H., Du, K., and Liu, X. (2022). Acoustic emission b value characteristics of granite under true triaxial stress. *Mathematics* 10 (3), 451. doi:10.3390/math10030451

Feng, X. -T., Zhang, X., Kong, R., and Wang, G. (2016). A novel Mogi type true triaxial testing apparatus and its use to obtain complete stress–strain curves of hard rocks. *Rock Mech. Rock Eng.* 49 (5), 1649–1662. doi:10.1007/s00603-015-0875-y

Fortin, J., Stanchits, S., Dresen, G., and Gueguen, Y. (2009). Acoustic emissions monitoring during inelastic deformation of porous sandstone: Comparison of three modes of deformation. *Pure Appl. Geophys.* 166 (5), 823–841. doi:10.1007/s00024-009-0479-0

Gao, Y.-H., Feng, X.-T., Zhang, X.-W., Feng, G.-L., Jiang, Q., and Qiu, S.-L. (2018). Characteristic stress levels and brittle fracturing of hard rocks subjected to true triaxial compression with low minimum principal stress. *Rock Mech. Rock Eng.* 51 (12), 3681–3697. doi:10.1007/s00603-018-1548-4

Kong, X., Wang, E., Hu, S., Shen, R., Li, X., and Zhan, T. (2016). Fractal characteristics and acoustic emission of coal containing methane in triaxial compression failure. *J. Appl. Geophys.* 124, 139–147. doi:10.1016/j.jappgeo.2015.11.018

Lei, X.-L. (2006). Typical phases of pre-failure damage in granitic rocks under differential compression. *Geol. Soc. Lond. Spec. Publ.* 261 (1), 11–29. doi:10.1144/gsl.sp.2006.261.01.02

Li, S., Hu, J., Amann, F., Li, L., Liu, H., Shi, S., et al. (2022). A multifunctional rock testing system for rock failure analysis under different stress states: Development and application. *J. Rock Mech. Geotechnical Eng.* 14, 1531–1544. doi:10.1016/j.jrmge.2021.12.017

Li, Y.-H., Liu, J.-P., Zhao, X.-D., and Yang, Y.-J. (2010). Experimental studies of the change of spatial correlation length of acoustic emission events during rock fracture process. *Int. J. Rock Mech. Min. Sci.* 47 (8), 1254–1262. doi:10.1016/j.ijrmms.2010.08.002

Lou, Q., and He, X. (2018). Experimental study on infrared radiation temperature field of concrete under uniaxial compression. *Infrared Phys. Technol.* 90, 20–30. doi:10.1016/j.infrared.2018.01.033

Ma, L., and Sun, H. (2018). Spatial-temporal infrared radiation precursors of coal failure under uniaxial compressive loading. *Infrared Phys. Technol.* 93, 144–153. doi:10.1016/j.infrared.2018.07.034

Ma, X., Rudnicki, J. W., and Haimson, B. C. (2017). The application of a Matsuoka-Nakai-Lade-Duncan failure criterion to two porous sandstones. *Int. J. Rock Mech. Min. Sci.* 92, 9–18. doi:10.1016/j.ijrmms.2016.12.004

Ma, Z. -Y., Liao, H. -J., and Dang, F. -N. (2014). Effect of intermediate principal stress on strength of soft rock under complex stress states. *J. Central South Univ.* 21 (4), 1583–1593. doi:10.1007/s11771-014-2099-9

Mogi, K. (1971). Fracture and flow of rocks under high triaxial compression. *J. Geophys. Res.* 76 (5), 1255–1269. doi:10.1029/jb076i005p01255

Moradian, Z., Einstein, H. H., and Ballivy, G. (2016). Detection of cracking levels in brittle rocks by parametric analysis of the acoustic emission signals. *Rock Mech. Rock Eng.* 49 (3), 785–800. doi:10.1007/s00603-015-0775-1

Su, G. -S., Jiang, Q., Zhai, S. -B., and Zhang, G. L. (2017). Influence of tunnel axis stress on strainburst: An experimental study. *Rock Mech. Rock Eng.* 50, 1551–1567. doi:10.1007/s00603-017-1181-7

Tyupkin, Y. S., and Di Giovambattista, R. (2005). Correlation length as an indicator of critical point behavior prior to a large earthquake. *Earth Planet. Sci. Lett.* 230 (1-2), 85–96. doi:10.1016/j.epsl.2004.10.037

Vachaparampil, A., and Ghassemi, A. (2017). Failure characteristics of three shales under true-triaxial compression. *Int. J. Rock Mech. Min. Sci.* 100, 151–159. doi:10.1016/j.ijrmms.2017.10.018

Wang, Z., Wu, Z., Chu, Z., Weng, L., Liu, Y., and Liu, Q. (2022). Study on mesoscopic failure mechanism of grout-infilled sandstone under uniaxial compression using an improved AE localization technique. *Int. J. Rock Mech. Min. Sci.* 160, 105275. doi:10.1016/j.ijrmms.2022.105275

Xu, D.-P., Liu, X.-Y., Jiang, Q., Li, S.-J., Zhou, Y.-Y., Qiu, S.-L., et al. (2022). A local homogenization approach for simulating the reinforcement effect of the fully grouted bolt in deep underground openings. *Int. J. Min. Sci. Technol.* 32 (2), 247–259. doi:10.1016/j.ijmst.2022.01.003

Xu, J., Jiang, J., Zuo, L., and Gao, Y. (2017). Acoustic emission monitoring and failure precursors of sandstone samples under various loading and unloading paths. *Shock Vib.* 2017, 1–11. doi:10.1155/2017/9760940

Yang, S.-Q., Jing, H.-W., and Wang, S.-Y. (2012). Experimental investigation on the strength, deformability, failure behavior and acoustic emission locations of red sandstone under triaxial compression. *Rock Mech. rock Eng.* 45 (4), 583–606. doi:10.1007/s00603-011-0208-8

Yin, S., Li, Z., Song, D., He, X., Qiu, L., Lou, Q., et al. (2021). Experimental study on the infrared precursor characteristics of gas-bearing coal failure under loading. *Int. J. Min. Sci. Technol.* 31 (5), 901–912. doi:10.1016/j.ijmst.2021.07.003

Zhang, Y., Feng, X.-T., Yang, C.-X., Han, Q., Wang, Z.-F., and Kong, R. (2021). Evaluation method of rock brittleness under true triaxial stress states based on pre-peak deformation characteristic and post-peak energy evolution. *Rock Mech. Rock Eng.* 54 (1), 1277–1291. doi:10.1007/s00603-020-02330-w

Zhang, Y., Feng, X.-T., Yang, C.-X., Zhang, X.-W., Sharifzadeh, M., and Wang, Z.-F. (2019). Fracturing evolution analysis of Beishan granite under true triaxial compression based on acoustic emission and strain energy. *Int. J. Rock Mech. Min. Sci.* 117, 150–161. doi:10.1016/j.ijrmms.2019.03.029

Zhao, J.-S., Chen, B.-R., Jiang, Q., Lu, J.-F., Hao, X. J., Pei, S.-F., et al. (2022a). Microseismic monitoring of rock mass fracture response to blasting excavation of large underground caverns under high geo-stress. *Rock Mech. Rock Eng.* 55, 733–750. doi:10.1007/s00603-021-02709-3

Zhao, J.-S., Jiang, Q., Lu, J.-F., Chen, B.-R., Pei, S.-F., and Wang, Z.-L. (2022b). Rock fracturing observation based on microseismic monitoring and borehole imaging: *In situ* investigation in a large underground cavern under high geo-stress. *Tunn. Undergr. Space Technol.* 126, 104549. doi:10.1016/j.tust.2022.104549

Zhao, X.-G., Cai, M., Wang, J., Li, P.-F., and Ma, L.-K. (2015). Objective determination of crack initiation stress of brittle rocks under compression using AE measurement. *Rock Mech. Rock Eng.* 48 (6), 2473–2484. doi:10.1007/s00603-014-0703-9

frontiers | Frontiers in Earth Science

TYPE Original Research
PUBLISHED 06 July 2023
DOI 10.3389/feart.2023.1195552

OPEN ACCESS

EDITED BY
Guangjin Wang,
Kunming University of Science and Technology, China

REVIEWED BY
Ze Zhang,
Northeast Forestry University, China
Zhongqiong Zhang,
Chinese Academy of Sciences (CAS), China

*CORRESPONDENCE
Gang Wang,
double729422@gmail.com

RECEIVED 28 March 2023
ACCEPTED 26 June 2023
PUBLISHED 06 July 2023

CITATION
Shangguan Y, Xue D, Wang G, Li D, Bao S and Wang W (2023), A study on soil arching effect of anti-slide pile considering different pile arrangements. *Front. Earth Sci.* 11:1195552. doi: 10.3389/feart.2023.1195552

A study on soil arching effect of anti-slide pile considering different pile arrangements

Yunlong Shangguan[1], Dongsheng Xue[1], Gang Wang[2]*, Dongxin Li[1], Shuochao Bao[2] and Wenhua Wang[3]

[1]College of Transportation Science and Engineering, Jilin Jianzhu University, Changchun, China, [2]College of Civil Engineering, Jilin Jianzhu University, Changchun, China, [3]School of Civil Engineering, Changchun Institute of Technology, Changchun, China

Among the methods of landslide treatment, anti-slide piles are an effective measure. The soil arching effect cannot be ignored in the design of anti-slide piles, which has a significant impact on the supporting. Based on the field investigation, this paper selects the Xinyan landslide in Yanbian area of Jilin Province and uses Flac-3D to build a numerical model to simulate its soil arching effect with different pile arrangements. The simulation results show that the pile arrangement has a significant influence on the soil arching effect. When arranging piles in parallel, the soil arches between the front and rear rows of piles are distributed parallel to each other. When arranging piles in quincunx-shape, the soil arches between the rear rows of piles are the same as when laying piles in parallel. The soil between the piles flows around once when the piles are laid out in parallel, while it flows around twice when the piles are laid out in a quincunx-shape. The latter has better support than the former.

KEYWORDS

anti-slide pile, soil arching effect, landslide, double-row piles, pile arrangements

Introduction

Landslide is a natural phenomenon in which the shear strength of the rock-soil mass on a slope is reduced by environmental influence and slides along a soft surface or weak zone towards the front of the slope as a whole or in pieces under the action of gravity. With the continuous growth of global population and the gradual extension of human activities (Zhang et al., 2023a), landslide disasters are occurring more frequently and causing more serious loss of life and property. Therefore, according to the engineering geological characteristics of rock-soil mass in landslide areas, it is of great practical significance for the safety of people and properties to study the genetic mechanism of landslides and develop reasonable support design to improve the stability of slopes (Ukleja, 2020; Zhu et al., 2021; Zhang et al., 2023b).

Several principles of landslide management were summarized through years of engineering experience: Several principles of landslide management were summarized through years of engineering experience: 1) find out the history of landslide occurrence, the current situation and engineering geological characteristics (Jimenez-Peralvarez, 2018); 2) try to avoid landslide areas or pre-reinforcement (Zhang et al., 2021); 3) eliminate landslide hazards at once to avoid repeated treatment (Tiranti and Cremonini, 2019); 4) if the scale of landslides is large, the overall planning should be done; 5) timely management in the early development period of landslide (Yin et al., 2014); 6) to ensure the premise of safety to minimize the cost of the project (Martin et al., 2021); 7) to take effective design solutions

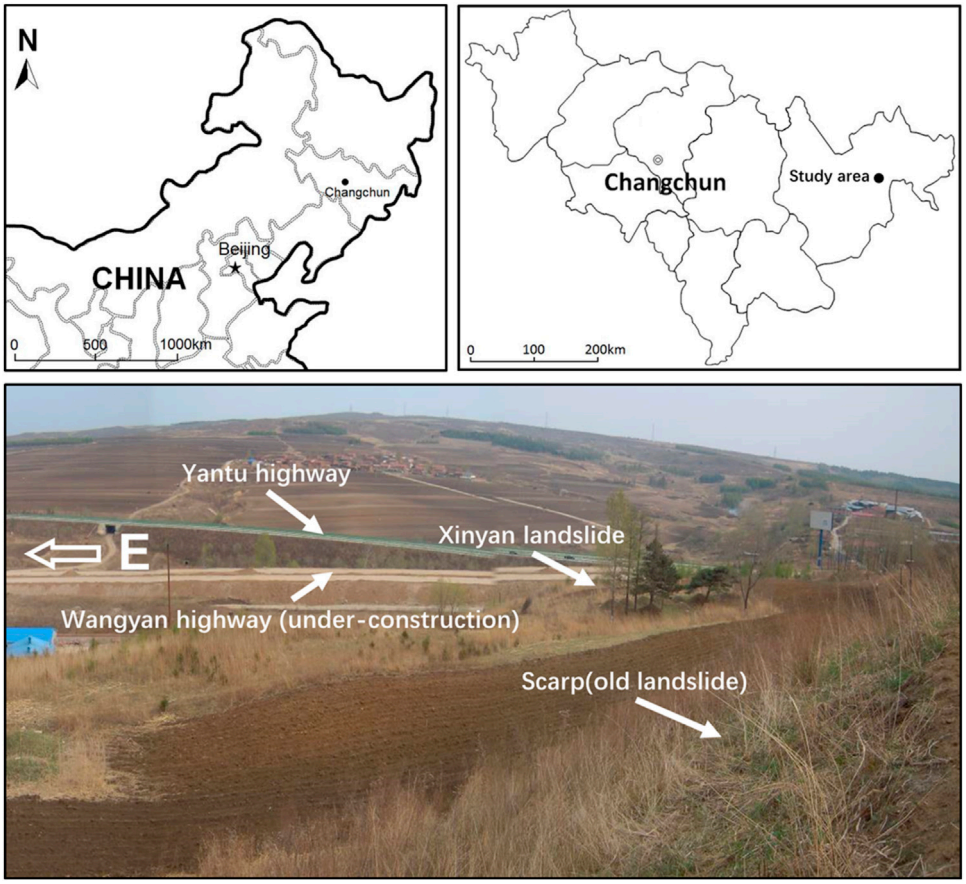

FIGURE 1
Location and overall topography of Xinyan landslide.

and scientific and efficient construction (Cui et al., 2022); 8) Form a dynamic response mechanism to ensure dynamic design and dynamic construction (He et al., 2008; Wang et al., 2022b); 9) focus on inspection, repair and maintenance of facilities (Liao et al., 2022).

The main methods of landslide management include bypassing (Bhasin and Aarset, 2020), drainage (Haugen, 2017; Wang G. et al., 2022) and mechanical balance (Du et al., 2021). The Xinyan landslide is an existing road slide, which cannot be rerouted. The cost of using culvert or bridge solution is too high, and the method of chemical improvement is technically complex, difficult and costly. Therefore, a combination of drainage and mechanical balance is chosen to ensure complete management of the Xinyan landslide.

Among the methods of landslide treatment, anti-slide piles are an effective measure (Zhang, 2000). Earlier, when calculating the load distribution of anti-slide pile, the pile group is usually simplified to single pile for force analysis. However, the anti-slide pile interacts with the soil between the piles, i.e., there is an arching effect, which makes the stress migrate from the soil to the pile, so that the anti-slip pile acts as an obstacle to sliding, and the corresponding stress characteristics of pile become more complex (Xia et al., 2008). Therefore, the formation mechanism and influencing factors of soil arching effect must be studied in depth in order to improve the supporting of anti-slide pile on landslide and to obtain more accurate load distribution characteristics of pile (Zheng, 2005).

The current research focuses on the influence factors of soil arch, such as pile spacing and material parameters between piles and soil, but not enough research on the arrangement of piles (Liang et al., 2020). Therefore, this paper selects the Xinyan landslide in Yanbian area of Jilin Province, which is an expansive rock slope, establishes the three-dimensional model of the Xinyan landslide, and simulates the effect of pile arrangements of anti-slide piles on the soil arching effect between piles. The overall three-dimensional model avoids the disadvantages of the two-dimensional plane model and the partial three-dimensional model of insufficient consideration of spatial and boundary effects, making the simulation study results more accurate and reliable.

Data and method

Date

The Xinyan slide is located within pile number K58 + 750 to K59 + 030 of the under-construction Wangyan highway, and the filling subgrade at the bottom of the highway is cut through by the Xinyan slide body (location and overall topography of the landslide is shown

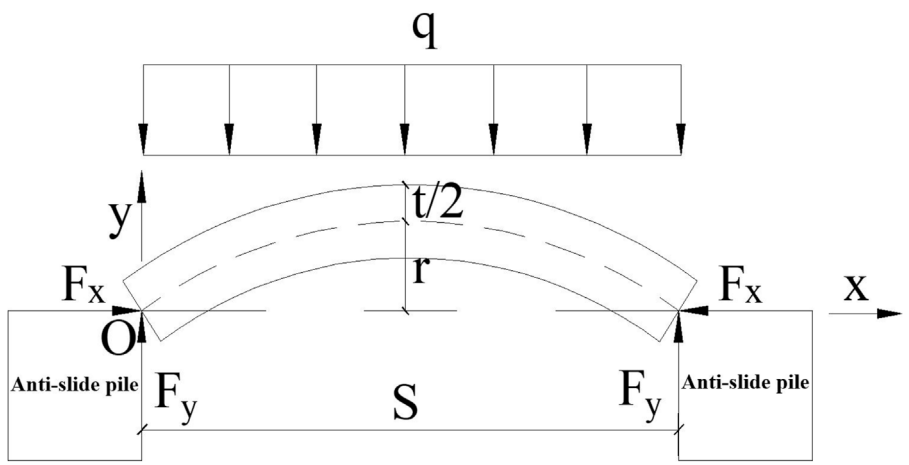

FIGURE 2
Simplified model of soil arching.

in Figure 1). The plane morphology of the slide body is spindle-shaped, with a long axis length of about 230 m and a short axis length of about 110 m. The intersection angle between the main sliding direction (113°) and the extension direction of Wangyan highway is about 60°. The landslide plane area is about 1.7×10^4 m^2, the slope height is about 15 m, the average thickness of the slide body is about 8 m, and the total volume of the slide body is about 1.36×10^5 m^3. The slide material composition from top to bottom is fill, silty clay, fully weathered mudstone and sandstone respectively.

Method

For the soil arch effect, the theory that the residual sliding force at the rear of the pile is borne by the soil arch behind the pile was propose by Chang (1998). On this basis, Zhou et al. (2004) derived the mechanical model of the soil arch behind the pile by considering the static balance of shear strength and sliding force of the soil in the triangular compression zone behind the piles (Zhou et al., 2009). The calculation model is shown in Figure 2.

In the Figure 2, S is the net distance between adjacent anti-slide piles, t is the section thickness of the soil arch, r is the height of the soil arch, q is the residual sliding force (assumed as uniform force) at the rear of the pile, F_x and F_y are the reaction forces at the end of the soil arch, and the equation of the soil arch axis is:

$$y = \frac{4Ax(S-x)}{S} \tag{1}$$

In Equation 1, $A = r/L$, where L is the distance between the centers of the adjacent piles, and the reaction force at the end of the arch is:

$$\begin{cases} F_x = \dfrac{qS\lambda}{8A} \\ F_y = \dfrac{qS}{2} \end{cases} \tag{2}$$

In Equation 2, λ is:

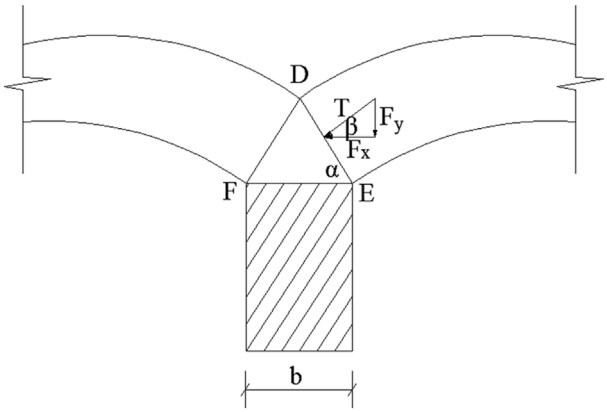

FIGURE 3
Illustration of the arch foot compression.

$$\lambda = \left(1 + \frac{5B^2}{512A^3k_2}\right) \Big/ \left(1 + \frac{10B^2}{512A^3k_1}\right) \tag{3}$$

In Equation 3, $B = t/S$, where k_1 , k_2 are:

$$\begin{cases} k_1 = \ln\left(\dfrac{k_0 - 4A}{k_0 + 4A}\right) \\ k_2 = k_1 + 8Ak_0 \end{cases} \tag{4}$$

In Equation 4, $k_0 = \sqrt{1 + 16A^2}$

The following conditions should be satisfied during the model calculation:

(1) The model should satisfy the static balance, and the side friction of the pile should not be less than the pressure on the soil arch.
(2) The model should satisfy the strength conditions of the soil arch on dangerous section, and the maximum value of sectional stress should not be greater than the allowable value.

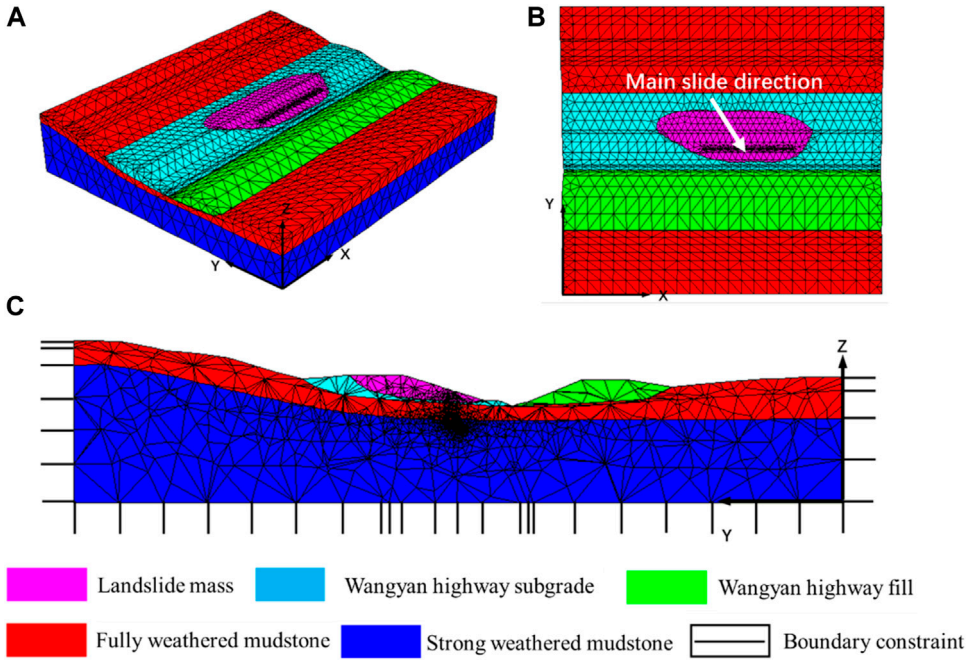

FIGURE 4
Illustration of 3D model and mesh subdivision: **(A)** Side view; **(B)** Plan view; **(C)** Cutaway view.

(3) The model should satisfy the triangular compression zone is not damaged, and anti-slide piles need to provide the arch foot (Figure 3).

According to the geometric characteristics of the triangular compression zone at the arch foot, the calculated expression of the pile spacing can be obtained as:

$$L = S + b = \frac{cb}{q\cos\alpha}^{2}\left(45° + \frac{\varphi}{2}\right) + b \tag{5}$$

where b is the width of the pile, c is the cohesion, φ is the internal friction angle, α is the base angle of the triangle.

Results

According to the genetic mechanism of the Xinyan landslide, anchor cable, anti-slide pile and pressure foot treatment measures were developed for the influencing factors of the landslide, and combined with the drainage of the slope surface and slope body. All three methods can improve the landslide stability. There are many methods for predicting slope stability (Wang et al., 2022a), and the highest values of 39.79%, 43.13%, and 85.28% are improved respectively by using Janbu, Sarma, and Morgenstern-Price method to calculate the safety coefficients of the three known profiles after treatment in this paper (Shanguan, 2014). Anti-slide piles have the advantages of large anti-slide capacity, good support effect, flexible setting and small disturbance to the slide, which is one of the common methods for landslide management.

This paper mainly studies the soil arching effect of anti-slide pile, so the modeling process is based on the geological characteristics of the Xinyan landslide area, and the Flac-3D software is used to build the landslide 3D model (Figure 4). The model is used to study the soil arching effect between piles at different positions, and focuses on the influence of double-row piles arrangements on soil arching effect. The values of material parameters in the model are shown in Table 1.

To avoid the effect of boundary constraint, the extent of the model boundary should be two times the extent of the studied landslide. Therefore, the model area is 445 m long in the y-direction and 500 m long in the x-direction. The boundary of the mechanical model is constrained on the left and right sides (x-direction), with horizontal constraints on the front and rear sides (y-direction), vertical constraints on the undersurface (z-direction), and no constraints on the superface. Considering that the neotectonic movement of the tectonic stress at the location of the Xinyan landslide is not active, and that the stratum there is mainly composed of fill, fully weathered fine sandstone and clay rock, such rock-soil mass is not enough to store the *in-situ* stress. Therefore, when considering the initial stress field of the model, only the effect of the gravity field is considered, and the tectonic stress field is not considered (Shanguan, 2014). All the constitutive models of rock-soil mass are used the Moore-Coulomb model, and the elasticity model is used for the anti-slide piles. The subdivision elements are tetrahedral elements, and the elements get larger gradually from top to bottom.

The cross-sectional form of double-row anti-slide piles is circular, which is divided into parallel arrangement and quincunx arrangement. Pile diameter (d) is 2.5 m, pile distance (L=8d) is 20 m, and pile row distance (L'=3d) is 7.5 m, as shown in Figure 5.

TABLE 1 The values of material parameters in the model.

	Density (kg/m^3)	Poisson ratio	Compression modulus (MPa)	Bulk modulus (MPa)	Shear modulus (MPa)	Internal friction angle (°)	Cohesion (KPa)	Tensile strength (MPa)
Anti-slide Pile	2,500	0.15	25,000	11,904	10,869	-	-	-
Landslide mass	1890	0.35	30	33.33	11.11	7.00	15.00	0.02
Subgrade	1890	0.35	30	33.33	11.11	10.00	20.00	0.02
Fill	1890	0.34	40	39.22	15.04	20.00	20.00	0.03
Fully weathered mudstone	1950	0.32	50	46.30	18.94	17.00	25.00	0.03
Strong weathered mudstone	2000	0.30	2000	1667.00	769.23	25.00	50.00	0.03

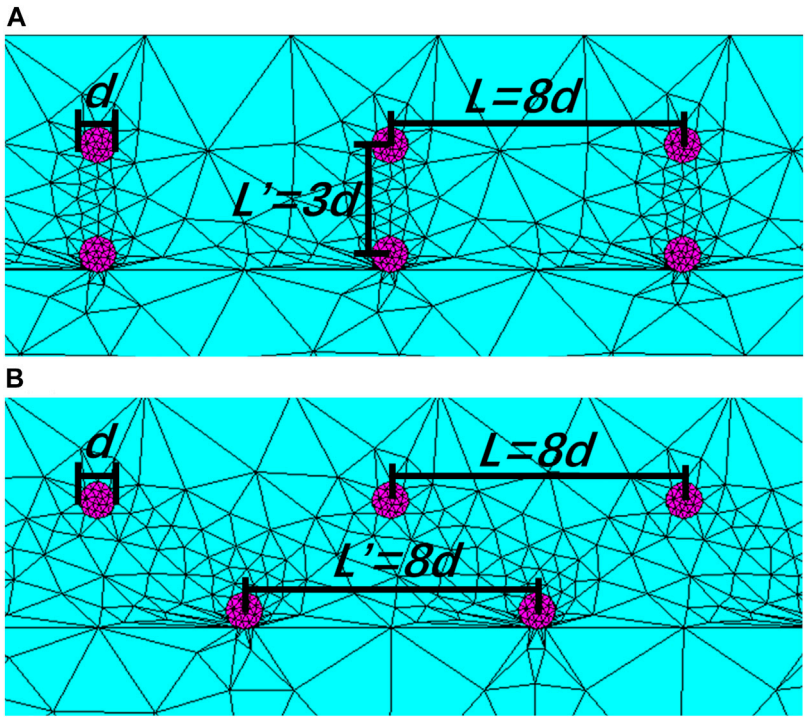

FIGURE 5
Different pile arrangements of double-row anti-slide pile: **(A)** Parallel arrangement; **(B)** Quincunx arrangement.

Discussion

Stress distribution of soil between piles

When the anti-slide pile passes through the landslide layer, the sliding displacement of the soil between the piles is larger and the soil arch effect is significant, which bears most of the load. Therefore, the plane at a depth of 22.6 m is chosen to observe the soil stress distribution between the piles. Stress distribution (σ_y) under different pile arrangements is shown in Figure 6. The dark blue area in the graph indicates greater stress and the orange area indicates less stress. From the rear to the front of the pile, the stress decreases gradually. The stress is small near the pile and it is large at both sides behind the pile, the stress at the back of the pile on both sides is large, and the stress distribution shows an arch shape. In the two arrangement forms, the radius of curvature of the soil arch line behind the rear row of piles is larger, while the radius is smaller behind the front row. The soil arching effect between the rear row piles is relatively obvious, and the soil arch effect is limited by the occlusion in the front row piles.

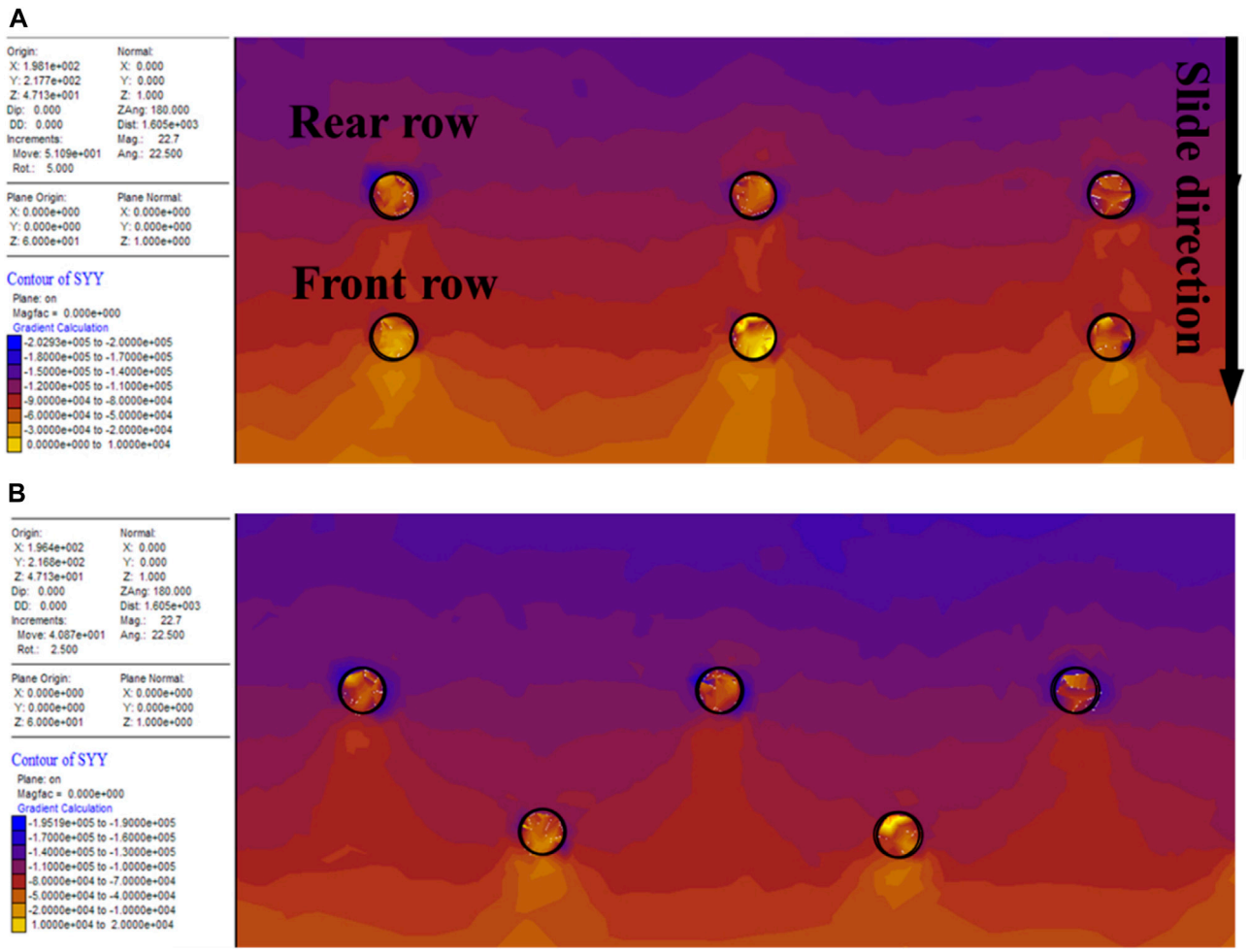

FIGURE 6
Stress distribution with different pile arrangements: **(A)** Parallel arrangement; **(B)** Quincunx arrangement.

Comparing the two arrangement forms, the soil arches between the front and rear rows of piles are distributed parallel to each other when the double-row piles are laid in parallel, and the soil arch is generated between two adjacent piles in the same row. The soil arch between the rear row piles is the same as the parallel arrangement in the double-row quincunx arrangement, while the soil arch between the front row piles is not between the two adjacent piles in the front row, but between the front row piles and the rear row piles, and the arch axis skews crossing the arch axis of the rear row piles at an angle. Two small soil arches are formed between the front row pile and the two adjacent rear row piles, which form a triangle with the soil arch between the rear row piles, and prevent the soil between the piles from sliding toward the front of the slope. Assuming that the distance between two arch feet is the arch length, the arch length of the soil arch between the piles is $2L$ with the parallel arrangement, while the arch length is $L + \sqrt{4L'^2 + L^2}$, with the quincunx arrangement. If the soil arch effect is evaluated only by the arch length without considering other factors, the soil arching effect with quincunx arrangement is more obvious than that with parallel arrangement.

Displacement distribution of soil between piles

Figure 7 shows the horizontal (y-direction) displacement distribution of soil between piles under different pile arrangements. The blue area in the graph indicates smaller displacement and the red area indicates larger displacement. The displacement of the soil from the rear piles to the front piles gradually decreases, and the displacement in the middle is large and small on both sides. The shape is distributed in an arch convex to the front of the pile, which is the displacement arch. Compared with the parallel arrangement, the soil displacement between piles is smaller in quincunx arrangement, and the soil displacement between piles decreases faster from the rear row piles to the front row piles.

Figure 8 shows the x-direction displacement distribution of soil between piles under different pile arrangements. The blue area indicates larger displacement in the x-negative direction, the red area indicates larger displacement in the x-positive direction, and the green area indicates smaller displacement and close to zero in the x-direction. the x-direction displacement of the soil on the side of the

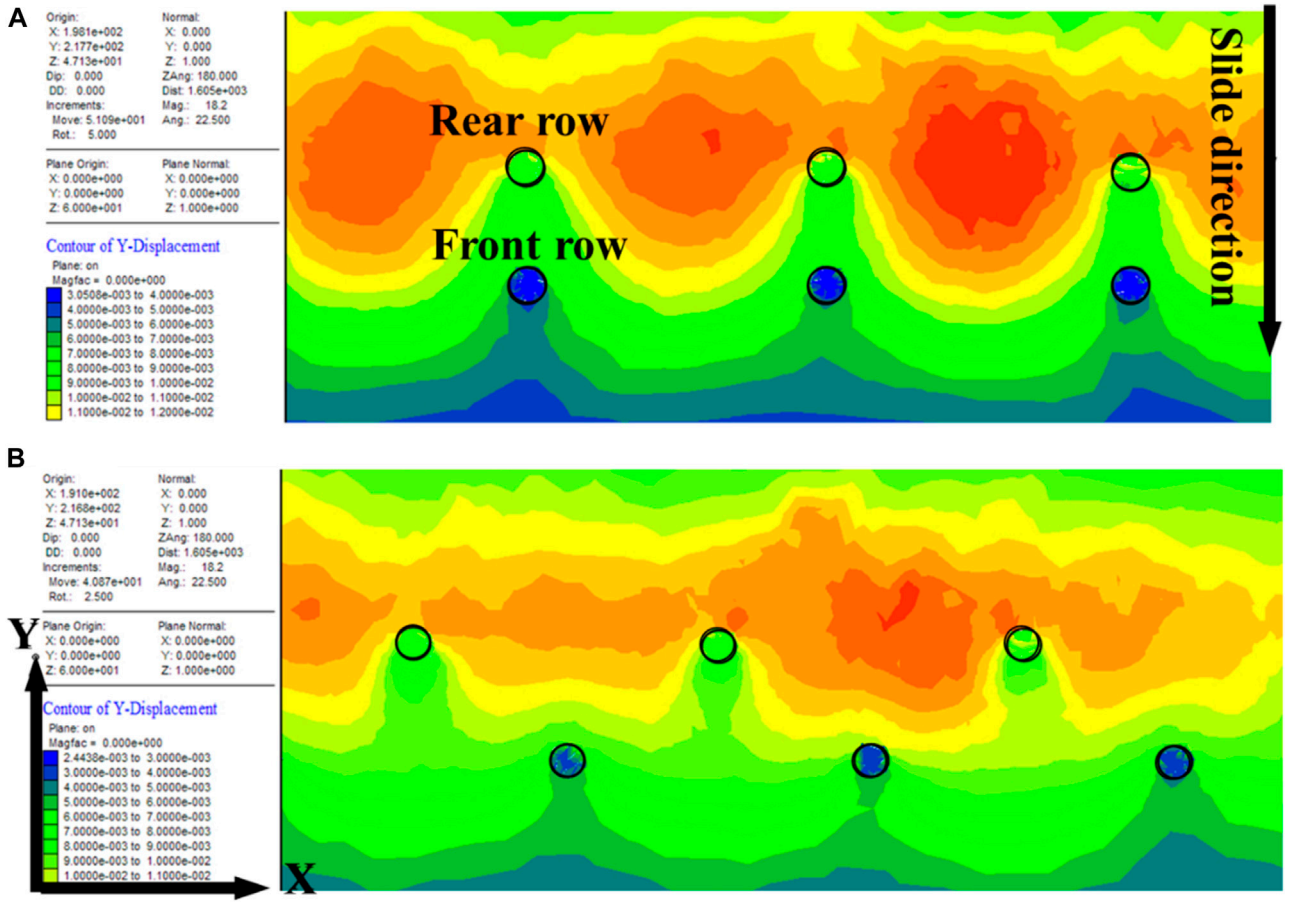

FIGURE 7
Displacement distribution in *y*-direction with different pile arrangements: **(A)** Parallel arrangement; **(B)** Quincunx arrangement.

pile is larger while the *x*-direction displacement of the soil between the piles is small and close to zero with parallel arrangement. The soil displacement is mainly in the *y*-direction of the vertical pile center line, while the *x*-direction displacement at the pile side of the front row piles is significantly reduced compared with the rear row piles. Large *x*-directional displacements occur in the soil on the side of both the front and rear rows piles with the quincunx arrangement.

Anti-slide piles are arranged in vertical sliding direction, when the soil is prevented from moving behind the piles to the front of the piles by the anti-slide piles, it will flow around both sides. The soil mainly flows around the rear row piles, and most of the soil only flows around once in the process of moving to the front slope with parallel arrangement, while the soil flows around the front and rear rows piles, and most of the soil needs to flow around twice to reach the front slope with quincunx arrangement. Therefore, the quincunx pile arrangement is more conducive to stopping the forward creep slipping of the soil between the piles.

The quincunx arrangement can effectively stop the soil between piles from sliding toward the front of the slope, mainly because the quincunx arrangement indirectly shortens the pile distance. According to previous research results (Wang, 2005), the influence of pile distance on soil arching effect is most significant, so any method that can directly or indirectly shorten pile distance can effectively enhance the soil arching effect between piles.

Load sharing ratio of pile with two pile arrangements

The load sharing ratio of piles is an important indicator of the soil arching effect (Cao and Meng, 2012). For the double-row piles, the front and rear rows piles and the soil between the rows form a whole and resist the residual sliding force of the landslide together (Wu and Zhang, 2007). The load sharing ratio among the three is important for the effect of double-row anti-slide piles to reinforce the slope and design safe and economical anti-slide piles. The anti-slide pile within a depth of 6 m is located within the slip body, which bears most of the load. Due to the soil in front of the piles being less at a depth of 2 m and above, the horizontal cross-sections at depth of 3 m, 4 m, 5 m and 6 m are chosen to calculate the load sharing ratio of the front and rear rows piles and soil between piles (Table 2).

Table 3 shows the load sharing ratio of double-row anti-slide piles in parallel and quincunx arrangements. The maximum value of load sharing ratio for quincunx arrangement appears at a depth of 3 m as 76%, the maximum value for parallel arrangement appears at a depth of 4 m as

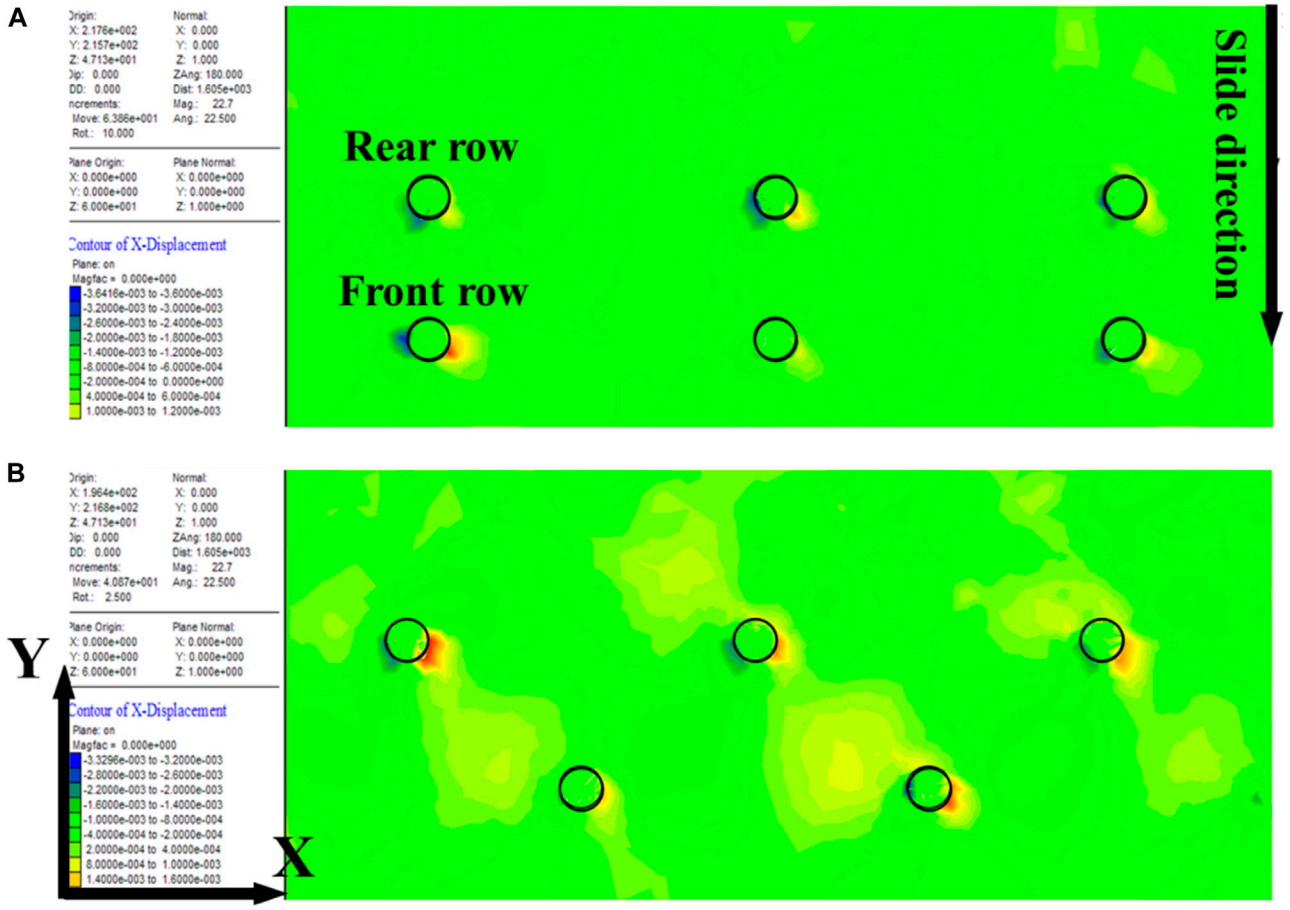

FIGURE 8
Displacement distribution in *x*-direction with different pile arrangements: **(A)** Parallel arrangement; **(B)** Quincunx arrangement.

TABLE 2 The load sharing ratio of the front and rear rows piles and soil between piles.

Pile arrangement	Depth/m	Rear row piles/%	Front row piles/%	Soil between piles/%
Parallel arrangement	3	45	37	18
	4	63	35	2
	5	42	55	3
	6	44	51	5
Quincunx arrangement	3	65	35	0
	4	53	44	3
	5	49	51	0
	6	44	49	7

69%, and the average value for both is 67.25% and 60%. Both the maximum and average values of quincunx arrangement are larger than parallel arrangement, so the quincunx arrangement is conducive to the soil arching effect, which makes more residual sliding force to migrate to the pile body.

From Table 2 and Table 3, the load sharing ratio of front and rear piles is different with increasing depth, the load in depth 3–5 m is mainly borne by rear piles, while the load in depth 5–6 m is mainly borne by front piles. But the load sharing ratio of rear piles is greater than that of front piles, the design should improve the strength of rear piles, increase the reinforcement, or reduce the diameter of front piles appropriately. The load sharing ratio of the row piles is greater than that of the parallel arrangement in the quincunx arrangement, and the load sharing ratio of the front row of piles is similar in both cases. The soil

TABLE 3 The load sharing ratio of the whole piles.

Pile arrangement	Depth/m	Load sharing ratio	Average value
Parallel arrangement	3	60	60
	4	69	
	5	48	
	6	63	
Quincunx arrangement	3	76	67.25
	4	64	
	5	75	
	6	54	

between the rows in the quincunx arrangement bears little load, while the soil between the rows in the parallel arrangement bears a larger load, so that the anti-slide force provided by the soil between the piles can be used as a safety reserve to improve the safety factor of the slope.

Conclusion

Due to the expansibility of the rock-soil mass of the Xinyan landslide, its sliding damage is influenced by a variety of factors. In this paper, based on the anti-slide pile reinforcement scheme of the Xinyan landslide, a three-dimensional model was established by FLAC-3D to simulate the soil arching effect between piles with different arrangements of double-row piles, the following conclusions are drawn:

(1) The soil arch is generated between two adjacent piles in the same row and parallel to each other in parallel arrangement; while it is generated between the front row pile and the adjacent rear piles in quincunx arrangement.
(2) The soil flows around the piles only once in parallel arrangement, while it flows around piles twice in quincunx arrangement, which is more conducive to stopping the creep slipping of the soil between the piles.
(3) When piles are arranged in double rows, the rear row piles bear a greater load than the front row piles. Compared with parallel arrangement, the load sharing ratio of rear pile is greater and the support effect is better with quincunx arrangement.
(4) In this paper, the study of soil arch effect is limited to numerical simulation analysis, which makes the deviation between simulated and real values. The next research will focus on establishing a physical model of the landslide and adjusting the numerical model through physical model tests to making the simulation results closer to the real values.

Data availability statement

The data that support the findings of this study are available from SB but restrictions apply to the availability of these data, which were used under license for the current study, and so are not publicly available. Data are however available from the authors upon reasonable request and with permission of DX. Requests to access the datasets should be directed to DX, 13921785992@163.com.

Author contributions

YS: Investigation, Resources, Writing–Original Draft DX: Data Curation GW: Methodology, Writing–Review and Editing DL: Data Curation SB: Software WW: Validation. All authors contributed to the article and approved the submitted version.

Funding

This study is supported by the National Natural Science Foundation of China (No. 42207209), Doctoral Research Initial Fund of Jilin Jianzhu University (No. 86122401) and Jilin Provincial Science and Technology Development Project of China (No. YDZJ202201ZYTS647). The work is also supported by Crosswise Tasks of Changchun Jianye Group Corporation (No. 73800801) and Jilin Gongcheng Project Management Limited Company (No. 73800801). The funders were not involved in the study design, collection, analysis, interpretation of data, the writing of this article, or the decision to submit it for publication.

Conflict of interest

The authors declare that the research was conducted in the absence of any commercial or financial relationships that could be construed as a potential conflict of interest.

Publisher's note

References

Bhaisin, R., and Aarset, A. (2020). Application of Norwegian Method of Tunnelling (NMT) principles to bypass landslides in mountainous terrain. *Geotechnics Sustain. Infrastructure Dev.* 62, 273–279. doi:10.1007/978-981-15-2184-3_34

Cao, Q. L., and Meng, Y. K. (2012). Study on the load-sharing ratio of piles and soil about the squared piles composite foundation of sluice. *Adv. Hydrology Hydraulic Eng.* 212, 963–969. doi:10.4028/www.scientific.net/AMM.212-213.963

Chang, B. P. (1998). A study on soil arch between stabilizing piles and critical span. *Proc. Landslides* 3, 73–78. doi:10.3969/j.issn.1004-9665.2004.01.018

Cui, P., Ge, Y. G., Li, S. J., Li, Z. H., Xu, X. W., Zhou, G. G. D., et al. (2022). Scientific challenges in disaster risk reduction for the Sichuan-Tibet Railway. *Eng. Geol.* 309, 106837. doi:10.1016/j.enggeo.2022.106837

Du, Y., Yan, E. C., Gao, X., Mwizerwa, S., Yuan, L. W., and Zhao, S. (2021). Identification of the main control factors and failure modes for the failure of Baiyuzui landslide control project. *Geotechnical Geol. Eng.* 39 (5), 3499–3516. doi:10.1007/s10706-021-01707-0

Haugen, B. D. (2017). A design method for landslide surface water drainage control. *Environ. Eng. Geoscience* 23 (4), 275–289. doi:10.2113/gseegeosci.23.4.275

He, K. Q., Wang, S. Q., Du, H., and Wang, S. J. (2008). The dynamic parameter of rainfall: Its importance in the prediction of colluvial landslides. *Bull. Eng. Geol. Environ.* 67 (3), 345–351. doi:10.1007/s10064-008-0143-4

Jimenez-Peralvarez, J. D. (2018). Landslide-risk mapping in a developing hilly area with limited information on landslide occurrence. *Landslides* 15 (4), 741–752. doi:10.1007/s10346-017-0903-y

Liang, L. J., Xu, C. J., Chen, Q. Z., and Chen, Q. S. (2020). Experimental and theoretical investigations on evolution of soil-arching effect in 2D trapdoor problem. *Int. J. Geomechanics* 20, 06020007. doi:10.1061/(ASCE)GM.1943-5622.0001643

Liao, S. F., Ye, M. Z., Yuan, R. C., and Ma, W. Z. (2022). Unmanned aerial vehicle surveying and mapping trajectory scheduling and autonomous control for landslide monitoring. *J. Robotics* 2022, 1–13. doi:10.1155/2022/2365006

Martin, J. G. C., Scolobig, A., Linnerooth-Bayer, J., Liu, W., and Balsiger, J. (2021). Catalyzing innovation: Governance enablers of nature-based solutions. *Sustainability* 13 (4), 1971. doi:10.3390/su13041971

Shanguan, Y. L. (2014). "Study on genetic mechanism and pile-soil contact effect of anti-slide piles of Xinyan landslide,". dissertation/doctor's thesis (Changchun, China: Jilin University).

Tiranti, D., and Cremonini, R. (2019). Editorial: Landslide hazard in a changing environment. *Front. Earth Sci.* 7, 1–3. doi:10.3389/feart.2019.00003

Ukleja, J. (2020). Stabilization of landslides sliding layer using electrokinetic phenomena and vacuum treatment. *Geosciences* 10 (8), 284. doi:10.3390/geosciences10080284

Wang, G. J., Zhao, B., Wu, B. S., Wang, M. L., Liu, W. L., Zhou, H. M., et al. (2022a). Research on the macro-mesoscopic response mechanism of multisphere approximated heteromorphic tailing particles. *Lithosphere* 2022, 1977890. doi:10.2113/2022/1977890

Wang, G. J., Zhao, B., Wu, B. S., Zhang, C., and Liu, W. L. (2022b). Intelligent prediction of slope stability based on visual exploratory data analysis of 77 *in situ* cases. *Int. J. Min. Sci. Technol.* 33 (1), 47–59. doi:10.1016/j.ijmst.2022.07.002

Wang, G., Zhao, B., Lan, R., Liu, D. W., Wu, B. S., Li, Y. J., et al. (2022c). Experimental study on failure model of tailing dam overtopping under heavy rainfall. *Lithosphere* 2022, 5922501. doi:10.2113/2022/5922501

Wang, Q. K. (2005). Discussion on the soil arching effect and the critical spacing between adjacent anti-slide piles. *J. Wuhan Univ. Technol.* 27 (8), 64–67. doi:10.3321/j.issn:1671-4431.2005.08.019

Wu, C. J., and Zhang, Z. X. (2007). Numerical analysis of soil arching effect in piles in the slope engineering. *Chin. J. Undergr. Space Eng.* 3 (7), 1305–1309. doi:10.3969/j.issn.1673-0836.2007.z1.027

Xia, Y. Y., Zheng, X. Y., and Rui, R. (2008). "Numerical analysis of soil-arch effect of anti-slide piles," in *Landslides and engineered slopes: From the past to the future* (Boca Raton, Florida, United States: CRC Press), 1011–1016.

Yin, Z. Q., Qin, X. G., Yin, Y. P., Zhao, W. J., and Wei, G. (2014). Landslide developmental characteristics and response to climate change since the last glacial in the upper reaches of the Yellow River, NE Tibetan Plateau. *ACTA Geol. Sinica-English Ed.* 88 (2), 635–646. doi:10.1111/1755-6724.12219

Zhang, C. L., Jiang, J. L., Lei, D., Asghar, A., Su, L. J., and Wang, Z. M. (2021). Large-scale shaking table test on seismic behaviour of anti-slide pile-reinforced bridge foundation and gravel landslide: A case study. *Bull. Eng. Geol. Environ.* 80 (2), 1303–1316. doi:10.1007/s10064-020-02006-3

Zhang, Z. Q., Li, M., Wang, J., Yin, Z. Q., Yang, Y. Z., Xun, X. Y., et al. (2023a). A calculation model for the spatial distribution and reserves of ground ice - a case study of the Northeast China permafrost area. *Eng. Geol.* 315, 107022. doi:10.1016/j.enggeo.2023.107022

Zhang, Z. Q., Li, M., Wen, Z., Yin, Z. Q., Tang, Y. F., Gao, S. R., et al. (2023b). Degraded frozen soil and reduced frost heave in China due to climate warming. *Sci. Total Environ.* 893, 164914. doi:10.1016/j.scitotenv.2023.164914

Zhang, Z. Y. (2000). The present status, technical advance and development trends of landslide remedial measures. *J. Geol. Hazards Environ. Preserv.* 2, 89–97+181. doi:10.3969/j.issn.1006-4362.2000.02.001

Zheng, X. Y. (2005). "Numerical simulation studies on the sustentation structure of anti-sliding piles,". dissertation/master's thesis (Wuhan, Hubei: Wuhan University of Technology).

Zhou, D. P., Wang, H. L., and Sun, H. W. (2009). Micro-pile composite structure and its design theory. *Chin. J. Rock Mech. Eng.* 28 (7), 1353–1362. doi:10.3321/j.issn:1000-6915.2009.07.008

Zhou, D. P., Xiao, S. G., and Xia, X. (2004). Discussion on rational spacing between adjacent anti-slide piles in some cutting slope projects. *Chin. J. Geotechnical Eng.* 27 (8), 64–67. doi:10.3321/j.issn:1000-4548.2004.01.025

Zhu, C. G., Yang, F., Zheng, J. L., Lin, G. J., and Tian, Z. Y. (2021). Interaction and treatment for tunnels orthogonally traversing large bedrock landslides. *KSCE J. Civ. Eng.* 25 (7), 2758–2769. doi:10.1007/s12205-021-2231-y

frontiers | Frontiers in Earth Science

TYPE Original Research
PUBLISHED 07 July 2023
DOI 10.3389/feart.2023.1236829

OPEN ACCESS

EDITED BY
Wenzhuo Cao,
Imperial College London,
United Kingdom

REVIEWED BY
Zhitang Lu,
Hefei University of Technology, China
Haoran Zhang,
China Earthquake Administration, China

*CORRESPONDENCE
Linfang Shen,
shenlinfang@kust.edu.cn

RECEIVED 08 June 2023
ACCEPTED 27 June 2023
PUBLISHED 07 July 2023

CITATION
Tian L, Shen L, Wang Z and Luo J (2023), Numerical calculation of phase change heat conduction in freezing soil by lattice Boltzmann method based on enthalpy method.
Front. Earth Sci. 11:1236829.
doi: 10.3389/feart.2023.1236829

Numerical calculation of phase change heat conduction in freezing soil by lattice Boltzmann method based on enthalpy method

Lin Tian[1], Linfang Shen[1]*, Zhiliang Wang[1] and Junyao Luo[2]

[1]Faculty of Civil Engineering and Mechanics, Kunming University of Science and Technology, Kunming, China, [2]Power China Kunming Engineering Corporation Limited, Kunming, China

In the freezing process, the soil is accompanied by heat conduction, heat release for ice-water phase change, phase change interface movement, and a change in thermal diffusion coefficient, which is a complex nonlinear problem and is hard to solve. This study uses the enthalpy method to establish a unified control equation for heat conduction in the entire calculation region (including the solid-phase zone, liquid-phase zone, and phase change interface). It solves the equation numerically, relying on the D2Q4 model of the lattice Boltzmann method, and determines the evolution of the temperature field and solid-liquid phase change interface position with time. The trends in the soil's temperature field evolution and freezing front movement under unilateral and bilateral cold sources are discussed using an example from an artificial freezing project. The results show that when −10°C is taken as the limit for freezing wall temperature, the freezing wall thickness developed at 5, 10, 20, 30, and 40 days under the unilateral cold source is 0.24, 0.33, 0.47, 0.57, and 0.66 m, respectively. The overall temperature in the soil drops below −13.6°C and −26.4°C at 35 days and 45 days under the bilateral cold sources. These values can provide a basis for engineering design.

KEYWORDS

lattice Boltzmann method, enthalpy method, temperature field, freezing soil, numerical simulation

1 Introduction

In building underground projects, the heat conduction problem accompanied by phase change frequently occurs, such as in tunnelling projects in cold areas (Hunag et al., 1986), constructing underground projects, including subways (Van Dorst, 2013), artificial freezing reinforcement of soil during shaft sinking at mine (Levin et al., 2021), treatment of underground repositories of permanently isolated radioactive waste (Jing et al., 1995), and others. If the development mechanism of the temperature field of the geotechnical materials in the freezing process cannot be comprehended in engineering practice, it will seriously affect the project's safety and directly or indirectly cause significant economic losses. For example, a shaft submergence accident occurred in an auxiliary shaft of Huainan Xieqiao Mining Area due to the freezing tube fracture, resulting in direct economic losses of over 10 million yuan. Repeated water-bursting accidents happened during excavation in a concealed excavation tunnel in Shenzhen because of a frozen wall connection failure. Due to the water gushing at the frozen wall in the intermediate wind well in the tunnel of Shanghai

Metro Line 4, a severe surface collapse occurred, and the entire tunnel was destroyed by Huangpu River water gushing, resulting in an economic loss of nearly 150 million yuan. Therefore, a systematic and in-depth study of the development trends of the solid-liquid phase change interface, and the evolution of the temperature field during the soil freezing process, can provide a valuable technical foundation for projects associated with soil freezing. This has significant value for theoretical research and offers broad engineering application prospects.

When soil water condenses into ice and forms a solid-liquid phase change interface, heat will be released at the interface, and the interface will move continuously with time during freezing. Thus, the heat conduction problem with phase change is highly nonlinear. Due to the nonlinear nature of the phase change system at its moving interfaces, it is difficult to predict its behaviour, and no rigorous theory can be developed (Rabin and Korin, 1993; Costa et al., 1998). A large number of practical engineering problems are often solved with the assistance of numerical algorithms. In dealing with phase change boundaries, current computational methods include the heat capacity (Rabin and Korin, 1993; Alva et al., 2006), Kirchhoff transformation (Voller et al., 1990), and enthalpy methods (Costa et al., 1998; Jiaung et al., 2001; Miller and Succi, 2002; Eshraghi and Felicelli, 2012). In dealing with phase change interfaces, the enthalpy approach has been widely used because of its advantages, such as clear physical meaning, no need to trace the interface, and ease of numerical calculation. The lattice Boltzmann method is a mesoscopic numerical calculation technique that can establish the relation between macroscopic and microscopic computations in numerical simulation of heat conduction. The method core is to establish a bridge between the microscopic and macroscopic scales. It does not need to consider the motion law of individual particles but instead considers the motion of all particles as a whole and describes their overall macroscopic motion characteristics using the distribution function. Due to its clear physical concepts, ease in dealing with complex boundaries, simple implementation of procedures, and suitability for parallel computation, it has gained increasing attention for phase change heat conduction problems. Jiaung et al. (Jiaung et al., 2001) improved the lattice Boltzmann model using the enthalpy method to simulate the heat conduction problem associated with solid-liquid phase changes. Miller and Succi (Miller and Succi, 2002) simulated two-dimensional crystal solidification and dendrite growth by introducing a time-dependent phase change fraction. Eshraghi and Felicelli (Eshraghi and Felicelli, 2012) developed an implicit lattice Boltzmann model for phase change heat conduction using the D2Q9 model and considering different boundary conditions.

By combining the enthalpy method and the lattice Boltzmann method, the strengths of both approaches can be leveraged, enhancing the accuracy and reliability of heat conduction studies in soil. Both the enthalpy method and the lattice Boltzmann method are capable of dealing with intricate geometries and boundary conditions. This enables more precise simulations of heat conduction in soil with complex structures and spatial heterogeneity. The lattice Boltzmann method inherently lends itself to parallel computing. When combined with the enthalpy method, the parallel computing advantage can be further exploited, accelerating the computational speed of heat conduction simulations and improving efficiency. The enthalpy and lattice Boltzmann methods allow for modeling at different scales. Their combination enables multiscale heat conduction simulations, encompassing various scales from micro to macro, facilitating a comprehensive understanding of heat transfer behavior in soil.

This study uses the lattice Boltzmann model relying on the enthalpy method to transform the heat conduction problem solved by partitioning it into a nonlinear heat conduction problem with a phase change over the entire region. The enthalpy method establishes a unified control equation for the entire computational region (solid-phase zone, liquid-phase zone, and solid-liquid phase change interface). The heat conduction equation with phase change is solved numerically in the discrete calculation region utilizing the lattice Boltzmann method. The temperature field and the solid-liquid phase change interface's position are derived as a time function based on the relationship between enthalpy and temperature. The calculation method validity is verified by combining the Neumann solution of the semi-infinite space solid-liquid phase change heat conduction problem. Finally, trends of temperature field evolution and freezing front movement in the soil under unilateral and bilateral cold sources are discussed using an example from an artificial freezing project.

2 Materials and methods

2.1 Physical model of soil freezing

In order to study the temperature field evolution in the soil during freezing and the movement trend of the freezing front, a schematic diagram of the freezing model for the soil's solid-liquid phase in a semi-infinite region is established (Figure 1), where the X-axis direction represents the soil's freezing direction; L is the length of the freezing influence range; the adiabatic boundary is located at $y = L$; T_0 is the constant cold source temperature; T_f is the soil's freezing temperature; T_i is the soil's initial temperature; $s(t)$ is the location of the interface for the solid-liquid phase change in the soil.

2.1.1 Basic assumptions

In order to numerically solve the heat conduction equation while considering the phase change, the following basic assumptions were made: 1) The soil was considered a homogeneous isotropic continuous medium, which was divided into solid and liquid phase zones according to the physical state of the internal moisture. The thermophysical parameters of each phase zone were fixed at constant values and were made independent of the temperature; 2) The effects of moisture migration, soil frost heaving, and stress field change were ignored. Whereas the heat conduction effect during the freezing process was only considered; 3) The heat conduction and the movement of the phase change interface during the soil's freezing process are along a single direction; 4) The effect of the solid-liquid phase change interface's thickness in the soil body is not considered; 5) The soil's freezing temperature is constant. Besides, the freezing process was completed instantaneously, ignoring its physical evolution process.

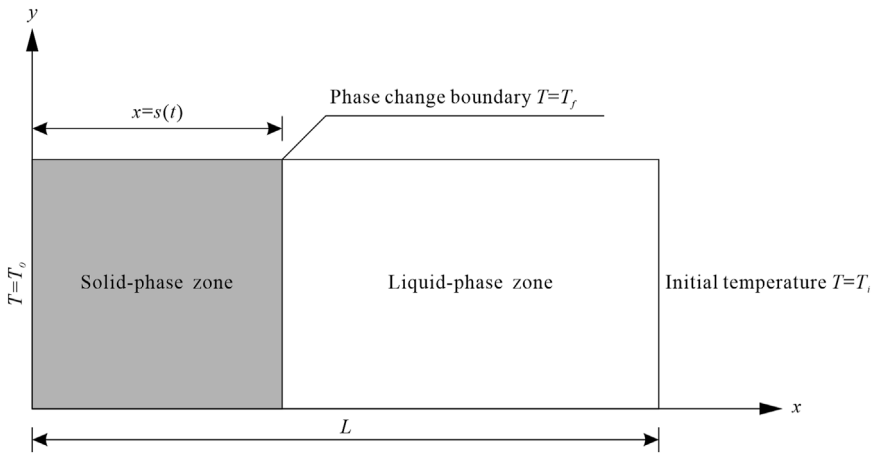

FIGURE 1
Schematic diagram of the soil's solid-liquid phase freezing model in a semi-infinite region.

2.1.2 Mathematical equations

The mathematical equation for the temperature field evolution can be simplified according to the temperature-induced change in the physical state of water in the soil, which is divided into the solid-phase zone and liquid-phase zones (Ozisik, 1993) as follows:

Solid-phase zone:

$$\frac{\partial T_s(x,t)}{\partial t} = \alpha_s \frac{\partial^2 T_s(x,t)}{\partial x^2} \quad (0 < x < s(t)) \tag{1}$$

Liquid-phase zone:

$$\frac{\partial T_l(x,t)}{\partial t} = \alpha_l \frac{\partial^2 T_l(x,t)}{\partial x^2} \quad (s(t) < x < L) \tag{2}$$

where T_s and T_l are the soil's temperatures in the solid-phase zone and liquid-phase zone, respectively; α_s and α_l are the thermal diffusion coefficients of the soil in the solid-phase zone and liquid-phase zone, respectively, in which $\alpha = k/(\rho C_p)$, where ρ is the density, C_p is the specific heat capacity, and k is the thermal conductivity that can be obtained from the volume fraction of water (or ice), soil particles, and air in the soil and their respective thermophysical parameters (Radoslwa et al., 2006); t is the freezing time.

2.1.3 The enthalpy method model

In order to study the movement process for the phase change interface during soil freezing, the enthalpy parameter was introduced into the heat conduction equation according to the enthalpy model proposed by Shamsundar and Sparrow (Shamsundar and Sparrow, 1975) as follows:

$$\rho \frac{\partial H}{\partial t} = k \frac{\partial^2 T}{\partial x^2} \tag{3}$$

where H is the enthalpy; C_p is the soil's specific heat capacity, which is assumed to not change with temperature; H can be expressed as:

$$H = C_p T + \varphi L_a \tag{4}$$

where φ is the liquid-phase fraction, in which $\varphi = 1$ in the liquid phase and $\varphi = 0$ in the solid phase.

Substituting Eq. 4 into Eq. 5 yields the following:

$$\frac{\partial T}{\partial t} = \alpha \frac{\partial^2 T}{\partial x^2} - \frac{L_a}{C_p} \frac{\partial \varphi}{\partial t} \tag{5}$$

Comparing Eq. 5 to the heat conduction in Eqs. 1, 2, it can be seen that Eq. 5 adds a source term related to the latent heat of the phase change L_a in the heat conduction equation.

When the soil's freezing temperature is a constant value T_f, the relationship between the liquid-phase fraction and the enthalpy can be defined as follows:

$$\varphi = \begin{cases} 0 & H < C_p T_f \\ \dfrac{H - C_p T_f}{L_a} & C_p T_f \le H \le C_p T_f + L_a \\ 1 & H > C_p T_f + L_a \end{cases} \tag{6}$$

2.1.4 Boundary conditions

The temperature of the soil's cold source can be defined as follows:

$$T(0,t) = T_0 \tag{7}$$

The soil body has a constant initial temperature that is defined as follows:

$$T(x,0) = T_i \tag{8}$$

At the solid-liquid phase change interface $y = s(t)$:

$$T_s(x,t) = T_l(x,t) = T_f \tag{9}$$

$$k_s \frac{\partial T_s(x,t)}{\partial x} - k_l \frac{\partial T_l(x,t)}{\partial x} = \rho_s L_a \frac{ds(t)}{dt} \tag{10}$$

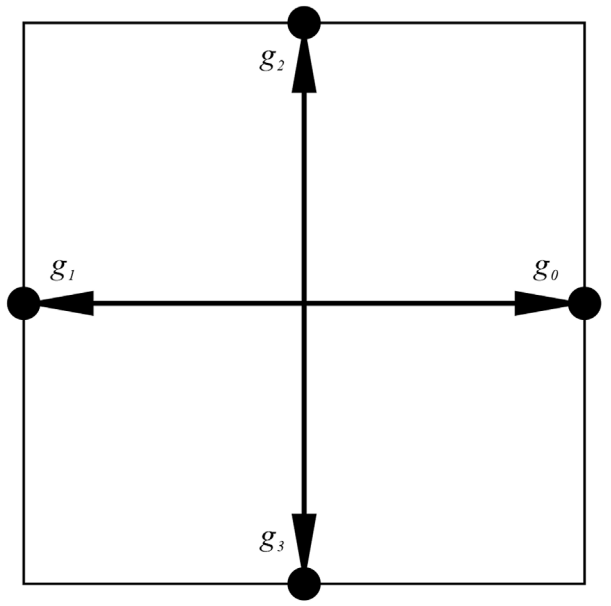

FIGURE 2
Schematic showing the 4 discrete velocity directions in the D2Q4 model.

2.1.5 Dimensionless processing

In order to simplify the calculation, the soil's heat conduction equation and the corresponding boundary conditions are normalized as follows:

$$\begin{cases} X = \dfrac{x}{L} \\ S = \dfrac{s}{L} \\ F_0 = \dfrac{\alpha_s t}{L^2} \\ \theta = \dfrac{T - T_0}{T_i - T_0} \end{cases} \tag{11}$$

where X is the dimensionless length; S is the dimensionless solid-liquid phase change position; F_0 is the dimensionless time; θ is the dimensionless temperature.

Substituting Eq. 11 into Eqs. 1, 2 yields the following:

Solid-phase zone:

$$\frac{\partial \theta_s(X,F_0)}{\partial F_0} = \frac{\partial^2 \theta_s(X,F_0)}{\partial X^2} \quad (0 < X < S(F_0)) \tag{12}$$

Liquid-phase zone:

$$\frac{\partial \theta_l(X,F_0)}{\partial F_0} = \frac{\alpha_s}{\alpha_l}\frac{\partial^2 \theta_l(X,F_0)}{\partial X^2} \quad (S(F_0) < X < 1) \tag{13}$$

The corresponding boundary condition transformations are cold source temperature $\theta_s(0,F_0) = 0$ and initial temperature $\theta_l(X,0) = 1$.

The following equations are valid at the solid-liquid phase change interface $X = S(F_0)$:

$$\theta_s(X,F_0) = \theta_l(X,F_0) = \frac{T_f - T_i}{T_0 - T_i} \tag{14}$$

$$\frac{\partial \theta_s(X,F_0)}{\partial X} - \frac{k_l}{k_s}\frac{\partial \theta_l(X,F_0)}{\partial X} = \frac{\frac{T_f - T_i}{T_0 - T_i}}{Ste}\frac{dS(F_0)}{dF_0} \tag{15}$$

where Ste is the Stephen number, a dimensionless quantity that is related to the phase change process, $Ste = \frac{C_p(T_f - T_0)}{L_a}$.

2.2 Lattice Boltzmann model based on the enthalpy method

2.2.1 Lattice Boltzmann model

In this study, the temperature in the macroscopic heat conduction equation is taken as a scalar, and the D2Q4 model proposed by Qian et al. (Qian et al., 1992) is used for the soil's temperature field evolution process during freezing (Figure 2). The time evolution of the particle temperature distribution function $g_i(r,t)$ can be expressed by the discrete lattice Boltzmann equation in the form of BGK (Bhatnagar, Gross, and Krook) as:

$$g_i(r + \mathbf{e_i}\delta_t, t + \delta_t) - g_i(r,t) = -\frac{g_i(r,t) - g_i^{eq}(r,t)}{\tau} + Sr_i\delta_t \quad (i = 0,1,2,3) \tag{16}$$

where $g_i(r,t)$ is the particle temperature distribution function along direction i at lattice point r and moment t; e_i is the discrete velocity, which consists of a set of velocity vectors in four directions defined as follows:

$$\mathbf{e} = c[(1,0), (-1,0), (0,1), (0,-1)] \tag{17}$$

where c is the lattice velocity, $c = \frac{\delta_x}{\delta_t}$; δ_x and δ_t are the discrete lattice step and time step, respectively; τ is the dimensionless relaxation time, in which a stable solution is usually obtained for $\tau = 1.0$ (Sukop and Thorne, 2006); $g_i^{eq}(r,t)$ is the equilibrium state distribution function. Since the convection effect was not considered in the soil freezing process, the D2Q4 model $g_i^{eq}(r,t)$ can be expressed by the following equation:

$$g_i^{eq}(r,t) = \omega_i T(r,t) \tag{18}$$

where ω_i is the weight factor, $\omega_0 = \omega_1 = \omega_2 = \omega_3 = \frac{1}{4}$.

The discrete source term Sr_i in Eq. 16 is defined as:

$$Sr_i = \omega_i Sr \tag{19}$$

where Sr can be obtained from Eq. 5 as:

$$Sr = \frac{L_a}{C_p}\frac{\partial \varphi}{\partial t} \tag{20}$$

Substituting Eqs. 18, 19, and 20 into Eq. 16, the final discrete lattice Boltzmann equation for the freezing process of the soil is obtained as follows:

$$g_i(r + e_i\delta_t, t + \delta_t) - g_i(r,t) = -\frac{g_i(r,t) - g_i^{eq}(r,t)}{\tau} + \omega_i\frac{L_a}{C_p}\left[\varphi(t + \delta_t) - \varphi(t)\right] \quad (i = 0,1,2,3) \tag{21}$$

In this study, Eq. 21 was implemented in two steps for the convenience of the programming calculations. These steps are as follows:

(1) Collision

$$g_i(r,t+\delta_t)-g_i(r,t)=-\frac{g_i(r,t)-g_i^{eq}(r,t)}{\tau}+\omega_i\frac{L_a}{C_p}\left[\varphi(t+\delta_t)-\varphi(t)\right]\quad(i=0,1,2,3) \tag{22}$$

(2) Migration

$$g_i(r+e_i\delta_t,t+\delta_t)=g_i(r,t+\delta_t)\quad(i=0,1,2,3) \tag{23}$$

Based on the Chapman-Enskog multiscale expansion method, the lattice Boltzmann Eq. 21 can be reduced to Eq. 5 that contains the phase change by considering the relationship between the macroscopic temperature T and the particle temperature distribution function (i.e., $T=\sum_{i=0}^{3}g_i(r,t)$). The expression for the thermal diffusion coefficient α was obtained (Mohamad, 2011) as follows:

$$\alpha=c_s^2\left(\tau-\frac{1}{2}\right)\delta_t \tag{24}$$

where c_s is the lattice speed of sound. For the D2Q4 model, $c_s^2=\frac{1}{2}c^2$.

Since the soil's thermal diffusion coefficients in the liquid and solid phase zones during freezing soil differ, the relaxation times also vary. In this paper, the variation of the variable relaxation time with the liquid-phase fraction was considered and set according to the thermal diffusion coefficients of different phases as follows:

$$\tau=\frac{\varphi\alpha_l+(1-\varphi)\alpha_s}{\delta_t c_s^2}+\frac{1}{2} \tag{25}$$

The soil's thermal diffusion coefficient is found according to the percentage of the liquid phase fraction among different phases. Consequently, a unified equation can solve the thermal diffusion coefficient of different phases according to the changes in liquid phase fraction. During the numerical calculation, the relaxation time is obtained from Eq. 25, which is then brought into Eq. 16 for the evolution of the temperature field.

2.2.2 Boundary conditions

Accurate simulation of the boundary conditions is an important part of the numerical calculation that significantly influences accuracy, efficiency, and stability. The following determines the corresponding particle temperature distribution functions according to the macroscopic boundary conditions:

(1) Initial conditions

Assuming that the temperature of the soil body at the initial moment is constant T_i, and the particle temperature distribution function at each grid point is in equilibrium, then:

$$g_i(x,0)=\omega_i T_i\ (i=0,1,2,3) \tag{26}$$

(2) Boundary conditions

The non-equilibrium state extrapolation format proposed by Guo et al. (Guo et al., 2002) was used to handle the seepage field boundary of the soil. For the temperature field boundary, there is no essential difference between the two in terms of application (Yong et al., 2009; Gao et al., 2014). This method produces the distribution function with overall second-order accuracy. The basic idea is that the particle temperature distribution function $g_i(B,t)$ on the boundary lattice point B can be decomposed into two parts: the equilibrium state $g_i^{eq}(B,t)$ and the non-equilibrium state $g_i^{neq}(B,t)$, that is:

$$g_i(B,t)=g_i^{eq}(B,t)+g_i^{neq}(B,t) \tag{27}$$

For the equilibrium part $g_i^{eq}(B,t)$, the cold source constant temperature boundary (temperature is always T_0) can be obtained from Eq. 18. The adiabatic boundary can be taken as $g_i^{eq}(O,t)$ with its neighbouring grid point O. The solution of the non-equilibrium part $g_i^{neq}(B,t)$ is complicated. However, the calculation can be simplified by approximating $g_i^{neq}(O,t)$ of the adjacent lattice points in the temperature field as follows:

$$g_i(B,t)=g_i^{eq}(B,t)+\left[g_i(O,t)-g_i^{eq}(O,t)\right] \tag{28}$$

2.2.3 Unit conversions

The program's parameters are typically taken in lattice units during the numerical calculation of the lattice Boltzmann method. In contrast, physical problems are usually taken in physical units. Hence, a conversion relationship between physical and lattice units must be established. For this purpose, all physical and lattice units involved in the calculation must be dimensionless separately to ensure that the heat conduction criterion before and after dimensionless processing remains the same. Accordingly, a dimensionless parameter was used as a connection bridge to realize the unit conversion between the physical and lattice units.

Based on the dimensionless time, the relationship between the physical time t and the lattice time step can be established as follows:

$$F_0=\frac{\alpha_p t_p}{L_p^2}=\frac{\alpha_L t_L}{L_L^2} \tag{29}$$

where α_p and α_L are the thermal diffusion coefficients of the physical and lattice units, respectively; t_p and t_L are the times of the physical and lattice units, respectively ($t_L=N\delta_t$, where N is the number of calculation time steps); L_P and L_L are the reference lengths of physical and lattice units, respectively.

If L_P is the length of the whole calculation domain, then $L_L=n\delta x$, where n is the number of lattices in the calculation domain.

The correspondence between the physical unit phase change parameters (latent heat of phase change L_α, specific heat capacity C_p and the lattice unit can be established by combining the dimensionless temperature based on the dimensionless Ste number as follows:

$$Ste=\frac{C_{pp}\left(T_{fp}-T_{0p}\right)}{L_{ap}}=\frac{C_{pL}\left(T_{fL}-T_{0L}\right)}{L_{aL}} \tag{30}$$

where C_{pp} and C_{pL} are the specific heat capacities of the physical and lattice units, respectively; L_{ap} and L_{aL} are the latent heats of phase change in the physical and lattice units, respectively; T_{fp} and T_{fL} are the phase change temperatures of the physical and lattice units, respectively; T_{0p} and T_{0L} are the cold source temperatures of the physical and lattice units, respectively.

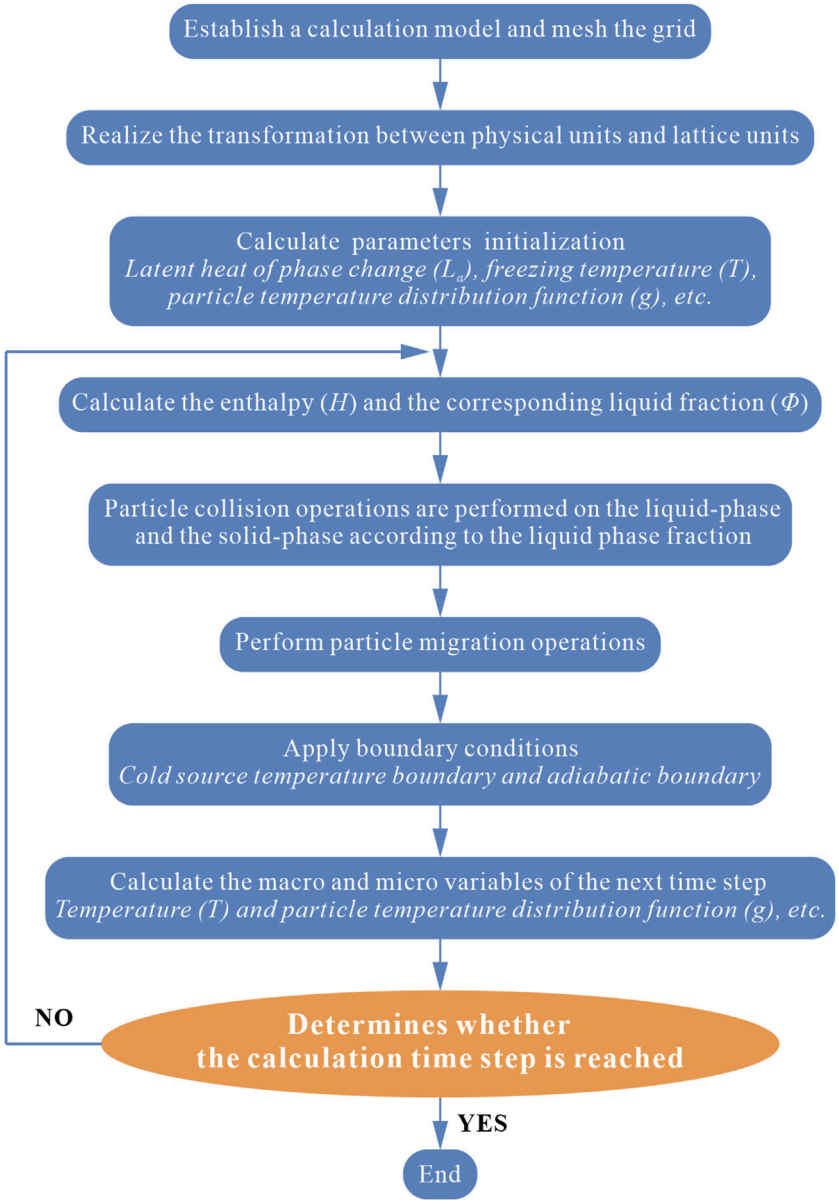

FIGURE 3
Flowchart of the program for investigating soil freezing.

2.2.4 Flow chart of the calculation procedure

In this study, a lattice Boltzmann model based on the enthalpy method is established, and the corresponding calculation procedure is prepared by considering the effects of heat conduction, latent heat release from solid-liquid phase change, and phase change interface movement in the soil's freezing process. The adopted flowchart is shown in Figure 3.

3 Results

3.1 Algorithm validation

In order to verify the accuracy and rationality of this numerical calculation method, the Neumann solution of the unidirectional solid-liquid phase change heat conduction process in a semi-infinite region was solved based on Eqs. 31, 32, 33, and 34 (Ozisik, 1993).

$$\frac{e^{-\lambda^2}}{erf(\lambda)}+\frac{k_l}{k_s}\left(\frac{\alpha_s}{\alpha_l}\right)^{1/2}\frac{T_f-T_i}{T_f-T_0}\frac{e^{-\lambda(\alpha_s/\alpha_l)}}{erfc\left[\lambda(\alpha_s/\alpha_l)^{1/2}\right]}=\frac{\lambda L\sqrt{\pi}}{C_{ps}(T_f-T_0)} \tag{31}$$

$$\frac{T_s(x,t)-T_0}{T_f-T_0}=\frac{erf\left[x/2(\alpha_s t)^{1/2}\right]}{erf(\lambda)} \tag{32}$$

$$\frac{T_l(x,t)-T_0}{T_f-T_0}=\frac{erfc\left[x/2(\alpha_s t)^{1/2}\right]}{erfc\left[\lambda(\alpha_s/\alpha_l)^{1/2}\right]} \tag{33}$$

$$s(t)=2\lambda(\alpha_s t)^{1/2} \tag{34}$$

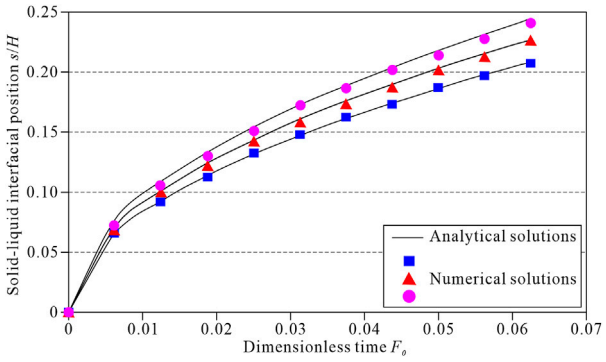

FIGURE 4
Comparison between the numerical and analytical solutions. The top black curve represents $\alpha_s/\alpha_l = 5$, the middle black curve represents $\alpha_s/\alpha_l = 2$, and the bottom black curve represents $\alpha_s/\alpha_l = 1$. The blue square represents $\alpha_s/\alpha_l = 1$, the red triangle represents $\alpha_s/\alpha_l = 2$, and the pink circle represents $\alpha_s/\alpha_l = 5$.

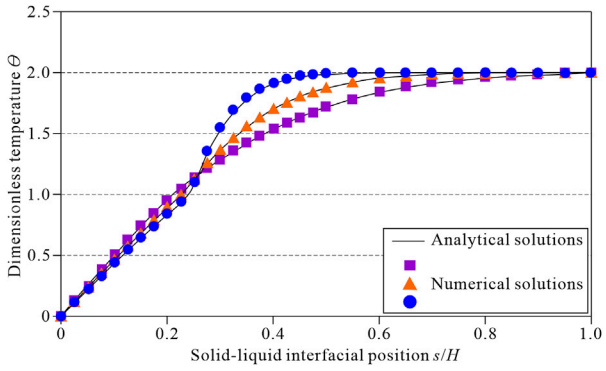

FIGURE 5
Comparison between the numerical and analytical solutions when $F_0 = 0.0625$ (the calculated time step is 10,000). The top black curve represents $\alpha_s/\alpha_l = 5$, the middle black curve represents $\alpha_s/\alpha_l = 2$, and the bottom black curve represents $\alpha_s/\alpha_l = 1$. The purple square represents $\alpha_s/\alpha_l = 1$, the orange triangle represents $\alpha_s/\alpha_l = 2$, and the blue circle represents $\alpha_s/\alpha_l = 5$.

The calculation area was set into a 200 × 10 grid. The calculation model is shown in Figure 1. The macroscopic calculation parameters were all based on the dimensionless parameters. The initial temperature of the calculation region is $T_i = 2$, the cold source temperature on the left side of the model is $T_0 = 0$, the freezing temperature of the solid-liquid phase change is $T_f = 1$, the latent heat of the phase change is $L_\alpha = 0.5$, the specific heat capacity is $C_p = 1.0$, and the thermal diffusion coefficient of the solid-phase is $\alpha_s = 0.25$. The position of the liquid-phase fraction $\varphi = 0.5$ was set to the solid-liquid phase change interface. The boundary conditions were set to the non-equilibrium extrapolation format at the microscopic level. For the lattice Boltzmann model, the parameters were taken as follows: the time step is $\delta_t = 1.0$, the transverse and longitudinal are equal to the lattice steps $\delta_x = \delta_y = 1.0$, lattice velocity is $c = 1.0$, and lattice sound velocity is $c = 1/\sqrt{2}$.

Figure 4 shows the solid-liquid phase change interface variation with time when $\alpha_s/\alpha_l = 1, 2, and\ 5$, respectively. It can be seen that the numerical solution of the lattice Boltzmann method in this paper matches well with the analytical solution. The error gradually increases with the decrease in the thermal diffusion coefficient of the liquid phase. The maximum relative errors are 1.16%, 1.69%, and 6.17% when $\frac{\alpha_s}{\alpha_l}$ =1, 2, and 5, respectively. This is mainly because the relaxation time gradually decreases as the thermal diffusion coefficient of the liquid phase decreases at a fixed lattice step and time step, which affects the accuracy of the numerical calculation (Gao, 2001). Based on the soil freezing problem calculated numerically herein, it can be seen that the calculation accuracy can meet the needs of engineering construction, given that the difference between the thermal diffusion coefficients of the soil before and after freezing is not significant.

Figure 5 shows a comparison between the numerical calculation results and the analytical solutions for the temperature field at a dimensionless time of $F_0 = 0.0625$ (the calculated time step is 10,000) and $\alpha_s/\alpha_l = 1, 2, and\ 5$, respectively. It can be seen that the numerical and analytical solutions of the lattice Boltzmann method are consistent. In contrast, the error increases with the decrease in the thermal diffusion coefficient of the liquid phase. The maximum relative errors are 0.42%, 0.84%, and 2.58% when $\alpha_s/\alpha_l = 1, 2, and\ 5$, respectively. The maximum error occurs at the solid-liquid phase change interface, and the farther the distance from the interface, the smaller the error.

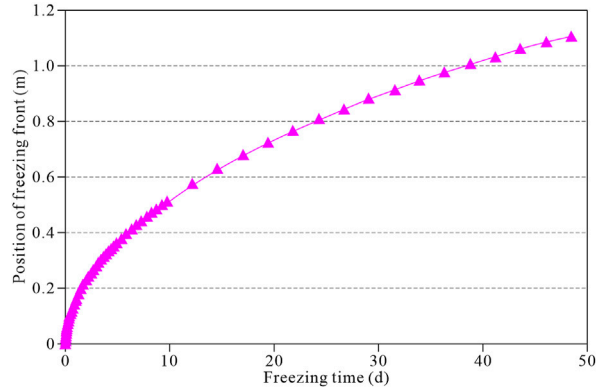

FIGURE 6
Position of freezing front plotted against freezing time.

3.2 An example of the temperature field evolution

As many researchers have done, all the methods should be verified by examples (Wang et al., 2019; Lei et al., 2022; Wang et al., 2023; Zhao et al., 2023). We have chosen an engineering example in Shanghai to validate the lattice Boltzmann model based on the enthalpy method. The foundation soil of an artificial freezing project in Shanghai is straw-yellow sandy silt. The thermophysical

parameters were measured according to the physical property tests of samples in the normal state and the frozen state as follows: the thermal diffusion coefficient of the formation is $\alpha_s = 5.97 \times 10^{-7} m^2/s$ in the solid-phase zone and $\alpha_l = 4.86 \times 10^{-7} m^2/s$ in the liquid-phase zone; the latent heat of phase change is $L_\alpha = 121.09\, kJ/kg$; the specific heat capacity is $C_p = 1.449\, kJ/(kg \cdot ℃)$. The soil's initial measured temperature is $T_i = 10℃$, the freezing temperature is $T_f = 0℃$, and the cold source temperature is $T_0 = -30℃$. For the convenience of calculation, the length of the calculation area was assumed as $L = 2\, m$. Besides, the same settings for the basic parameters and boundary conditions of the lattice Boltzmann model were made as in the validation example. At the same time, the length of the calculation range was taken as $L = 2000$. Moreover, a unit transformation was carried out to correspond to the soil's freezing parameters and obtain the calculation parameters of the corresponding lattice Boltzmann model, as shown in Table 1.

3.2.1 Evolution of temperature field in the soil under unilateral cold source

Under a unilateral cold source, the temperature of the soil body decreases rapidly, leading to the freezing front's formation by condensing internal water into ice. Figure 6 shows the evolution of the freezing front in the soil body with time. The figure shows that at the early stage of freezing, the freezing front in the soil body moves faster, and the evolution rate slows down with time. Besides, the frozen front moved 0.37, 0.52, 0.74, 0.89, and 1.02 m at 5, 10, 20, 30, and 40 days, respectively.

Figure 7 shows the development of the soil's temperature field under the unilateral cold source. The soil temperature decreases rapidly at the early stage of freezing because the cold source temperature is −30℃, much lower than the initial temperature of 10℃. Thereafter, over time, the temperature field decreases because the temperature difference in the soil gradually becomes smaller. Considering the freezing front as the boundary, the two sides present

TABLE 1 Parameter values used in the simulation.

Variables	Value of physical unit	Value of lattice unit
L_a	121.09 kJ/kg	1.0
α_s	5.97×10^{-7} m^2/s	0.25
α_l	4.86×10^{-7} m^2/s	0.2035
C_p	1.449 kJ/(kg.°C)	0.4787
T_i	10°C	1.0
T_f	0°C	0.75
T_0	−30°C	0.0

Notes: L_a is the latent heat of phase change; α_s is the thermal diffusion coefficient in the solid-phase zone; α_l is the thermal diffusion coefficient in the liquid-phase zone; C_p is the specific heat capacity; T_i is the initial temperature; T_f is the freezing temperature; T_0 is the cold source temperature.

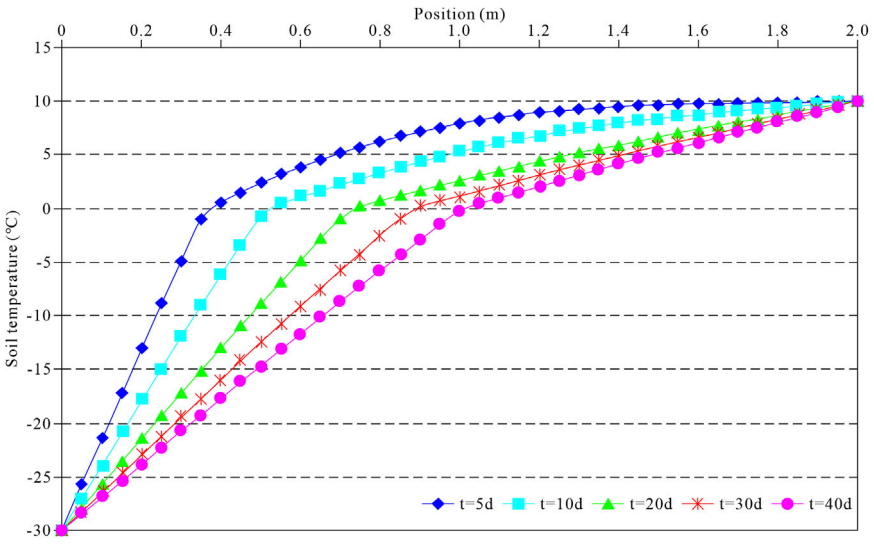

FIGURE 7
Distribution of soil temperature field when time *t* is different.

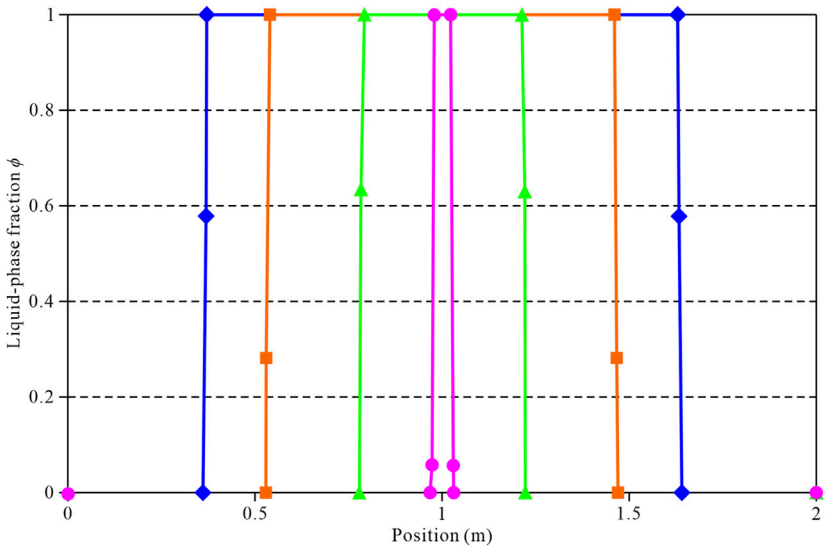

FIGURE 8
Distribution of the liquid-phase fraction φ when time t is different under the bilateral cold source. The blue rhombus represents t = 5d, the orange square represents t = 10d, the green triangle represents t = 20d, and the pink circle represents t = 30d .

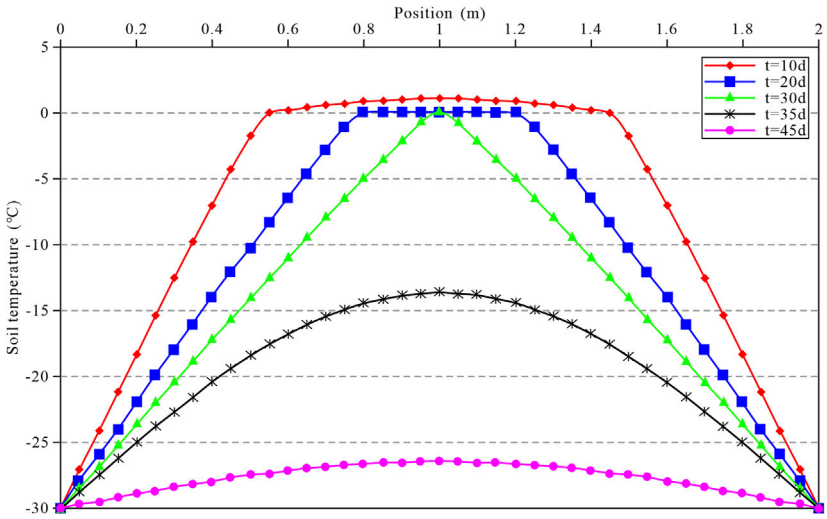

FIGURE 9
Variation in the soil temperature field when time t is different under the bilateral cold source.

a significant difference in the trend of the temperature field due to the influence of heat release from the solid-liquid phase change and different thermal diffusion coefficients. The soil temperature in the solid-phase zone develops faster and is approximately linear; in the liquid-phase zone, the soil develops slowly and gradually converges to the initial temperature of the soil. According to the code (DG/T J08-902, 2016), when the soil excavation depth is 12–30 m, the design reference value of the average temperature in the freezing wall must be taken as −8 ~ − 10°C. Therefore, when −10°C is taken as the limit for freezing wall temperature, the thickness of the freezing wall developed at 5, 10, 20, 30, and 40 days under the unilateral cold source is 0.24, 0.33, 0.47, 0.57, and 0.66 m, respectively.

3.2.2 Evolution of temperature field in the soil under the action of bilateral cold sources

In artificial freezing works, multiple tubes are usually used to form the soil's freezing curtain. Therefore, the interaction between two or more cold sources must be studied. For this purpose, the temperature of the cold source was applied on both sides of the soil within 2.0 m width to study the variation of the temperature field in

the soil. Figure 8 shows the trend in the variation of the liquid-phase fraction in the soil for 5, 10, 20, and 30 days. It can be seen that the position of the freezing front moves 0.37, 0.54, 0.78, and 0.98 m under the action of the bilateral cold sources for the time periods of 5, 10, 20, and 30 days. Compared to the unilateral cold source, the freezing front's movement has moved faster with time.

Figure 9 shows that due to the bilateral cold sources, the temperature in the soil gradually decreases from both sides to the middle. The overall temperature in the soil drops below 0℃ in about 30 days, and all the water condenses into ice. The temperature in the soil decreases rapidly after that, and at 35 days and 45 days, the overall temperature in the soil drops below −13.6℃ and −26.4℃, which are less than the average temperature of the frozen wall design's reference value. Hence, the excavation work of underground works can be carried out.

4 Conclusion and discussion

This study considers the effects of heat conduction, heat release from solid-liquid phase change, phase change interface movement, and heat diffusion coefficient changes during soil freezing to establish a unified evolution equation in the entire calculation region (solid-phase zone, liquid-phase zone, and phase change interface) using the enthalpy method. It numerically solves the D2Q4 model based on the lattice Boltzmann method for the heat conduction equation accompanied by the phase change. Combined with an engineering example of an artificial freezing method in Shanghai, the temperature field in the soil, the development trend of the freezing front with time, and the formation time of the freezing wall under the influence of unilateral and bilateral cold sources (considering the interaction between the cold sources) are determined, and the following conclusions are drawn:

(1) The numerical calculation results are analysed based on the lattice Boltzmann method and compared to the Neumann solution of the solid-liquid phase change heat conduction problem in semi-infinite space, which verifies the accuracy of the present numerical calculation method.
(2) According to the code (DG/T J08-902, 2016), when −10℃ is taken as the limit for freezing wall temperature, the thickness of the freezing wall developed at 5, 10, 20, 30, and 40 days under the unilateral cold source is 0.24, 0.33, 0.47, 0.57, and 0.66 m, respectively. These values can provide a basis for engineering design.
(3) Compared to the unilateral cold source, the freezing front's movement moves faster under the bilateral cold sources. The position of the freezing front moves 0.37, 0.54, 0.78, and 0.98 m for the time periods of 5, 10, 20, and 30 days. The overall temperature in the soil drops below −13.6℃ and −26.4℃ at 35 days and 45 days, which are less than the average temperature of the frozen wall design's reference value. Hence, the excavation work of underground works can be carried out.
(4) The lattice Boltzmann model based on the enthalpy method established in this paper can be used to deal with the heat conduction problem accompanied by phase change in underground engineering. However, the effect of moisture migration during the freezing process of soil and the resulting freezing deformation are not considered. The next step is to study the coupled heat transfer mechanism between the moisture field and soil particles using the double distribution function. Besides, a numerical model for simulating the freezing process of soil at the pore scale needs to be established by considering the freezing phase change of the moisture field and the influence of moisture migration heat conduction.

Data availability statement

The original contributions presented in the study are included in the article/Supplementary Material, further inquiries can be directed to the corresponding author.

Author contributions

LT, and LS contributed to conception and methodology of the study. JL organized the database. ZW performed the statistical analysis. LT and LS wrote the first draft of the manuscript. LT, LS, ZW, and JL wrote sections of the manuscript. All authors contributed to the article and approved the submitted version.

Funding

This work was supported by the National Natural Science Foundation of China (Grant Numbers 11962008, 42167022, and 42067043).

Acknowledgments

The authors thank Chao Yang and Qiming Zhou for their invaluable assistance in plotting figures.

Conflict of interest

Author JL was employed by Power China Kunming Engineering Corporation Limited, Kunming, China.

The remaining authors declare that the research was conducted in the absence of any commercial or financial relationships that could be construed as a potential conflict of interest.

Publisher's note

References

Alva, L. H., González, J. E., and Dukhan, N. (2006). Initial analysis of PCM integrated solar collectors. *J. Sol. Energy Eng.* 128, 173–177. doi:10.1115/1.2188532

Costa, M., Buddhi, D., and Oliva, A. (1998). Numerical simulation of a latent heat thermal energy storage system with enhanced heat conduction. *Energy Convers. manage.* 39, 319–330. doi:10.1016/S0196-8904(96)00193-8

DG/T J08 902 (2016). *Technical code for crosspassage freezing method*. Shanghai, China: Shanghai Municipal Commission of Housing and Urban-Rural Development.

Eshraghi, M., and Felicelli, S. D. (2012). An implicit lattice Boltzmann model for heat conduction with phase change. *Int. J. Heat. Mass Transf.* 55, 2420–2428. doi:10.1016/j.ijheatmasstransfer.2012.01.018

Gao, D. Y., Chen, Z. Q., and Chen, L. H. (2014). A thermal lattice Boltzmann model for natural convection in porous media under local thermal non-equilibrium conditions. *Int. J. Heat. Mass Transf.* 70, 979–989. doi:10.1016/j.ijheatmasstransfer.2013.11.050

Gao, D. Y. (2001). *Study on solid-liquid phase change heat transfer in metal foams based on lattice Boltzmann method. Doctor Thesis*. Nanjing: Southeast University.

Guo, Z. L., Zheng, C. G., and Shi, B. C. (2002). Non-equilibrium extrapolation method for velocity and pressure boundary conditions in the lattice Boltzmann method. *Chin. Phys.* 11, 366–374. doi:10.1088/1009-1963/11/4/310

Huang, S. L., Aughenbaugh, N. B., and Wu, M. C. (1986). Stability study of CRREL permafrost tunnel. *J. Geotech. Eng.* 112, 777–790. doi:10.1061/(ASCE)0733-9410(1986)112:8(777)

Jiaung, W. H., Ho, J. R., and Kuo, C. P. (2001). Lattice Boltzmann method for the heat conduction problem with phase change. *Numer. Heat. Transf. Part B* 39, 167–187. doi:10.1080/10407790150503495

Jing, L., Tsang, C. F., and Stephansson, O. (1995). DECOVALEX—An international co-operative research project on mathematical models of coupled THM processes for safety analysis of radioactive waste repositories. *Int. J. Rock Mech. Min. Sci. Geomech. Abstr.* 32, 389–398. doi:10.1016/0148-9062(95)00031-B

Lei, Z. D., Wu, B. S., Wu, S. S., Nie, Y. X., Cheng, S. Y., and Zhang, C. (2022). A material point-finite element (MPM-FEM) model for simulating three-dimensional soil-structure interactions with the hybrid contact method. *Comput. Geotechnics* 152, 105009. doi:10.1016/j.compgeo.2022.105009

Levin, L., Golovatyi, I., Zaitsev, A., Pugin, A., and Seminet, M. (2021). Thermal monitoring of frozen wall thawing after artificial ground freezing: Case study of Petrikov Potash Mine. *Tunn. Undergr. Space Technol.* 107, 103685. doi:10.1016/j.tust.2020.103685

Miller, W., and Succi, S. (2002). A lattice Boltzmann model for anisotropic crystal growth from melt. *J. Stat. Phys.* 107, 173–186. doi:10.1023/A:1014510704701

Mohamad, A. A. (2011). *Lattice Boltzmann method: Fundamentals and engineering applications with computer codes*. London: Springer-Verlag. doi:10.1007/978-0-85729-455-5

Ozisik, M. (1993). *Heat conduction*. New York: John Wiley and Sons.

Qian, Y. H., D'Humières, D. D., and Lallemand, P. (1992). Lattice BGK models for Navier-Stokes equation. *Europhys. Lett.* 17, 479–484. doi:10.1209/0295-5075/17/6/001

Rabin, Y., and Korin, E. (1993). An efficient numerical solution for the multidimensional solidification (or melting) problem using a microcomputer. *Int. J. Heat. Mass Transf.* 36, 673–683. doi:10.1016/0017-9310(93)80043-T

Radoslwa, L., Michaloeski, E., and Zhu, M. (2006). "Freezing and ice growth in frost-susceptible soils," in *Geotechnical symposium in roma, soil stress-strain behavior: Measurement, modeling and analysis* (Roma, Italy: Spinger). doi:10.1007/978-1-4020-6146-2_25

Shamsundar, N., and Sparrow, E. M. (1975). Analysis of multidimensional conduction phase change via the enthalpy model. *J. Heat. Transf.* 97, 333–340. doi:10.1115/1.3450375

Sukop, M. C., and Thorne, D. T. (2006). *Lattice Boltzmann Modeling: An introduction for geoscientists and engineers*. Berlin: Springer-Verlag. doi:10.1007/978-3-540-27982-2

Van Dorst, A. A. E. (2013). Artificial ground freezing as a construction method for underground spaces in densely built up areas. Master thesis. Delft: Delft University of Technology.

Voller, V. R., Swaminathan, C. R., and Thomas, B. G. (1990). Fixed grid techniques for phase change problems: A review. *Int. J. Numer. Meth. Engng.* 30, 875–898. doi:10.1002/nme.1620300419

Wang, G. J., Tian, S., Hu, B., Xu, Z. F., Chen, J., and Kong, X. Y. (2019). Evolution pattern of tailings flow from dam failure and the buffering effect of debris blocking dams. *Water* 11, 2388. doi:10.3390/w11112388

Wang, G. J., Zhao, B., Wu, B. S., Zhang, C., and Liu, W. L. (2023). Intelligent prediction of slope stability based on visual exploratory data analysis of 77 *in situ* cases. *Int. J. Min. Sci. Technol.* 33, 47–59. doi:10.1016/j.ijmst.2022.07.002

Yong, Y. M., Yang, C., and Mao, Z. S. (2009). Numerical simulation of thermal convection in triangular enclosure using lattice Boltzmann method. *Chin. J. Process Eng.* 9, 841–847. doi:10.3321/j.issn:1009-606X.2009.05.002

Zhao, B., Wang, G. J., Wu, B. S., and Kong, X. Y. (2023). A study on mechanical properties and permeability of steam-cured mortar with iron-copper tailings. *Constr. Build. Mat.* 383, 131372. doi:10.1016/j.conbuildmat.2023.131372

frontiers | Frontiers in Earth Science

TYPE Original Research
PUBLISHED 24 August 2023
DOI 10.3389/feart.2023.1192269

OPEN ACCESS

EDITED BY
Wenzhuo Cao,
Imperial College London,
United Kingdom

REVIEWED BY
Yi Xue,
Xi'an University of Technology, China
Xiaoping Zhou,
Chongqing University, China
Jie Liu,
Hunan Institute of Engineering, China

*CORRESPONDENCE
Jun Du,
dujun0605@126.com

RECEIVED 23 March 2023
ACCEPTED 09 August 2023
PUBLISHED 24 August 2023

CITATION
Du J, Shen X, Li C, Zhu W and Feng G (2023), Effect of dry-wet cycles on the strength and deformation of the red-bed rockfill material in western Yunnan. *Front. Earth Sci.* 11:1192269. doi: 10.3389/feart.2023.1192269

Effect of dry-wet cycles on the strength and deformation of the red-bed rockfill material in western Yunnan

Jun Du*, Xinggang Shen, Chenchen Li, Weiwei Zhu and Guojian Feng

College of Architecture and Civil Engineering, Kunming University, Kunming, China

Introduction: The shear strength deterioration of red-bed rockfill under the dry-wet cycle is the key factor affecting the slope stability of accumulation body. Studying the strength deterioration law and deterioration mechanism of red-bed rockfill can provide theoretical support for slope stability control.

Methods: Through the disintegration resistance test of argillaceous siltstone rockfill in Lanping lead-zinc Mine, the disintegration characteristics of red-bed soft rock were studied. The effects of the number of dry-wet cycles on the cohesion, internal friction angle, shear dilation rate and shear modulus of the red-bed rockfill were investigated by using a dry-wet cycle shear tester to conduct shear tests on the reduced scale graded soil material, and the strength deterioration mechanism of the soils was revealed from the perspective of meso-structure.

Results: The results showed that argillaceous siltstone was rich in clay minerals and produces strong disintegration when exposed to water. The disintegration process could be divided into three stages: massive disintegration stage, transitional stage and stabilization stage. With the accumulation of dry-wet cycles, the shear dilation rate and shear modulus of the argillaceous siltstone rockfill gradually decrease, and the shear failure developed gradually from strain hardening to shear plastic flow, and the characteristic of weak stress softening occurred. After eight dry-wet cycles, the cohesion and internal friction angle of argillaceous siltstone rockfill materials decreased by 89.87% and 18.94%, respectively, indicating a higher effect on the cohesion than on the internal friction angle.

Discussion: The thickening of the bound water between the fine particles on the shear surface, the weakening of the coarse particle attachment, and the increase in the number of directionally arranged fine particles were the main reasons for the continuous deterioration of the soil strength.

KEYWORDS

argillaceous siltstone, rockfill material, dry-wet cycle, disintegration, deterioration of strength

1 Introduction

The red Jurassic and Cretaceous strata are widely distributed in Yunnan, China. Bounded by the Erhai-Honghe Fault, the eastern and western parts are called the Central Yunnan Red Bed and the Western Yunnan Red Bed, respectively, due to their different phase zones. The Western Yunnan Red Bed is mainly composed of inland lacustrine formations. Its lithology is clastic sedimentary rocks such as mudstone, siltstone, argillaceous siltstone, and sandstone (Luo et al., 2003). These rocks are rich in clay minerals, poorly permeable, hydrophilic, easily swollen, and disintegrated by water, with a large softening property (Zhang et al., 2017; Zhang et al., 2019; Zeng et al., 2021). In recent years, the continuous exploitation of mineral resources in western Yunnan has led to the gradual excavation and stripping of red-bed rocks. As a result, large amounts of waste rock materials are frequently deposited around, forming large loose accumulation slopes. Under frequent rainfall infiltration and evaporation, the mechanical properties of the rockfill material inevitably deteriorate (Oliveira et al., 2021; Wen and Yuan, 2022; Xue et al., 2023), reducing the stability of the slope (Pan et al., 2020; Nguyen et al., 2023) and aggravating its long-term deformation (Zhou et al., 2014; Cook et al., 2023; Wei et al., 2023). In order to analyze the stability of loose accumulation slope, it is of great importance to study the performance deterioration of red-bed rockfill materials in western Yunnan under alternating wet and dry environments.

Loose accumulations formed by geological tectonic movements or human engineering activities are widely distributed in nature. These geological bodies have a typical soil-rock binary mixed structure, and no single part can represent the characteristics of the entire body (Wang et al., 2012; Zhou et al., 2018). The particle gradation composition, the contact type of the blocks, and the mineral composition of the parent rock significantly affect the strength and deformation of the soil (Cavarretta et al., 2010; Yuan et al., 2018; Pham et al., 2022; Xue et al., 2023). Firstly, the particle composition of the rockfill material is complex. The percentage of coarse and fine particles and the size of the blocks are constantly changing in space. The contact interaction between soil particles is exceptionally significant in the variation of soil grading, and the different contact relationships between particles control the ability of the soil to resist deformation and damage (Wu et al., 2020; Tran et al., 2021). With the increased size of block stones and increased block stone content in the soil, the squeezing and interlocking between the particles are continuously enhanced, and the shear damage resistance of the soil is significantly increased. However, the increase in block content can also cause massive soil pores to penetrate each other, weakening the resistance of the soil against infiltration deformation damage. Secondly, the mechanical properties of rockfill materials are mainly shear yielding. These materials are highly susceptible to particle breakage under stress concentration (Li et al., 2019; Zhou et al., 2019; Wu et al., 2021), with obvious shear dilation characteristics during shear deformation (Chen et al., 2018; Ahmed et al., 2023). The fragmentation of the block particles changes the original particle contact relationship in the soil, reducing the interlocking force and friction strength between the particles. As the stress increases, relative sliding continuously occurs among the yield-ruptured soil particles, resulting in irrecoverable plastic deformation of the soil body and damage. Therefore, a series of granular material mechanical behaviors in the shear deformation of rockfill materials make their shear strength properties exceptionally complex, which requires continuous in-depth research.

In addition, the mechanical properties of the soil are closely related to environmental conditions. The deterioration of rockfill materials under dry-wet cycles reduces their shear strength and deformation modulus, which is the main cause of excessive deformation and instability of high-fill slopes (Silvani et al., 2008; Peng and Zhang, 2012; Zhou et al., 2019; Wu et al., 2021). In order to analyze the strength deterioration characteristics of soil, several scholars have conducted experimental studies on the strength and deformation of soil under dry-wet cycles (Rasul et al., 2018; Zhou et al., 2019; Xu et al., 2021; Li et al., 2022; Abbas et al., 2023). The triaxial wetting deformation test of rockfill materials showed that particle water immersion disintegration and fragmentation are the main reasons for increased soil deformation (Wei and Zhu, 2006; Jia et al., 2019; Zhang and Zhou, 2020). The degree of particle fragmentation increased with the accumulation of dry-wet cycles (Zhang et al., 2015). The deterioration of rockfill material strength properties is mainly because the rock is rich in hydrophilic clay minerals (Jia et al., 2018). The block particles constantly crack in multiple wet and dry deformations, reducing the strength of the parent rock and weakening the shear strength of the soil. However, the stress levels in the existing experimental studies of rockfill materials undergoing wet-dry cycles are usually inconsistent with reality. Limited by the test conditions, the dry-wet cycle deterioration test is usually performed by soaking and air-drying the stone particles several times before loading them into the test machine. In reality, the fill slope only experiences rainfall infiltration and evaporation changes after completing soil accumulation, and the soil dry-wet cycle is completed under a specific consolidation stress state. Therefore, it is necessary to improve the existing geotechnical test equipment to realize the dry-wet cycle after sample preparation, thus revealing the deterioration characteristics of rockfill materials under consolidation stress conditions.

The strength deterioration of red-bed rockfill materials under alternating dry-wet environments is the key factor affecting the stability of loose accumulation slope. In order to study the strength deterioration characteristics and mechanisms of red-bed rockfill materials under dry-wet cycles, argillaceous siltstone rockfill materials from Lanping lead-zinc mine was selected as the research object. The disintegration characteristics, strength degradation, and deformation damage of rockfill materials were studied by water immersion disintegration test and dry-wet cycle shear test, and the mechanism of strength degradation of rockfill materials was revealed from the perspective of meso-structure. The research results could reveal the deterioration characteristics of red-bed rockfill from macro-meso structure, provide reasonable soil mechanical analysis parameters for mine dump heightening and expansion and slope design, and provide certain scientific guidance for the safety risk management of dump slope.

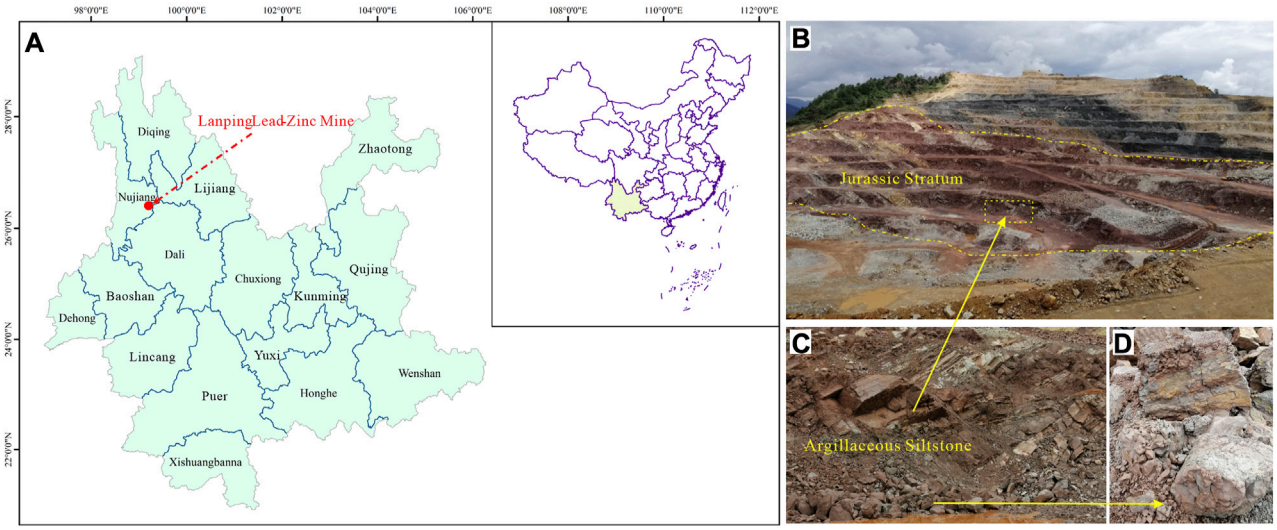

FIGURE 1
The location of Lanping lead-zinc mine. **(A)** Geographical location. **(B)** Mine overview. **(C)** Argillaceous siltstone. **(D)** Rock under wetting-drying cycles.

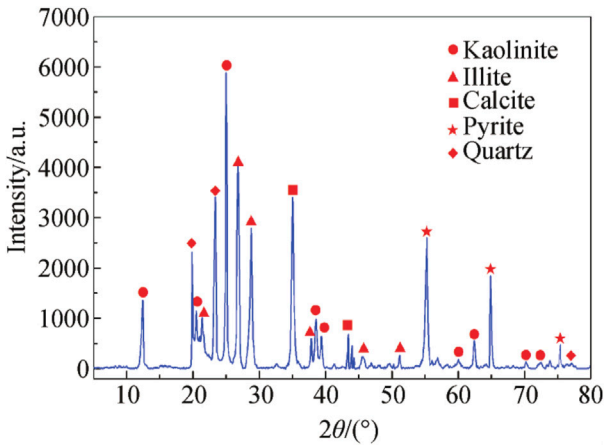

FIGURE 2
Mineralogical compositions of the argillaceous siltstone.

2 Performance deterioration test for rockfill materials during dry-wet cycles

2.1 Basic characteristics of the test material

The test material is argillaceous siltstone rockfill material, which was taken from the dumping site of Lanping lead-zinc mine in Yunnan Province (N26°24′, E99°25′). The waste rock of the dumping site mainly consists of purplish-red argillaceous siltstone of the Middle Jurassic Huakaizuo strata (J_2h) excavated from the open mine, as shown in Figure 1. The mining area is located on the southwest border of China, falling into the low-latitude mountain monsoon climate zone, with the vertical distribution of three-dimensional climate characteristics. The annual average temperature is 7°C, the annual rainfall is 1,002.4 mm, the annual average sunshine hour is 2008.7 h, and the annual average evaporation is 1,063 mm. Therefore, the rockfill materials in the dumping field are significantly affected by the alternating dry and wet climate. The frequent dry-wet cycles exacerbate the performance deterioration of the rockfill material, which can easily induce landslide geological hazards.

Figure 2 shows the mineral composition of the argillaceous siltstone obtained through X-ray diffraction analysis. The mineral composition of the argillaceous siltstone and its content are: quartz 22%, kaolinite 42%, illite 20%, calcite 11%, and pyrite 6%. The mineral composition of more than 60% indicates a high content of clay minerals.

Figure 3 shows the microstructure of the argillaceous siltstone by a scanning electron microscope (SEM). The SEM image of the rock at 500 times magnification (Figure 3A) reveals that the microstructure unit is dominated by agglomerated aggregates with large particle sizes. The contact between the particles is mainly surface-to-surface, which belongs to the laminating structure. Fine viscous particles are scattered on the surface of the agglomerates and gathered into clusters, and the geometric size, shape, and orientation of the particles differ significantly. Figures 3B, C show the SEM images of the rock at 2000 and 4,000 times magnification, respectively, clearly displaying the clay particles and quartz particles inside.

The rockfill material was sieved on site, and the dividing particle size of coarse and fine particles was 5 mm (Wang et al., 2009), i.e., particles below 5 mm were fine particles, and those beyond 5 mm were coarse particles. The coarse grain contents were expressed as P_5. Then, the equivalent alternative scaling was performed for field grading of test soil materials according to Eq. 1. The composition of the test soil grade is shown in Figure 4.

$$P_{5i} = P_{05i} \cdot \frac{P_5}{P_5 - P_0} \quad (1)$$

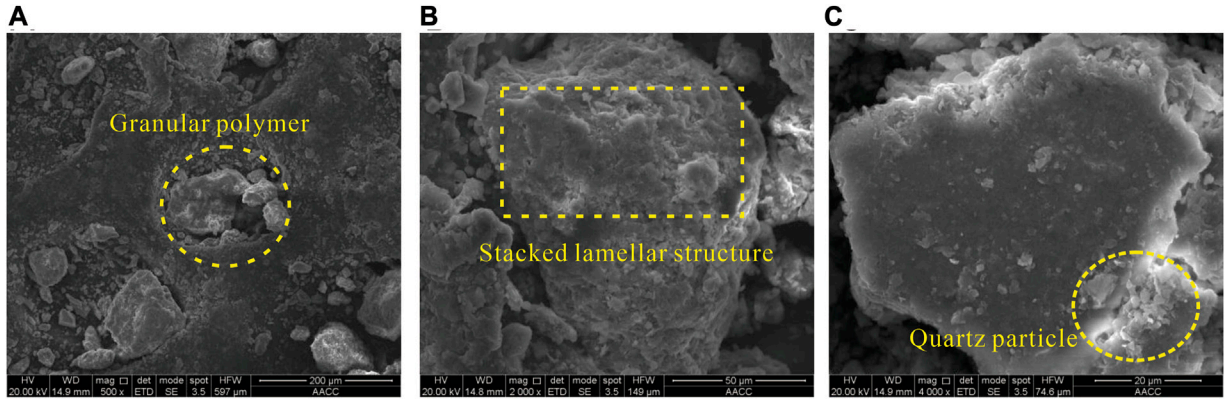

FIGURE 3
Microscopic image of the argillaceous siltstone. **(A)** 500 times. **(B)** 2000 times. **(C)** 4,000 times.

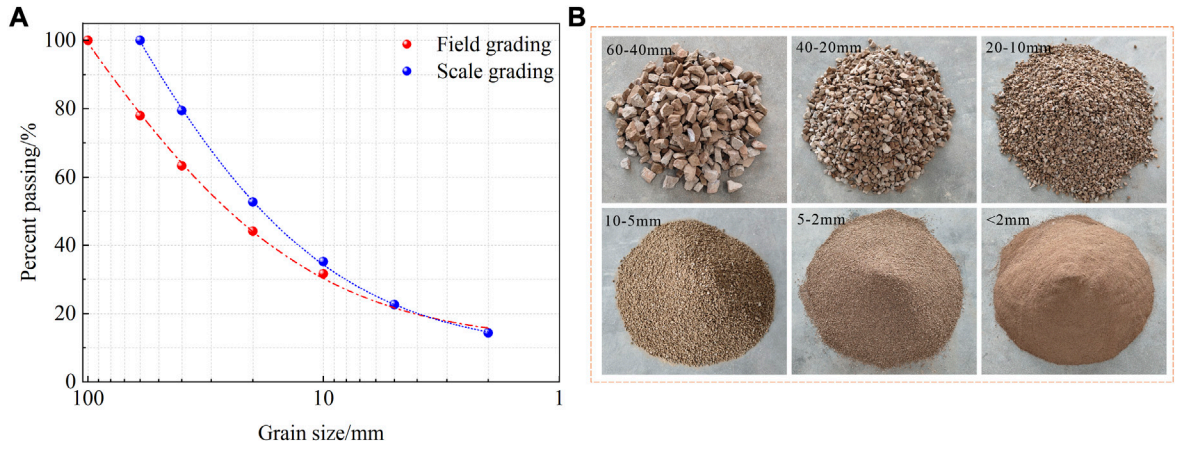

FIGURE 4
Particle grading components. **(A)** Grain size distribution. **(B)** Different grain groups of soil materials.

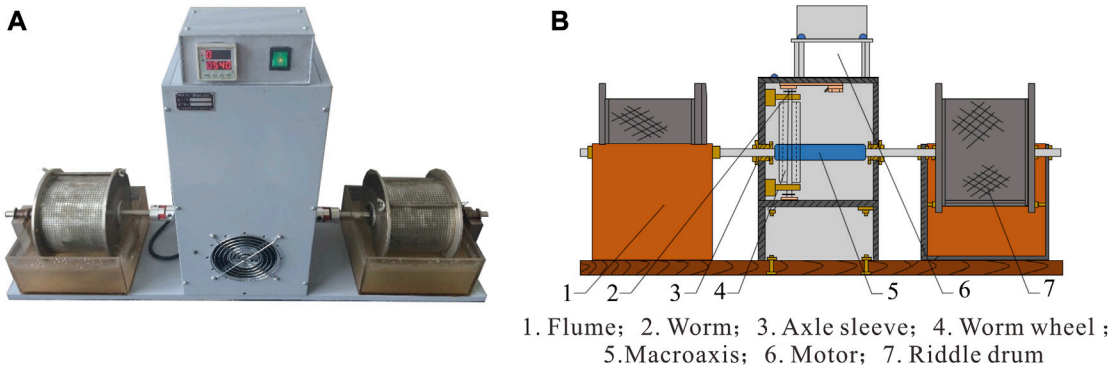

FIGURE 5
Disintegration resistance test instrument. **(A)** Instrument. **(B)** Instrument construction.

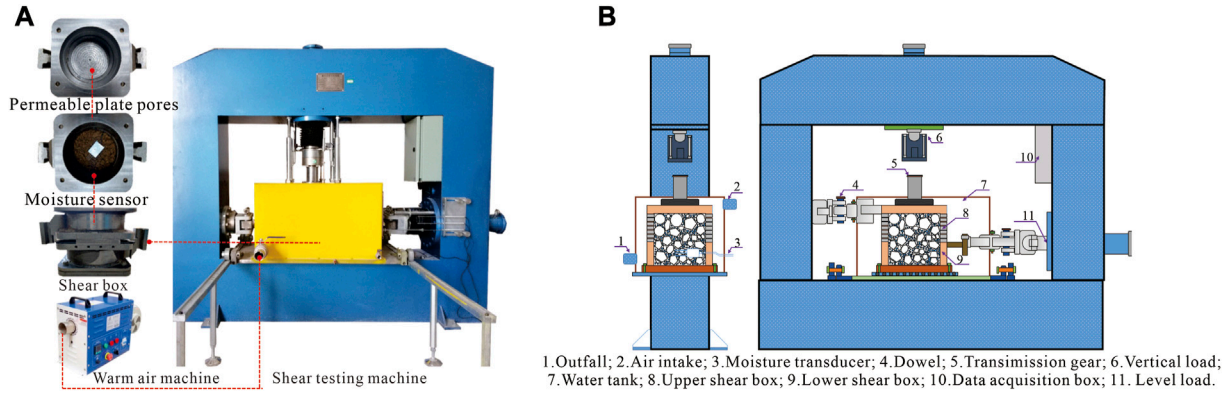

FIGURE 6
Shear testing machine of coarse-grained soil. **(A)** Test machine. **(B)** Machine construction.

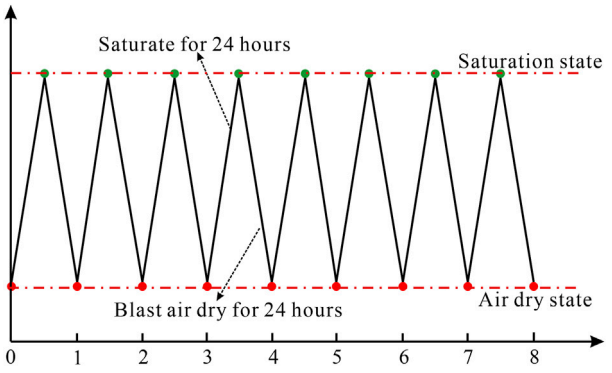

FIGURE 7
Dry-wet cycles method.

Where P_5 is coarse grain contents (%), P_{5i} is the content of a particle group with a particle size greater than 5 mm after scaling (%), P_{05i} is the content of a particle group with a particle size greater than 5 mm before scaling (%), and P_0 is percentage of particle mass with a particle size greater than 60 mm.

2.2 Disintegration resistance test

Figure 5 shows the disintegration resistance test apparatus for clay rocks. The coarse particles greater than 5 mm were weighed according to the composition of the test soil grade and loaded into the drum sieve of the disintegration resistance tester at dry room temperature. Referring to the *Standard for Rock Physical and Mechanical Properties Testing Method* (DZ/T 0276.9–2015), the drum sieve was placed into the water tank, followed by the injection of pure water to keep the water level about 20 mm below the rotation axis. Afterward, the drum sieve was rotated at r/min for 10 min before removing the test soil and drying at a constant temperature of 105–110°C for 24 h. The dried soil materials were passed through 40, 20, 10, and 5 mm sieves, weighed, and recorded to obtain the particle size distribution. The above test procedure was considered as one disintegration. The coarse particles greater than 5 mm were loaded into the sieve again, and the above test process was repeated eight times.

TABLE 1 Dry-wet cycle shear test scheme of rockfill material.

No	Dry-wet cycle *n*	Normal load σ/kPa			
T1	0	200	400	600	800
T2	1	200	400	600	800
T3	2	200	400	600	800
T4	4	200	400	600	800
T5	6	200	400	600	800
T6	8	200	400	600	800

2.3 Dry-wet cycle direct shear test

Figure 6 shows the DJH30 dry-wet cycle shear tester for coarse-grained soils. The tester is equipped with a computerized automatic data acquisition and processing system, allowing the collection and storage of load and displacement and the automatic control of the vertical load, horizontal load, and shear rate. The shear box of the tester is Φ300 × 240 mm, which can be used to determine the shear strength of coarse-grained soil with a grain diameter of less than 60 mm. Since the tester has a saturated water tank and a blower, the dry-wet cycle can be achieved inside the tester. When the specimen is prepared again after the wet-dry cycle outside the testing machine, the manual interference with the test soil can be overcome. The dry-wet cycle shear test path is designed by incorporating the functional characteristics of the test machine, as shown in Figure 7. The protocol of the dry-wet cycle shear test is shown in Table 1.

Referring to the *S. for Geotechnical Testing Method* (GB/T50123-2019), the test soil material was air-dried and sieved, and the specimens were prepared according to the moisture content of 4.32% and density of 2.05 g/cm^3 to complete the dry-wet cycle shear test. The main test steps are as follows.

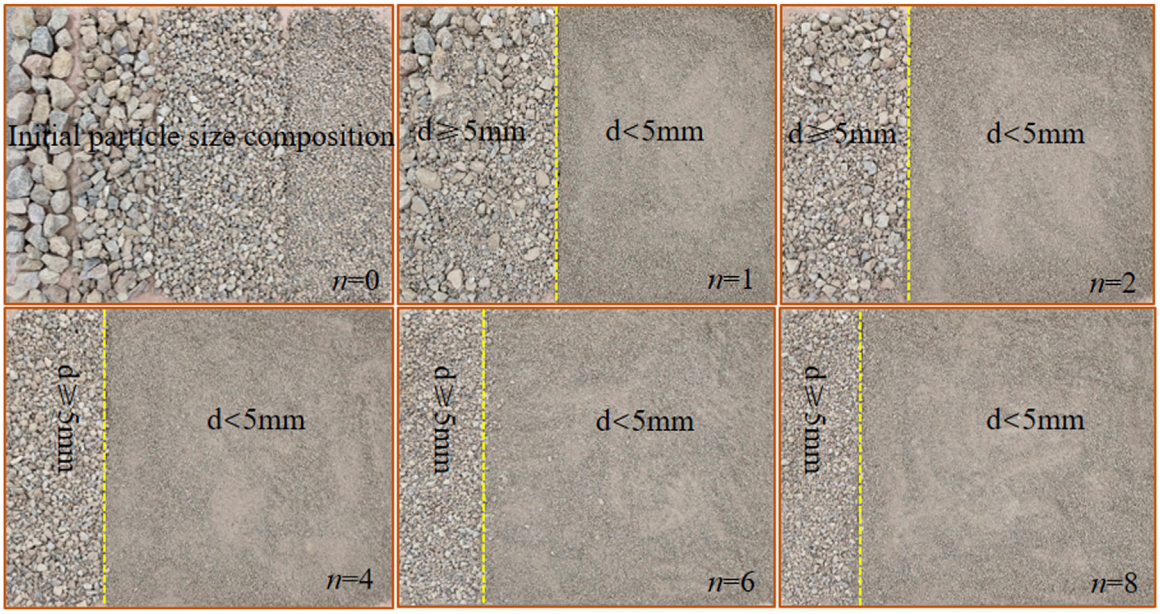

FIGURE 8
Rockfill disintegration resistance test phenomenon.

(1) According to the composition of the soil scale grading, three parts of air-dried soil are weighed and properly mixed after adding an appropriate amount of water. Afterward, three parts of the materials are filled into the shear box sequentially according to the density control conditions, and the layers are chiseled to reduce the effect of anisotropy.

(2) The dry-wet cycle process is realized for the prepared specimens. Firstly, the water tank is filled. Water along the permeable plate pores at the bottom of the shear box gradually penetrates upward to the interior of the specimen, allowing the specimen to be completely saturated. The time of saturation is 24 h. Then, the water tank is emptied, and the pore water inside the specimen is gradually emptied under differential pressure. In order to make the soil particles inside the sample fully dry, a blower is used to blow continuously inside the sample for 24 h, and the soil sample is regarded as dry when the water content is below 5% measured by the built-in moisture sensor in the sample. When the moisture content of the soil sample is below 5% and the blast drying is less than 24 h, it is still necessary to continue to blast for 24 h. The above operation is a dry-wet cycle. Finally, dry-wet cycles corresponding to each specimen are completed according to the test protocol.

(3) Specimens that have completed the wet-dry cycles are subjected to the direct shear test. The test loading is strain-controlled, and the shear rate is 1 mm/min. When the shear displacement reaches 15% of the specimen size, the specimen is considered to be shear damaged. In the test, the specimen shear box is round and the diameter is 300 mm. Therefore, when the shear displacement of the sample reaches 45 mm, the sample is shear damaged and the test is terminated.

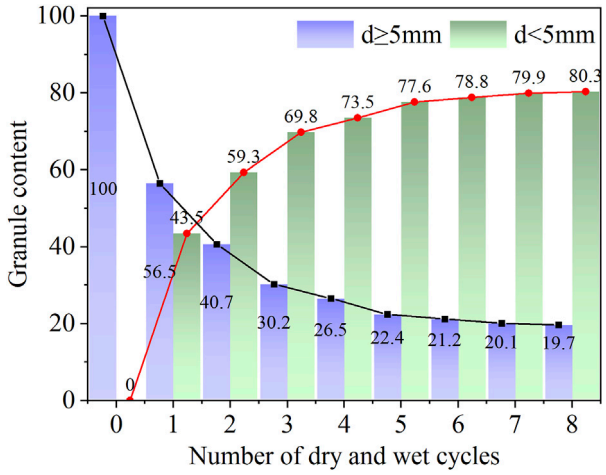

FIGURE 9
Change characteristics of disintegration under dry-wet cycles.

3 Analysis of disintegration resistance test results

3.1 Disintegration phenomenon

In the disintegration test, the test soil material disintegrates with the increasing number of wet-dry cycles *n*, as illustrated in Figure 8. As the argillaceous siltstone is rich in clay minerals, it reacts vigorously with water, and the blocks show different degrees of cracking along the primary structural surface. The large blocks gradually crack into disintegrated materials with

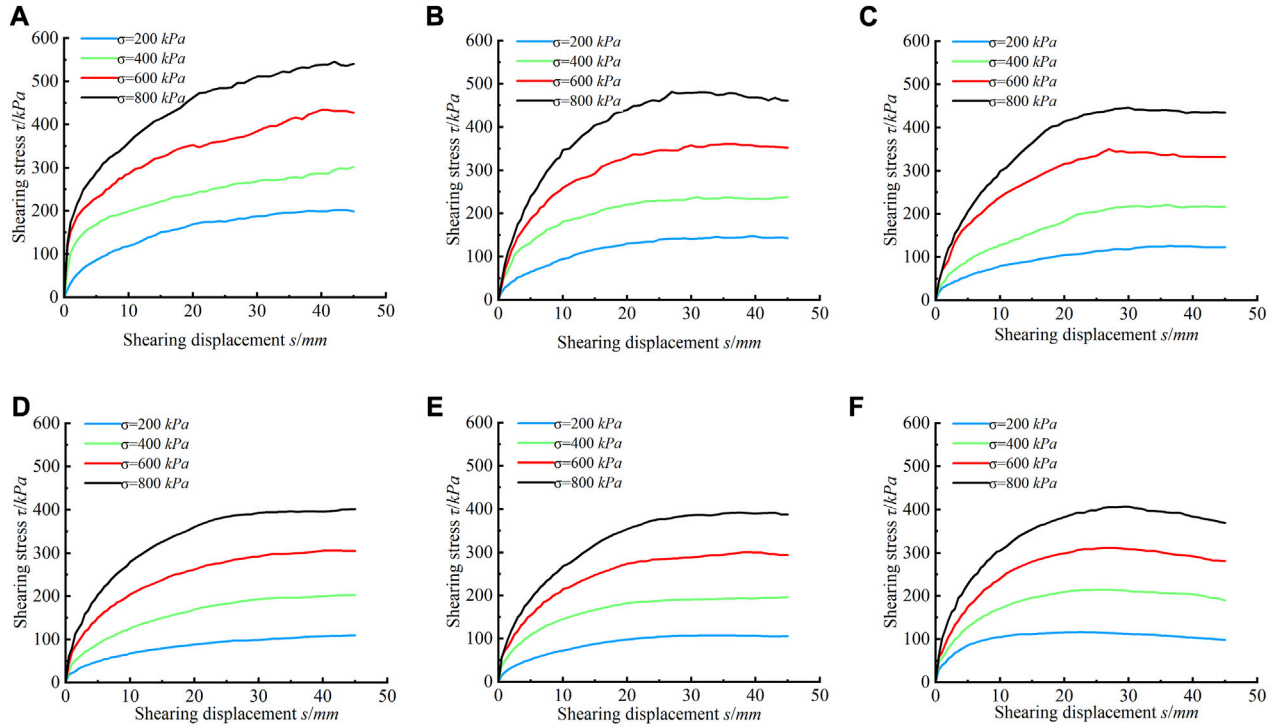

FIGURE 10
Shear stress-displacement curve. **(A)** N = 0 **(B)** n = 1 **(C)** n = 2 **(D)** n = 4 **(E)** n = 6 **(F)** n = 8.

smaller particle sizes. When comparing the soil gradation in the initial stage of the test, it can be seen that when n=1 (wet-dry cycle for 24 h), the content of particles larger than 5 mm is significantly reduced in the test soil material, and the roundness of the block increases. With the accumulation of dry-wet cycles, the blocks are further cracked, and the content of disintegrated materials is significantly increased. When a certain number of wet-dry cycles are reached, the disintegration rate of blocks with better integrity slows down, and the content of disintegrated material gradually stabilizes.

3.2 Content variation of disintegrated materials

The content variations of coarse particles ($d \geq 5$ mm) and disintegrated materials ($d < 5$ mm) with dry-wet cycles are shown in Figure 9. According to the disintegration degree of the coarse particles in Figure 9, the disintegration process can be divided into three stages.

(1) Massive disintegration stage ($n \leq 2$). In this stage, the rockfill material is massively disintegrated in water. With the increase of n, the content of coarse particles significantly decreases, and the content of disintegrated materials significantly increases.
(2) Transitional stage ($2 < n \leq 4$). In this stage, the disintegration rate of coarse particles in water slows, with less increase in disintegrated material content. The block is in the transitional stage from vigorous disintegration to disintegration completion.
(3) Stabilization stage ($n > 4$). After the disintegration of coarse particles in water reaches a certain value, it is difficult for coarse particles to crack, with almost no changes in the content of the disintegrated material. At this point, the soil disintegration is completed and is in the stabilization stage.

Taking the test soil material before dry-wet cycles as the benchmark, the coarse particle content decreases by 59.3% in the massive disintegration stage, further decreases by 18.3% in the transitional stage, and decreases by only 2.7% in the stabilization stage. The coarse particle content is 19.7% when n = 8. This result indicates that with the accumulation of wet-dry cycles, the coarse particle content of the argillaceous siltstone rockfill material decreases, and the block disintegration gradually slows down and finally stabilizes.

4 Analysis of dry-wet cycle shear test results

4.1 Soil strength properties

4.1.1 Shear stress-displacement characteristics

The shear stress-displacement curves of argillaceous siltstone rockfill materials under dry-wet cycles are shown in Figure 10. It can be seen that there are no significant peaks, and the changing patterns of the test curves corresponding to different numbers of wet-dry cycles are different. When the number of dry-wet cycles is 0, the shear stress increases with the increase of shear displacement. The

TABLE 2 Deterioration of shear strength of rockfill material under dry-wet cycles.

Dry-wet cycle *n*	σ=200 kPa		σ=400 kPa		σ=600 kPa		σ=800 kPa	
	τ/kPa	*δ*/%	*τ*/kPa	*δ*/%	*τ*/kPa	*δ*/%	*τ*/kPa	*δ*/%
0	198.37	0	302.16	0	427.54	0	540.83	0
1	142.18	28.33	237.46	21.41	352.17	17.63	461.09	14.74
2	122.98	38.01	215.97	28.52	331.92	22.37	434.99	19.57
4	110.05	44.52	203.17	32.76	305.49	28.55	402.31	25.61
6	105.28	46.93	195.95	35.15	293.92	31.25	387.87	28.28
8	97.99	50.61	189.36	37.33	281.44	34.17	369.19	31.74

variation curve is not smooth with some fluctuations, especially during soil shear yielding and damage stages. The reason is that the coarse particles that have not yet disintegrated are closely squeezed and interlocked. With the rapid increase of the shear stress, the local stress exceeds the particle contact strength, resulting in particle cracking. The strain energy stored in the soil due to particle squeezing and interlocking is rapidly released, which causes fluctuations in shear stress. Subsequently, the soil particles are arranged in a new orientation under pressure. The particles on the shear surface interlock and roll again as shear stress returns. This process is repeated until shear damage to the soil sample occurs. The soil shear stress-deformation relationship during this process exhibits a hardening characteristic. When the number of dry-wet cycles is 1 and 2, the coarse particles show strong disintegration due to immersion. The number of coarse particles squeezing and interlocking each other decreases, and the soil shear stress fluctuation and hardening characteristics gradually weaken with the development of shear deformation. When the number of dry-wet cycles is 4, the disintegration of coarse particles is basically completed. The content of fine particles sharply increases, and coarse particles are mostly suspended in fine particles. During the shear deformation of the soil, the interlocking and rolling among particles continuously disappear, and the particle contact is mostly adhesion and friction of fine particles. With the development and expansion of cracks on the shear surface, the soil shear stress slowly increases and tends to be constant until the occurrence of plastic flow damage. When the number of wet-dry cycles is 6 and 8, the shear-plastic flow characteristics of the soil become increasingly significant after yielding, accompanied by a weak stress softening. Based on the above results, the shear characteristics of argillaceous siltstone rockfill material under dry-wet cycles are closely related to the disintegration characteristics of coarse particles. With the accumulation of dry-wet cycles, the soil shear damage gradually develops from strain hardening to shear plastic flow, exhibiting specific stress softening characteristics.

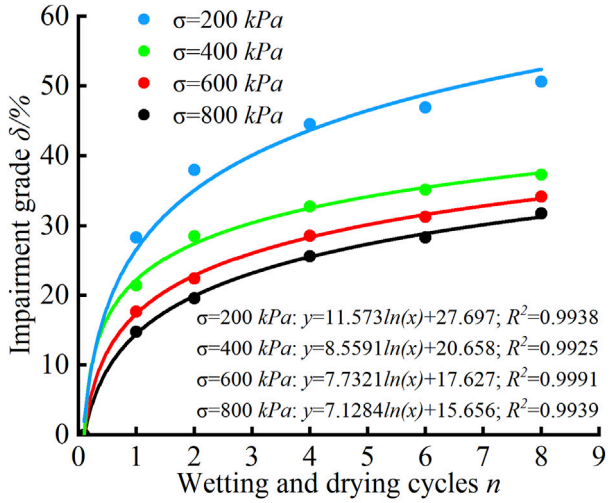

FIGURE 11
Deterioration degree of shear strength under dry-wet cycles.

4.1.2 Shear strength deterioration characteristics

Since there is no apparent peak stress for soil shear damage in the test, the strength corresponding to 45 mm of shear displacement is taken as the shear strength τ of the soil according to the *S. for Geotechnical Test Method* (GB/T50123-2019). To analyze the degradation of soil shear strength under dry-wet cycles, the degradation of soil shear strength δ is defined as follows:

$$\delta = \frac{\tau_0 - \tau_n}{\tau_0} \times 100\% \quad (2)$$

where τ_0 is the soil shear strength under 0 dry-wet cycles (kPa); τ_n is the soil shear strength under different numbers (n = 1, 2, 4, 6, 8) of dry-wet cycles (kPa).

The shear strength deterioration of the soil obtained by Eq. 2 is shown in Table 2.

It can be seen from Table 2 that the shear strength of the soil deteriorates significantly under dry-wet cycles, and the degree of strength deterioration varies under different vertical consolidation stresses. The degradation of soil shear strength under the dry-wet cycles decreases with the increase of vertical consolidation stresses, indicating the suppressive effect of vertical consolidation stresses on the degradation of soil strength in dry-wet cycles. After eight wet-dry cycles, the shear strength of the soil deteriorates by 50.61% at consolidation stress of 200 kPa, while its deterioration is 31.74% at 800 kPa.

TABLE 3 Shear strength parameters of soil under different dry-wet cycles.

Dry-wet cycle n	Shear strength parameters	
	Cohesion c (kPa)	Internal friction angle (°)
0	79	30.1
1	30	28.2
2	13.5	27.7
4	10.5	26.1
6	9	25.3
8	8	24.4

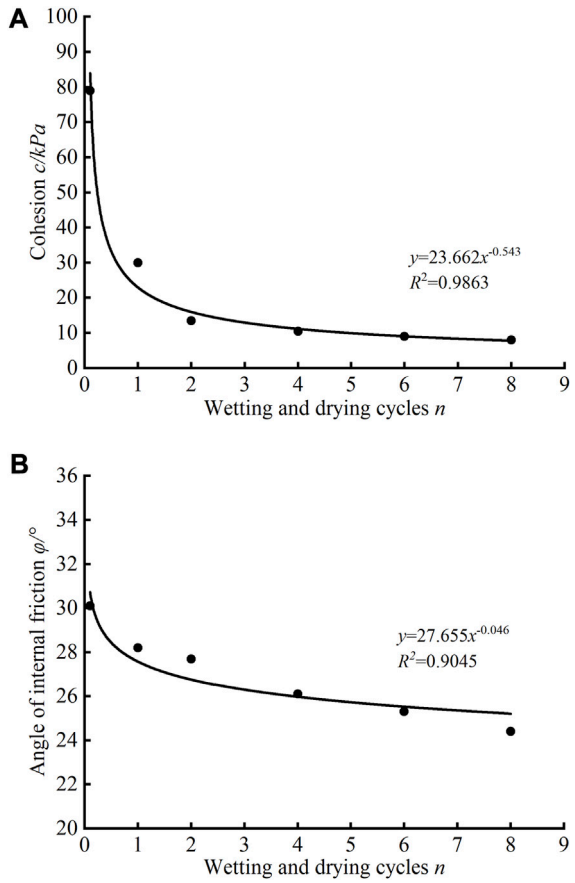

FIGURE 12
Deterioration characteristics of shear strength index under dry-wet cycles. **(A)** Cohesion. **(B)** Angle of internal friction.

Figure 11 shows the variation of soil shear strength with dry-wet cycles under different vertical consolidation stresses. To simplify the fitting function, 0.1 was used to represent 0 dry-wet cycles. It can be seen that the shear strength degradation of soil under the same vertical consolidation stress conforms to the logarithmic function, with significant non-uniformity under dry-wet cycles, which is closely related to the soil disintegration characteristics. During the massive disintegration stage ($n \leq 2$), the degradation of soil shear strength under dry-wet cycles is significantly increased. During the transitional stage ($2 < n \leq 4$), the disintegration of coarse soil particles in water slows down. The soil structure is relatively stable, and the rate of shear strength deterioration decreases. During the stabilization stage ($n > 4$), the block disintegration tends to be stable, with rare cracks generated by the coarse particles. The disintegrated material content remains almost unchanged, and the soil shear strength deterioration rate gradually reaches the limit value.

4.1.3 Variation pattern of the shear strength index

To analyze the variation pattern of soil shear strength index under dry-wet cycles, the Mohr-Coulomb criterion was used to fit σ and τ.

$$\tau = \sigma \tan \varphi + c \tag{3}$$

where σ and τ are the normal stress (kPa) and shear stress (kPa) on the soil shear plane. c and φ are the cohesion (kPa) and internal friction angle (o), respectively.

The shear strength index of the soil under different dry-wet cycles obtained by Eq. 3 is shown in Table 3.

Figure 12 shows the variation of soil shear strength with dry-wet cycles. Under dry-wet cycles, the degradations of soil cohesion and internal friction angle are consistent, both showing the trends of first decreasing and then stabilizing. However, the degradation of the cohesion is significantly larger than that of the internal friction angle. After one wet-dry cycle, the cohesive force and internal friction angle decrease by 62.03% and 6.32%, respectively. After four wet-dry cycles, the cohesion and internal friction angle decrease by 86.71% and 13.29%, respectively. After eight wet-dry cycles, the cohesion and internal friction angle decrease by 89.87% and 18.94%, respectively. The reason is that the cohesion and the internal friction angle of the rockfill material are composed of the interlocking force and friction strength between soil particles. Although the inter-particle friction strength decreases with the decreasing number of block particles, the broken particles still have a certain friction strength under the consolidation stress, leading to a relatively small internal friction angle.

Assuming that the damage to the soil by dry-wet cycles is a continuous process, the damage evolution equation for the shear strength parameters of the soil can be established. Statistical analysis reveals that the deterioration trend of shear strength parameters of argillaceous siltstone rockfill materials can be better fitted by the following power functions:

$$c = 23.662n^{-0.543}, \quad R^2 = 0.975 \tag{4}$$

$$\varphi = 27.665n^{-0.046}, \quad R^2 = 0.9029 \tag{5}$$

4.2 Soil deformation characteristics

4.2.1 Shear dilation rate

In addition to shape changes, volume changes also occur during soil shear damage. The volume dilation and volume contraction of soil due to shear stress is referred to as shear dilation (Huang et al., 2016). In the direct shear test, the upward vertical displacement of the soil indicates shear dilation, and the downward vertical

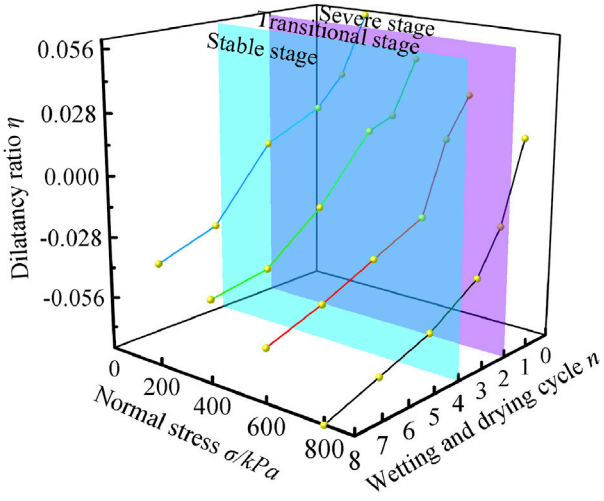

FIGURE 13
Curves of shear dilation rate under dry-wet cycles.

displacement indicates shear contraction. The shear dilation rate η for soil shear damage can be calculated based on Eq. 6:

$$\eta = \tan\psi = \frac{d\varepsilon_v}{d\varepsilon_\gamma} = \frac{dh/dD}{dx/dD} = \frac{dh}{dx} \tag{6}$$

where ψ is the shear dilation angle of the soil; $d\varepsilon_v$ is the volume strain increment; d_γ is the shear strain increment; h is the vertical displacement; x is the shear displacement; D is the thickness of the shear zone.

Figure 13 shows the variation of soil shear dilation rate η with different vertical loads σ and dry-wet cycles n. As the number of dry-wet cycles increases, the soils vary from shear dilation to shear contraction. By increasing the vertical consolidation stress, the number of dry-wet cycles for the change from shear dilation to shear contraction decreases. Therefore, the dry-wet cycle and vertical consolidation stress are two factors affecting the deformation of rockfill materials by shear dilation. The range analysis shows that the shear dilation of the soil is more prominently influenced by the wet-dry cycle.

As one of the basic properties of soil, shear dilation is a dominant factor influencing the deformation and damage properties of soil (Zhang et al., 2016). Soil shear dilation depends on the soil particle composition and the interaction between the particles. The dry-wet cycle intensifies the disintegration of the block particles in the soil, and the structural characteristics of the soil are constantly changing, with different shear dilations. When the number of dry-wet cycles is 0, the block particles are not disintegrated in water, and the friction between the block particles causes the gradual hollowing of some particles. At this time, the soil volume continuously increases, and the deformation caused by shear dilation significantly intensifies until the soil is damaged by yielding deformation. With the intensification of dry-wet cycles, the block particles are continuously disintegrated by water, and the dense skeleton structure of the soil is seriously damaged. Coupled with the stress concentration during shear deformation, the pores between the grains are gradually closed by pressure, reducing the volume of the soil. At this time, most fine particles formed by disintegration are

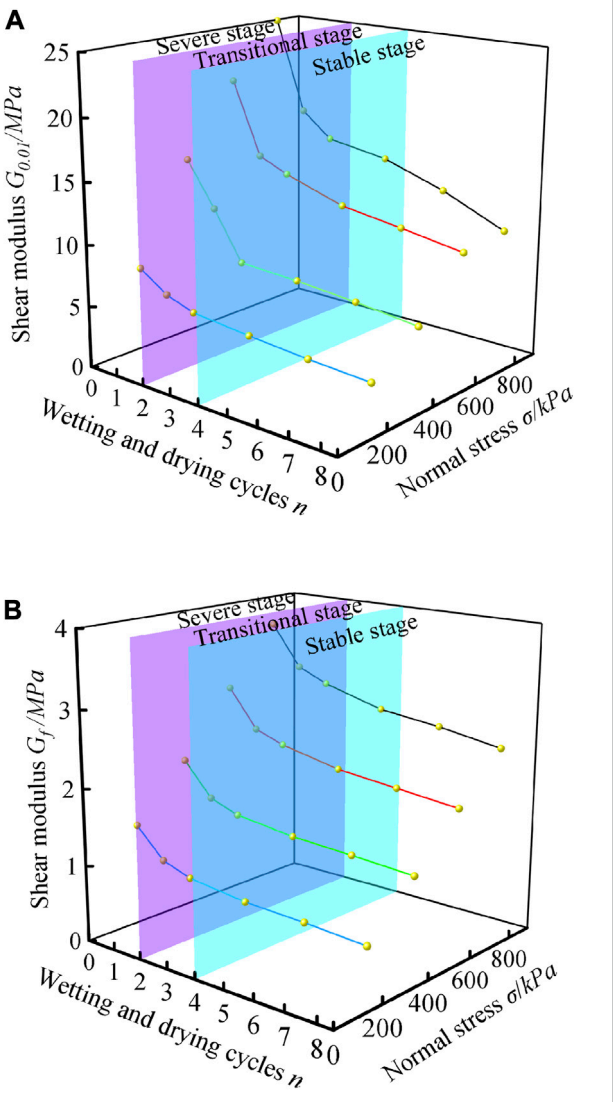

FIGURE 14
Curves of shear modulus under dry-wet cycles. **(A)** $G_{0.01}$. **(B)** G_f.

directionally arranged along the shear surface. With the increasing shear stress in the soil, the soil body shows shear plastic flow damage.

4.2.2 Shear modulus

The soil shear modulus G characterizes the ability of the soil to resist shear deformation. When shear deformation occurs in rockfill materials, the shear modulus continuously changes with the increase of shear displacement. Its value can be expressed by the slope of the tangent line at a point on the stress-shear strain curve. The shear modulus corresponding to shear strain 0.01 (shear displacement 3 mm) and shear damage (shear displacement 45 mm) are denoted as $G_{0.01}$ and G_f, respectively, and the variation of the shear modulus of rockfill materials with the accumulation of dry-wet cycles is plotted in Figure 14.

It can be seen from Figure 14 that the soil shear modulus $G_{0.01}$ is greater than G_f under the same test conditions. The reason is that during the initial stage of shear, the block stone particles in rockfill materials are closely interlocked, enhancing the rolling and friction

of the particle. The shear force required to develop a small shear deformation of the soil sample rapidly increases, and the shear modulus $G_{0.01}$ corresponding to a shear strain of 0.01 is large. During the shear damage stage, rupture occurs in the soil particle interlocking structure, resulting in a loose soil structure at the shear surface and a slow increase in shear stress. At this time, the shear modulus G_f of the soil relatively decreases. When the number of dry-wet cycles n is fixed, the soil is more densely squeezed with the increase of vertical load σ. The resistance to shear deformation is enhanced, and the soil shear modulus $G_{0.01}$ and G_f are increased. At a constant vertical load σ, the coarse particles in the soil continuously disintegrate until the disintegration is stable. The interlocking force between particles weakens, the number of fine particles arranged along the shear surface increases, and the shear deformation resistance of the soil gradually decreases and reaches a constant state. In this process, both $G_{0.01}$ and G_f exhibit the trend of first decreasing and then stabilizing.

5 Discussion

5.1 Relationship between strength degradation and disintegration characteristics

X-ray diffraction analysis shows that the argillaceous siltstone is rich in clay minerals, and the typical laminating structure of the rock microstructure is observed by a scanning electron microscope. The results indicating that the water stability of the argillaceous siltstone is poor, and it is easy to produce wet disintegration when it encounters water. After two dry-wet cycles, the argillaceous siltstone collapsed sharply, and the coarse particle content decreased from 100% before the test to 40.7%. After four dry-wet cycles, the disintegration rate of coarse particles slowed down and the content of coarse particles is 26.5%. After eight dry-wet cycles, it is difficult for coarse particles to disintegrate again and the content of coarse particles is 19.7%.

The strength deterioration of argillaceous siltstone rockfill also has the similar characteristics under the corresponding dry-wet cycle shear tests. When the dry-wet cycles are repeated twice, the coarse particles immersed in water to produce strong disintegration, the number of interlocking coarse particles decreased, and the shear hardening characteristics of the soil weakened. The deterioration of soil shear strength increases rapidly, and the deterioration reaches 38.01% for the soil sample with a normal load of 200 kPa. The soil cohesion decreases by 82.91% and the internal friction angle decreases by 7.97%. When the dry-wet cycles are repeated four times, the coarse particles in the soil are fully disintegrated, and the content of fine particles increased sharply. The occlusion and rolling friction of coarse particles in the shear deformation gradually disappeared, and the shear stress of soil increased slowly and tended to be stable, and the plastic flow trend began to appear. The deterioration of soil shear strength changes little, and the deterioration of the soil sample with normal load of 200 kPa is 44.52%. The soil cohesion decreases by 86.71% and the internal friction angle decreases by 13.29%. When the dry-wet cycles are repeated eight times, the soil showed plastic flow characteristics and weak stress softening phenomenon after shear yield. Because the coarse particle disintegration is basically stable, the shear strength deterioration of soil is relatively small. Taking the soil sample with 200 kPa normal load as an example, the deterioration only increased from 44.52% to 50.61% after four to eight dry-wet cycles. The soil cohesion decreases by 89.87% and the internal friction angle decreases by 18.94%.

By comparing and analyzing the results of disintegration test and strength deterioration test, it is not difficult to find that the shear strength characteristics of argillaceous siltstone rockfill under dry-wet cycles are mainly caused by wet disintegration of coarse particles in the rockfill, and the content of fine particles increases sharply. With the increase of the number of dry-wet cycles, the proportion of coarse and fine particles in the soil has changed significantly, and the skeleton structure of the soil has also changed. The coarse particles disintegrate with water, the content of fine particles is increasing, and the interlocking and rolling friction of the coarse particles are gradually weakened, which leads to the deterioration of the shear strength of the soil.

5.2 Degradation mechanism of the shear strength

The shear strength of the rockfill material is composed of the apparent cohesion and friction strength of the soil (Yang et al., 2021). The apparent cohesion reflects the adhesion degree of fine particles in the soil and the interlocking strength of coarse particles. The friction strength is a macroscopic representation of the frictional interaction of soil particles on the shear surface and the degree of directional particle arrangement. Under dry-wet cycles, the block particles in rockfill materials soften and disintegrate, the bound water between fine particles thickens, and the directional arranged fine particles on the shear surface significantly increase, resulting in the continuous deterioration of soil shear strength. The meso-mechanism of shear strength deterioration of rockfill materials under dry-wet cycles is shown in Figure 15.

Figure 15A shows the shear surface characteristics of soil samples under different dry-wet cycles. Compared with the shear surface of the soil sample after zero dry-wet cycle, the coarse particles on the shear surface after twice dry-wet cycles decreases significantly, and there is phenomenon of coarse particle breakage. After four times dry-wet cycles, the fine particles in the shear surface increased significantly, the occlusion of coarse particles decreased, and the shear surface is unsmooth. After eight times dry-wet cycles, only a small number of coarse particles are distributed on the shear surface. The shear surface is flat and smooth, and no trace of the occlusion and rolling friction of coarse particles is observed.

Figure 15B illustrates the deterioration of the apparent cohesion of the rockfill material under dry-wet cycles. It can be seen that disintegration occurs when the argillaceous siltstone rockfill material is exposed to water. The clay particles formed by disintegration are dissociated and negatively charged by water. After forming an electric field, the cations in the aqueous solution are tightly adsorbed on the surface of the clay particles through the electric field attraction to form a bound water membrane, exerting a certain bonding effect between the clay particles. However, after multiple wet-dry cycles, the coarse particles in the soil material are continuously wetted and cracked, significantly increasing the

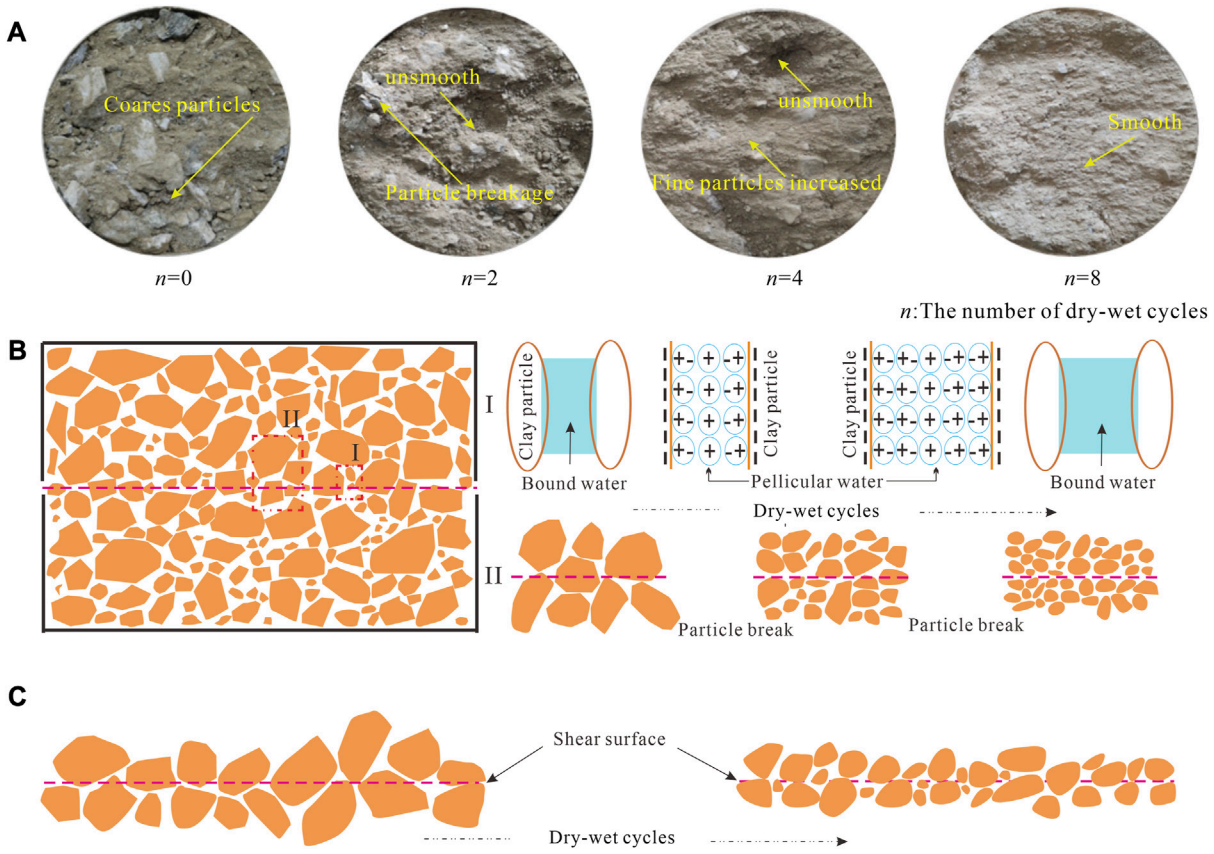

FIGURE 15
Schematic diagram of deterioration mechanism of shear strength of rockfill materials. **(A)** Shear surface of soil sample under different dry-wet cycles. **(B)** Deterioration of apparent cohesion. **(C)** Deterioration of friction strength.

number of clay particles. These particles are bound to each other through the bound water, and repeated immersion in the wetting environment thickens the bound water membrane between them. The electric field attraction is insufficient to overcome the gravitational water flow, weakening the binding strength between soil particles. Furthermore, the dry-wet cycles accelerate the shrinkage-expansion deformation of clay-rich mineral particles, with an increasing number of internal fractures. In the alternating changes of dry and wet environments, these fractures gradually open, widen, deepen, and penetrate. As a result, the disintegration of block particles continuously occurs, and the particle edges are gradually smoothed with increased roundness. The interlocking effect between particles continuously weakens, and the apparent cohesion of the soil body further deteriorates.

Figure 15C illustrates the particle distribution characteristics on the shear surface of the rockfill material under dry-wet cycles. It can be seen that under dry-wet cycles, the coarse particles are wetted and disintegrated, the number of fine particles significantly increases, the roundness of soil particles increases, and the interlocking friction between soil particles decreases significantly due to the decrease in particle size. In addition, the frictional impedance effect of the soil is weakened by the increasing number of fine particles directionally arranged on the shear surface. Due to the alternating dry and wet actions, cracks and defects sprout inside the block before the particle disintegration is completed. As a result, the soil can hardly form a stable bearing skeleton structure, and its friction strength is significantly weakened.

5.3 Analysis of the experimental limitations and sources of error

In the existing dry-wet cycle shear tests, soil material is mostly dipped and dried on the outside of the test machine and then filled into the test machine when a certain number of cycles. This test method is usually inconsistent with the stress state of soil in nature and ignores the consolidation stress condition of soil. This study realizes the dry-wet cycle process of the soil in the test machine, which can truly reflect the consolidation stress state of soil, thus avoiding the disturbance of soil structure during the preparation of the soil sample after the dry-wet circulation. Therefore, the test method is innovative. However, the direct shear test in this study still has some unavoidable experimental limitations and sources of error.

On the one hand, the shear surface of the soil in the indoor direct shear test is artificially fixed and decreases with shear, the shear zone is limited to the upper and lower shear box openings and the particles cannot be fully deformed. These defects in the test apparatus inevitably have an impact on the test results. On the other hand, as with existing indoor geotechnical test equipment for coarse-grained soils, the size of the test machine is limited by the

inability to carry out shear tests on full-scale graded soils. The maximum particle size allowed in the direct shear test is 60mm, which is very different from the maximum particle size in the field. Therefore, the test results can only reflect the change law of shear strength of soil and reveal the internal mechanism of action, but cannot reflect the real mechanical properties and strength index results of soil.

In order to eliminate the influence of artificial fixed shear surface on the test results, the laminated shear test should be carried out, that is, multiple shear planes are set in the test apparatus, and the shear strength characteristics of the soil are revealed by analyzing the most unfavorable shear weak plane in the soil. In addition, in order to eliminate the scale effect of the test soil material, it is necessary to carry out full scale *in-situ* test. *In-situ* tests require improved accuracy of data acquisition and stability of pressure control. This aspect of the research will be progressively improved in subsequent research work.

6 Conclusion

Based on the disintegration resistance test and dry-wet cycle shear test of the argillaceous siltstone rockfill materials, this paper reveals that the characteristics of wet disintegration and shear strength deterioration of rockfill materials, and analyzes the strength deterioration mechanism of rockfill materials from the meso-structure. The main conclusions are provided as follows.

(1) The argillaceous siltstone is rich in clay minerals, with a content of over 60%, and disintegrates strongly when exposed to water. The disintegration degree of argillaceous siltstone has the characteristics of three stages with the accumulation of dry-wet cycles. The massive disintegration stage ($n \leq 2$) has a significant reduction in coarse grain content and a significant increase in disintegrate content, the transitional stage ($2 < n \leq 4$) has a slower disintegration rate of coarse grains in water, the stabilization stage ($n > 4$) is difficult to produce further fractures of coarse grains and the disintegrate content almost ceases to change.
(2) The dry-wet cycle change condition of rockfill material inside shear testing machine is realized. With the accumulation of dry-wet cycles, the rockfill material experiences deformation from shear dilation to shear contraction. The shear damage of rockfill material gradually progresses from strain hardening to shear plastic flow, exhibiting a slight stress softening characteristic. Both soil cohesion and internal friction angle show the trend of first decreasing and then stabilizing under dry-wet cycles. However, the deterioration degree of cohesion is significantly greater than that of the internal friction angle.
(3) The weakening of the apparent cohesion and friction strength of soil are the main reasons for the shear strength deterioration of rockfill material in the alternating dry-wet cycle. The fine particles are bound to each other through the bound water, and repeated immersion in the wetting environment thickens the bound water membrane between them. The electric field attraction is insufficient to overcome the gravitational water flow, weakening the binding strength between soil particles. Meanwhile, the coarse particles are wetted and disintegrated, the number of fine particles significantly increases. The roundness of the particles on the shear surface increases, and the number of directionally arranged particles increases, weakening the frictional impedance effect of the soil.

Data availability statement

The original contributions presented in the study are included in the article/Supplementary Material, further inquiries can be directed to the corresponding author.

Author contributions

Conceptualization, JD, XS; validation, CL, GF; supervision, JD; writing—original draft preparation, JD, XS, and CL; writing—review and editing, WZ and GF. All authors contributed to the article and approved the submitted version.

Funding

This work was supported by the Special Basic Cooperative Research Programs of Yunnan Provincial Undergraduate University's Association (202001BA070001-066, 202101BA070001-137), Basic Research Project of Yunnan Province of China (202101AT070144), and Talent Introduction Program of Kunming University (XJ20220015).

Conflict of interest

The authors declare that the research was conducted in the absence of any commercial or financial relationships that could be construed as a potential conflict of interest.

Publisher's note

References

Abbas, M. F., Shaker, A. A., and Al-Shamrani, M. A. (2023). Hydraulic and volume change behaviors of compacted highly expansive soil under cyclic wetting and drying. *J. Rock Mech. Geotech.* 15 (2), 486–499. doi:10.1016/J.JRMGE.2022.05.015

Ahmed, S. S., Martinez, A., and DeJong, J. T. (2023). Effect of gradation on the strength and stress-dilation behavior of coarse-grained soils in drained and undrained triaxial compression. *J. Geotech. Geoenviron.* 149(5), 04023019. doi:10.1061/JGGEFK.GTENG-10972

Cavarretta, I., Coop, M., and O'Sullivan, C. (2010). The influence of particle characteristics on the behaviour of coarse grained soils. *Geotechnique* 60 (6), 413–423. doi:10.1680/geot.2010.60.6.413

Chen, X. B., Jia, Y., and Zhang, J. S. (2018). Stress-strain response and dilation of geogrid-reinforced coarse-grained soils in large-scale direct shear tests. *Geotech. Test. J.* 41 (3), 20160089–20160610. doi:10.1520/GTJ20160089

Cook, M. E., Brook, M. S., Hamling, I. J., Cave, M., Tunnicliffe, J. F., and Holley, R. (2023). Investigating slow-moving shallow soil landslides using Sentinel-1 InSAR data in Gisborne, New Zealand. *Landslides* 20, 427–446. doi:10.1007/s10346-022-01982-9

Huang, M. S., Yao, Y. P., Yin, Z. Y., Liu, E. L., and Lei, H. Y. (2016). An overview on elementary mechanical behaviors, constitutive modeling and failure criterion of soils. *China Civ. Eng. J.* 49 (7), 9–35. doi:10.15951/j.tmgcxb.2016.07.002

Jia, H. L., Wang, T., Xiang, W., Tan, L., Shen, Y. J., and Yang, G. S. (2018). Influence of water content on the physical and mechanical behaviour of argillaceous siltstone and some microscopic explanations. *Chin. J. Rock Mech. Eng.* 37 (7), 1618–1628. doi:10.13722/j.cnki.jrme.2017.1037

Jia, Y. F., Yao, S. E., and Chi, S. C. (2019). Wetting of coarse-grained soil under equal stress ratio path. *Chin. J. Geotech. Eng.* 41 (4), 648–654. doi:10.11779/CJGE201904007

Li, S. Y., He, Z. L., Zhu, P., Mei, L. X., Zeng, S. J., and Wang, S. W. (2022). Experimental study on the triaxial compression properties of coarse-grained filling soil under drying–wetting cycles. *Geofluids* 2022, 1–14. doi:10.1155/2022/1452916

Li, Z., Liu, L. L., Yan, S. H., Zhang, M. K., and Xie, Y. L. (2019). Properties of microscopic particle morphology and particle contact of renewable construction waste mixtures. *Constr. Build. Mat.* 207, 190–205. doi:10.1016/j.conbuildmat.2019.02.135

Luo, Y. H., Zhu, C. L., and Li, J. D. (2003). Research for distortion-destruction mechanism of slopes of red strata in Yunnan province and their hazard control. *Rock Soil Mech.* 24 (5), 836–839. doi:10.16285/j.rsm.2003.05.037

Nguyen, H. B. K., Rahman, M. M., and Karim, M. R. (2023). Effect of soil anisotropy and variability on the stability of undrained soil slope. *Front. Built Environ.* 9, 1117858. doi:10.3389/fbuil.2023.1117858

Oliveira, J., Cássaro, F., and Pires, L. (2021). Estimating soil porosity and pore size distribution changes due to wetting-drying cycles by morphometric image analysis. *Soil. till. Res.* 205, 104814. doi:10.1016/j.still.2020.104814

Pan, Y., Wu, G., Zhao, Z. M., and He, L. (2020). Analysis of rock slope stability under rainfall conditions considering the water-induced weakening of rock. *Comput. Geotech.* 128, 103806. doi:10.1016/j.compgeo.2020.103806

Peng, M., and Zhang, L. M. (2012). Breaching parameters of landslide dams. *Landslides* 9, 13–31. doi:10.1007/s10346-011-0271-y

Pham, T., Zaman, M. W., and Vu, T. (2022). Modeling triaxial testing with flexible membrane to investigate effects of particle size on strength and strain properties of cohesion less soil. *Transp. Infrastruct. Geotech.* 9, 417–441. doi:10.1007/s40515-021-00167-6

Rasul, J. M., Ghataora, G. S., and Burrow, M. P. N. (2018). The effect of wetting and drying on the performance of stabilized subgrade soils. *Transp. Geotech.* 14, 1–7. doi:10.1016/j.trgeo.2017.09.002

Silvani, C., Bonelli, S., Philippe, P., and Desoyer, T. (2008). Buoyancy and local friction effects on rockfill settlements: a discrete modelling. *Comput. Math. Appl.* 55 (2), 208–217. doi:10.1016/j.camwa.2007.04.011

Tran, K. M., Bui, H. H., and Nguyen, G. D. (2021). Hybrid discrete-continuum approach to model hydro mechanical behavior of soil during desiccation. *J. Geotech. Geoenviron.* 147 (10), 040211. doi:10.1061/(ASCE)GT.1943-5606.0002633

Wang, G. J., Yang, C. H., Kong, X. Y., and Liu, T. N. (2012). Research on fragmentation distribution and shear strength parameters of accumulate granulae with superhigh bench dumping site. *Rock Soil Mech.* 33 (10), 3087–3092+3161. doi:10.16285/j.rsm.2012.10.017

Wang, G. J., Yang, C. H., Zhang, C., Mao, H. J., and Wang, W. (2009). Experimental research on particle breakage and strength characteristics of rock and soil materials with different coarse-grain contents. *Rock Soil Mech.* 30 (12), 3649–3654. doi:10.16285/j.rsm.2009.12.031

Wei, H., Wu, D. Y., Wu, H. G., Tang, L., Wang, S., and Sun, H. (2023). Coordinated evolution and mechanism characteristics of the tunnel-landslide system under rainfall conditions. *Eng. Fail. Anal.* 146, 107118. doi:10.1016/j.engfailanal.2023.107118

Wei, S., and Zhu, J. G. (2006). Study on wetting breakage of coarse-grained materials in triaxial test. *Chin. J. Rock Mech. Eng.* 25 (6), 1252–1258. doi:10.1016/S1872-1508(06)60035-1

Wen, C. P., and Yuan, X. Q. (2022). Hyperbolic consolidation creep model of weathered red sandstone coarse-grained soil under the wet and dry cycles conditions. *Geotech. Geol. Eng.* 40, 5103–5113. doi:10.1007/s10706-022-02202-w

Wu, E. L., Zhu, J. G., Chen, G., and Wang, L. (2020). Experimental study of effect of gradation on compaction properties of rockfill materials. *Bull. Eng. Geol. Environ.* 79, 2863–2869. doi:10.1007/s10064-020-01737-7

Wu, E. L., Zhu, J. G., He, S. B., and Peng, W. M. (2021). A stress dilatancy relationship for coarse-grained soils incorporating particle breakage. *Granul. Matter.* 24 (1), 4. doi:10.1007/S10035-021-01147-W

Wu, Y. K., Shi, K. J., Han, Y., Han, T., Yu, J. L., and Li, D. D. (2021). Experimental study on strength characteristics of expansive soil improved by steel slag powder and cement under dry–wet cycles. *Iran. J. Sci. Technol. Trans. Civ. Eng.* 45, 941–952. doi:10.1007/s40996-020-00473-y

Xu, X. T., Shao, L. J., Huang, J. B., Xiang, X., Liu, D. Q., Xian, Z. X., et al. (2021). Effect of wet-dry cycles on shear strength of residual soil. *Soils Found.* 61 (3), 782–797. doi:10.1016/J.SANDF.2021.03.001

Xue, Y., Liang, X., Li, X., Wang, S. H., Ma, Z. Y., Zhang, S. W., et al. (2023). Influence mechanism of brine-gas two-phase flow on sealing property of anisotropic caprock for hydrogen and carbon energy underground storage. *Int. J. Hydrogen. Energy* 48 (30), 11287–11302. doi:10.1016/j.ijhydene.2022.05.173

Xue, Y., Liu, S., Chai, J. R., Liu, J., Ranjith, P. G., Cai, C. Z., et al. (2023). Effect of water-cooling shock on fracture initiation and morphology of high-temperature granite: application of hydraulic fracturing to enhanced geothermal systems. *Appl. Energ* 337, 120858. doi:10.1016/j.apenergy.2023.120858

Yang, Z. P., Zhao, Y. L., Hu, Y. X., Li, S. Q., Lei, X. D., and Li, X. Y. (2021). Effect of the strength of rock blocks on the shear characteristics of soil-rock mixtures. *Chin. J. Rock Mech. Eng.* 40 (4), 814–827. doi:10.13722/j.cnki.jrme.2020.0488

Yuan, J., Liu, Z. H., Hu, G. X., and Fang, Y. G. (2018). Experimental analysis of the influence of soil composition on strength characteristics. *Soil. Mech. Found. Eng.* 55, 325–332. doi:10.1007/s11204-018-9544-y

Zeng, L., Luo, J. T., Liu, J., Gao, Q. F., and Bian, H. B. (2021). Disintegration characteristics and mechanisms of carbonaceous mudstone subjected to load and cyclic drying–wetting. *J. Mat. Civ. Eng.* 33 (8), 04021195. doi:10.1061/(ASCE)MT.1943-5533.0003817

Zhang, B. Y., Zhang, J. H., and Sun, G. L. (2015). Deformation and shear strength of rockfill materials composed of soft siltstones subjected to stress, cyclical drying/wetting and temperature variations. *Eng. Geol.* 190, 87–97. doi:10.1016/j.enggeo.2015.03.006

Zhang, G., Wang, G., Yin, Z. Y., and Yang, Z. X. (2016). A critical review on the research of fundamental behavior and constitutive relationship of the soil. *China Civ. Eng. J.* 53 (2), 105–118. doi:10.15951/j.tmgcxb.2020.02.009

Zhang, H. J., Adoko, A. C., Meng, Z. J., Wang, H., and Jiao, Y. Y. (2017). Mechanism of the mudstone tunnel failures induced by expansive clay minerals. *Geotech. Geol. Eng.* 35 (1), 263–275. doi:10.1007/s10706-016-0102-y

Zhang, J. Z., and Zhou, X. P. (2020). AE event rate characteristics of flawed granite: from damage stress to ultimate failure. *Geophys. J. Int.* 222 (2), 795–814. doi:10.1093/gji/ggaa207

Zhang, J. Z., Zhou, X. P., Zhou, L. S., and Berto, F. (2019). Progressive failure of brittle rocks with non-isometric flaws: insights from acousto-optic-mechanical (AOM) data. *Fatigue Fract. Eng. Mater Struct.* 42 (8), 1787–1802. doi:10.1111/ffe.13019

Zhou, X., Ma, G., and Zhang, Y. D. (2019). Grain size and time effect on the deformation of rockfill dams: a case study on the shuibuya CFRD. *Geotechnique* 69 (7), 606–619. doi:10.1680/jgeot.17.P.299

Zhou, X. P., Cheng, H., and Feng, Y. F. (2014). An experimental study of crack coalescence behaviour in rock-like materials containing multiple flaws under uniaxial compression. *Rock Mech. Rock Eng.* 47 (6), 1961–1986. doi:10.1007/s00603-013-0511-7

Zhou, X. P., Lian, Y. J., Wong, L. N. Y., and Berto, F. (2018). Understanding the fracture behavior of brittle and ductile multi-flawed rocks by uniaxial loading by digital image correlation. *Eng. Fract. Mech.* 199, 438–460. doi:10.1016/j.engfracmech.2018.06.007

Zhou, X. P., Wang, Y. T., Zhang, J. Z., and Liu, F. N. (2019). Fracturing behavior study of three-flawed specimens by uniaxial compression and 3D digital image correlation: sensitivity to brittleness. *Rock Mech. Rock Eng.* 52 (3), 691–718. doi:10.1007/s00603-018-1600-4

Zhou, X. P., Zhang, J. Z., Qian, Q. H., and Niu, Y. (2019). Experimental investigation of progressive cracking processes in granite under uniaxial loading using digital imaging and AE techniques. *J. Struct. Geol.* 126, 129–145. doi:10.1016/j.jsg.2019.06.003

frontiers | Frontiers in Environmental Science

TYPE Original Research
PUBLISHED 11 October 2023
DOI 10.3389/fenvs.2023.1225916

OPEN ACCESS

EDITED BY
Guangjin Wang,
Kunming University of Science and Technology, China

REVIEWED BY
Bing Bai,
Beijing Jiaotong University, China
Yihui Niu,
Chongqing University of Science and Technology, China

*CORRESPONDENCE
Yongxing Lu,
luyongxing@mail.cgs.gov.cn ,
Yongxing.Lu_CSCSC@outlook.com
Guanxi Yan,
g.yan@uq.edu.au

RECEIVED 20 May 2023
ACCEPTED 05 September 2023
PUBLISHED 11 October 2023

CITATION
Lu Y, Dai L, Yan G, Huo Z, Chen W, Lan J, Zhang C, Xu Q, Deng S and Chen J (2023), Effects of various land utilization types on groundwater at different temporal scales: a case study of Huocheng plain, Xinjiang, China.
Front. Environ. Sci. 11:1225916.
doi: 10.3389/fenvs.2023.1225916

Effects of various land utilization types on groundwater at different temporal scales: a case study of Huocheng plain, Xinjiang, China

Yongxing Lu[1,2]*, Liangliang Dai[1], Guanxi Yan[3]*, Zhitao Huo[1], Wen Chen[1], Jingzhou Lan[1], Chaoming Zhang[1], Qingyang Xu[1], Shimin Deng[1] and Jian Chen[2]

[1]Changsha General Survey of Natural Resources Center, China Geological Survey, Changsha, Hunan, China, [2]School of Engineering and Technology, China University of Geosciences, Beijing, China, [3]School of Civil Engineering, University of Queensland, Brisbane, QLD, Australia

Different land utilization types have unignorable impacts on adjacent aquifers, so studying the effects of varying land utilization types on groundwater balance and groundwater table in arid and semi-arid areas is crucial to facilitate the rational development of territorial space and groundwater resource management. This study investigated the relationship between land utilization type variations and groundwater dynamics from spatial and temporal scales in Huocheng plain, Xinjiang, China, via taking advantage of different land utilization maps provided by remote sensing techniques in 1990, 2000, and 2015. Based on the analysis of results, the findings can be summarized as follows. First, the cultivated and construction land has expanded significantly in the past 25 years. The migration of the regional center of cultivated land was insignificant, as it is still located almost in the center of the entire study area. However, the transfer span of the location center of construction land was more prominent, and its moving direction was mainly from south to northeast, directly affecting the groundwater balance state and groundwater table. Second, the total amount of groundwater storage exhibited a remarkable reduction, from a recharge in 1990 to a continuous discharge in 2000–2015, during which the total recharge and discharge had both continuously declined. Meanwhile, recharging and discharging elements were also changed profoundly as less groundwater recharges from ambient aqueous environments and more groundwater extraction. Thus, human activities were the fundamental driving terms causing the changes in groundwater sources. Third, the groundwater table gradually and continuously dropped from south to northeast in the study area over time. The drawdown of spatially averaged groundwater tables was positively correlated with construction and cultivated area extension. In addition, compared to the former literature, this study offers an alternative approach for groundwater protection and optimization of territorial space development and utilization in arid and semi-arid areas.

KEYWORDS

land utilization type, groundwater balance, groundwater table, groundwater drawdown, Huocheng plain

1 Introduction

Since initiating China's modernization and globalization in the 1990s and accelerating the process of urbanization in the 2000s, the spatiotemporal variations of land utilization types have become the most straightforward manifestation of an expansion of human activities (e.g., the rapid expansion of cultivated and construction areas in recent decades). Meanwhile, underground aqueous resources, such as soil moisture in the vadose zone (Ma et al., 2014; Ma et al., 2015; Yan et al., 2022a; Yan et al., 2022b), perched water (Bear, 1972; Freeze and Cherry, 1979; Izbicki et al., 2015; Liu J. et al., 2019), shallow groundwater (Charbeneau and Sherif, 2002; Hancock, 2002; Hu et al., 2021), are scarce in arid and semi-arid regions. More adversely, the surging demand for water consumption leads to a nonnegligible groundwater table drawdown in these regions (Claessens et al., 2009; Chen et al., 2010; Lei-hua et al., 2012). As a result, the human beings-land interactive relationship is an essential component and core interest of modern research. More specifically, studying the effects of varying land utilizations on groundwater dynamics has become one of the current research challenges in environmental engineering and science.

Numerous environmental scholars have studied the impacts of various land utilization types on long-term groundwater dynamics by applying different methods. All those methods could be characterized into the following four categories. The first category is quantitative mathematical modeling. Mathematical models were used to simulate and analyze the varying land utilization types (Ghaffari et al., 2010; Tong et al., 2012) and their hydrological effects (Yan et al., 2021; Yan et al., 2022c; Ma et al., 2022), the influence of varying land utilization types on groundwater dynamics (Prabhakar and Tiwari, 2015; Elmahdy and Mohamed, 2016) and the spatiotemporal variation of earthen and aqueous environments (Deng, 2001; Ma et al., 2003), explicitly considering contamination transport during a hydrodynamic process (Bai et al., 2021a; Bai et al., 2021b). The second category is the geostatistical method. Based on the theory of geostatistics, the temporal and spatial changes of groundwater could be well revealed, and the spatial heterogeneity of seepage properties and groundwater table variation in responding to varying land utilization types has also been well analyzed (Liu J. et al., 2019; Hu et al., 2021; Zhang et al., 2022). The third category is the groundwater balance method. Through constructing a grid geographic information database, the groundwater balance method was applied to calculate the groundwater storage and study the effect of regional land utilization variation on groundwater recharge and discharge (Lei et al., 2017). The fourth category is the integration of remote sensing, hydrological survey, and consistent *in situ* monitoring; based on those three geological surveying methods, the varying land utilization types in response to groundwater dynamics have been further explored (Zhang et al., 2014; Cui et al., 2015; Shu et al., 2022; Liu et al., 2023). Although many scholars used different methods to analyze and study the impacts of underlying surface conditions variations on groundwater dynamics, few scholars have examined its impact on groundwater balance and groundwater table synthetically, and inadequate efforts have been devoted to comprehensively investigating this impact on regional long-term groundwater dynamics at multiscale.

The study aims to provide a more in-depth investigation of the research field for the selected region–Huocheng plain, Xingjiang, China. This plain is the gateway to central Asia, a vital node of the "Belt and Road Initiative." It is also an area experiencing rapid urbanization but vulnerable to many adverse ecological and environmental impacts. The current environmental challenges in using soil and water resources in this region can be summarized as the following points: 1) strongly influenced by a population boom and economic growth, the total relative carrying capacity of resources in this region has been overloaded (Fu et al., 2016); 2) the over-reclamation and overgrazing overloaded the land in this area, subsequently prone to land desertification (Kang and Zhang, 2012); 3) the inadequate regulations on daily water consumption (i.e., water wasted) and insufficient investments in hydraulic infrastructures (Yang and He, 2008); 4) there are uneven spatial and temporal distributions of regional water resources, so the contradiction of engineering water shortage is prominent. Therefore, it is of practical significance to study the influences of land utilization variations on groundwater dynamics in Huocheng plain.

Based on the aforementioned considerations in the literature review, this case study selected datasets of land utilization types in Huocheng plain for three periods in 1990, 2000, and 2015. First, it analyzes the dynamic variations and spatiotemporal migrations of land utilization on two different temporal scales, e.g., one longer of 1990–2015 and the other shorter of 2000–2015. In addition, it superimposes this analysis on the evolution of groundwater dynamics in this area during the same period. This series of investigations contributes to exploring the impact of changes in land utilization types on groundwater balance and the groundwater table. In general, this case study provides an alternative analyzing method for the rational utilization of groundwater resources and optimizing the development and utilization of territorial space in arid and semi-arid areas.

2 The overview of the case study region

Huocheng county is located west of the Tianshan mountains, north of the Ili river, adjacent to Kazakhstan in the west, Yining city in the east, and the administrative division of Ili Kazak autonomous prefecture of Xinjiang Uygur autonomous region (see Figures 1A, B). The elevation of this terrain is generally higher in the north and east, and lower in the south and west, with a medium-high mountainous area in the north, a hilly area in the central region, and a plain area in the southwest.

This paper focused on the southwest plain of Huocheng county as a study area with an elevation of 479–1,247 m. According to the geomorphic formation of Huocheng Plain, this region can be divided into the piedmont flood gravel plain, fine soil plain, eolian desert, and other geomorphic units from south to north (see Figure 1C). In addition, there are Horgos port (the largest land treaty port in Northwest China), Qingshuihe economic and technological development zone, and the fifth Production and Construction Corps, where we can collect the groundwater table data (see Figure 1D). The climate of this area is semi-arid (continental temperate). Its precipitation is far less than evaporation, e.g., its annual average precipitation of 220–700 mm compared to its evaporation in plain areas of 850–1,000 mm and evaporation in mountainous regions of less than 800 mm (Wang

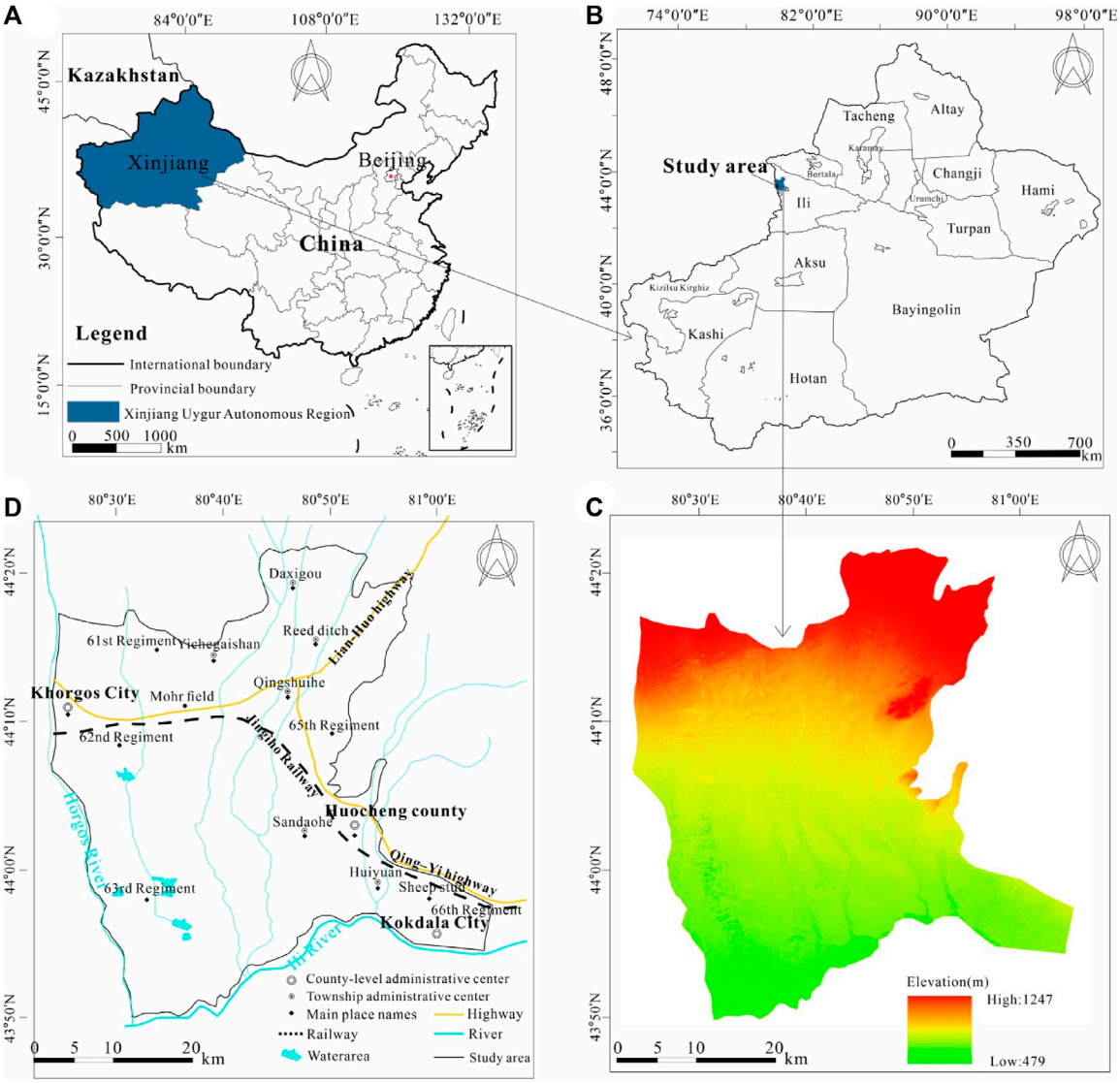

FIGURE 1
Geographic and administrative location of the study area: **(A)** The location of Xinjiang Uygur autonomous region in the map of China; **(B)** The selected study area in the map of Xinjiang; **(C)** The elevation map of Huocheng plain; **(D)** The brief information overview map for Huocheng plain in Xinjiang.

et al., 2012). There are seven main rivers, and gullies flow from north to south. The annual surface runoff is about 8.44×10^8 m^3, and the annual surface runoff only accounts for 6% of the total water storage in Ili valley. The groundwater is mainly stored in the gravel layer of the quaternary system. The hydraulic recharge from the upper part of an alluvial fan, which was geologically formed by the northern rivers running through the mountainous valleys, is an essential source of groundwater recharge (Li and Tao, 2015).

3 The collection of research database

3.1 Land utilization datasets

The land utilization datasets were obtained from the Data Center for Resources and Environmental Sciences, Chinese Academy of Sciences (http://www.resdc.cn) (Xu et al., 2018), using Landsat-MSS and Landsat 8 as image data sources. The secondary classification monitoring raster datasets of land utilization type with a spatial resolution of 30 m × 30 m in 1990, 2000, and 2015 were explicitly selected. Remote sensing image data were preprocessed by geometric correction and radiation distortion correction. Based on artificial intelligence and machine learning, the interactive visual interpretation and field investigation ensured the consistency of land utilization data processing and the reliability of interpretation accuracy. ArcGIS 10.2 software extracted and reclassified datasets in different years according to the geo-photographic mask. It was finally divided into six categories (see Figure 2): cultivated land, forest land, grassland, waterbody, construction land (urban and rural, industrial, mining, and residential land), and unused land (sandy land, Gobi, saline-alkali land, marshland, bare land, bare rock, and stony land and other unused lands).

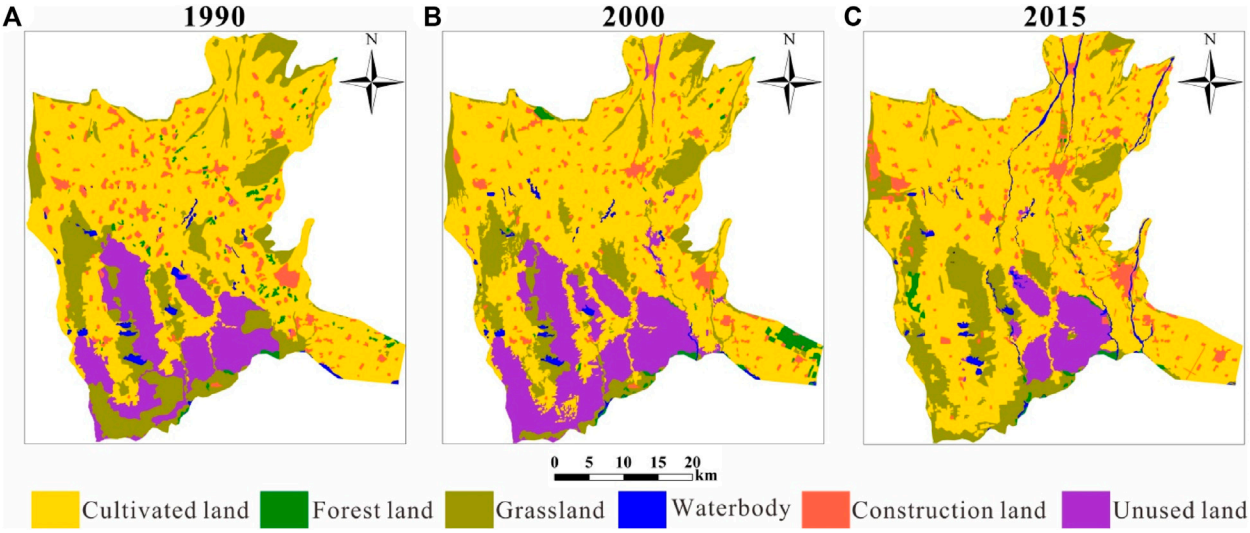

FIGURE 2
Type-distribution and evolution of land utilization in Huocheng plain in **(A)** 1990, **(B)** 2000, and **(C)** 2015 (the contour-plotted datasets were sourced from the Data Center for Resources and Environmental Sciences, Chinese Academy of Sciences (Xu et al., 2018).

3.2 Hydrological datasets

The groundwater datasets were mainly derived from the geological survey project of the China Geological Survey by Li et al. (2015) and the Regional Hydrogeological Survey Report of the People's Republic of China: Ili Region, and some of the data were from their field measurements. Hydrometeorological data, such as precipitation and evaporation, are sourced from the Ili meteorological station. The information on water resources development and utilization (e.g., artificial extraction, spring water excretion, river runoff, canal head diversion water, *etc.*) was collected from the annals of Huocheng county, the statistical bulletin of Huocheng county, the yearbook of Huocheng county, the demonstration of water resources of Braxi mine (Ili shoer, Xinjiang) project of China Power Investment Corporation and the statistical yearbook of Ili Kazak autonomous prefecture (the aforementioned collections of research data libraries are not publicly released from their affiliated institutions and have still been archived as confidential documents in those affiliations).

4 Data processing methods

4.1 A dynamic model of land utilization degree

A comprehensive analysis model can express the extent of human development and land utilization within a specific period in the selected study area from the perspective of ecology, and its calculation formula (Li et al., 2006) can be provided as follows:

$$L_i = \sum_{i=1}^{n} A_i \times C_i \times 100\% \quad (1)$$

where L_i is the land utilization degree composite index, A_i is the land utilization degree classification index of the ith type, C_i is the ratio of the area of the ith land utilization type to the study total area, and n is the number of classifications of land utilization degree. According to the actual situation of the study area and the existing research results (Wang et al., 2001), the land utilization degree classification index of construction land is assigned as the **4** points, cultivated land as the **3** points, forest land, grassland, and waterbody as the **2** points, and unused land as the **1** point.

4.2 Land utilization transfer matrix

The land utilization transfer matrix (Zhu and Li, 2003; Zheng et al., 2022) could be applied to reflect the dynamic processing information of mutual transformation among different types at the beginning and end of the study period in the selected investigation region. The mathematical form of the transfer matrix (S) could be given by

$$S = \begin{bmatrix} S_{11} & S_{12} & S_{13} & \cdots & S_{1n} \\ S_{21} & S_{22} & S_{23} & \cdots & S_{2n} \\ S_{31} & S_{32} & S_{33} & \cdots & S_{3n} \\ \cdots & \cdots & \cdots & \cdots & \cdots \\ S_{m1} & S_{m2} & S_{m3} & \cdots & S_{mn} \end{bmatrix} \quad (2)$$

where S_{mn} is the area transfer from the land utilization type m to the type n in km^2.

4.3 Standard deviation ellipse method

The standard deviation ellipse method (SDE) is the most direct modus to analyze the central, dispersion, and direction trends of data point sets or regions. This method quantitatively describes the overall characteristics of the spatial distribution of research objects through the spatial distribution ellipse with the center, major axis, minor axis, and azimuth Angle as the basic parameters. The

calculation formula of the center of gravity could be presented as follows:

$$\overline{X_w} = \frac{\sum_{i=1}^{n} w_i x_i}{\sum_{i=1}^{n} w_i}, \overline{Y_w} = \frac{\sum_{i=1}^{n} w_i y_i}{\sum_{i=1}^{n} w_i}$$

where $(\overline{X_w}, \overline{Y_w})$ is the center of gravity, indicating the relative position of geographical elements in two-dimensional space; w_i is the weight value; (x_i, y_i) is the spatial location coordinate.

4.4 Groundwater balance method

On the one hand, groundwater recharge has precipitation infiltration, river recharge, channel recharge, reservoir recharge, field irrigation, and lateral runoff recharge. On the other hand, groundwater discharge includes evaporation discharge, spring outflow, artificial extraction, and lateral drainage. In addition, the groundwater balance method was used to calculate and analyze the number of groundwater recharging/discharging sources. Thus, for comparing the groundwater recharging/discharging sources in different years, the mass balance of groundwater should be given as (Liu R. et al., 2019; Zhao et al., 2021):

$$\Delta Q = Q_{in} - Q_{out} \quad (4)$$

$$Q_{in} = R_p + R_r + R_c + R_{re} + R_f + R_l \quad (5)$$

$$Q_{out} = D_e + D_s + D_a + D_l \quad (6)$$

where ΔQ is the variation of groundwater storage; Q_{in} is the inflow for groundwater recharge; Q_{out} is the outflow for groundwater discharge; R_p is precipitation infiltration; R_r is river recharge; R_c is channel recharge; R_{re} is reservoir recharge; R_f is field irrigation; R_l is lateral runoff recharge; D_e is evaporation discharge; D_s is spring outflow; D_a is artificial extraction; D_l is lateral drainage.

5 Results and analysis

5.1 Analysis of temporal and spatial changes in land utilization

5.1.1 Dynamic analysis of land utilization

Based on the land utilization status datasets in 1990, 2000, and 2015, the evolutions and mutual transfers of land utilization types in the study area in the past 25 years were obtained (see Figure 3). This paper used the dynamic model of land utilization degree and land utilization transfer matrix to calculate the land utilization degree composite index and variation (see Table 1), transfer matrix (see Supplementary Table S1 in Supplementary Appendix S1), and its Sankey diagram (see Figure 4), and net land change of six land utilization types (see Table 2). The cultivated land and grassland are this selected area's primary land utilization types. Since the 1990s, Huocheng plain has gradually evolved from agriculture and animal habitation to a comprehensive area including agricultural area, animal habitation, and industrial and commercial functionality.

5.1.1.1 Long-term change in land utilization

From 1990 to 2015, the land utilization degree composite index of cultivated land, construction land, and waterbody showed an increasing trend in the selected period. Meanwhile, the land utilization degree variation of the cultivated and construction land was rapidly growing, and their areas significantly increased. The cultivated land area increased from 1,081.12 to 1,225.11 km^2, increasing by 13.32%, with an average annual increasing rate of 0.53%. The construction land area increased from 103.03 to 119.46 km^2, increasing by 15.95%, with an average annual increasing rate of 0.64%. During the same period, the area of unused land, forest land, and grassland decreased significantly. The area of forest land decreased from 23.65 to 14.68 km^2, decreasing by 37.93%, with an average annual declining rate of −1.52%. The area of unused land decreased from 259.05 to 118.01 km^2 by 54.45%, with an average yearly declining rate of −2.18%.

Over the past 25 years, land utilization in this region has evolved, and the cultivated land has increased continuously. The primary types of land utilization transferred were grassland, unused land, and forest land, whose areas were 82.65, 60.36, and 15.44 km^2, respectively. The main transferred types were waterbody and construction land. The net transfer of cultivated land to waterbody was 8.81 km^2, and the net transfer to construction land was 5.65 km^2, mainly caused by continuous reclamation in the local area. Construction land increased significantly and mostly occupied cultivated land and grassland. The area of unused land was reduced considerably, which was the primary transfer type in the area, among which 60.36 and 80.58 km^2 were transferred into cultivated land and grassland, respectively, reflecting the significant success of local desert control. Overall, the characteristics of land utilization change in Huocheng plain were attributed to the construction land occupying cultivated land and grassland and the cultivated land occupying grassland, unused land, and forest land.

5.1.1.2 Short-term change in land utilization

From 2000 to 2015, the land utilization degree composite index of cultivated land, construction land, and grassland showed an increasing trend in the selected period. Except for the cultivated land area, the construction land increased remarkably, and its area increased from 81.57 to 119.46 km^2, with an increase of 46.45% and an average annual rate of change of 3.10%. In comparison, the unused and forest land area decreased significantly. As a result, the area of unused land decreased by 65.35% from 340.56 to 118.01 km^2, with an annual rate of change of −4.36%.

Over the past 15 years, construction land increased substantially, and the primary transferred types were cultivated land, grassland, and unused land, whose areas were 18.27, 16.00, and 2.98 km^2, respectively. On the other hand, the area of unused land had been significantly reduced, which was the main transferred type except for forestland. To a certain extent, this reflected that with the advancement of urbanization and economic development, more of the population was migrating to Huocheng county, Khorgos city, Qingshuihe town, and other areas in the selected region of Huocheng plain.

5.1.2 Temporal and spatial migration analysis of land utilization

As identified above, cultivated land and construction land were the two types with the most significant changes in Huocheng Plain, and their area continued to increase during 1990–2015. In addition,

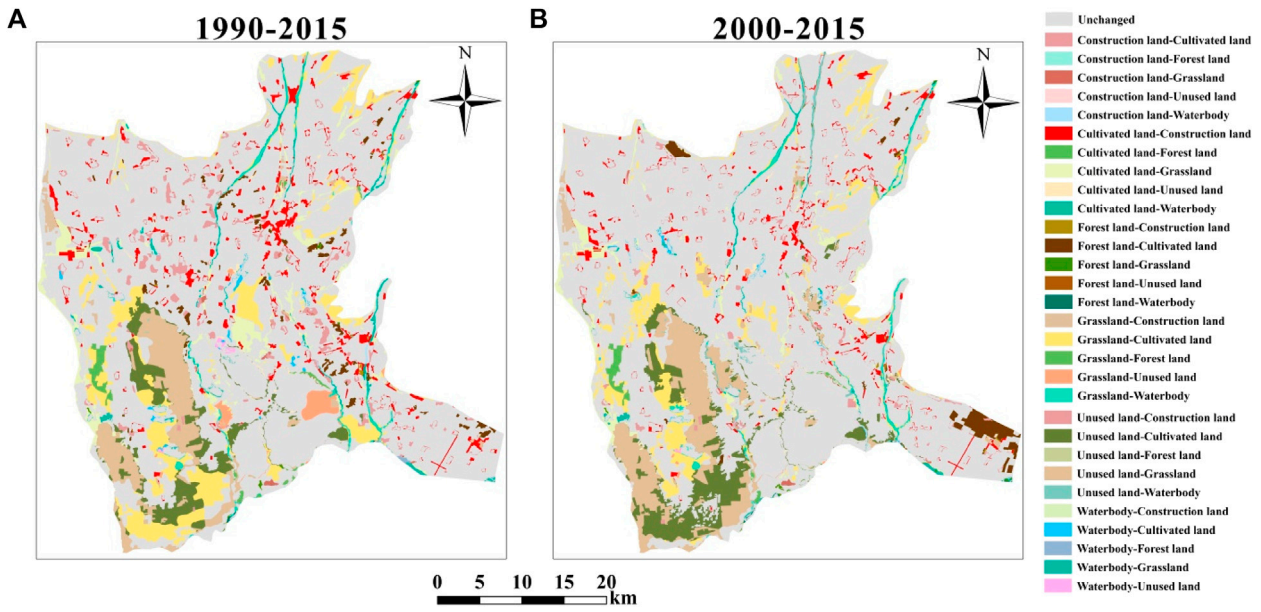

FIGURE 3
Variations of land utilization types from 1990 to 2015 based on datasets in a spatial resolution of 30 m: **(A)** 1990–2015 and **(B)** 2000–2015.

TABLE 1 The land utilization degree composite index and variation in Huocheng plain.

Type	Land utilization degree composite index			Land utilization degree variation	
	1990	2000	2015	1990–2015	2000–2015
Cultivated land	176.86	177.53	200.42	23.56	22.89
Forest land	2.58	3.10	1.60	−0.98	−1.50
Grassland	37.75	30.48	34.64	−3.11	4.15
Waterbody	2.28	2.02	4.25	1.98	2.23
Construction land	22.47	17.79	26.06	3.58	8.26
Unused land	14.13	18.57	6.44	−7.69	−12.14

cultivated land and construction land were the main factors affecting the depth of groundwater balance and groundwater table in this region, so this paper mainly analyzed and discussed these two types of land utilization.

The spatial overlaying analysis of land utilization type images in three periods from 1990 to 2015 was carried out. During the dynamic evolution, the location centers of cultivated and construction land were super-combined to form the location center migration diagram of the two land utilization types (see Figure 5). During the study period, the shift of the location centers of cultivated land was slight, almost migrating towards the center of the entire study area. The transfer of the location center of construction land had a larger span and involved a much wider range than that of cultivated land. The transfer direction of the location center of construction land was mainly from south to northeast. From 1990 to 2000, the location center of construction land migrated to the southeast, with a distance of 1.82 km. From 2000 to 2015, the location center migrated to the northeast, and the migration distance was up to 8.90 km.

5.2 Groundwater balance analysis

In this paper, the complete datasets for each decade in the selected representative years (1990, 2000, and 2015) were chosen as the temporal interval to analyze the groundwater dynamics since the 1990s. According to hydrogeological parameters, borehole datasets, and meteorological datasets of Huocheng county in different periods, groundwater recharging and discharging sources were calculated by the groundwater balance equation to determine the total recharge and discharge amount in different periods. Then, the changes in each recharging/discharging source were analyzed individually. As a result, the analysis of groundwater balance elements can be provided in Figure 6 (see Supplementary Table S2 in Supplementary Appendix S1), and the variations of groundwater balance elements are provided in Table 3.

According to Figure 6 (see Supplementary Table S2 in Supplementary Appendix S1) and Table 3, the amount of change in groundwater storage in the three typical years was

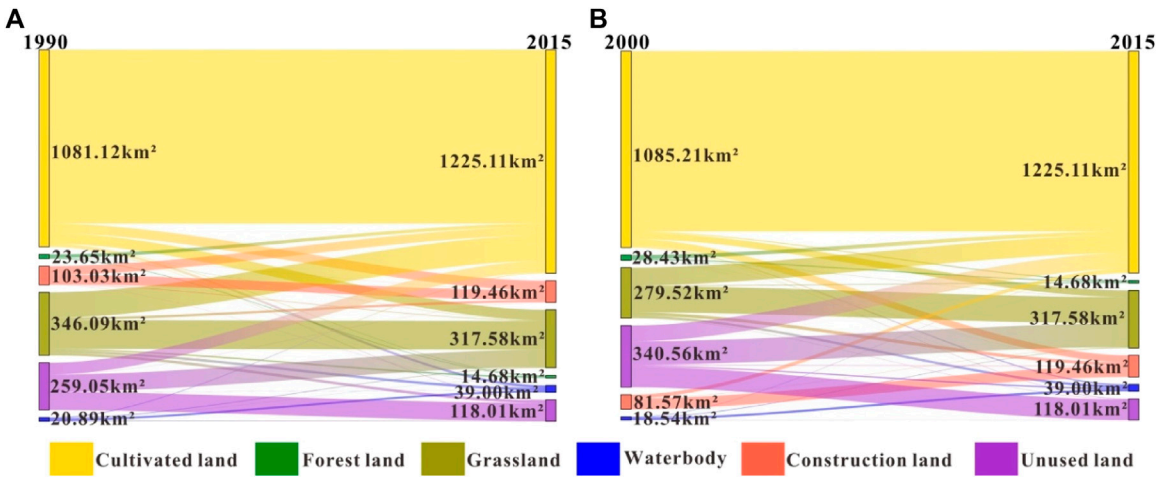

FIGURE 4
Sankey diagram of the land utilization transfer matrix in Huocheng plain: **(A)** 1990–2015 and **(B)** 2000–2015.

TABLE 2 The net land utilization change (km²) in Huocheng plain.

Time	Type	2015						
		Cultivated land	Forest land	Grassland	Waterbody	Construction land	Unused land	Net change
1990	Cultivated land	0.00	15.44	82.65	−8.81	−5.65	60.36	143.99
	Forest land	−15.44	0.00	6.79	0.40	−0.83	0.10	−8.97
	Grassland	−82.65	−6.79	0.00	−9.74	−9.91	80.58	−28.51
	Waterbody	8.81	−0.40	9.74	0.00	0.92	−0.96	18.10
	Construction land	5.65	0.83	9.91	−0.92	0.00	0.97	16.43
	Unused land	−60.36	−0.10	−80.58	0.96	−0.97	0.00	−141.04
2000	Cultivated land	0.00	15.09	62.11	−3.90	−18.27	84.87	139.90
	Forest land	−15.09	0.00	2.41	−0.24	−0.82	−0.01	−13.75
	Grassland	−62.11	−2.41	0.00	−9.66	−16.00	128.24	38.06
	Waterbody	3.90	0.24	9.66	0.00	0.19	6.47	20.45
	Construction land	18.27	0.82	16.00	−0.19	0.00	2.98	37.89
	Unused land	−84.87	0.01	−128.24	−6.47	−2.98	0.00	−222.55

69.10×10^5, -186.50×10^5, -137.60×10^5 m^3/year, respectively. It was found that the trend of groundwater storage in the long-term temporal scale (1990–2015) evolved from incremental to decremental. Specifically, the groundwater storage in Huocheng plain was recharged in the 1990s. After that, the amount of groundwater storage exhibited a decreasing trend, and the decreasing rate gradually increased. Therefore, by comparing the changing pace of groundwater storage in those different periods (1990–2015), it is apparent that the decreasing rate of groundwater storage significantly increased in the former decade (1990–2000) and then decreased gradually in the latter 1.5 decades (2000–2015).

From 1990 to 2015, the total groundwater recharge presented a significant downward trend, and the total amount of groundwater recharge decreased by 2.09×10^8 m^3/year. From 2000 to 2015, the decreasing rate of groundwater recharging sources was 1.82 times that from 1990 to 2000. The elements of groundwater recharging sources were similar in 1990 and 2000, among which the channel and river recharge accounted for 82%–85% of the total inflow, and field irrigation accounted for a minor proportion. However, the elements of recharging sources changed remarkably in 2015, including channel recharge, river recharge, and reservoir recharge in descending order. Compared to the amount of groundwater recharging elements in 1990 and 2000, the variations of field irrigation increased by 892.64% and 288.42%. Nevertheless, reservoir recharge decreased by 56.58% and 51.31%, and channel recharge reduced by 40.53% and 34.93%.

From 1990 to 2015, the total groundwater discharge exhibited a significant decline trend as well, and the total amount of

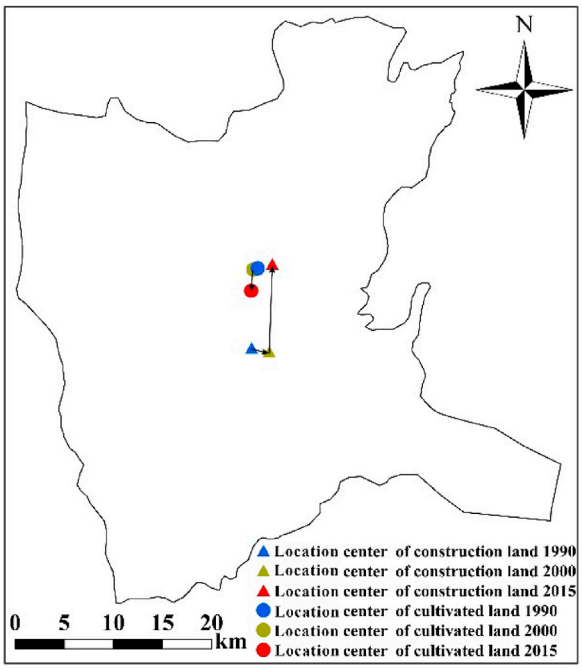

FIGURE 5
Location center transfer map of cultivated and construction land from 1990 to 2015.

groundwater discharge decreased by 1.88 × 10^8 m^3/year. From 1990 to 2000, the gross discharge decreased by 3.04 × 10^7 m^3/year, and the decreasing rate of discharge was 3.04 × 10^6 m^3/year. From 2000 to 2015, total groundwater discharge decreased by 1.58 × 10^8 m^3/year, and the decreasing rate of discharge was 1.05 × 10^7 m^3/year. Lateral drainage and spring outflow most significantly contribute to groundwater discharge. Compared to the amount of groundwater discharging elements in 1990 and 2000, the variations of artificial extraction increased by 1995.60% and 603.22%, yet spring outflow decreased by 59.76% and 56.38%.

In conclusion, both the total groundwater recharge and discharge continued to decline, mainly due to the increasing human activities. Human activities were the fundamental driving forces that caused the changes in groundwater recharging/discharging sources. With the spiking demand for groundwater extraction and limited available surface water, the groundwater storage dropped prominently because of the increasing urbanization and modernization, the expansion of cultivated land and construction areas, and increased irrigation demand and domestic water consumption.

5.3 Characteristics of the groundwater dynamics

Based on the groundwater table datasets collected in the selected region, the depth-mapping groundwater table in Huocheng plain in 1990, 2000, and 2015 is shown in Figure 7. Through comparative analysis in the three selected years, the depth-contour of the groundwater table was mainly shown as relative shallows in the northeast and south regions, consistent with the topography of this study area. In 1990, the depths of the groundwater table in the northern inclined plain, near the mountainous valleys, were 10–50 m. In the central Aeolian desert area, the depths of the groundwater table were 5–10 m. Some of those were wetlands, where the depths of the groundwater table were much shallower, between 1 m and 3 m. In the southern alluvial plain, the depths of the groundwater table were 3–5 m. From 1990 to 2015, the depths of the groundwater table in most areas of Huocheng plain increased, i.e., the drawdown of groundwater storage in those areas continuously occurred during this period. For example, the depths of the groundwater table in Huocheng county were 7–10 m in 1990, 10–20 m in 2000, and 20–35 m in 2015, respectively. In the southern alluvial plain, the subdivision boundary between the shallower (0–10 m) and deeper groundwater tables (10–150 m), compared to that in 1990, moved northward obviously, and the groundwater table dropped more remarkably in the north in 2015 and 2000.

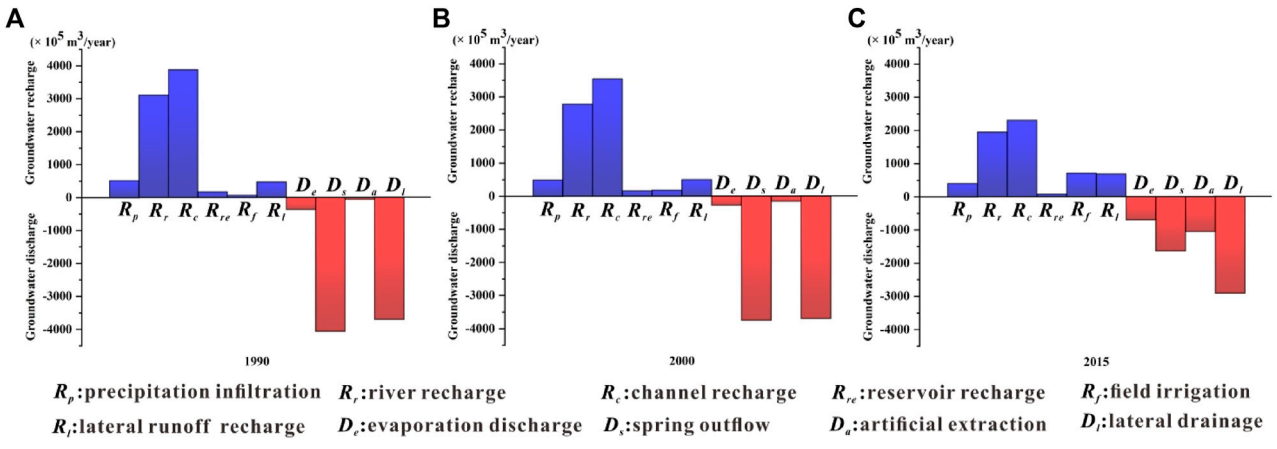

FIGURE 6
Analysis of groundwater balance elements in Huocheng plain from 1990 to 2015: **(A)** 1990, **(B)** 2000, and **(C)** 2015.

TABLE 3 Variations of groundwater balance elements in Huocheng plain.

Groundwater balance elements		Variations (%)		
		1990–2000	2000–2015	1990–2015
Groundwater recharge	Precipitation infiltration	−4.29	−17.92	−21.44
	River recharge	−10.49	−29.91	−37.26
	Channel recharge	−8.62	−34.93	−40.53
	Reservoir recharge	−10.81	−51.31	−56.58
	Field irrigation	155.56	288.42	892.64
	Lateral runoff recharge	6.38	36.04	44.72
Groundwater discharge	Evaporation discharge	−24.29	155.76	93.64
	Spring outflow	−7.76	−56.38	−59.76
	Artificial extraction	198.00	603.22	1995.60
	Lateral drainage	−0.03	−21.36	−21.38

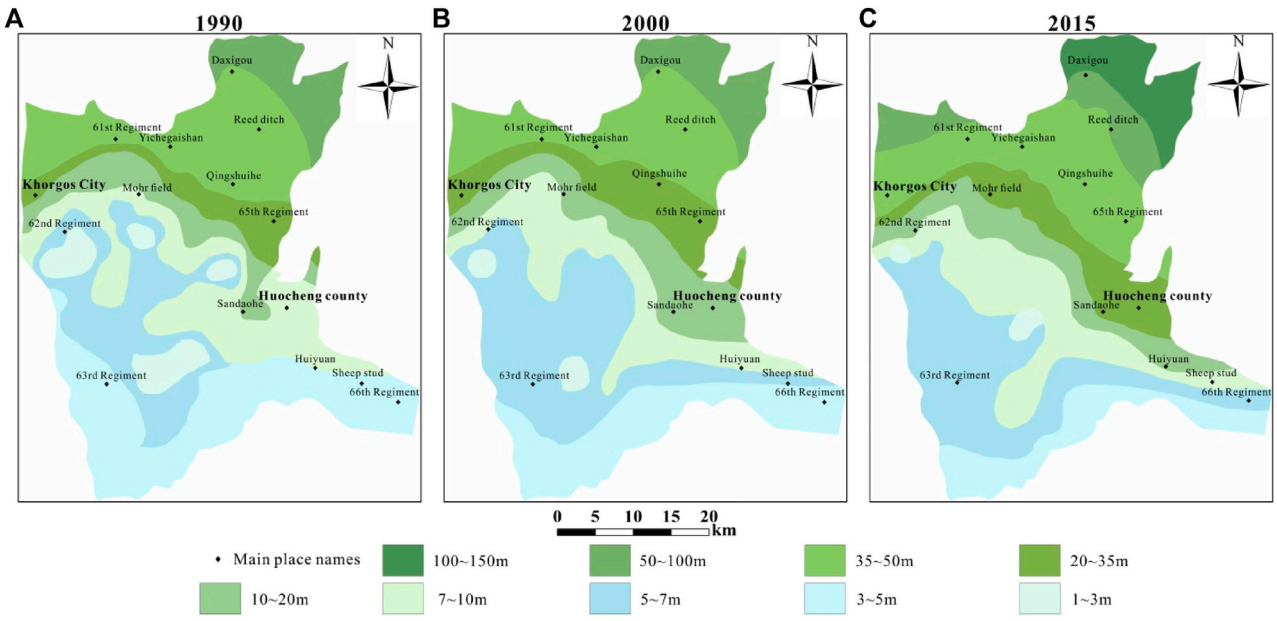

FIGURE 7
Depth-mapping groundwater table in Huocheng plain in **(A)** 1990, **(B)** 2000, and **(C)** 2015.

5.4 The effects of varying land utilizations on groundwater dynamics

After analyzing the distribution of land utilization types in 1990, 2000, and 2015, the different ranges of groundwater tables corresponding to each land utilization type were extracted from the aforementioned databases. First, the ratios of the region's land utilization types in different depths of groundwater tables were calculated and presented in Figure 8 (see Supplementary Table S3 in Supplementary Appendix S1). Then, the changes in the average depths of groundwater table corresponding to the land utilization types in different periods were obtained, as shown in Figure 9.

In general, between the years 1990 and 2000, the relationship of the average depth of groundwater table corresponding to each land utilization type was as follows: cultivated land > construction land > grassland > forest land > waterbody > unused land. However, in 2015, it was changed as follows: construction land > cultivated land > grassland > waterbody > forest land > unused land. The average depth of the groundwater table corresponding to construction land increased the most over this period, from 18.90 m in 1990 to 22.82 m in 2000 and ending at 37.06 m in 2015. It was followed by cultivated land, the groundwater table of which deepened from 22.92 m in 1990 to 23.30 m in 2000 and eventually approached 32.67 m in 2015. Unused land had a minor

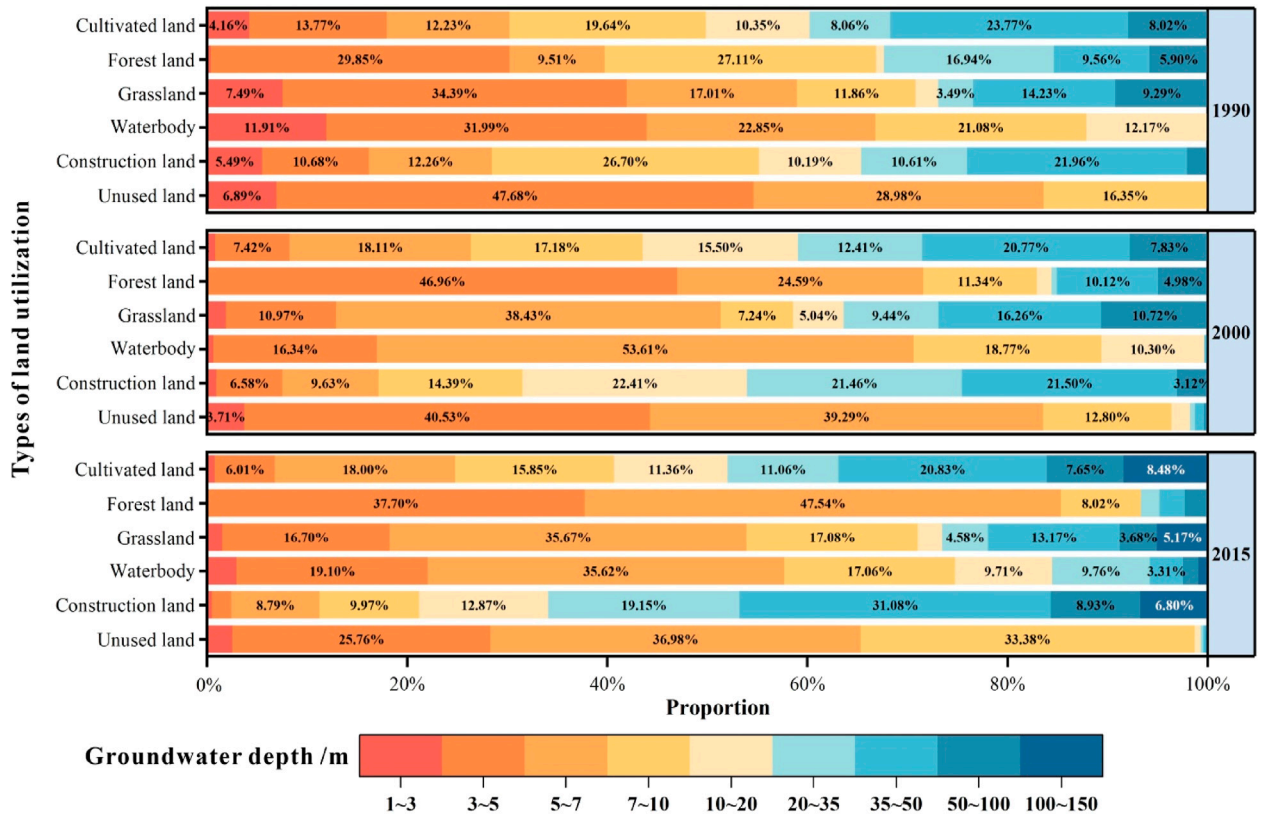

FIGURE 8
The ratios of land utilization types in different groundwater tables in 1990, 2000, and 2015 (the ratios less than 3% are not visible).

variation of groundwater table during this study period, maintained at 5–6 m. Nonetheless, the groundwater table of forest land became shallower over this duration, e.g., its corresponding depths decreased from 17.34 m in 1990 to 12.72 m in 2000 and finally down to 8.40 m in 2015.

The study area's average depth of groundwater table gradually increased over time. For example, in 1990, the average depth of groundwater table was 18.98 m. However, due to the gradual expansion of the proportion of cultivated land and construction land in this study area, the average depth of groundwater table decreased to 19.54 and 28.55 m in 2000 and 2015, respectively, in this region.

By depth-mapping the groundwater table variations for the two selected periods (the longer one of 1990–2015 and the shorter one of 2000–2015), it was capable of determining the incremental/decremental variations of the groundwater table in the form of contouring maps for the investigated area (see Figure 10). Then, the outcomes could be superimposed with the area transfers among various land utilization types during 1990–2015 and 2000–2015 for additional in-depth analysis. As a result, the area changes of each land utilization type *versus* its corresponding depth variations of groundwater table in both shorter and longer periods are obtained in Figure 11 (see Supplementary Tables S4, S5).

As for the longer study period (1990–2015), the area where the depth of the groundwater table increased by more than 1 m was approaching 1,149.94 km^2, accounting for 62.71% of the study area,

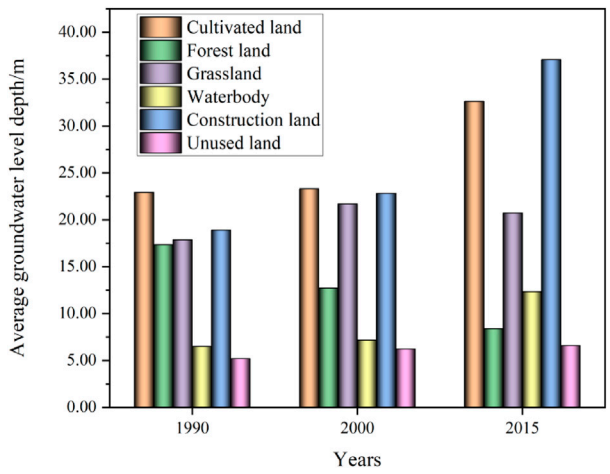

FIGURE 9
The average depths of groundwater table for various types of land utilization in Huocheng plain.

as shown in Figure 5, including the area of cultivated land having increased by 65.24 km^2, the area of construction land having increased by 10.88 km^2, and the area of unused land having increased by 64.69 km^2. The newly expanded area of cultivated land was mainly transferred from the sandy desert in the southern region of Huocheng plain since the sandy desert control

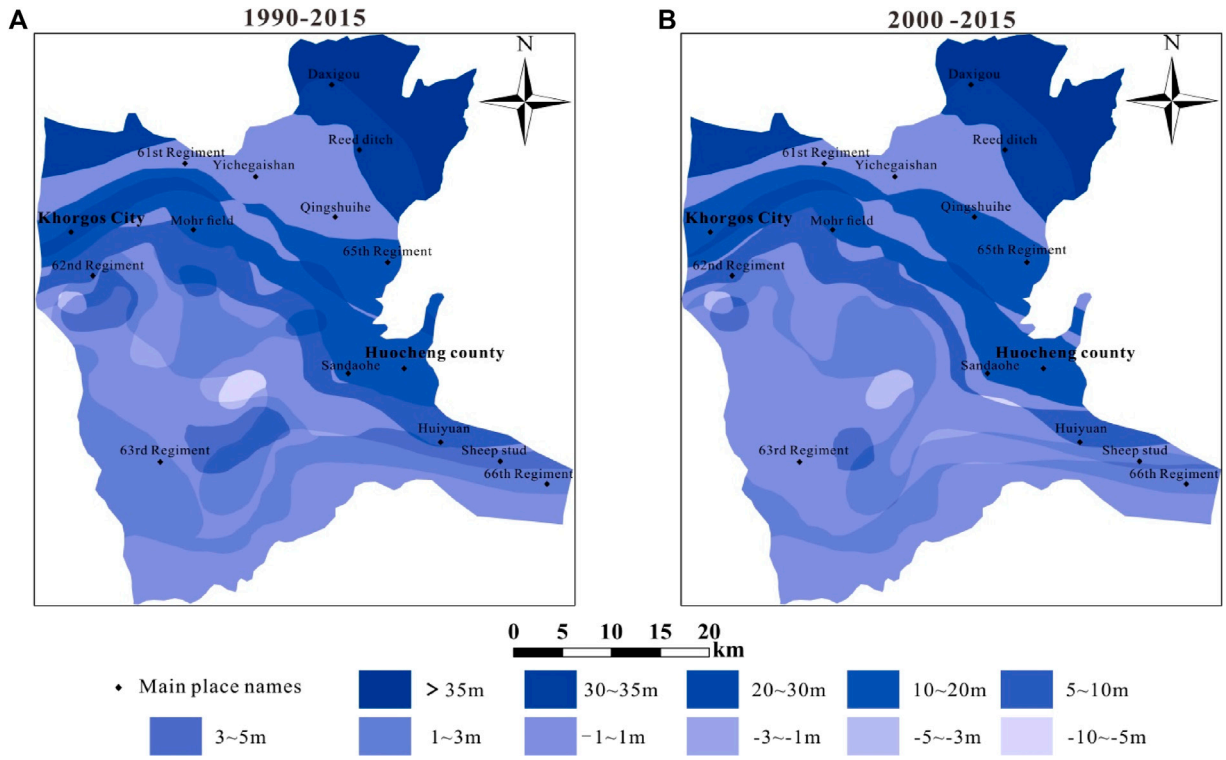

FIGURE 10
The spatial contour of the depth variation of the groundwater table in Huocheng plain: **(A)** 1990–2015 and **(B)** 2000–2015.

became the primary goal in this region. Nevertheless, the surface water stored in adjacent rivers decreased due to increased catchment water discharging into ambient groundwater systems. Also, the surface water was almost cut off at all times except during the flood season, leading to decreased groundwater recharge from ambient surface water systems (e.g., rivers, creeks, other surface runoff, *etc.*). Simultaneously, under the influence of overirrigation in this area for a very extended period, the amount of irrigation into cultivated land per unit area was much higher than the water demand for crop growth, resulting in the constantly increasing groundwater consumption endlessly extracted from deep underground. Therefore, under the concurrent effect of multiple factors mentioned previously, such as the decrease of surface water supply and the continuous increase of groundwater extraction, the expansion of cultivated land area became the main reason for the groundwater table drawdown in Huocheng plain.

As for the shorter study period (2000–2015), the area where the depth of the groundwater table increased by more than 1 m ended with 999.02 km^2, accounting for 54.48% of the entire study area, as shown in Figure 5; e.g., the area of cultivated land increased by 49.37 km^2; the area of construction land increased by 28.16 km^2; the area of unused land decreased by 84.39 km^2. In addition, the construction land area increased significantly during this period, straightforwardly reflecting the continuous progress of urbanization in this region and the increasing dependence on groundwater consumption from which urban living and production were in need. The statistical analysis showed that the proportion of groundwater in the total water supply had increased nearly four times since 2000. Therefore, the expanding construction land area also became another reason for the decrease in the groundwater table in Huocheng plain.

6 Discussions

Through exploring the variations of land utilization types and groundwater tables in two different temporal scales in the Huocheng plain, the research findings could be summarized as follows.

(1) For the longer temporal scale (1990–2015), the expansion of cultivated land led to the increasing irrigation demand, promoting the increase of canal systems and groundwater extraction, and finally resulted in the groundwater drawdown. On the one hand, the utilization coefficient of the canal systems increased from 0.48 in 1990 to 0.68 in 2014. The proportion of irrigation consumption accounted for more than half of the annual surface water runoff by 2015, proving the decreasing groundwater recharge from ambient surface water in the region. On the other hand, since the groundwater extraction mainly relied on mechanical pumping through artificial wells, the number of electromechanical pumped wells increased by 3.7 times in this area from 2000 to 2011, and the proportion of groundwater artificially extracted in this area increased by 5.35 times from 2000 to 2015. Those correlative analyses and research findings are consistent with the results and findings of Yang and He (2008) and the statistical analysis of surveying data

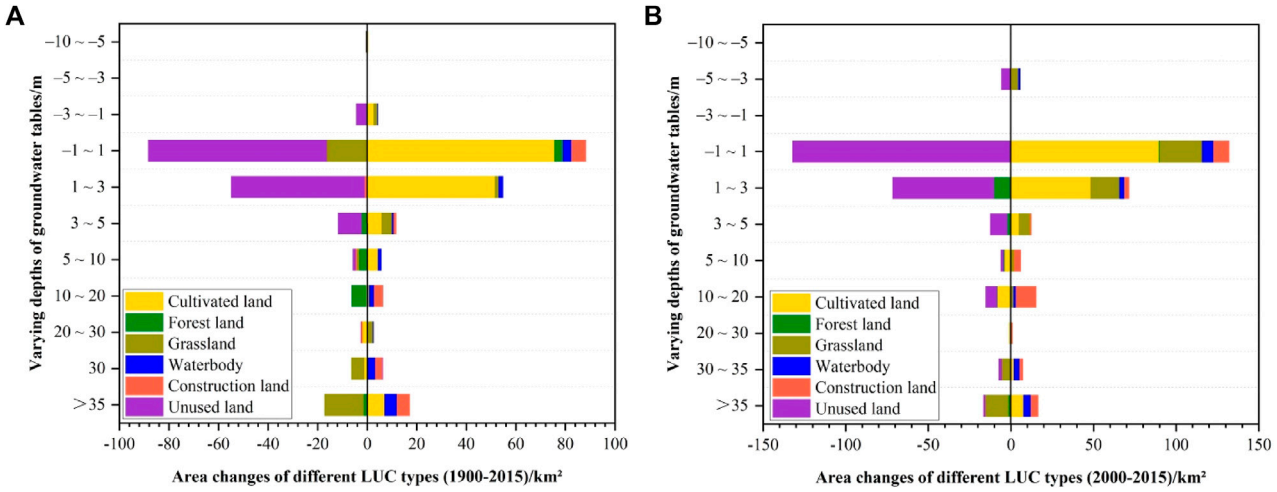

FIGURE 11
Area changes of land utilization types to varying depths of groundwater tables in Huocheng plain: **(A)** 1990–2015 and **(B)** 2000–2015.

on mechanical and electromechanical wells in Huocheng county.

(2) For the shorter temporal scale (2000–2015), the expansion of construction land was another reason for the drawdown of groundwater table in this region. This can be confirmed by the numerical simulation results of groundwater dynamics under the newly built industrial zone in this area (Yin, 2016). Through numerical simulations of groundwater dynamics in this industrial zone (Yin, 2016), the simulated results and their post-analysis predicted that the annual variation of groundwater table near the industrial park in the future would be about 2–4 times that of other areas in Huocheng plain.

(3) During 1990–2015, the subdivision boundary of the groundwater table moved northeastward significantly. The main reason was attributable to the fact that the population distribution in the following areas, including Huocheng county, Khorgoz city, Qingshuihe town, and the 63rd regiment of the Xinjiang Production and Construction Corps were increasingly dense, so the agricultural, industrial, and residential needs were increasing. With a limited amount of surface water, large-scale groundwater extraction increased the depths of groundwater table in Huocheng plain. Those correlative analyses are consistent with the research outcomes of Huo et al. (2020).

(4) The datasets of long-term observations of groundwater recharging/discharging sources and groundwater table variations in this area are still yet to be adequate and, therefore, need to be more comprehensive and sufficient. Besides, further attention should be paid to groundwater extraction by *in situ* hydrogeological investigation in order to collect more data on actual groundwater consumption from various land utilization types, including human-impact factors. Moreover, to further study the impact of varying types of land utilization on groundwater storage, it is necessary to eliminate the influence of natural impact factors on groundwater in/outflow. Last but not least, to acquire the evaporation discharge accurately, it is also necessary to consider the total amount of ecological water or plant water, such as soil water taken up by plants from the ground, released by plants by evapotranspiration, and retained in plants.

7 Conclusion

Based on the datasets of land utilization types for Huocheng plain from 1990 to 2015, this paper analyzed the dynamic characteristics of land utilization change and the spatiotemporal migration characteristics in the study area by using the dynamic model of land utilization degree, the transferring matrix method and standard deviation ellipse method. The effects of land utilization variations on groundwater balance and groundwater table were explored. The concluding points can finally be summarised as follows.

(1) In the study period, land utilization types frequently changed. For the longer temporal scale (1990–2015), the cultivated and construction land were the two types with the most significant changes in the region, and their area continued to increase constantly. The expansion was mainly transferred from grassland, unused, and forest land. For the shorter temporal scale (2000–2015), the construction land area increased significantly in this study area, and the primary transferred categories included cultivated land, grassland, and unused land. In the spatiotemporal migration of land utilization, the shift of the location center of cultivated land was slight and almost limited in the center of the entire study area. However, the transfer span of the location center of construction land was more extensive, and its migrating direction was mainly from south to northeast.

(2) During the past 25 years, the total amount of groundwater storage in the study area exhibited a downward trend from initial storage growth in positive in 1990 towards an eventual storage reduction in negative between 2000 and 2015. Also, the total recharge amount decreased by 2.09×10^8 m^3/year, and discharge continuously declined by 1.88×10^8 m^3/year. Meanwhile, the groundwater

recharging and discharging elements were significantly altered, among which field irrigation and artificial extraction were the elements with the most significant variations. Thus, human activities were the fundamental driving terms that caused the changes in groundwater sources.

(3) Compared with 2000 and 2015, the subdivision boundary of the groundwater table, i.e., the boundary between the shallower (0–10 m) and deeper groundwater tables (10–150 m), migrated from south to northeast remarkably since the 1990s and the decrease in the groundwater table was more significant in the north. The average depths of the groundwater table decreased continuously in the study area over this period. The intermediate groundwater table corresponding to the construction land dropped the most over this period, followed by the cultivated land, and the unused land encountered the most minor changes in groundwater drawdown, which proved the temporal and spatial variation of the groundwater table was significantly affected by artificial extraction.

In conclusion, variation in land utilization types has been identified and recognized as one of the main driving factors for changing the groundwater balance state and reducing groundwater storage in this region. The dynamic evolutions of groundwater table and storage are highly correlated with the areal change in cultivated and construction land.

Data availability statement

The raw data supporting the conclusion of this article will be made available by the authors, without undue reservation.

Author contributions

Conceptualization, YL, and WC; methodology, YL, and GY; software, YL, QX, and SD; validation, GY, and ZH; formal analysis, YL, and GY; investigation, WC, and CZ; resources, WC, and YL; data curation, GY, and LD; writing—original draft preparation, YL, WC, and GY; writing—review and editing, YL, and GY; visualization, SD, QX; supervision, JC, GY, and ZH; project administration, LD; funding acquisition, LD. All authors contributed to the article and approved the submitted version.

Funding

This research was supported and funded by the China Geological Survey Project (DD20230480 and DD2016008117).

Acknowledgments

The authors would like to acknowledge the technical support from Chong Xu at the Institute of Crustal Dynamics, China Earthquake Administration, China, and Haogang Dong at Changsha Comprehensive Survey Center of Natural Resources, China Geological Survey, China.

Conflict of interest

The authors declare that the research was conducted in the absence of any commercial or financial relationships that could be construed as a potential conflict of interest.

Publisher's note

Supplementary material

The Supplementary Material for this article can be found online at: https://www.frontiersin.org/articles/10.3389/fenvs.2023.1225916/full#supplementary-material

References

Bai, B., Jiang, S., Liu, L., Li, X., and Wu, H. (2021a). The transport of silica powders and lead ions under unsteady flow and variable injection concentrations. *Powder Technol.* 387, 22–30. doi:10.1016/j.powtec.2021.04.014

Bai, B., Nie, Q., Zhang, Y., Wang, X., and Hu, W. (2021b). Cotransport of heavy metals and SiO2 particles at different temperatures by seepage. *J. Hydrology* 597, 125771. doi:10.1016/j.jhydrol.2020.125771

Bear, J. (1972). *Dynamics of fluids in porous media*. New York, USA: American Elsevier Publishing Company, Inc.

Charbeneau, Rj, and Sherif, Sa (2002). Groundwater hydraulics and pollutant transport. *Appl. Mech. Rev.* 55 (2), B38–B39. doi:10.1115/1.1451232

Chen, X., Tu, X., Xie, P., and Li, Y. (2010). Progresses in the research of human induced variability of hydrological elements. *Adv. Earth Sci.* 25 (8), 800–811.

Claessens, L., Schoorl, J. M., Verburg, P. H., Geraedts, L., and Veldkamp, A. (2009). Modelling interactions and feedback mechanisms between land use change and landscape processes. *Agric. Ecosyst. Environ.* 129 (1-3), 157–170. doi:10.1016/j.agee.2008.08.008

Cui, J., Du, J., and Li, X. (2015). Effects of land use change on groundwater quality in Qiqihar city. *Earth Environ.* 43 (3), 308–315.

Deng, H.-P. (2001). Impacts of climate change and land use-land cover change on hydrology and water resources. *Adv. Earth Sci.* 16 (3), 436–441.

Elmahdy, S. I., and Mohamed, M. M. (2016). Land use/land cover change impact on groundwater quantity and quality: A case study of ajman emirate, the United Arab Emirates, using remote sensing and GIS. *Arabian J. Geosciences* 9 (19), 722–735. doi:10.1007/s12517-016-2725-y

Freeze, R. A., and Cherry, J. A. (1979). *Groundwater*. Cliffs, NJ: Prentice-Hall.

Fu, Q., Yang, D., Zhang, X., Xia, F., and Fei, W. (2016). Time and space differentiation of relative carrying capacity of resources in Ili based on improved model. *J. Univ. Chin. Acad. Sci.* 33 (2), 170–177.

Ghaffari, G., Keesstra, S., Ghodousi, J., and Ahmadi, H. (2010). SWAT-simulated hydrological impact of land-use change in the Zanjanrood basin, Northwest Iran. *Hydrological Process. Int. J.* 24 (7), 892–903. doi:10.1002/hyp.7530

Hancock, P. J. (2002). Human impacts on the stream–groundwater exchange zone. *Environ. Manag.* 29 (6), 763–781. doi:10.1007/s00267-001-0064-5

Hu, X., Wu, B., Gao, F., Du, M., and Zhang, W. (2021). Response of groundwater level dynamics to land use change in hutubi county. *J. Soil Water Conservation* 35 (5), 227–234.

Huo, S., Wang, W., and Duan, L. (2020). An analysis of groundwater resources composition and driving force in Huocheng county. *Hydrogeology Eng. Geol.* 47 (2), 51–59.

Izbicki, J. A., Teague, N. F., Hatzinger, P. B., Böhlke, J. K., and Sturchio, N. C. (2015). Groundwater movement, recharge, and perchlorate occurrence in a faulted alluvial aquifer in California (USA). *Hydrogeology J.* 23 (3), 467–491. doi:10.1007/s10040-014-1217-y

Kang, L., and Zhang, H. (2012). Assessment of the land desertification sensitivity of newly reclaimed area in Yili, Xinjiang. *Resour. Sci.* 34 (5), 896–902.

Lei, M., Kong, X., Zhang, X., and Wu, F. (2017). Land use change and impact on groundwater storage in the Huang-Huai-Hai Plain. *Resour. Sci.* 39 (6), 1099–1116.

Lei-Hua, D., Li-Hua, X., Kun-Xia, Y., and Shuai, L. (2012). Research advances in effects of climate change and human activities on hydrology. *Adv. Water Sci.* 23 (2), 278–285.

Li, L., Huang, X., and Zhong, T. (2006). A likely molecular basis of the susceptibility of Giardia lamblia towards oxygen. *Res. Soil Water Conservation* 13 (2), 202–211. doi:10.1111/j.1365-2958.2005.04896.x

Li, Y., and Tao, Z. (2015). *Investigation and evaluation report on groundwater resources and environment in Ili river valley, Xinjiang*. Xi'an, Shaanxi, China: Xi'an Center of Geological Survey, China Geological Survey.

Liu, B., Yan, G., Ma, Y., and Scheuermann, A. (2023). Measurement of *in-situ* flow rate in borehole by heat pulse flowmeter: Field-case study and reflection. *Geosciences* 13 (5), 146. doi:10.3390/geosciences13050146

Liu, J., Yu, Q., Yue, D., Zhang, Q., and Wu, Y. (2019a). miRNA-223-3p and let-7b-3p as potential blood biomarkers associated with the ischemic penumbra in rats. *Trans. Chin. Soc. Agric. Mach.* 50 (12), 205–216.

Liu, R., Wang, J., Zhou, Y., Huang, H., and Chen, C. (2019b). Simulation of karst groundwater balance in the Westshan mountains, Heqing county, Yunnan Province. *Carsologica Sin.* 38 (4), 532–538.

Ma, X.-W., Li, B.-G., Wu, C.-R., Peng, H.-J., and Guo, Y.-Z. (2003). Predicting of temporal-spatial change of groundwater table resulted from current land use in Minqin oasis. *Adv. Water Sci.* 14 (1), 85–90.

Ma, Y., Kong, X. Z., Scheuermann, A., Galindo-Torres, S., Bringemeier, D., and Li, L. (2015). Microbubble transport in water-saturated porous media. *Water Resour. Res.* 51 (6), 4359–4373. doi:10.1002/2014wr016019

Ma, Y., Yan, G., and Scheuermann, A. (2022). Discrete bubble flow in granular porous media via multiphase computational fluid dynamic simulation. *Front. Earth Sci.* 10, 947625. doi:10.3389/feart.2022.947625

Ma, Y., Yan, G., Scheuermann, A., Li, L., Galindo-Torres, S., and Bringemeier, D. (2014). "Discrete microbubbles flow in transparent porous media," in Proceedings of the 6th International Conference on Unsaturated Soils (UNSAT 2014), Australia , Sydney, July 2014, 1219–1223.

Prabhakar, A., and Tiwari, H. (2015). Land use and land cover effect on groundwater storage. *Model. Earth Syst. Environ.* 1 (4), 45–10. doi:10.1007/s40808-015-0053-y

Shu, L., Xu, L., Yuan, Y., Lv, Y., Lu, C., and Liu, B. (2022). Analysis on variation of groundwater flow field and its main influencing factors in the typical district of Sanjiang Plain. *J. Hydraulic Eng.* 53 (6), 644–654.

Tong, S. T., Sun, Y., Ranatunga, T., He, J., and Yang, Y. J. (2012). Predicting plausible impacts of sets of climate and land use change scenarios on water resources. *Appl. Geogr.* 32 (2), 477–489. doi:10.1016/j.apgeog.2011.06.014

Wang, S., Liu, J., Zhang, Z., Zhou, Q., and Zhao, X. (2001). Analysis on spatial-temporal features of land use in China. *Acta Geographica Sinica* 56 (6), 631–639.

Wang, Z., Xaymurat, A., and Hu, X.-G. (2012). Analysis on water environment change and its influence factors in Huocheng county of Xinjiang. *Water Conservancy Sci. Technol. Econ.* 18 (6), 3–8.

Xu, X., Liu, J., Zhang, S., Li, R., Yan, C., and Wu, S. (2018). "China many periods of land use land cover remote sensing monitoring data set (CNLUCC)," in *Resources and environment science data center data registration and publication system, Chinese Academy of sciences*. Beijing, China: Chinese Academy of Science.

Yan, G., Bore, T., Bhuyan, H., Schlaeger, S., and Scheuermann, A. (2022a). The technical challenges for applying unsaturated soil sensors to conduct laboratory-scale seepage experiments. *Sensors* 22 (10), 3724. doi:10.3390/s22103724

Yan, G., Bore, T., Schlaeger, S., Scheuermann, A., and Li, L. (2022b). Investigating scale effects in soil water retention curve via spatial time domain reflectometry. *J. Hydrology* 612, 128238. doi:10.1016/j.jhydrol.2022.128238

Yan, G., Li, Z., Bore, T., Galindo Torres, S. A., Scheuermann, A., and Li, L. (2022c). A lattice Boltzmann exploration of two-phase displacement in 2D porous media under various pressure boundary conditions. *J. Rock Mech. Geotechnical Eng.* 14 (6), 1782–1798. doi:10.1016/j.jrmge.2022.05.003

Yan, G., Li, Z., Bore, T., Torres, S. a. G., Scheuermann, A., and Li, L. (2021). Discovery of dynamic two-phase flow in porous media using two-dimensional multiphase lattice Boltzmann simulation. *Energies* 14 (13), 4044. doi:10.3390/en14134044

Yang, L., and He, G. (2008). *Consid. water-saving irrigation Ili River Basin* Yangtze River 39 (20), 50–51.

Yin, X. (2016). *Aquifer structure study and groundwater resource evaluation in Huocheng Basin*. Master of Engineering Thesis. New Delhi, India: Institute of Disaster Prevention.

Zhang, X., Zhang, L., and Gu, J. (2014). Spatial and temporal variation characteristics of groundwater and its response to land use/cover change in dunhuang oasis. *J. Lanzhou Univ. Nat. Sci.* 50 (3), 311–317.

Zhang, Y., Sheng, L., Yuan, G., Ge, Y.-Y., and Yu, J.-X. (2022). An analysis of the relationship between the groundwater depth and the land use change in arid and semi-arid areas: Taking kashgar delta as an example. *China Rural Water Hydropower* 475 (5), 38–44.

Zhao, Y., Zou, S., Shen, H., Zhou, C., Fan, L., Zhu, D., et al. (2021). Dynamic characteristics and equilibrium of water level of the karst groundwater system beneath the Huixian wetland. *Carsologica Sin.* 40 (2), 325–333.

Zheng, J., Wang, H., and Liu, B. (2022). Impact of the long-term precipitation and land use changes on runoff variations in a humid subtropical river basin of China. *J. Hydrology Regional Stud.* 42, 101136. doi:10.1016/j.ejrh.2022.101136

Zhu, H., and Li, X. (2003). Discussion on the index method of regional land use change. *Acta Geogr. Sin.* 58 (5), 643–650.

Frontiers in Earth Science

Investigates the processes operating within the major spheres of our planet

Advances our understanding across the earth sciences, providing a theoretical background for better use of our planet's resources and equipping us to face major environmental challenges.

Discover the latest Research Topics

See more →

Frontiers

Avenue du Tribunal-Fédéral 34
1005 Lausanne, Switzerland
frontiersin.org

Contact us

+41 (0)21 510 17 00
frontiersin.org/about/contact